UC San Diego
UC San Diego Electronic Theses and Dissertations

Title
Fusogenic Porous Silicon Nanoparticles as a Platform Technology for Gene Therapy

Permalink
https://escholarship.org/uc/item/650030mf

Author
Kim, Byungji

Publication Date
2019

Peer reviewed|Thesis/dissertation

UNIVERSITY OF CALIFORNIA SAN DIEGO

Fusogenic Porous Silicon Nanoparticles
as a Platform Technology for Gene Therapy

A dissertation submission in partial satisfaction of the requirements for the degree

Doctor of Philosophy

in

Materials Science and Engineering

by

Byungji Kim

Committee in charge:

        Professor Michael J. Sailor, Chair
        Professor Stephen B. Howell, Co-Chair
        Professor Jesse Jokerst
        Professor Ester Kwon
        Professor Nicole Steinmetz
        Professor Liangfang Zhang

2019

The Dissertation of Byungji Kim is approved, and it is acceptable in quality and form for

publication on microfilm and electronically:

_____

_____

_____

_____

_____

Co-Chair

_____

Chair

University of California San Diego

2019

iii

DEDICATION

To my father, mother, and brother.

TABLE OF CONTENTS

LIST OF FIGURES

LIST OF TABLES

ACKNOWLEDGEMENTS

I would like to give special thanks to:

Prof. Michael J. Sailor for being the best mentor I could have ever had the fortune to work with. Thanks for always giving me guidance on how to improve on little to large aspects of being an academic, and nurturing me to become the best scientist that I can be. I will miss stealing chocolate from your desk and ingesting inappropriately large amounts of sugar during teleconferences, as well as our in-depth discussions on superhero movies.

The Sailor lab members, especially Joanna Wang, Geoffrey Ian Hollett, Jon Zuidema for the fun conversations and spending/surviving the last five years together with me. As well as Tushar Kumeria, Tiffany Chen, Qinglin Yang, Ruhan Fan for keeping me pleasant company in lab, at lunch and at the occasional outings to Convoy for food.

Friends, particularly the Blixicorns who introduced me to the ultimate nerdom of board games and anime, which kept me sane and young. Joanna, for numerous foodie trips to introduce me to San Diego, and for being my local bestie. Gif for always having a ready ear for our concerns and jokes, as well as an open-mind regarding my unappetizing yet delicious food creations. Eleanor for providing music therapy with her brilliance on the piano, and for lending me her flute and piccolo for impromptu jams. And Alessandra McGinnis for being the most supportive cheerleader and for being the model that I channel to become a kinder human being.

Finally, my family who take corresponding authorship on helping me grow up to be who I am today. Thank you for always believing in me, for keeping me healthy and relaxed through what is supposed to be a highly stressful time, for being my beta-testers in practicing non-technical explanations of my research, for supporting my weird obsession with Iron Man, for always thinking I lost weight when I didn't, for always having a Korean drama on recommendation, and for being my primary mentors and role models in life.

Chapter 1, in full, has been submitted for publication of the material as it may appear in **Kim, B.**, Park, J., Sailor, M.J., Rekindling RNAi Therapy: Materials Design Requirements for In Vivo siRNA Delivery. *Adv Mater.* Submitted. The author of this dissertation was the primary author of the material.

Chapter 2, in full, is a reprint of the material as it appears in **Kim, B.**, Sailor, M.J. Synthesis, Functionalization, and Characterization of Fusogenic Porous Silicon Nanoparticles for Oligonucleotide Delivery. *J. Vis. Exp.* (146), e59440, doi:10.3791/59440 (2019). The author of this dissertation was the primary author of the material.

Chapter 3, in full, has been submitted for publication of the material as it may appear in **Kim, B.**, Varner, J.A., Howell, S.B., Ruoslahti, E., Sailor, M.J. Securing the Payload, Finding the Cell, Avoiding the Endosome: Peptide-Targeted, Fusogenic Porous Silicon Nanoparticles for More Effective Delivery of siRNA Therapies. *Adv Mater.* Submitted. The author of this dissertation was the primary author of the material.

Chapter 4, in full, has been submitted for publication of the material as it may appear in **Kim, B.**, Varner, J.A., Howell, S.B., Ruoslahti, E., Sailor, M.J. Securing the Payload, Finding the Cell, Avoiding the Endosome: Peptide-Targeted, Fusogenic Porous Silicon Nanoparticles for More Effective Delivery of siRNA Therapies. *Adv Mater.* Submitted. The author of this dissertation was the primary author of the material.

Chapter 5, in full, is a reprint of the material as it appears in **Kim, B.***, Pang, H.*, Kang, J., Park, J., Ruoslahti, E., Sailor, M.J. Immunogene therapy with fusogenic nanoparticles modulates macrophage response to Staphylococcus aureus. *Nat Commun*, (2018). The author of this dissertation was the primary author of the material.

Chapter 6, in full, is currently being prepared for submission for publication. **Kim, B.**, Yang, Q., Bhatia, S., Ruoslahti, E., Sailor, M.J. Wide-spectrum immunotherapy against bacterial

infection using fusogenic nanoparticles. Manuscript in Preparation. The author of this

dissertation was the primary author of the material.

VITA

Dec. 2011   Bachelor of Science and Engineering in Materials Science and Engineering

University of Michigan, Ann Arbor

Feb. 2014   Master of Science in Bio and Brain Engineering

Korea Advanced Institute of Science and Technology, South Korea

Jun. 2019   Doctor of Philosophy in Materials Science and Engineering

University of California San Diego

PUBLICATIONS

1.   Saavedra, S. L., Teulier, C., Smith, B. A., **Kim, B.**, Beutler, B. D., Martin, B. J. & Ulrich, B. D. Vibration-induced motor responses of infants with and without myelomeningocele. *Phys Ther* 92, 537-550, doi:10.2522/ptj.20110074 (2012).

2.   Quan, Y. H., **Kim, B.**, Park, J. H., Choi, Y., Choi, Y. H. & Kim, H. K. Highly sensitive and selective anticancer effect by conjugated HA-cisplatin in non-small cell lung cancer overexpressed with CD44. *Exp Lung Res* 40, 475-484, doi:10.3109/01902148.2014.905656 (2014).

3.   Lee, J., Kim, J., Jeong, M., Lee, H., Goh, U., Kim, H., **Kim, B.** & Park, J. H. Liposome-based engineering of cells to package hydrophobic compounds in membrane vesicles for tumor penetration. *Nano Lett* 15, 2938-2944, doi:10.1021/nl5047494 (2015).

4.   Hussain, S., Joo, J., Kang, J., **Kim, B.**, Braun, G.B., She, Z., Kim, D., Mann, A.P., Mölder, T., Teesalu, T., Carnazza, S., Guglielmino, S., Sailor, M.J., Ruoslahti, E. Enhanced antibacterial efficacy of antiobiotic-loaded nanoparticles targeted to the site of infection. *Nat Biomed Eng*, (2018).

5.   **Kim, B.***, Pang, H.*, Kang, J., Park, J., Ruoslahti, E., Sailor, M.J. Immunogene therapy with fusogenic nanoparticles modulates macrophage response to Staphylococcus aureus. *Nat Commun*, (2018).

6.   **Kim, B.**, Sailor, M.J. Synthesis, Functionalization, and Characterization of Fusogenic Porous Silicon Nanoparticles for Oligonucleotide Delivery. *J. Vis. Exp.* (146), e59440, doi:10.3791/59440 (2019).

7.   Robbiano, V., Mariani, S., Iglio, R., La Mattina, A.A., Wang, J., **Kim, B.**, Kumeria, T., Sailor, M.J., Barillaro, G. Moldless Printing of High-Magnification PDMS Smart Lenses Embedding Nanostructured Porous Silicon Optical Components for Hand-Held Low-Cost Microscopy. *Adv Mater.* Submitted.

8. **Kim, B.**, Sun, S., Varner, J.A., Howell, S.B., Ruoslahti, E., Sailor, M.J. Securing the Payload, Finding the Cell, Avoiding the Endosome: Peptide-Targeted, Fusogenic Porous Silicon Nanoparticles for More Effective Delivery of siRNA Therapies. *Adv Mater.* Submitted.

9. **Kim, B.**, Park, J., Sailor, M.J., Rekindling RNAi Therapy: Materials Design Requirements for In Vivo siRNA Delivery. *Adv Mater.* Submitted.

10. Kumeria, T., Wang, J., **Kim, B.**, Park, J., Zuidema, J., Klempner, M., Cavacini, L., Wang, Y., Sailor, M.J. Enteric polymer-coated porous silicon nanoparticles for site-specific oral protein delivery. Manuscript in Preparation.

11. **Kim, B.**, Yang, Q., Bhatia, S., Ruoslahti, E., Sailor, M.J. Wide-spectrum immunotherapy against bacterial infection using fusogenic nanoparticles. Manuscript in Preparation.

12. Hollett, G., Kumeria, T., **Kim, B.**, Martin, T., Ipekci, I., Palomba, J., Leonard, H., Wang, J., Chan, N., Pierron, A., Ayres, J., Sailor, M.J. Longer Acting Injectables: Continuous, Linear Release of a Crystalline Contraceptive from a Porous Silicon Host. Manuscript in Preparation.

PATENT

1. Sailor, M.J., **Kim, B.**, Kang, J. 2015. Fusogenic liposome-coated porous silicon nanoparticles. US Patent Application Number WO2017008059A1, filed July 9, 2016.

Fusogenic Porous Silicon Nanoparticles
as a Platform Technology for Gene Therapy

by

Byungji Kim

Doctor of Philosophy in Materials Science and Engineering

University of California, San Diego, 2019

Professor Michael J. Sailor, Chair
Professor Stephen B. Howell, Co-Chair

With increasing discoveries in genetic and biological pathways with respect to disease treatment, the potential for gene therapy is growing exponentially. In parallel, gene modulating tools have also expanded; catalyzed by the discovery of the RNA interference and zinc finger proteins in the 1990s, the 21st century has seen a variety of mechanisms for editing genetic expression (e.g. double-stranded oligonucleotides, zinc finger nucleases (ZFNs), transcription activator-like effector nuclease (TALENS), clustered regularly interspaced short palindromic repeats (CRISPR/Cas), etc.). However, a primary roadblock in enabling these gene editing tools for clinical translation is the biological clearance and degradation mechanisms that prevent the tools from reaching the target cells. The fusogenic porous silicon nanoparticles (FNPs) present an effective solution to this delivery challenge.

Chapter one provides introductory overview of gene therapy, their limitations, as well as the current state-of-the-art technologies with the aim of delineating materials design criteria of RNAi therapeutics. Furthermore, a brief analysis and discussion on trends of publications and clinical translations of RNAi therapy formulations are provided.

Chapter two details the synthesis protocol of fusogenic porous silicon nanoparticles. As the FNPs comprise of multi-layer structure (ie. payload-loaded pSiNPs, calcium silicate sealing, lipid bilayer encapsulation, targeting peptide decoration), the protocol requires delicate and precise handling for formation of stable nanoparticles. Examples of successful versus unsuccessful syntheses are presented, and critical steps to positive outcome are highlighted. The potential for variations and alternative optimizations to the protocol are discussed.

Chapter three delves into the material properties that enable FNP function, and the biological pathways that FNPs depend on for its unique cellular uptake and processing. The intracellular fate and metabolism of individual components of the FNP system (e.g. oligonucleotide payload, pSiNP core, and lipid bilayer shell) are also presented. The fundamental information gained from studying the material interaction at a single-cell level is used to inform the following chapters that deal with application of FNPs in disease models.

Chapters 4-6 demonstrate the FNPs as a platform technology that can be developed into a wide range of therapeutic formulations. By simple exchange of targeting peptides and the siRNA payload, the FNPs demonstrate successful therapeutic outcomes in mouse models of cancer (Chapter 4) and bacterial infections (Chapters 5 and 6).

Chapter 1:

Introduction

1.1 Abstract

With the recent FDA approval of the first siRNA-derived therapeutic, RNA interference (RNAi)-mediated gene therapy is undergoing a transition from research to the clinical space. The primary obstacle to realization of RNAi therapy has been the delivery of oligonucleotide payloads. This review aims to identify and describe key design features needed for nanoscale vehicles to achieve effective delivery of siRNA-mediated gene silencing agents *in vivo*. We break the problem into three elements: (1) protection of siRNA from degradation and clearance; (2) selective homing to target cell types; and (3) cytoplasmic release of the siRNA payload by escaping or bypassing endocytic uptake. The *in vitro* and *in vivo* gene silencing efficiency values that have been reported in publications over the past decade are quantitatively summarized by material type (lipid, polymer, metal, mesoporous silica, and porous silicon), and the overall trends in research publication and in clinical translation are discussed to reflect on the direction of the RNAi therapeutics field.

1.2 Gene Editing: RNA Interference

1.2.1. Brief History of Gene Editing Tools

Since the completion of the Human Genome Project in 2003[1-4], through which we mapped the complete DNA sequence of the human race, we have made significant strides to decipher the function and mechanism of genetic pathways with regard to disease pathogenesis. The concept of disease treatment by genetic modification was first discussed in the 1960s, when exogenous DNA-based *in vitro* cell modulation in viral infections was observed and actively pursued for the first generation of research in gene therapy[5]. Next, the 1970s saw the initial attempts for gene modification using recombinant DNAs (rDNAs; a combination of more than one DNA sequence from one or more species)[6] with viral infection or calcium phosphate as the primary transfection methods. This discovery led to developments of cell lines[7], genetically

modified mice[8], and human protein (*e.g.* insulin) production in bacterial (e.g. *Escherichia coli*)[9]. Additionally, the first *in vitro* messenger RNA (mRNA) transfection using liposomes to express rabbit globin in mouse lymphocytes was conducted in 1978[10]. The fast-evolution of genetic engineering catalyzed important discussions in the ethics, policies, and economics of the field, resulting in guidelines and regulations that limit and restrict hierarchies of gene modification research (i.e. from bacterial modifications to plants, mammalian systems, to humans) for patentable materials and FDA-approvable systems[5,11-14].

The late 1980s and early 1990s saw emergence of new classes of gene editing tools. Zinc finger motif in the transcription factor IIIA (TFIIIA) was initially discovered in 1982[15], which led to the 1994 discovery and development of the zinc finger nuclease (ZFN) that could cleave specific DNA domains by altering the DNA-binding motif of the system[16,17]. Nearly 20 years later, similar restriction enzyme-based systems — TALEN[18] and CRISPR/Cas[19] — were discovered and developed into potential tools for gene therapy in 2010 and 2012, respectively.

In the meantime, sequence-specific mRNA degradation *via* double-stranded RNA (dsRNA)-mediated transient silencing was discovered in 1997 by Mello[20], and further developed by Fire[21] in 1998; the phenomenon was termed "RNA interference (RNAi)". The mechanism for RNAi was elucidated soon after, with the identification of short interfering RNAs (siRNAs) and the RNA-induced silencing complex (RISC)[22,23]. The discovery was ground-breaking in that RNA-based gene modification offered a simpler, reversible, and more transient effect than the DNA- and restriction enzyme-based approaches, and thus presented a more favorable option when relatively short-term effects are desired (*i.e.* in acute disease treatment).

An overview of each gene editing tool is summarized in **Table 1.1**. In particular, the following review focuses on the use of RNAi for gene therapy, and the full mechanism of RNAi is described in the following section.

1.2.2. RNA Interference

RNA interference is a transient gene silencing mechanism found endogenously in eukaryotic cells. **Figure 1.1** details the mechanism by which siRNAs silences gene expression. The pathway is initiated by the presence of siRNAs (either artificially synthesized and delivered into the cell, or endogenously produced by dicer-mediated cleavage of dsRNAs into shorter 21-25 base-pair sequences) in the perinuclear region of the cell cytoplasm. Here, the siRNA binds to the RISC, and is unwound into a single-stranded RNA by Argonaut 2 (AGO2; a component of the RISC)-mediated cleavage of the unnecessary strand.[24] Next, the RISC guides the now single-stranded siRNA to its complementary sequence on the cell's endogenous mRNA for base-pair binding, at which point the RISC cleaves the mRNA for degradation.[22,24-26] After cleavage of the mRNA, the RISC and single-stranded siRNA are free to bind to other mRNAs, effectively preventing translation of the complementary mRNA sequence into proteins. Thus, siRNA-mediated RNAi silences the ability of the gene to express proteins.

Another nucleic acid sequence that is able to induce RNAi is microRNA (miRNA), as shown in **Figure 1.2**. There are three major differences between siRNA and miRNA. First is that miRNA may be synthesized artificially or it may be endogenously generated from the cell's nucleus as a hairpin structure that loops on itself to form a double-stranded sequence (pre-miRNA). When exported out of the nucleus to the cytoplasm, endogenous miRNAs are cleaved by the dicer to remove the hairpin loop. Second, miRNA is not able to completely bind to the complement mRNA sequence due to its non-linear structure; instead, only 2-7 of the nucleotide sequences at the 5' end (called the "seed sequence") of the miRNA bind to the mRNA.[24] This short binding region results in weaker attachment to the mRNA, which leads to lower specificity, but to a consequently wider range of mRNA targets that can be silenced. Thus, whereas siRNAs silence a specific target sequence, miRNAs may regulate a family of gene expressions.

Lastly, there are two classes of miRNA; one that undergoes the same RNAi pathway as siRNAs, and another that undergoes an alternative pathway that simply binds to the complementary mRNA sequence to block its translation into protein.[27-29]

Overall, RNAi is an innate cellular machine that allows one to silence the expression of essentially any target gene. However, for therapeutic applications RNAi is only feasible with a supportive technology to deliver the oligonucleotides to the site of action: the cell cytoplasm.

1.3   Limitations and Material Design Requirements in RNAi Therapy

Whereas there is a wide range of gene modification tools available (**Table 1**), there is an unmet need for platforms that can effectively and selectively deliver them to targeted cells *in vivo.* A successful system must overcome substantial extracellular and intracellular barriers to RNAi delivery. The design requirements can be broken into three components *(1) protection of the siRNA payload; (2) targeting this payload to a specific subset of cells; and (3) effective release of siRNA into the cytoplasm*.

1.3.1. Extracellular Barriers

The RNAi therapeutic must traffic from the site of administration to the target cell it needs to modify, and this is a particular challenge when local administration is not available. On its way to the targeted cell, an siRNA therapuetic must overcome many obstacles; primary among these are: (a) degradation by nucleolytic enzymes; (b) uptake by cells of the immune system; and (c) inefficient tissue penetration (**Figure 1.3)**. As a consequence of its strong anionic charge, its impermeability to cells, and its (often) sequence-dependent toxicity, free siRNA is typically degraded and cleared from circulation with a plasma half-life of a mere 10 minutes.[24,25,30-36]

Serum endonucleases are largely responsible for the degradation of siRNA post-administration (**Figure 1.3a**). In particular, ribonucleases bind specifically to RNAs in blood circulation and generate fragments for degradation.[31,37-40] The enzymes attack the unstable ends of the siRNA to begin separation of the strands and degradation of the RNA fragments; many of the early RNAi studies implemented various chemical strategies to modify the ends of siRNA (*i.e.* by hairpin formation, sequence modification, or locked nucleic acids (LNAs))[37,39-42] as a protection strategy. There are also numerous chemically-modified and –stabilized siRNAs— (for example, the *N*-acetylgalactosamine (GalNAc)-conjugated siRNAs that have been used for targeting the asialoglycoprotein receptor (ASGPR) in liver hepatocytes, as a potential alternative treatment for diseases requiring liver transplantation.[43-45] Because even chemically modified siRNA has the potential for degradation or other complications, researchers have resorted to the use of nanocarriers to temporarily encapsulate the oligonucleotide therapeutics, thereby limiting access of enzymes and other potential inhibitors.

As shown in **Figure 1.3b**, the *mononuclear phagocytic system* (MPS; also known as reticuloendothelial system (RES)) plays a strong role in clearance of siRNAs from blood circulation, especially when a nanocarrier is used to protect the oligonucleotide. While siRNAs and other small molecules (with sizes < 8 nm) are removed via renal clearance, larger nano-scale objects are readily identified by the body's immune system to be phagocytosed by macrophages in the major RES organs, such as the liver, spleen, and lungs.[46] The primary mechanism by which the immune cells recognize and clear these objects is by opsonization, where molecules that recognize foreign body (opsonins; *e.g.* antibodies) bind to the surface of the target to label them for phagocytic clearance by the complement immune response.[47-49] The effect may be diminished by adjusting the particle properties, such as size and shape,[46,50-54] surface chemistry (*e.g.* PEGylation),[31,32,50,55,56] and surface charge (decreased clearance is observed in positive compared to neutral and negative surface charges).[50,56-58] While this

phenomenon can be used for passive homing when the target disease is localized in the RES organs, it remains a major barrier not only in siRNA delivery, but also in other nanodelivery systems.

Lastly, *tissue penetration* to transport the siRNA from the lumen of the blood vessel into the target tissue is required if the target cell for gene silencing is in tissues far removed from the vascular walls (**Figure 1.3c**). The strongly anionic nature of siRNA repels it from the cellular membrane, which is also negatively charged. Thus, oligonucleotides have difficulty undergoing extravasation, and they avoid clearance by diffusing either through (transcellular diffusion) or between (paracellular diffusion) endothelial cells; these diffusion pathways are of critical importance when targeting the brain through the blood-brain barrier (BBB).[59,60] This obstacle may be overcome when a nano-carrier is used to deliver siRNA, but as the pores in the vascular capillaries are in the 60-80 nm diameter range, larger carriers can require additional features in order to penetrate tissues.[61]

1.3.2. Extracellular Barriers

Once the siRNA reaches its target cell, it must get into the cell to perform its gene silencing task. As aforementioned, the siRNA must localize in the cytoplasm, particularly in the perinuclear region. However, due to the anionic charge, siRNA is generally cell impermeable in its native state.[62,63] While a number of proteins have been reported as oligonucleotide-specific receptors or transporters in cells, none have been fully validated as of yet.[64-66]

Nano-carriers that are employed to overcome this obstacle must be able to induce cytosolic release of their siRNA payload. A common means of entering the cell is through endocytosis. The endocytic pathways are mediated by different proteins and are often differentiated as either dynamin-dependent (*e.g.* caveolin, clathrin)[64,67,68] or dynamin-independent (*e.g.* macropinocytosis, CLIC)[64,67,69,70] routes. However, cellular uptake by way of

endocytosis entraps the siRNA-loaded carriers within endosomal vesicles that steadily progress from early (pH 6-6.5) to late (pH 5-5.5) endosomes, and finally to lysosomes (pH 4.5-5).[71]

As a primary nano-carrier used for siRNA delivery, lipid nanoparticles (to be discussed in the following section) are one of the only systems to have been rigorously studied for quantification and mechanism of cytosolic siRNA delivery. Studies investigating the primary uptake pathway of lipid nanoparticles and the intracellular fate of their siRNA payloads demonstrated that approximately 70% of the siRNA molecules that initially enter the cell are excreted within the first 24 h (**Figure 1.4a**), and that only 1-2% of the total siRNA is able to escape from the early endosomes into the cytoplasm to undergo RNAi (**Figure 1.4c**).[72,73] These findings suggest that a great majority of the delivered siRNA undergoes exocytosis and lysosomal degradation (**Figure 1.4b**) if it is unable to localize in the cytoplasm by the early endosome stage. While there are numerous nanosystems in addition to lipid nanoparticles that have been used to enhance siRNA delivery across a wide range of cell types, and many report significant RNAi-induced gene silencing, there is very little information available on the efficiency of cytosolic delivery of siRNA. So it is unclear how limiting the endocytosis pathway is for siRNA delivery in general. Nevertheless, overcoming endocytosis by way of escaping the endosome (*e.g.* proton sponge), or bypassing endocytosis (*e.g. via* fusion, membrane penetration) (**Figures 1.4c, d**) incorporated into the particle design is expected to greatly improve RNAi efficiency.

1.4   Protective Carriers for siRNA Delivery

As opposed to restriction enzyme-based tools that require the delivery of multiple payloads (*e.g.* enzyme, guide nucleotide sequence, and DNA fragments for gene insertion), RNAi therapeutics present a simpler and more feasible payload for genetic modification, as they are singular anionic oligonucleotides. There has been a robust effort to develop delivery

vehicles for RNA-based therapeutics to diminish their vulnerability to degradation and clearance.[74] Delivery vehicles can offer a dual function, both in protecting the oligonucleotide from the extracellular barriers leading to clearance, and in overcoming the intracellular barriers that limit cytosolic delivery of siRNAs. While viruses serve as one of the more common transfectants (albeit more so for DNA vectors), they carry concerns of immunogenicity and cytotoxicity.[75,76] Focussing on non-viral nanoparticle-based carrier systems for siRNA delivery, **Figure 1.5** shows a generalized schematic of each carrier type to be discussed, with representative electron micrograph images.

Table 1.2 and **Figure 1.6** compile materials used in the last decade for *in vitro* and *in vivo* siRNA delivery, and their knockdown (KD) efficiency in selected *in vitro* and *in vivo* models. Of note, we have listed only those publications that reported the *in vivo* KD efficiency *via* quantitative measurements (e.g. qRT-PCR), rather than qualitative or indirect observation (e.g. Western blot, therapeutic outcome). The average gene silencing effect seen across the literature seems to be relatively similar regardless of material type; with *in vitro* rates ranging from approximately 60-80%, and *in vivo* rates ranging from approximately 55-80%. As might be expected, the *in vitro* effects are greater than *in vivo* effects overall, and lipid-based systems performed consistently strongly both *in vitro* and *in vivo*.

1.4.1. Lipid-based Nanoparticles

Nanoparticles made of lipids represent the most widely used material for gene delivery.[30,38,47,62] Within the umbrella of lipid nano-carriers, there are micelles (small unilamellar vesicles with a hydrophobic core and a hydrophilic exterior), solid lipid nanoparticles (SLNs; micellar vesicles with a hydrophobic solid lipid core that prevents lipid permeation and degradation[121]), and liposomes (large vesicles with a lipid bilayer that forms a hydrophilic core and exterior[47]). The primary advantage of these lipid constructs are the simplicity in synthesis

9

and versatility of particle function that can be achieved by varying the lipid composition. However, they suffer from relatively low loading capacity for siRNA and premature leakage of payloads, and they require additional cationic materials to condense the highly anionic payloads into the liposomal core. Commonly used condensers include protamine, peptides, and polyethylenimine (PEI).[89,122-126]

As can be seen in **Table 1.2** and **Figure 1.6**, lipid-based systems tend to report relatively strong *in vitro* and *in vivo* gene silencing effects, with an average knockdown efficiency of 80.4 ± 13.8% *in vitro* and 79.3 ± 15.2% *in vivo.* These numbers are representative of a wide range of lipid particles, including liposomes, SLNs, and peptidomimetic lipoplexes, which have been documented in numerous reviews over the years.[24,30,32,36,38,61,62,74,121,127,128]

Among those considered here, a promising system is the stable nucleic acid lipid particle (SNALP; now simply called the lipid nanoparticle (LNP)), which is a formulation that was optimized specifically for siRNA delivery.[92,129,130] The lipid shell is composed of a mix of natural and artificially synthesized materials – DLinDMA, DSPC (1,2-distearoyl-*sn*-glycero-3-phosphocoline), cholesterol, and PEG-c-DMA (3-*N*-[ω-methoxypoly(ethylene glyol)$_{2000}$carbamoyl]dimyristyloxy-propylamine). The ionizable DLinDMA lipid comprises 40% of the molar ratio, and provides an essential cationic surface charge that helps attract the particle toward the cell membrane to better facilitate uptake. The DSPC is a minor component at 10% molar ratio of incorporation, but it plays a key role in stabilizing the structure during synthesis and in circulation. Cholesterol (typically 40% of the molar ratio), plays a stabilizing function in many liposomal formulations; by incorporating itself into the lipid bilayer to decrease membrane fluidity and permeability, cholesterol helps reduce premature payload leakage from the liposomes.[131,132] Lastly, the PEG-c-DMA lipid displays an interesting property that is not commonly observed in other PEGylated systems. While PEG is known to provide particle stability, hydrophilicity, and stealth properties, the PEG-c-DMA has an activating component,

10

such that the molecule dissociates from the complete liposome soon after it is introduced to the body *via* intravenous injection. Once the PEG-c-DMA leaves, the particle returns to its transfection-optimal cationic charge and is able to transfect cells efficiently.[91,92,129] LNP formulations have been reported to load as much as 5 wt% siRNA,[91] and to silence genes in a dose-dependent manner in animals ranging from mice to non-human primates.[91,92,129,130] Indeed, LNP formulations have completed multiple clinical trials for delivery of siRNA, such as those against PLK-1 (TKM-080301) for the treatment of neuroendocrine tumors (NET), adrenocortical carcinoma (ACC), and primary/secondary liver cancer.[133,134] With the substantial achievements in siRNA loading, lipid design, and lipid composition, lipid-based nanoparticles have enjoyed the greatest success in translation from benchtop development to clinical trials, which led to the first FDA-approved siRNA-based LNP therapeutic, Patisiran.[91,135-137]

1.4.2. Polymer Nanoparticles

After lipids, polymers represent the second most widely used material type for siRNA delivery. Based on published data accumulated over the past decade, average gene silencing efficiencies of 64.6 ± 24.7% *in vitro* and 61.5 ± 19.6% *in vivo* have been achieved (**Figure 1.6 and Table 1.2**). The three most frequently employed types of polymer nanoparticles for siRNA delivery have been solid polymeric nanoparticles, dendrimers, and hydrogels,[30,32,49,135] but across the wide range of structural designs in polymeric delivery systems, there are a number of proven components that are regularly used: poly(lactic-co-glycolic acid) (PLGA), poly-L-lysine (PLL), chitosan, and polyethyleneimine (PEI).[31,56,93,94,96,97,104,138-141]

PLGA, PLL, and chitosan generally play a structural role in forming the primary skeleton for siRNA loading. PLGA nanoparticles have high stability and biocompatibility, and is an FDA-approved material. However, PLGA nanoparticles require additional cationic condensers for effective siRNA loading, such as PEI.[127,138,142] On the other hand, PLL is a polycation, and so it

can form complexes with siRNA without the need for an additional condenser. PLL's primary advantage is in its relatively high biocompatibility compared to the fairly toxic PEI, but PLL systems suffer from diminished transfection efficiency in the presence of high serum content; in an environment that is clinically relevant and reflective of our vasculature (which has high serum content), the PLL systems have difficulty forming stable structures due to competition with serum proteins (which are generally anionic) for binding to the siRNA payloads.[139,143] Thus, recent efforts have focused on developing PPL derivatives and co-polymers to reinforce their vulnerability to high serum content environments.[104,139,143-145] Lastly, chitosan is a cationic polysaccharide, which offers high biocompatibility and many amine and hydroxyl groups available for chemical modification. However its low *in vivo* solubility is a critical drawback; PEGylation or hyaluronan-conjugation of the particles have been reported to increase solubility, as well as to offer a specific and controllable site for further surface modifications (e.g. attachment of targeting moieties), but much work remains to develop a platform with reliable and consistent performance.[97,139,146,147]

As a condenser, PEI is the most widely used polymer. It is used in numerous all-polymer systems as well as in hybrid systems (containing lipids, metals, silica/silicon, *etc.*) that require a cationic component for stable siRNA loading. A key design factor in PEI-based nanoparticles for siRNA delivery is the N/P ratio, which is the molar ratio between the nitrogen in the PEI to the phosphorus in the siRNA. An N/P ratio greater than 10 is recommended, as it accommodates stronger siRNA integration that leads to decreased payload leakage and degradation. However, while stronger and greater siRNA binding to the polymer mitigates its excessively cationic charge, the increased PEI content inevitably leads to rapid RES-mediated clearance and high cytotoxicity.[50,148] On the other hand, an N/P ratio less than 10 results in more anionic particles that have difficulty loading siRNAs and being taken up by target cells.[148] Thus,

there is growing trend in developing novel polymeric nanoparticles that use non-PEI condensers to enable biosafe and effective siRNA loading and delivery.[93,94,101]

1.4.3. Metallic Nanoparticles

Metallic vehicles (primarily gold or iron oxide nanoparticles) for siRNA tend to underperform *in vivo* based on measurements of gene silencing efficiency, with average efficiencies of 72.3 ± 16.3% *in vitro* and 54.7 ± 19.6% *in vivo* (**Table 1.2** and **Figure 1.6**). This trend may be attributed to the solid structure of the constructs, which leads to formulations in which the siRNA payloads are covalently bound or chemically adhered to the surface of the particles (e.g. thiol-gold chemistry).[37,58,102,104,106,149] This surface-loading mechanism leaves the siRNA molecules exposed to the degrading conditions of the *in vivo* environment during circulation, which underscores the necessity for an siRNA-protective design; thus, metallic systems generally employ cationic polymer/lipid coatings to facilitate loading and protection of the siRNA payload.[51,99,102,104,106,108,109,136]

Nonetheless, metallic particles have advantages over other organic material-based systems in their longer shelf life, their facile surface chemistry, their higher physical stability (to temperature or pH excursions), their precisely tunable physical properties, and their potential for multi-modality (e.g. phototherapy, MRI imaging).[150-152] The surface chemistry of most metallic systems is amenable to attachment of a wide variety of targeting moieties or components that can facilitate endosomal escape (**Table 1.2**).[102-106,153-155] In particular, gold-based systems have demonstrated the ability to induce controlled release of siRNAs *via* light-activation,[156,157] as well as providing a photothermal therapeutic effect as a secondary function.[154,155,158,159] Iron oxide-based systems have also demonstrated unique characteristics, such as magnetofection,[160,161] magnet-guided particle accumulation and release,[162,163] and MRI-based particle tracking and tumor imaging.[99,153,164,165]

While metallic nanoparticles show an average *in vivo* gene silencing effect that is relatively low compared to other materials, they offer innate multi-modality that other systems lack. In particular, the ability to directly image and track the siRNA carriers can provide important pharmacokinetic and pharmacodynamic information (e.g. bioavailability and biodistribution of the nanoparticle) in RNAi therapeutics;[108,152,153,163,164] many studies use indirect fluorescent dye-tracking methods, or simply analyze mRNA or protein level changes in the target site post-administration. In order to set itself apart from the organic materials that excel in effective siRNA delivery and transfection of genes, the metallic delivery systems could perhaps benefit most by focusing on their unique material properties for multi-modal theranostic applications.

1.4.4. Mesoporous Silica Nanoparticles

Unlike the above systems, which are comprised of hollow spherical, core-shell, or solid or semi-solid structures, mesoporous silica nanoparticles (MSNs) consist of a network of pores within a silicon oxide framework. These materials display relaticely large and tunable pores that are able to sequester payloads akin to a rigid sponge. The porous structure affords a much greater surface area for binding compared to other systems, and it is thus able to load large quantities of siRNA.[152] However, the native silicon oxide surface is anionic, necessitating cationic condensers. With the aid of cationic lipids and polymers to form hybrid structures, MSNs have reported average gene silencing efficiencies of 75.7 ± 19.4% *in vitro* and 63.2 ± 17.0% *in vivo* (**Figure 1.6 and Table 1.2**)— quite promising considering that these particles have not been studied for siRNA delivery nearly as thoroughly as lipid- and polymer-based vehicles.

A major drawback to MSN delivery systems is their questionable biosafety, where MSNs have shown dose-, size-, shape-, and administration-dependent toxicity in various drug delivery

applications.[166-169] This concern is particularly important for siRNA delivery, as the majority of MSN studies use the cytotoxic PEI polymer as a condenser.[112,116,170-172] Moreover, most studies of PEI-MSN hybrid systems fail to demonstrate successful endosomal escape using the theorized proton sponge effect induced by the PEI, and most do not report rigorous dose-dependent toxicity studies; the general publication trend leans toward demonstration of a positive gene silencing effect and a lack of toxicity at the selected dose. In order to validate MSN-mediated RNAi therapeutics for clinical translation, more fundamental studies on the individual components of the hybrid system (the MSN, the condenser, and the siRNA) are needed. The oxide surface on MSNs provides entry into a wide pallette of surface chemistries that may offer a better alternative to PEI and other potentially toxic condensers for siRNA loading. While there is much room for further investigation, MSNs have so far demonstrated excellent *in vivo* gene silencing effects.

One of the more innovative MSN-based transfection agents that has been developed is the Protocell from the Brinker group.[173-176] Protocells were first introduced in 2009 as MSNs that were encapsulated within cationic liposomes to enhance delivery of anionic and cell-impermeable fluorescent dye (calcein) as a model oligonucleotide.[174] Then in 2011, the group demonstrated the ability of a Protocell to conjugate targeting peptide (SP94 peptide) and a endosomolytic peptide (H5WYG) to deliver a wide range of payloads (small molecule anticancer drugs, quantum dots, siRNAs, etc.) to target human hepatocellular carcinoma (HCC) cells.[173] The particles demonstrated up to 90% gene silencing efficiency *in vitro.*[176] This hybrid organic/inorganic system provides a prime example of how hybrid nanoparticles can combine the advantages of organic (e.g. liposome's biosafety and facile modification of properties by adjustment of lipid composition) and inorganic (e.g. >10-fold higher loading capacity and >5-fold diminished payload leakage by loading siRNA within MSNs) components. The promising *in vitro* performance[175] has yet to be tested *in vivo.*

1.4.5. Porous Silicon Nanoparticles

Porous silicon (pSi) is a relative newcomer in the field of RNAi. However, the few reports on *in vivo* siRNA delivery are extremely promising. With tunable pore sizes ranging from micropores (d < 2 nm) to meso- (d= 2-50 nm) and macropores (d > 50 nm), facile surface chemistry, and biosafe and biocompatible degradation, porous silicon boasts a relatively high loading capacity and compatibility with a diverse set of payloads. Moreover, when synthesized as a hybrid nanoparticle with lipids or polymers, pSi-based nanoparticles have demonstrated average gene silencing efficiencies of 75.6 ± 21.3% *in vitro* and 80.4 ± 2.7% *in vivo* (**Figure 1.6 and Table 1.2**) that rival the best liposomal systems.

While structurally similar to MSNs, porous silicon retains a crystalline silicon core in the porous skeleton. With dimensions on the order of 5 nm, the crystalline silicon domains in the skeleton function as quantum dots, producing an intrinsic photoluminescence.[177-181] This unique property allows pSi materials to take advantage of both MSN's large surface area and porous structure to attain high loading capacities, as well as the metallic system's potential for multi-modal imaging.

Within the limited number of studies on pSi-based materials for siRNA delivery, there have been a variety of effective structures. The Ferrari group has primarily focused on the development a multi-stage delivery system that consists of a larger pSi microparticle loaded with liposomal siRNA. This yielded an extended gene silencing effect, showing *in vivo* knockdown efficiency as high as 80% for a period of 20 days after systemic delivery.[120,182-184] The group of Stevens developed a related pSi system, but in the form of nanoneedles for transdermal delivery of siRNA. That work demonstrated > 90% transfection efficiency *in vitro*, as well as a demonstrable phenotypic outcome (e.g. neovascularization) *in vivo*.[185] At the smaller scale, the Voelcker group developed PEI-functionalized pSi nanoparticles for systemic administration,

attaining 30-63% gene silencing effect *in vitro* and up to 82% *in vivo.*[119,186] While the use of PEI

raises the above-mentioned concerns regarding dose-dependent cytotoxicity, silicon is

amenable to other condenser chemistries. The common silica functionalization reagent (3-

aminopropyl)-dimethylethoxysilane places a positively charged amine group on the surface of

the inner pore walls, and this combined with a graphene oxide shell allowed entrapment of

siRNA in pSi nanoparticles that induced 65% gene silencing effect *in vitro.* By targeting the

compromised blood-brain barrier (BBB) in a mouse brain injury model and through the agency

of the RVG (rabies virus glycoprotein) peptide, this system was able to achieve enhanced

siRNA-delivery efficiency *in vivo.*[187] A similar structure, lacking the graphene oxide shell and

conjugated with the CAQK brain injury targeting peptide attained 70% gene silencing effect *in

vitro.*[188]

An alternative condenser involving calcium chloride-mediated formation of a calcium

silicate binder with the pSi nanoparticles has also been developed. This method successfully

trapped siRNA and was able to attain a modest 52.8% gene silencing efficiency *in vitro.*[33]

A most recent development for pSi-based siRNA therapeutics is fusogenic lipid-coated

pSi nanoparticles (FNPs; **Figure 1.7**).[117,118,189] Using the above calcium silicate condenser

chemistry,[33] the FNPs were able to obtain loading capacity up to 25 wt% of siRNA, a

significantly higher loading capacity compared with other materials of similar size and

structure.[33,117] Like Brinker's MSN-based Protocell, the inorganic pSi core prevents premature

leakage of siRNA payloads from the liposomal shell, and inversely, the liposomal shell is able to

protect the pSi core from dissolution.[118] Currently, the FNP system represents the most

thoroughly investigated pSi-based siRNA delivery technology, as its material properties,

biological mechanism of action, and its *in vitro* and *in vivo* behavior and therapeutic effects have

been delineated.[117,118,189] Overall, the FNPs are able to undergo a plasma membrane fusion to

directly deposit the siRNA-loaded pSi core particles in the cytoplasm, where the pSi quickly

degrades to release the siRNA for RNAi. Moreover, the FNPs have demonstrated strong

selective homing when decorated with targeting peptides, while retaining their fusogenic uptake

characteristic. These factors led to 85-96% *in vitro* gene silencing efficiencies across different

cell lines (macrophages and tumor cells), as well as 76-83% *in vivo* gene silencing efficiencies

post-intravenous administration. Moreover, FNPs represent a modular therapeutic platform; by

exchanging the siRNA sequence and the homing peptide, the FNPs have been be configured

for three different disease targets (anti-inflammatory, chemo-sensitizing, and tumor-associated

macrophage reprogramming). This system has demonstrated remarkable therapeutic effects in

bacterial infection models (Gram positive *Staphylococcus aureus*, Gram negative *Pseudomonas

aeruginosa*, and Methicilin-resistant *S. aureus* (MRSA)), as well as in ovarian peritoneal

carcinomatosis.[117,118]

1.5   Selective Tissue Targeting

Realization of RNAi therapy requires the delivery vehicle to overcome the

aforementioned extracellular barriers by either local administration or controlled homing to the

target site. For tumor models, nanoparticles have traditionally relied on the enhanced

permeation and retention (EPR) effect, where the porous tumor vasculature allows greater

uptake and retention compared with normal tissues.[190] A recent review of the literature by Chan,

which focused on the quantity of nanoparticles accumulated in solid tumors *via* the EPR effect,

highlighted the very poor efficiency of this process; on average, a mere 0.7% of the injected

dose of particles actually reaches the tumor.[191] Active targeting, via the agency of a pendant

molecular species that has some affinity for the tumor, showed a minor improvement over EPR-

mediated particle accumulation. However, in other (non-tumor) animal disease models, the use

of selective homing agents can generate more substantial accumulation of

siRNA.[98,101,127,135,149,173,191-194] For applications beyond local administration and passive MPS-

mediated homing to clearance organs (*e.g.* liver, lungs, spleen), the literature shows a wide variety of homing moieties that can be decorated on the surface of carrier particles for *in vivo* targeting, including aptamers[122,127,195-202] and receptor-specific ligands.[195,203-208] But currently peptides and antibodies have been the most widely used targeting agents.

1.5.1. Antibodies

With several FDA-approved entities already in clinical use, antibodies offer a reliable means of targeting cells.[195,209,210] Homing antibodies fall into two categories: (1) monoclonal antibodies (mAb); and (2) antibody fragments (or antigen-binding fragments, Fab). Monoclonal antibodies are those generated from a single cell lineage that bind to a single epitope on their target (as opposed to polyclonal antibodies that are generated by a range of B cells that bind to multiple epitopes on their target). The most commonly used mAb for targeted delivery of siRNA is Trastuzumab, an IgG1 mAb against human epidermal growth factor 2 (HER2) for selective targeting of breast cancer.[114,116,211] Another common antibody, useful for targeting the wider epidermal growth factor receptor (EGFR) family is Cetuximab.[163,212-214] A major concern in using mAbs with nanoparticles is their large size (approximately 150 kDa), which limits the number of mAbs that can be placed on a single nanoparticle. The rationale here is that when multiple targeting groups are placed on a nanoparticle, the targeting efficiency is enhanced by a factor larger than the scalar number of targeting groups—so-called multivalency. Another issue with antibodies is that they contain the Fc domain, which can trigger cellular responses that may or may not be desirable—such as an antigenic reaction. The problem is mitigated somewhat when the Fab domain alone is used rather than the full antibody (which is composed of two Fab domains for bidning to target receptors and one Fc domain for activity).[210,214,215]

Fragment antibodies make use of only the Fab binding motifs, making the molecule much smaller (approximately 50 kDa) and more economical to produce.[195,215] Moreover, the lack

19

of the Fc domain reduces the chance that the targeting moiety will inadvertently cause adverse downstream activities (e.g. immunogenicity, cytotoxicity).[32,195,210,215] The argument has been made that the Fc domain is necessary in order to better stabilize the antibody against RES clearance and that, with their smaller size, Fabs are too quickly cleared from the body.[215] However, it appears that conjugation to nanoparticles can mitigate these effects for siRNA delivery. For example, studies have demonstrated effective siRNA-mediated gene silencing *in vivo* using Fab-conjugated nanoparticles.[216-218] Moreover, although Fab technology is relatively new compared to whole antibodies, three Fabs have already been approved for use by the FDA (Abciximab, Ranibizumab, Certolizumab pegol).[219-221]

1.5.2. Peptides

Targeting peptides are a sequence of linear or cyclic amino acids that are able to take advantage of specific binding sites on transmembrane receptors to selectively guide their carrier to the target cells. Specific peptide sequences may be identified through phage display either *in vitro* or *in vivo*, where populations of bacteriophages displaying different peptide sequences (that altogether form a library of peptides) undergo multiple rounds of binding assays to select for the sequence with the highest binding affinity.[222-225] While an *in vitro* phage screen can identify peptides that bind to a specifically chosen binding receptor, an *in vivo* phage screen isolates peptides that bind to the disease tissue of interest—even though the receptors or the cell types may be as yet unknown. A further advantage is that the peptides that survive an *in vivo* screen are more likely to be able to perform the same *in vivo* tissue targeting task when they are bound to nanoparticles other than a phage.[188,222-228] With an *in vitro* screen, the major question of whether or not the targeting peptide identified will survive all the varied clearance mechanisms of the in vivo environment remains unanswered.

Table 1.3 shows a representative list of peptides that have been used for targeting disease-specific cells or tissues. While most peptides bind to specific receptors on the cellular membrane and are known or expected to initiate receptor-mediated endocytosis, there are only few peptides where the true target and uptake mechanisms have been clearly demonstrated. Of particular significance are peptides classified as "CendR", which stands for C-end-Rule, discovered in 2009 by the Ruoslahti group.[223,229] In general, these peptides display an R/KXXR/K sequence (e.g. iRGD and LyP-1 peptides; **Table 1.3**), with an essential C-terminal arginine (or occasionally lysine) motif that is exposed for activation by a primary receptor, which initiates a proteolytic cleavage of the peptide. The cleaved inner peptide sequence is then activated for a secondary binding to the neuropilin (NRP1/2) receptor to undergo cellular endocytosis. While many peptides carry the CendR motif (e.g. TAT cell penetrating peptide), the peptide homing must be primary receptor-specific, and cellular uptake must be activated by the initial docking; as opposed to cell-penetrating sequences that are active independent of binding and receptor recognition events.[225,229] The net result is a very selective peptide.

With regard to *in vivo* siRNA delivery, the fusogenic porous silicon nanoparticles (FNPs) demonstrated effective use of targeting peptides to induce siRNA-mediated gene silencing in multiple cell targets within a single mouse model.[118] **Figure 1.8** shows a significant example of the versatility of the approach, where three different targeting peptides were used to bring FNPs to their three respective targets with high selectivity. First, in a FNP platform decorated with the CRV peptide, the particles were selectively taken up by the activated macrophages in an infection site (**Figure 1.8a**). Second, FNPs decorated with the LyP-1 peptide selectively homed to tumor-associated macrophages (TAMs) in an ovarian peritoneal carcinomatosis model (**Figure 1.8b**) to induce knockdown only in the TAMs. Third, FNPs with iRGD peptide homed to ovarian cancer cells in the same tumor model (**Figure 1.8c**) and induced a significant gene

silencing in those cells. All three formulations resulted in a significant therapeutic outcome in diseased mice.[117,118]

1.6 Strategies against Endocytosis

Whereas most drug delivery systems could benefit from payload protection and selective tissue targeting, intracellular drug release may not be necessary. However, cytosolic delivery is critical for RNAi therapeutics. Thus, approaches that either avoid endocytosis or escape from endocytic vesicles are essential to activating the RNAi machinery for gene silencing. Natural viral or bacterial transduction mechanisms have built-in endosomal escape pathways (e.g. membrane fusion, pore formation), which have inspired development of artificial systems that can avoid or escape the endosome.[238,239] **Table 1.4** lists some techniques that have been used to escape or bypass endocytosis in nanoparticle-mediated siRNA delivery.

1.6.1. Endosomal Escape

One method to induce cytosolic localization of siRNA is to escape the endosome before degradation or excretion (**Figure 1.4c**). The most utilized method to instigate endosomal escape is *via* a mechanism called the 'proton sponge' hypothesis.[94,246,247] As the early endosomes fuse with late endosomes and lysosomes, the intravesicular pH decreases to initiate degradation of the contents. But if an endosmolytic molecule (e.g histidine-rich molecule, poly(amido amine) polymers)[61,238] is trapped within, it will buffer the pH of the vesicles and allow a continuous influx of H^+, Cl^-, and water molecules that increase the osmotic pressure. Eventually, the vesicle swells and ruptures to release its entrapped payload.[61,64,141,238] For inorganic and polymeric nanoparticles, polyethyleneimine (PEI) is the most commonly used molecule, with its abundance of nitrogen groups available to buffer the pH and sponge up protons.[99,102,112,138,248,249]

While the proton sponge mechanism of PEI is still under debate,[247-249] its endosomal escape

phenomenon has been replicated numerous times, and has been extensively used to

demonstrate effective *in vivo* gene silencing effect in numerous nanosystems, as shown in

Table 1.2.

Endosomal escape may also occur as a result of membrane fusion and pore formation.

Herpes simplex virus innately carries glycoprotein H, which induces fusion in a pH-sensitive

manner to help its virus escape lysosomal degradation. One notable study has used the peptide

analogue of the fusogenic domain of glycoprotein H for *in vitro* transfection and demonstrated

membrane fusion and enhanced transfection efficiency.[250] Two other fusion peptides were

derived from the haemagglutinin subunit HA-2 of the influenza virus, called KALA and

GALA.[111,112,238,241-243] Both KALA and GALA peptides behave in a pH-sensitive manner; the

peptides undergo a conformational change after embedding into the membrane of acidic

endosomal or lysosomal vesicles, and form a helical channel through which the payloads may

escape.[238,243] **Table 1.2** shows two mesoporous silica-based systems that employed KALA by

the Gu group to attain gene silencing efficiencies of 80% *in vitro* and approximately 50-60% *in

vivo.*[111,112] While not as widely used as the PEI and other polycations, these peptides offer a

promising and potentially safer method to induce endosomal escape.

1.6.2. Endocytosis Bypass

There are several reported methods to bypass endocytosis, such as membrane

penetration, and membrane fusogenic uptake. Cell penetrating peptides (CPPs) are employed

for diffusive uptake into the cell through the plasma membrane and directly into the cytoplasm.

Although the exact uptake mechanism is highly debated, TAT, penetratin, and other CPPs have

demonstrated successful cytosolic delivery of their carriers.[30,62,63,237,251] While some penetrating

peptides are observed to undergo endocytosis with translocation afterward to transit to the

23

cytoplasm, penetratin has been observed to cytoplasmically localize in cells even at 4°C, by electrostatically penetrating through anionic phospholipids without an external driving force (e.g. pH-sensitivity, osmotic gradient).[245,252] On the other hand, the efficient penetrative activity of CPPs has led to reports of cell line-, cargo-, peptide size-, and dose-dependent cytotoxicity.[223,251-253] At biosafe doses, these peptides may provide a synergistic effect when combined with tissue-targeting peptides to help guide the nano-carriers to selective cells and allow them to efficiently activate RNAi in the cell cytoplasm. Conde, *et al.* demonstrated this idea on gold nanoparticles that were surface modified to display PEG, siRNAs (against c-myc), RGD tumor-targeting peptide, and the TAT cell penetrating peptide; the particle was able to demonstrate gene silencing efficiencies of 70% *in vitro* and 65.2% *in vivo.*[105] Additionally Mahajan, *et al.* decorated superparamagnetic iron oxide nanoparticles (SPION) with dextran, myristoylated polyarginine peptides (MPAPs), EPPT1 (tumor antigen-targeting peptide), and siRNAs (against PLK-1), which attained a modest 35% gene silencing efficiency *in vivo.*[108]

The process of fusogenic uptake into cells (**Figure 1.4d**) may be mediated by specific compositions of liposomes.[239,254] Various fusogenic liposome compositions have been developed, although they were initially intended for biological studies on membrane fusion, rather than for siRNA delivery.[255-259] The most widely used compositions contain 1,2-dioleoyl-3-glycero-phosphatidylethanolamine (DOPE), and a cationic lipid such as *N*-[1-(2,3-dioleoyloxy)propyl]-*N*,*N*,*N*-trimethyammonium chloride (DOTMA), or 1,2-dioleoyl-3-trimethylammonium-propane (DOTAP).[62,125,126,193,202,260] While the exact mechanism and role of these lipids are not clear, it is theorized that a mix of aromatic molecule, cationic surface charge, and conical lipid structure are involved in membrane fusion.[261] Another effective fusogenic composition is that of 1,2-dimyristoyl-sn-glycero-3-phosphocholine (DMPC), 1,2-distearoyl-sn-glycero-3-phosphoethanolamine-N-[amino(polyethylene glycol)-2000] (DSPE-PEG$_{2000}$), and DOTAP.[117,118,189,244] Lee, *et al.* first demonstrated cell line-dependent fusogenicity of this

composition (**Figure 1.9a**), and their ability to modify exosomes and microvesicles excreted from target cells.[244] Our group has furthered the use of these liposomes by applying the technology for siRNA-delivery. The fusogenic porous silicon nanoparticles (FNPs) described above were found to undergo fusogenic uptake (**Figure 1.9c**) that was independent of the major routes of endocytosis (e.g. macropinocytosis, caveolin-, clathrin-mediated uptake), and were able to retain fusogenic uptake in the absence of, or with downregulation of other major markers of vesicle traffic (e.g. Rab11, Rab5A). However, knockdown of intracellular vesicle fusion pathways prevented fusogenic uptake, and the fusogenic liposomes were found within the lysosomal compartments, indicating endocytosis (**Figure 1.9b**).[118] Although the specific cellular mechanisms are as yet unknown, it is clear that there is pathway-dependence of liposomal fusion to the plasma membrane.

1.7 Future Prospective

1.7.1. Trends in siRNA Therapeutics

Using the PubMed search engine of the MEDLINE database, we attempted to track research trends based on generic query terms, such as "siRNA", "delivery", and "nanoparticle", relevant to publications on siRNA therapeutics. Out of over 3,000 papers published on nanoparticle-mediated delivery of siRNAs for therapeutic applications since 2009, over 1,000 publications report *in vivo* gene silencing effects either directly (e.g. qRT-PCR, Western blot) or indirectly (e.g. therapeutic or downstream signaling effect). Among them, over 300 studies met at least two of the three design requirements described in this review: (1) siRNA protection; (2) selective targeting; and (3) cytoplasmic localization of siRNA.

Figure 1.10 shows the number of publications on siRNA delivery systems by material type in the last decade. Ten years after the initial discovery of siRNA, research articles relating

to nanoparticle-mediated delivery of siRNA reached nearly 200 publications in 2010, and continued to produce increasing numbers of publications with a peak at over 400 publications in 2016 (grey bars, **Figure 1.10**). By material type, the lipid-based (which included liposomes, micelles, and solid lipid nanoparticles; yellow bars, **Figure 1.10**) and polymeric nanoparticles (green bars, **Figure 1.10**) were far more studied for siRNA delivery, compared to metallic (which included gold and iron oxide; blue bars, **Figure 1.10**) and silica/silicon-based systems (red and orange bars, **Figure 1.10**).

With the discovery of CRISPR systems in 2011, and its subsequent exponential increase in research publications (black dotted line, **Figure 1.10**), the overall number of publications on siRNA delivery began decreasing from 2017. The decline also coincides with a controversial shutdown of a large RNAi program in the pharmaceutical industry; Alnylam Pharmaceuticals, one of the industry giants in RNAi therapy, had found potential toxicity in their lead siRNA formulation for the treatment of ATTR-amyloidosis.[262]

However, Alnylam made a breakthrough only two years later with another formulation for the same disease;[137] Patisiran demonstrated significant therapeutic outcome in patients and became the first FDA-approved RNAi/siRNA therapeutic in 2018. This pioneering achievement signals that we may be only at the beginning of the RNAi therapy story.

1.7.2. Clinical Translation

Table 1.5 lists all siRNA-based therapeutics that have been, or are currently under clinical trials, or have gained FDA-approval. The first time an siRNA therapeutic underwent Phase 3 clinical trials in the United States was in 2007, when Bevasiranib (Cand5) was formulated as a free-siRNA against VEGF-A in age-related macular degeneration (AMD). Since then, there have been over 30 clinical trials with siRNA-based therapeutics that were used to

silence over 25 genes in over 40 different diseases (approximately 40% of which were cancer models). Beginning from 2004, when the first clinical trials of siRNA-based therapeutics were conducted, it took 14 years for the first siRNA-based therapeutic to be approved; a trajectory that aligns closely with the history of antibody-based therapeutics.[98,137]

Based on **Table 1.5**, siRNA formulations without protective carriers have all been terminated or discontinued with the exception of the QPI-1007 formulation for local administration into the eye. Also, while GalNAc-siRNA conjugate systems (developed and pursued primarily by Alnylam Pharmaceuticals) are showing consistently strong performance with continued passages from Phases 1 to 3 (with the exception of Revusiran, which showed toxicity in Phase 3, and has been discontinued[90,262]), liver-targeted applications are somewhat limited.[43-45] On the other hand, increasing numbers of carrier-based siRNA therapeutics have entered clinical trials since the late 2000s, and there are currently six trials that are active (four of which are SNALP/LNP formulations) for a wide range of applications (e.g. fibrosis, cancer, hemophilia, etc.).

1.8   Conclusions

While many challenges remain in the development of clinically translatable RNAi therapeutics (*e.g.* biosafe siRNA sequence selection,[263,264] mass production[265,266]), it appears we are quickly approaching a point when multiple therapeutic options will be approved for human use. In particular, the clinical trials are moving increasingly toward nanoformulations for siRNA protection and delivery, despite the declining number of publications on siRNA delivery systems from the academic community in recent years. This is clearly an opportunity for those of us working on advanced materials (and for the authors and readers of *Advanced Materials*). We hope this review has illustrated how rational materials design can generate new classes of

nanoformulations that are able to protect, target, and deploy siRNA therapeutics to the desired

cell types for safe and efficious *in vivo* outcomes.

1.9   References

1   Collins, F. S., Morgan, M. & Patrinos, A. The Human Genome Project: lessons from large-scale biology. *Science* **300**, 286-290, doi:10.1126/science.1084564 (2003).

2   Collins, F. S., Patrinos, A., Jordan, E., Chakravarti, A., Gesteland, R. & Walters, L. New goals for the U.S. Human Genome Project: 1998-2003. *Science* **282**, 682-689 (1998).

3   Olson, M. V. The human genome project. *Proc Natl Acad Sci U S A* **90**, 4338-4344, doi:10.1073/pnas.90.10.4338 (1993).

4   Wilson, B. J. & Nicholls, S. G. The Human Genome Project, and recent advances in personalized genomics. *Risk Manag Healthc Policy* **8**, 9-20, doi:10.2147/RMHP.S58728 (2015).

5   Friedmann, T. A brief history of gene therapy. *Nature Genetics* **2**, 93-98, doi:10.1038/ng1092-93 (1992).

6   Jackson, D. A., Symons, R. H. & Berg, P. Biochemical method for inserting new genetic information into DNA of Simian Virus 40: circular SV40 DNA molecules containing lambda phage genes and the galactose operon of Escherichia coli. *Proc Natl Acad Sci U S A* **69**, 2904-2909, doi:10.1073/pnas.69.10.2904 (1972).

7   Lai, T., Yang, Y. & Ng, S. K. Advances in Mammalian cell line development technologies for recombinant protein production. *Pharmaceuticals (Basel)* **6**, 579-603, doi:10.3390/ph6050579 (2013).

8   Jaenisch, R. & Mintz, B. Simian virus 40 DNA sequences in DNA of healthy adult mice derived from preimplantation blastocysts injected with viral DNA. *Proc Natl Acad Sci U S A* **71**, 1250-1254, doi:10.1073/pnas.71.4.1250 (1974).

9   Goeddel, D. V., Kleid, D. G., Bolivar, F., Heyneker, H. L., Yansura, D. G., Crea, R., Hirose, T., Kraszewski, A., Itakura, K. & Riggs, A. D. Expression in Escherichia coli of chemically synthesized genes for human insulin. *Proc Natl Acad Sci U S A* **76**, 106-110, doi:10.1073/pnas.76.1.106 (1979).

10   Dimitriadis, G. J. Translation of rabbit globin mRNA introduced by liposomes into mouse lymphocytes. *Nature* **274**, 923-924 (1978).

11   Anderson, W. F. Human gene therapy: scientific and ethical considerations. *Recomb DNA Tech Bull* **8**, 55-63 (1985).

12   Rabino, I. Gene therapy: ethical issues. *Theor Med Bioeth* **24**, 31-58 (2003).

13   Walters, L. Human gene therapy: ethics and public policy. *Hum Gene Ther* **2**, 115-122, doi:10.1089/hum.1991.2.2-115 (1991).

14   Fletcher, J. C. Evolution of ethical debate about human gene therapy. *Hum Gene Ther* **1**, 55-68, doi:10.1089/hum.1990.1.1-55 (1990).

15   Miller, J., McLachlan, A. D. & Klug, A. Repetitive zinc-binding domains in the protein transcription factor IIIA from Xenopus oocytes. *EMBO J* **4**, 1609-1614 (1985).

16   Kim, Y. G. & Chandrasegaran, S. Chimeric restriction endonuclease. *Proc Natl Acad Sci U S A* **91**, 883-887, doi:10.1073/pnas.91.3.883 (1994).

17   Carroll, D. Genome engineering with zinc-finger nucleases. *Genetics* **188**, 773-782, doi:10.1534/genetics.111.131433 (2011).

18   Christian, M., Cermak, T., Doyle, E. L., Schmidt, C., Zhang, F., Hummel, A., Bogdanove, A. J. & Voytas, D. F. Targeting DNA double-strand breaks with TAL effector nucleases. *Genetics* **186**, 757-761, doi:10.1534/genetics.110.120717 (2010).

19   Jinek, M., Chylinski, K., Fonfara, I., Hauer, M., Doudna, J. A. & Charpentier, E. A programmable dual-RNA-guided DNA endonuclease in adaptive bacterial immunity. *Science* **337**, 816-821, doi:10.1126/science.1225829 (2012).

20   Rocheleau, C. E., Downs, W. D., Lin, R., Wittmann, C., Bei, Y., Cha, Y. H., Ali, M., Priess, J. R. & Mello, C. C. Wnt signaling and an APC-related gene specify endoderm in early C. elegans embryos. *Cell* **90**, 707-716 (1997).

21   Fire, A., Xu, S., Montgomery, M. K., Kostas, S. A., Driver, S. E. & Mello, C. C. Potent and specific genetic interference by double-stranded RNA in Caenorhabditis elegans. *Nature* **391**, 806-811, doi:10.1038/35888 (1998).

22   Bernstein, E., Caudy, A. A., Hammond, S. M. & Hannon, G. J. Role for a bidentate ribonuclease in the initiation step of RNA interference. *Nature* **409**, 363-366, doi:10.1038/35053110 (2001).

23   Hammond, S. M., Bernstein, E., Beach, D. & Hannon, G. J. An RNA-directed nuclease mediates post-transcriptional gene silencing in Drosophila cells. *Nature* **404**, 293-296, doi:10.1038/35005107 (2000).

24   Lam, J. K., Chow, M. Y., Zhang, Y. & Leung, S. W. siRNA Versus miRNA as Therapeutics for Gene Silencing. *Mol Ther Nucleic Acids* **4**, e252, doi:10.1038/mtna.2015.23 (2015).

25   Reynolds, A., Leake, D., Boese, Q., Scaringe, S., Marshall, W. S. & Khvorova, A. Rational siRNA design for RNA interference. *Nat Biotechnol* **22**, 326-330, doi:10.1038/nbt936 (2004).

26   Nakanishi, K. Anatomy of RISC: how do small RNAs and chaperones activate Argonaute proteins? *Wiley Interdiscip Rev RNA* **7**, 637-660, doi:10.1002/wrna.1356 (2016).

27   Montgomery, M. K. RNA interference: historical overview and significance. *Methods Mol Biol* **265**, 3-21, doi:10.1385/1-59259-775-0:003 (2004).

28   Lee, R. C., Feinbaum, R. L. & Ambros, V. The C. elegans heterochronic gene lin-4 encodes small RNAs with antisense complementarity to lin-14. *Cell* **75**, 843-854 (1993).

29   Wightman, B., Ha, I. & Ruvkun, G. Posttranscriptional regulation of the heterochronic gene lin-14 by lin-4 mediates temporal pattern formation in C. elegans. *Cell* **75**, 855-862 (1993).

30   Wang, J., Lu, Z., Wientjes, M. G. & Au, J. L. Delivery of siRNA therapeutics: barriers and carriers. *AAPS J* **12**, 492-503, doi:10.1208/s12248-010-9210-4 (2010).

31   Iversen, F., Yang, C., Dagnaes-Hansen, F., Schaffert, D. H., Kjems, J. & Gao, S. Optimized siRNA-PEG conjugates for extended blood circulation and reduced urine excretion in mice. *Theranostics* **3**, 201-209, doi:10.7150/thno.5743 (2013).

32   Juliano, R. L. The delivery of therapeutic oligonucleotides. *Nucleic Acids Res* **44**, 6518-6548, doi:10.1093/nar/gkw236 (2016).

33   Kang, J., Joo, J., Kwon, E. J., Skalak, M., Hussain, S., She, Z. G., Ruoslahti, E., Bhatia, S. N. & Sailor, M. J. Self-Sealing Porous Silicon-Calcium Silicate Core-Shell Nanoparticles for Targeted siRNA Delivery to the Injured Brain. *Adv Mater* **28**, 7962-7969, doi:10.1002/adma.201600634 (2016).

34   Scherer, L. & Rossi, J. J. Therapeutic applications of RNA interference: recent advances in siRNA design. *Adv Genet* **52**, 1-21, doi:10.1016/S0065-2660(04)52001-1 (2004).

35   Kawabata, K., Takakura, Y. & Hashida, M. The fate of plasmid DNA after intravenous injection in mice: involvement of scavenger receptors in its hepatic uptake. *Pharm Res* **12**, 825-830 (1995).

36   Yin, H., Kanasty, R. L., Eltoukhy, A. A., Vegas, A. J., Dorkin, J. R. & Anderson, D. G. Non-viral vectors for gene-based therapy. *Nat Rev Genet* **15**, 541-555, doi:10.1038/nrg3763 (2014).

37   Barnaby, S. N., Lee, A. & Mirkin, C. A. Probing the inherent stability of siRNA immobilized on nanoparticle constructs. *Proc Natl Acad Sci U S A* **111**, 9739-9744, doi:10.1073/pnas.1409431111 (2014).

38   Burnett, J. C., Rossi, J. J. & Tiemann, K. Current progress of siRNA/shRNA therapeutics in clinical trials. *Biotechnol J* **6**, 1130-1146, doi:10.1002/biot.201100054 (2011).

39   Hoerter, J. A. & Walter, N. G. Chemical modification resolves the asymmetry of siRNA strand degradation in human blood serum. *RNA* **13**, 1887-1893, doi:10.1261/rna.602307 (2007).

40   Allison, S. J. & Milner, J. RNA Interference by Single- and Double-stranded siRNA With a DNA Extension Containing a 3' Nuclease-resistant Mini-hairpin Structure. *Mol Ther Nucleic Acids* **2**, e141, doi:10.1038/mtna.2013.68 (2014).

41   Castanotto, D. & Rossi, J. J. The promises and pitfalls of RNA-interference-based therapeutics. *Nature* **457**, 426-433, doi:10.1038/nature07758 (2009).

42   Elmen, J., Thonberg, H., Ljungberg, K., Frieden, M., Westergaard, M., Xu, Y., Wahren, B., Liang, Z., Orum, H., Koch, T. & Wahlestedt, C. Locked nucleic acid (LNA) mediated

improvements in siRNA stability and functionality. *Nucleic Acids Res* **33**, 439-447, doi:10.1093/nar/gki193 (2005).

43   Huang, Y. Preclinical and Clinical Advances of GalNAc-Decorated Nucleic Acid Therapeutics. *Mol Ther Nucleic Acids* **6**, 116-132, doi:10.1016/j.omtn.2016.12.003 (2017).

44   Janas, M. M., Schlegel, M. K., Harbison, C. E., Yilmaz, V. O., Jiang, Y., Parmar, R., Zlatev, I., Castoreno, A., Xu, H., Shulga-Morskaya, S., Rajeev, K. G., Manoharan, M., Keirstead, N. D., Maier, M. A. & Jadhav, V. Selection of GalNAc-conjugated siRNAs with limited off-target-driven rat hepatotoxicity. *Nature Communications* **9**, 723, doi:10.1038/s41467-018-02989-4 (2018).

45   Springer, A. D. & Dowdy, S. F. GalNAc-siRNA Conjugates: Leading the Way for Delivery of RNAi Therapeutics. *Nucleic Acid Therapeutics* **28**, 109-118, doi:10.1089/nat.2018.0736 (2018).

46   Longmire, M., Choyke, P. L. & Kobayashi, H. Clearance properties of nano-sized particles and molecules as imaging agents: considerations and caveats. *Nanomedicine (Lond)* **3**, 703-717, doi:10.2217/17435889.3.5.703 (2008).

47   Falsini, S., Ciani, L., Ristori, S., Fortunato, A. & Arcangeli, A. Advances in lipid-based platforms for RNAi therapeutics. *J Med Chem* **57**, 1138-1146, doi:10.1021/jm400791q (2014).

48   Xu, X., Li, Z., Zhao, X., Keen, L. & Kong, X. Calcium phosphate nanoparticles-based systems for siRNA delivery. *Regen Biomater* **3**, 187-195, doi:10.1093/rb/rbw010 (2016).

49   Irimie, A. I., Sonea, L., Jurj, A., Mehterov, N., Zimta, A. A., Budisan, L., Braicu, C. & Berindan-Neagoe, I. Future trends and emerging issues for nanodelivery systems in oral and oropharyngeal cancer. *Int J Nanomedicine* **12**, 4593-4606, doi:10.2147/IJN.S133219 (2017).

50   Alexis, F., Pridgen, E., Molnar, L. K. & Farokhzad, O. C. Factors affecting the clearance and biodistribution of polymeric nanoparticles. *Mol Pharm* **5**, 505-515, doi:10.1021/mp800051m (2008).

51   Anderson, D. S., Patchin, E. S., Silva, R. M., Uyeminami, D. L., Sharmah, A., Guo, T., Das, G. K., Brown, J. M., Shannahan, J., Gordon, T., Chen, L. C., Pinkerton, K. E. & Van Winkle, L. S. Influence of particle size on persistence and clearance of aerosolized silver nanoparticles in the rat lung. *Toxicol Sci* **144**, 366-381, doi:10.1093/toxsci/kfv005 (2015).

52   Choi, H. S., Liu, W., Misra, P., Tanaka, E., Zimmer, J. P., Itty Ipe, B., Bawendi, M. G. & Frangioni, J. V. Renal clearance of quantum dots. *Nat Biotechnol* **25**, 1165-1170, doi:10.1038/nbt1340 (2007).

53   Hoshyar, N., Gray, S., Han, H. & Bao, G. The effect of nanoparticle size on in vivo pharmacokinetics and cellular interaction. *Nanomedicine (Lond)* **11**, 673-692, doi:10.2217/nnm.16.5 (2016).

54   Toy, R., Peiris, P. M., Ghaghada, K. B. & Karathanasis, E. Shaping cancer nanomedicine: the effect of particle shape on the in vivo journey of nanoparticles. *Nanomedicine (Lond)* **9**, 121-134, doi:10.2217/nnm.13.191 (2014).

55   Qie, Y., Yuan, H., von Roemeling, C. A., Chen, Y., Liu, X., Shih, K. D., Knight, J. A., Tun, H. W., Wharen, R. E., Jiang, W. & Kim, B. Y. S. Surface modification of nanoparticles enables selective evasion of phagocytic clearance by distinct macrophage phenotypes. *Scientific Reports* **6**, 26269, doi:10.1038/srep26269 (2016).

56   Xiao, K., Li, Y., Luo, J., Lee, J. S., Xiao, W., Gonik, A. M., Agarwal, R. G. & Lam, K. S. The effect of surface charge on in vivo biodistribution of PEG-oligocholic acid based micellar nanoparticles. *Biomaterials* **32**, 3435-3446, doi:10.1016/j.biomaterials.2011.01.021 (2011).

57   Gregoriadis, G. & Neerunjun, D. E. Control of the rate of hepatic uptake and catabolism of liposome-entrapped proteins injected into rats. Possible therapeutic applications. *Eur J Biochem* **47**, 179-185 (1974).

58   Hirn, S., Semmler-Behnke, M., Schleh, C., Wenk, A., Lipka, J., Schaffler, M., Takenaka, S., Moller, W., Schmid, G., Simon, U. & Kreyling, W. G. Particle size-dependent and surface charge-dependent biodistribution of gold nanoparticles after intravenous administration. *Eur J Pharm Biopharm* **77**, 407-416, doi:10.1016/j.ejpb.2010.12.029 (2011).

59   Stamatovic, S. M., Keep, R. F. & Andjelkovic, A. V. Brain endothelial cell-cell junctions: how to "open" the blood brain barrier. *Curr Neuropharmacol* **6**, 179-192, doi:10.2174/157015908785777210 (2008).

60   Knowland, D., Arac, A., Sekiguchi, K. J., Hsu, M., Lutz, S. E., Perrino, J., Steinberg, G. K., Barres, B. A., Nimmerjahn, A. & Agalliu, D. Stepwise recruitment of transcellular and paracellular pathways underlies blood-brain barrier breakdown in stroke. *Neuron* **82**, 603-617, doi:10.1016/j.neuron.2014.03.003 (2014).

61   Tatiparti, K., Sau, S., Kashaw, S. K. & Iyer, A. K. siRNA Delivery Strategies: A Comprehensive Review of Recent Developments. *Nanomaterials (Basel)* **7**, doi:10.3390/nano7040077 (2017).

62   Gooding, M., Browne, L. P., Quinteiro, F. M. & Selwood, D. L. siRNA delivery: from lipids to cell-penetrating peptides and their mimics. *Chem Biol Drug Des* **80**, 787-809, doi:10.1111/cbdd.12052 (2012).

63   Ervin, E. H., Pook, M., Teino, I., Kasuk, V., Trei, A., Pooga, M. & Maimets, T. Targeted gene silencing in human embryonic stem cells using cell-penetrating peptide PepFect 14. *Stem Cell Res Ther* **10**, 43, doi:10.1186/s13287-019-1144-x (2019).

64   Juliano, R. L. & Carver, K. Cellular uptake and intracellular trafficking of oligonucleotides. *Adv Drug Deliv Rev* **87**, 35-45, doi:10.1016/j.addr.2015.04.005 (2015).

65   Butler, M., Crooke, R. M., Graham, M. J., Lemonidis, K. M., Lougheed, M., Murray, S. F., Witchell, D., Steinbrecher, U. & Bennett, C. F. Phosphorothioate oligodeoxynucleotides

distribute similarly in class A scavenger receptor knockout and wild-type mice. *J Pharmacol Exp Ther* **292**, 489-496 (2000).

66   Wagenaar, T. R., Tolstykh, T., Shi, C., Jiang, L., Zhang, J., Li, Z., Yu, Q., Qu, H., Sun, F., Cao, H., Pollard, J., Dai, S., Gao, Q., Zhang, B., Arlt, H., Cindhuchao, M., Hoffmann, D., Light, M., Jensen, K., Hopke, J., Newcombe, R., Garcia-Echeverria, C., Winter, C., Zabludoff, S. & Wiederschain, D. Identification of the endosomal sorting complex required for transport-I (ESCRT-I) as an important modulator of anti-miR uptake by cancer cells. *Nucleic Acids Res* **43**, 1204-1215, doi:10.1093/nar/gku1367 (2015).

67   Mayor, S., Parton, R. G. & Donaldson, J. G. Clathrin-independent pathways of endocytosis. *Cold Spring Harb Perspect Biol* **6**, doi:10.1101/cshperspect.a016758 (2014).

68   Lajoie, P. & Nabi, I. R. Lipid rafts, caveolae, and their endocytosis. *Int Rev Cell Mol Biol* **282**, 135-163, doi:10.1016/S1937-6448(10)82003-9 (2010).

69   Kerr, M. C. & Teasdale, R. D. Defining macropinocytosis. *Traffic* **10**, 364-371, doi:10.1111/j.1600-0854.2009.00878.x (2009).

70   Doherty, G. J. & McMahon, H. T. Mechanisms of endocytosis. *Annu Rev Biochem* **78**, 857-902, doi:10.1146/annurev.biochem.78.081307.110540 (2009).

71   Hu, Y. B., Dammer, E. B., Ren, R. J. & Wang, G. The endosomal-lysosomal system: from acidification and cargo sorting to neurodegeneration. *Transl Neurodegener* **4**, 18, doi:10.1186/s40035-015-0041-1 (2015).

72   Sahay, G., Querbes, W., Alabi, C., Eltoukhy, A., Sarkar, S., Zurenko, C., Karagiannis, E., Love, K., Chen, D., Zoncu, R., Buganim, Y., Schroeder, A., Langer, R. & Anderson, D. G. Efficiency of siRNA delivery by lipid nanoparticles is limited by endocytic recycling. *Nat Biotechnol* **31**, 653-658, doi:10.1038/nbt.2614 (2013).

73   Gilleron, J., Querbes, W., Zeigerer, A., Borodovsky, A., Marsico, G., Schubert, U., Manygoats, K., Seifert, S., Andree, C., Stoter, M., Epstein-Barash, H., Zhang, L., Koteliansky, V., Fitzgerald, K., Fava, E., Bickle, M., Kalaidzidis, Y., Akinc, A., Maier, M. & Zerial, M. Image-based analysis of lipid nanoparticle-mediated siRNA delivery, intracellular trafficking and endosomal escape. *Nat Biotechnol* **31**, 638-646, doi:10.1038/nbt.2612 (2013).

74   Hardee, C. L., Arevalo-Soliz, L. M., Hornstein, B. D. & Zechiedrich, L. Advances in Non-Viral DNA Vectors for Gene Therapy. *Genes (Basel)* **8**, doi:10.3390/genes8020065 (2017).

75   Kimchi-Sarfaty, C., Brittain, S., Garfield, S., Caplen, N. J., Tang, Q. & Gottesman, M. M. Efficient delivery of RNA interference effectors via in vitro-packaged SV40 pseudovirions. *Hum Gene Ther* **16**, 1110-1115, doi:10.1089/hum.2005.16.1110 (2005).

76   Oliveira, S., Storm, G. & Schiffelers, R. M. Targeted delivery of siRNA. *J Biomed Biotechnol* **2006**, 63675, doi:10.1155/JBB/2006/63675 (2006).

77   Gubernator, J., Lipka, D., Korycinska, M., Kempinska, K., Milczarek, M., Wietrzyk, J., Hrynyk, R., Barnert, S., Suss, R. & Kozubek, A. Efficient human breast cancer xenograft regression after a single treatment with a novel liposomal formulation of epirubicin prepared using the EDTA ion gradient method. *PLoS One* **9**, e91487, doi:10.1371/journal.pone.0091487 (2014).

78   Brown, A., Patel, S., Ward, C., Lorenz, A., Ortiz, M., DuRoss, A., Wieghardt, F., Esch, A., Otten, E. G., Heiser, L. M., Korolchuk, V. I., Sun, C., Sarkar, S. & Sahay, G. PEG-lipid micelles enable cholesterol efflux in Niemann-Pick Type C1 disease-based lysosomal storage disorder. *Scientific Reports* **6**, 31750, doi:10.1038/srep31750 https://www.nature.com/articles/srep31750#supplementary-information (2016).

79   Yakimova, L. S., Shurpik, D. N., Guralnik, E. G., Evtugyn, V. G., Osin, Y. N. & Stoikov, I. I. Fluorescein-Loaded Solid Lipid Nanoparticles Based on Monoamine Pillar[5]arene: Synthesis and Interaction with DNA. *ChemNanoMat* **4**, 919-923, doi:10.1002/cnma.201800207 (2018).

80   García-Díaz, M., Foged, C. & Nielsen, H. M. Improved insulin loading in poly(lactic-co-glycolic) acid (PLGA) nanoparticles upon self-assembly with lipids. *International Journal of Pharmaceutics* **482**, 84-91, doi:https://doi.org/10.1016/j.ijpharm.2014.11.047 (2015).

81   Jackson, C. L., Chanzy, H. D., Booy, F. P., Drake, B. J., Tomalia, D. A., Bauer, B. J. & Amis, E. J. Visualization of Dendrimer Molecules by Transmission Electron Microscopy (TEM): Staining Methods and Cryo-TEM of Vitrified Solutions. *Macromolecules* **31**, 6259-6265, doi:10.1021/ma9806155 (1998).

82   Meen, T.-H., Tsai, J.-K., Chao, S.-M., Lin, Y.-C., Wu, T.-C., Chang, T.-Y., Ji, L.-W., Water, W., Chen, W.-R., Tang, I. T. & Huang, C.-J. Surface plasma resonant effect of gold nanoparticles on the photoelectrodes of dye-sensitized solar cells. *Nanoscale Research Letters* **8**, 450, doi:10.1186/1556-276X-8-450 (2013).

83   Wierzbinski, K. R., Szymanski, T., Rozwadowska, N., Rybka, J. D., Zimna, A., Zalewski, T., Nowicka-Bauer, K., Malcher, A., Nowaczyk, M., Krupinski, M., Fiedorowicz, M., Bogorodzki, P., Grieb, P., Giersig, M. & Kurpisz, M. K. Potential use of superparamagnetic iron oxide nanoparticles for in vitro and in vivo bioimaging of human myoblasts. *Scientific Reports* **8**, 3682, doi:10.1038/s41598-018-22018-0 (2018).

84   Lu, J., Liong, M., Zink, J. I. & Tamanoi, F. Mesoporous Silica Nanoparticles as a Delivery System for Hydrophobic Anticancer Drugs. *Small* **3**, 1341-1346, doi:10.1002/smll.200700005 (2007).

85   Hegde, V., Hickerson, R. P., Nainamalai, S., Campbell, P. A., Smith, F. J., McLean, W. H. & Pedrioli, D. M. In vivo gene silencing following non-invasive siRNA delivery into the skin using a novel topical formulation. *J Control Release* **196**, 355-362, doi:10.1016/j.jconrel.2014.10.022 (2014).

86   Pei, Y., Hancock, P. J., Zhang, H., Bartz, R., Cherrin, C., Innocent, N., Pomerantz, C. J., Seitzer, J., Koser, M. L., Abrams, M. T., Xu, Y., Kuklin, N. A., Burke, P. A., Sachs, A. B., Sepp-Lorenzino, L. & Barnett, S. F. Quantitative evaluation of siRNA delivery in vivo. *RNA* **16**, 2553-2563, doi:10.1261/rna.2255810 (2010).

87   Zhou, A., Du, J., Jiao, M., Xie, D., Wang, Q., Xue, L., Ju, C., Hua, Z. & Zhang, C. Co-delivery of TRAIL and siHSP70 using hierarchically modular assembly formulations achieves enhanced TRAIL-resistant cancer therapy. *J Control Release*, doi:10.1016/j.jconrel.2019.05.013 (2019).

88   Xiao, H., Altangerel, A., Gerile, G., Wu, Y. & Baigude, H. Design of Highly Potent Lipid-Functionalized Peptidomimetics for Efficient in Vivo siRNA Delivery. *ACS Appl Mater Interfaces* **8**, 7638-7645, doi:10.1021/acsami.5b12144 (2016).

89   Ganbold, T., Gerile, G., Xiao, H. & Baigude, H. Efficient in vivo siRNA delivery by stabilized d-peptide-based lipid nanoparticles. *RSC Advances* **7**, 8823-8831, doi:10.1039/C6RA25862J (2017).

90   Coelho, T., Adams, D., Silva, A., Lozeron, P., Hawkins, P. N., Mant, T., Perez, J., Chiesa, J., Warrington, S., Tranter, E., Munisamy, M., Falzone, R., Harrop, J., Cehelsky, J., Bettencourt, B. R., Geissler, M., Butler, J. S., Sehgal, A., Meyers, R. E., Chen, Q., Borland, T., Hutabarat, R. M., Clausen, V. A., Alvarez, R., Fitzgerald, K., Gamba-Vitalo, C., Nochur, S. V., Vaishnaw, A. K., Sah, D. W., Gollob, J. A. & Suhr, O. B. Safety and efficacy of RNAi therapy for transthyretin amyloidosis. *N Engl J Med* **369**, 819-829, doi:10.1056/NEJMoa1208760 (2013).

91   Semple, S. C., Akinc, A., Chen, J., Sandhu, A. P., Mui, B. L., Cho, C. K., Sah, D. W. Y., Stebbing, D., Crosley, E. J., Yaworski, E., Hafez, I. M., Dorkin, J. R., Qin, J., Lam, K., Rajeev, K. G., Wong, K. F., Jeffs, L. B., Nechev, L., Eisenhardt, M. L., Jayaraman, M., Kazem, M., Maier, M. A., Srinivasulu, M., Weinstein, M. J., Chen, Q., Alvarez, R., Barros, S. A., De, S., Klimuk, S. K., Borland, T., Kosovrasti, V., Cantley, W. L., Tam, Y. K., Manoharan, M., Ciufolini, M. A., Tracy, M. A., de Fougerolles, A., MacLachlan, I., Cullis, P. R., Madden, T. D. & Hope, M. J. Rational design of cationic lipids for siRNA delivery. *Nature Biotechnology* **28**, 172, doi:10.1038/nbt.1602 (2010).

92   Judge, A. D., Robbins, M., Tavakoli, I., Levi, J., Hu, L., Fronda, A., Ambegia, E., McClintock, K. & MacLachlan, I. Confirming the RNAi-mediated mechanism of action of siRNA-based cancer therapeutics in mice. *J Clin Invest* **119**, 661-673, doi:10.1172/JCI37515 (2009).

93   Wang, D., Lin, J., Jia, F., Tan, X., Wang, Y., Sun, X., Cao, X., Che, F., Lu, H., Gao, X., Shimkonis, J. C., Nyoni, Z., Lu, X. & Zhang, K. Bottlebrush-architectured poly(ethylene glycol) as an efficient vector for RNA interference in vivo. *Sci Adv* **5**, eaav9322, doi:10.1126/sciadv.aav9322 (2019).

94   Du, L., Zhou, J., Meng, L., Wang, X., Wang, C., Huang, Y., Zheng, S., Deng, L., Cao, H., Liang, Z., Dong, A. & Cheng, Q. The pH-Triggered Triblock Nanocarrier Enabled Highly Efficient siRNA Delivery for Cancer Therapy. *Theranostics* **7**, 3432-3445, doi:10.7150/thno.20297 (2017).

95   Cui, J., Piotrowski-Daspit, A. S., Zhang, J., Shao, M., Bracaglia, L. G., Utsumi, T., Seo, Y. E., DiRito, J., Song, E., Wu, C., Inada, A., Tietjen, G. T., Pober, J. S., Iwakiri, Y. & Saltzman, W. M. Poly(amine-co-ester) nanoparticles for effective Nogo-B knockdown in the liver. *J Control Release*, doi:10.1016/j.jconrel.2019.04.044 (2019).

96   Alameh, M., Lavertu, M., Tran-Khanh, N., Chang, C. Y., Lesage, F., Bail, M., Darras, V., Chevrier, A. & Buschmann, M. D. siRNA Delivery with Chitosan: Influence of Chitosan Molecular Weight, Degree of Deacetylation, and Amine to Phosphate Ratio on in Vitro Silencing Efficiency, Hemocompatibility, Biodistribution, and in Vivo Efficacy. *Biomacromolecules* **19**, 112-131, doi:10.1021/acs.biomac.7b01297 (2018).

97   Han, H. D., Mangala, L. S., Lee, J. W., Shahzad, M. M., Kim, H. S., Shen, D., Nam, E. J., Mora, E. M., Stone, R. L., Lu, C., Lee, S. J., Roh, J. W., Nick, A. M., Lopez-Berestein, G. & Sood, A. K. Targeted gene silencing using RGD-labeled chitosan nanoparticles. *Clin Cancer Res* **16**, 3910-3922, doi:10.1158/1078-0432.CCR-10-0005 (2010).

98   Davis, M. E., Zuckerman, J. E., Choi, C. H., Seligson, D., Tolcher, A., Alabi, C. A., Yen, Y., Heidel, J. D. & Ribas, A. Evidence of RNAi in humans from systemically administered siRNA via targeted nanoparticles. *Nature* **464**, 1067-1070, doi:10.1038/nature08956 (2010).

99   Liu, G., Xie, J., Zhang, F., Wang, Z., Luo, K., Zhu, L., Quan, Q., Niu, G., Lee, S., Ai, H. & Chen, X. N-Alkyl-PEI-functionalized iron oxide nanoclusters for efficient siRNA delivery. *Small* **7**, 2742-2749, doi:10.1002/smll.201100825 (2011).

100   Dahlman, J. E., Barnes, C., Khan, O., Thiriot, A., Jhunjunwala, S., Shaw, T. E., Xing, Y., Sager, H. B., Sahay, G., Speciner, L., Bader, A., Bogorad, R. L., Yin, H., Racie, T., Dong, Y., Jiang, S., Seedorf, D., Dave, A., Sandu, K. S., Webber, M. J., Novobrantseva, T., Ruda, V. M., Lytton-Jean, A. K. R., Levins, C. G., Kalish, B., Mudge, D. K., Perez, M., Abezgauz, L., Dutta, P., Smith, L., Charisse, K., Kieran, M. W., Fitzgerald, K., Nahrendorf, M., Danino, D., Tuder, R. M., von Andrian, U. H., Akinc, A., Schroeder, A., Panigrahy, D., Kotelianski, V., Langer, R. & Anderson, D. G. In vivo endothelial siRNA delivery using polymeric nanoparticles with low molecular weight. *Nat Nanotechnol* **9**, 648-655, doi:10.1038/nnano.2014.84 (2014).

101   Choi, K. Y., Silvestre, O. F., Huang, X., Min, K. H., Howard, G. P., Hida, N., Jin, A. J., Carvajal, N., Lee, S. W., Hong, J. I. & Chen, X. Versatile RNA interference nanoplatform for systemic delivery of RNAs. *ACS Nano* **8**, 4559-4570, doi:10.1021/nn500085k (2014).

102   Kong, L., Qiu, J., Sun, W., Yang, J., Shen, M., Wang, L. & Shi, X. Multifunctional PEI-entrapped gold nanoparticles enable efficient delivery of therapeutic siRNA into glioblastoma cells. *Biomater Sci* **5**, 258-266, doi:10.1039/c6bm00708b (2017).

103   Lee, M. Y., Park, S. J., Park, K., Kim, K. S., Lee, H. & Hahn, S. K. Target-specific gene silencing of layer-by-layer assembled gold-cysteamine/siRNA/PEI/HA nanocomplex. *ACS Nano* **5**, 6138-6147, doi:10.1021/nn2017793 (2011).

104   Yi, Y., Kim, H. J., Mi, P., Zheng, M., Takemoto, H., Toh, K., Kim, B. S., Hayashi, K., Naito, M., Matsumoto, Y., Miyata, K. & Kataoka, K. Targeted systemic delivery of siRNA to cervical cancer model using cyclic RGD-installed unimer polyion complex-assembled gold nanoparticles. *J Control Release* **244**, 247-256, doi:10.1016/j.jconrel.2016.08.041 (2016).

105   Conde, J., Ambrosone, A., Sanz, V., Hernandez, Y., Marchesano, V., Tian, F., Child, H., Berry, C. C., Ibarra, M. R., Baptista, P. V., Tortiglione, C. & de la Fuente, J. M. Design of

multifunctional gold nanoparticles for in vitro and in vivo gene silencing. *ACS Nano* **6**, 8316-8324, doi:10.1021/nn3030223 (2012).

106   Vio, V., Riveros, A. L., Tapia-Bustos, A., Lespay-Rebolledo, C., Perez-Lobos, R., Munoz, L., Pismante, P., Morales, P., Araya, E., Hassan, N., Herrera-Marschitz, M. & Kogan, M. J. Gold nanorods/siRNA complex administration for knockdown of PARP-1: a potential treatment for perinatal asphyxia. *Int J Nanomedicine* **13**, 6839-6854, doi:10.2147/IJN.S175076 (2018).

107   Agrawal, A., Min, D. H., Singh, N., Zhu, H., Birjiniuk, A., von Maltzahn, G., Harris, T. J., Xing, D., Woolfenden, S. D., Sharp, P. A., Charest, A. & Bhatia, S. Functional delivery of siRNA in mice using dendriworms. *ACS Nano* **3**, 2495-2504, doi:10.1021/nn900201e (2009).

108   Mahajan, U. M., Teller, S., Sendler, M., Palankar, R., van den Brandt, C., Schwaiger, T., Kuhn, J. P., Ribback, S., Glockl, G., Evert, M., Weitschies, W., Hosten, N., Dombrowski, F., Delcea, M., Weiss, F. U., Lerch, M. M. & Mayerle, J. Tumour-specific delivery of siRNA-coupled superparamagnetic iron oxide nanoparticles, targeted against PLK1, stops progression of pancreatic cancer. *Gut* **65**, 1838-1849, doi:10.1136/gutjnl-2016-311393 (2016).

109   Yang, Z., Duan, J., Wang, J., Liu, Q., Shang, R., Yang, X., Lu, P., Xia, C., Wang, L. & Dou, K. Superparamagnetic iron oxide nanoparticles modified with polyethylenimine and galactose for siRNA targeted delivery in hepatocellular carcinoma therapy. *Int J Nanomedicine* **13**, 1851-1865, doi:10.2147/IJN.S155537 (2018).

110   Meng, H., Mai, W. X., Zhang, H., Xue, M., Xia, T., Lin, S., Wang, X., Zhao, Y., Ji, Z., Zink, J. I. & Nel, A. E. Codelivery of an optimal drug/siRNA combination using mesoporous silica nanoparticles to overcome drug resistance in breast cancer in vitro and in vivo. *ACS Nano* **7**, 994-1005, doi:10.1021/nn3044066 (2013).

111   Chen, Y., Wang, X., Liu, T., Zhang, D. S., Wang, Y., Gu, H. & Di, W. Highly effective antiangiogenesis via magnetic mesoporous silica-based siRNA vehicle targeting the VEGF gene for orthotopic ovarian cancer therapy. *Int J Nanomedicine* **10**, 2579-2594, doi:10.2147/IJN.S78774 (2015).

112   Li, X., Chen, Y., Wang, M., Ma, Y., Xia, W. & Gu, H. A mesoporous silica nanoparticle--PEI--fusogenic peptide system for siRNA delivery in cancer therapy. *Biomaterials* **34**, 1391-1401, doi:10.1016/j.biomaterials.2012.10.072 (2013).

113   Finlay, J., Roberts, C. M., Dong, J., Zink, J. I., Tamanoi, F. & Glackin, C. A. Mesoporous silica nanoparticle delivery of chemically modified siRNA against TWIST1 leads to reduced tumor burden. *Nanomedicine* **11**, 1657-1666, doi:10.1016/j.nano.2015.05.011 (2015).

114   Morry, J., Ngamcherdtrakul, W., Gu, S., Reda, M., Castro, D. J., Sangvanich, T., Gray, J. W. & Yantasee, W. Targeted Treatment of Metastatic Breast Cancer by PLK1 siRNA Delivered by an Antioxidant Nanoparticle Platform. *Mol Cancer Ther* **16**, 763-772, doi:10.1158/1535-7163.MCT-16-0644 (2017).

115 Morry, J., Ngamcherdtrakul, W., Gu, S., Goodyear, S. M., Castro, D. J., Reda, M. M., Sangvanich, T. & Yantasee, W. Dermal delivery of HSP47 siRNA with NOX4-modulating mesoporous silica-based nanoparticles for treating fibrosis. *Biomaterials* **66**, 41-52, doi:10.1016/j.biomaterials.2015.07.005 (2015).

116 Ngamcherdtrakul, W., Morry, J., Gu, S., Castro, D. J., Goodyear, S. M., Sangvanich, T., Reda, M. M., Lee, R., Mihelic, S. A., Beckman, B. L., Hu, Z., Gray, J. W. & Yantasee, W. Cationic Polymer Modified Mesoporous Silica Nanoparticles for Targeted SiRNA Delivery to HER2+ Breast Cancer. *Adv Funct Mater* **25**, 2646-2659, doi:10.1002/adfm.201404629 (2015).

117 Kim, B., Pang, H. B., Kang, J., Park, J. H., Ruoslahti, E. & Sailor, M. J. Immunogene therapy with fusogenic nanoparticles modulates macrophage response to Staphylococcus aureus. *Nat Commun* **9**, 1969, doi:10.1038/s41467-018-04390-7 (2018).

118 Kim, B., Sun, S., Varner, J. A., Howell, S. B., Ruoslahti, E. & Sailor, M. J. Securing the Payload, Finding the Cell, Avoiding the Endosome: Peptide-Targeted, Fusogenic Porous Silicon Nanoparticles for More Effective Delivery of siRNA Therapies. *Submitted* (2019).

119 Tong, W. Y., Alnakhli, M., Bhardwaj, R., Apostolou, S., Sinha, S., Fraser, C., Kuchel, T., Kuss, B. & Voelcker, N. H. Delivery of siRNA in vitro and in vivo using PEI-capped porous silicon nanoparticles to silence MRP1 and inhibit proliferation in glioblastoma. *J Nanobiotechnology* **16**, 38, doi:10.1186/s12951-018-0365-y (2018).

120 Tanaka, T., Mangala, L. S., Vivas-Mejia, P. E., Nieves-Alicea, R., Mann, A. P., Mora, E., Han, H. D., Shahzad, M. M., Liu, X., Bhavane, R., Gu, J., Fakhoury, J. R., Chiappini, C., Lu, C., Matsuo, K., Godin, B., Stone, R. L., Nick, A. M., Lopez-Berestein, G., Sood, A. K. & Ferrari, M. Sustained small interfering RNA delivery by mesoporous silicon particles. *Cancer Res* **70**, 3687-3696, doi:10.1158/0008-5472.CAN-09-3931 (2010).

121 Weiss, J., Decker, E. A., McClements, D. J., Kristbergsson, K., Helgason, T. & Awad, T. Solid Lipid Nanoparticles as Delivery Systems for Bioactive Food Components. *Food Biophysics* **3**, 146-154, doi:10.1007/s11483-008-9065-8 (2008).

122 Alshaer, W., Hillaireau, H., Vergnaud, J., Mura, S., Delomenie, C., Sauvage, F., Ismail, S. & Fattal, E. Aptamer-guided siRNA-loaded nanomedicines for systemic gene silencing in CD-44 expressing murine triple-negative breast cancer model. *J Control Release* **271**, 98-106, doi:10.1016/j.jconrel.2017.12.022 (2018).

123 Rengaswamy, V., Zimmer, D., Suss, R. & Rossler, J. RGD liposome-protamine-siRNA (LPR) nanoparticles targeting PAX3-FOXO1 for alveolar rhabdomyosarcoma therapy. *J Control Release* **235**, 319-327, doi:10.1016/j.jconrel.2016.05.063 (2016).

124 Ewe, A., Panchal, O., Pinnapireddy, S. R., Bakowsky, U., Przybylski, S., Temme, A. & Aigner, A. Liposome-polyethylenimine complexes (DPPC-PEI lipopolyplexes) for therapeutic siRNA delivery in vivo. *Nanomedicine* **13**, 209-218, doi:10.1016/j.nano.2016.08.005 (2017).

125 Pinnapireddy, S. R., Duse, L., Strehlow, B., Schafer, J. & Bakowsky, U. Composite liposome-PEI/nucleic acid lipopolyplexes for safe and efficient gene delivery and gene

knowdown. *Colloids Surf B Biointerfaces* **158**, 93-101, doi:10.1016/j.colsurfb.2017.06.022 (2017).

126   Bender, H. R., Kane, S. & Zabel, M. D. Delivery of Therapeutic siRNA to the CNS Using Cationic and Anionic Liposomes. *J Vis Exp*, doi:10.3791/54106 (2016).

127   Lee, J. M., Yoon, T. J. & Cho, Y. S. Recent developments in nanoparticle-based siRNA delivery for cancer therapy. *Biomed Res Int* **2013**, 782041, doi:10.1155/2013/782041 (2013).

128   Whitehead, K. A., Langer, R. & Anderson, D. G. Knocking down barriers: advances in siRNA delivery. *Nature Reviews Drug Discovery* **8**, 129, doi:10.1038/nrd2742 (2009).

129   Morrissey, D. V., Lockridge, J. A., Shaw, L., Blanchard, K., Jensen, K., Breen, W., Hartsough, K., Machemer, L., Radka, S., Jadhav, V., Vaish, N., Zinnen, S., Vargeese, C., Bowman, K., Shaffer, C. S., Jeffs, L. B., Judge, A., MacLachlan, I. & Polisky, B. Potent and persistent in vivo anti-HBV activity of chemically modified siRNAs. *Nat Biotechnol* **23**, 1002-1007, doi:10.1038/nbt1122 (2005).

130   Morrissey, D. V., Blanchard, K., Shaw, L., Jensen, K., Lockridge, J. A., Dickinson, B., McSwiggen, J. A., Vargeese, C., Bowman, K., Shaffer, C. S., Polisky, B. A. & Zinnen, S. Activity of stabilized short interfering RNA in a mouse model of hepatitis B virus replication. *Hepatology* **41**, 1349-1356, doi:10.1002/hep.20702 (2005).

131   Briuglia, M. L., Rotella, C., McFarlane, A. & Lamprou, D. A. Influence of cholesterol on liposome stability and on in vitro drug release. *Drug Deliv Transl Res* **5**, 231-242, doi:10.1007/s13346-015-0220-8 (2015).

132   Kaddah, S., Khreich, N., Kaddah, F., Charcosset, C. & Greige-Gerges, H. Cholesterol modulates the liposome membrane fluidity and permeability for a hydrophilic molecule. *Food Chem Toxicol* **113**, 40-48, doi:10.1016/j.fct.2018.01.017 (2018).

133   (https://ClinicalTrials.gov/show/NCT01262235).

134   (https://ClinicalTrials.gov/show/NCT01437007).

135   Draz, M. S., Fang, B. A., Zhang, P., Hu, Z., Gu, S., Weng, K. C., Gray, J. W. & Chen, F. F. Nanoparticle-mediated systemic delivery of siRNA for treatment of cancers and viral infections. *Theranostics* **4**, 872-892, doi:10.7150/thno.9404 (2014).

136   Akinc, A., Zumbuehl, A., Goldberg, M., Leshchiner, E. S., Busini, V., Hossain, N., Bacallado, S. A., Nguyen, D. N., Fuller, J., Alvarez, R., Borodovsky, A., Borland, T., Constien, R., de Fougerolles, A., Dorkin, J. R., Narayanannair Jayaprakash, K., Jayaraman, M., John, M., Koteliansky, V., Manoharan, M., Nechev, L., Qin, J., Racie, T., Raitcheva, D., Rajeev, K. G., Sah, D. W., Soutschek, J., Toudjarska, I., Vornlocher, H. P., Zimmermann, T. S., Langer, R. & Anderson, D. G. A combinatorial library of lipid-like materials for delivery of RNAi therapeutics. *Nat Biotechnol* **26**, 561-569, doi:10.1038/nbt1402 (2008).

137   Wood, H. FDA approves patisiran to treat hereditary transthyretin amyloidosis. *Nat Rev Neurol* **14**, 570, doi:10.1038/s41582-018-0065-0 (2018).

138   Patil, Y. & Panyam, J. Polymeric nanoparticles for siRNA delivery and gene silencing. *Int J Pharm* **367**, 195-203, doi:10.1016/j.ijpharm.2008.09.039 (2009).

139   Cavallaro, G., Sardo, C., Craparo, E. F., Porsio, B. & Giammona, G. Polymeric nanoparticles for siRNA delivery: Production and applications. *Int J Pharm* **525**, 313-333, doi:10.1016/j.ijpharm.2017.04.008 (2017).

140   Cooper, B. M. & Putnam, D. Polymers for siRNA Delivery: A Critical Assessment of Current Technology Prospects for Clinical Application. *ACS Biomaterials Science & Engineering* **2**, 1837-1850, doi:10.1021/acsbiomaterials.6b00363 (2016).

141   Dong, Y., Siegwart, D. J. & Anderson, D. G. Strategies, design, and chemistry in siRNA delivery systems. *Advanced Drug Delivery Reviews*, doi:https://doi.org/10.1016/j.addr.2019.05.004 (2019).

142   Makadia, H. K. & Siegel, S. J. Poly Lactic-co-Glycolic Acid (PLGA) as Biodegradable Controlled Drug Delivery Carrier. *Polymers (Basel)* **3**, 1377-1397, doi:10.3390/polym3031377 (2011).

143   Buyens, K., Meyer, M., Wagner, E., Demeester, J., De Smedt, S. C. & Sanders, N. N. Monitoring the disassembly of siRNA polyplexes in serum is crucial for predicting their biological efficacy. *Journal of Controlled Release* **141**, 38-41, doi:https://doi.org/10.1016/j.jconrel.2009.08.026 (2010).

144   Qi, R., Liu, S., Chen, J., Xiao, H., Yan, L., Huang, Y. & Jing, X. Biodegradable copolymers with identical cationic segments and their performance in siRNA delivery. *Journal of Controlled Release* **159**, 251-260, doi:https://doi.org/10.1016/j.jconrel.2012.01.015 (2012).

145   Zheng, C., Zheng, M., Gong, P., Deng, J., Yi, H., Zhang, P., Zhang, Y., Liu, P., Ma, Y. & Cai, L. Polypeptide cationic micelles mediated co-delivery of docetaxel and siRNA for synergistic tumor therapy. *Biomaterials* **34**, 3431-3438, doi:https://doi.org/10.1016/j.biomaterials.2013.01.053 (2013).

146   Mao, S., Sun, W. & Kissel, T. Chitosan-based formulations for delivery of DNA and siRNA. *Advanced Drug Delivery Reviews* **62**, 12-27, doi:https://doi.org/10.1016/j.addr.2009.08.004 (2010).

147   Raemdonck, K., Martens, T. F., Braeckmans, K., Demeester, J. & De Smedt, S. C. Polysaccharide-based nucleic acid nanoformulations. *Advanced Drug Delivery Reviews* **65**, 1123-1147, doi:https://doi.org/10.1016/j.addr.2013.05.002 (2013).

148   Li, J., Yu, X., Wang, Y., Yuan, Y., Xiao, H., Cheng, D. & Shuai, X. A reduction and pH dual-sensitive polymeric vector for long-circulating and tumor-targeted siRNA delivery. *Adv Mater* **26**, 8217-8224, doi:10.1002/adma.201403877 (2014).

149   Xin, Y., Huang, M., Guo, W. W., Huang, Q., Zhang, L. Z. & Jiang, G. Nano-based delivery of RNAi in cancer therapy. *Mol Cancer* **16**, 134, doi:10.1186/s12943-017-0683-y (2017).

150   Conde, J., Ambrosone, A., Hernandez, Y., Tian, F., McCully, M., Berry, C. C., Baptista, P. V., Tortiglione, C. & de la Fuente, J. M. 15 years on siRNA delivery: Beyond the State-of-the-Art on inorganic nanoparticles for RNAi therapeutics. *Nano Today* **10**, 421-450, doi:https://doi.org/10.1016/j.nantod.2015.06.008 (2015).

151   Hardie, J., Huo, S., Jiang, Y., Liang, X.-J., Farkas, M. E. & Rotello, V. M. in *Handbook of Nanomaterials for Cancer Theranostics*   (ed João Conde) 537-550 (Elsevier, 2018).

152   Jiang, Y., Huo, S., Hardie, J., Liang, X. J. & Rotello, V. M. Progress and perspective of inorganic nanoparticle-based siRNA delivery systems. *Expert Opin Drug Deliv* **13**, 547-559, doi:10.1517/17425247.2016.1134486 (2016).

153   Lee, J.-H., Lee, K., Moon, S. H., Lee, Y., Park, T. G. & Cheon, J. All-in-One Target-Cell-Specific Magnetic Nanoparticles for Simultaneous Molecular Imaging and siRNA Delivery. *Angewandte Chemie International Edition* **48**, 4174-4179, doi:10.1002/anie.200805998 (2009).

154   Artiga, Á., Serrano-Sevilla, I., De Matteis, L., Mitchell, S. G. & de la Fuente, J. M. Current status and future perspectives of gold nanoparticle vectors for siRNA delivery. *Journal of Materials Chemistry B* **7**, 876-896, doi:10.1039/C8TB02484G (2019).

155   Shen, J., Kim, H. C., Mu, C., Gentile, E., Mai, J., Wolfram, J., Ji, L. N., Ferrari, M., Mao, Z. W. & Shen, H. Multifunctional gold nanorods for siRNA gene silencing and photothermal therapy. *Adv Healthc Mater* **3**, 1629-1637, doi:10.1002/adhm.201400103 (2014).

156   Wang, Z., Li, S., Zhang, M., Ma, Y., Liu, Y., Gao, W., Zhang, J. & Gu, Y. Laser-Triggered Small Interfering RNA Releasing Gold Nanoshells against Heat Shock Protein for Sensitized Photothermal Therapy. *Adv Sci (Weinh)* **4**, 1600327, doi:10.1002/advs.201600327 (2017).

157   Riley, R. S., Dang, M. N., Billingsley, M. M., Abraham, B., Gundlach, L. & Day, E. S. Evaluating the Mechanisms of Light-Triggered siRNA Release from Nanoshells for Temporal Control Over Gene Regulation. *Nano Lett* **18**, 3565-3570, doi:10.1021/acs.nanolett.8b00681 (2018).

158   Liu, Y., Xu, M., Zhao, Y., Chen, X., Zhu, X., Wei, C., Zhao, S., Liu, J. & Qin, X. Flower-like gold nanoparticles for enhanced photothermal anticancer therapy by the delivery of pooled siRNA to inhibit heat shock stress response. *Journal of Materials Chemistry B* **7**, 586-597, doi:10.1039/C8TB02418A (2019).

159   Kumal, R. R., Abu-Laban, M., Hamal, P., Kruger, B., Smith, H. T., Hayes, D. J. & Haber, L. H. Near-Infrared Photothermal Release of siRNA from the Surface of Colloidal Gold-Silver-Gold Core-Shell-Shell Nanoparticles Studied with Second-Harmonic Generation. *J Phys Chem C Nanomater Interfaces* **122**, 19699-19704, doi:10.1021/acs.jpcc.8b06117 (2018).

160   Jiang, S., Eltoukhy, A. A., Love, K. T., Langer, R. & Anderson, D. G. Lipidoid-Coated Iron Oxide Nanoparticles for Efficient DNA and siRNA delivery. *Nano Letters* **13**, 1059-1064, doi:10.1021/nl304287a (2013).

161   Zhang, L., Wang, T., Li, L., Wang, C., Su, Z. & Li, J. Multifunctional fluorescent-magnetic polyethyleneimine functionalized Fe3O4-mesoporous silica yolk-shell nanocapsules for siRNA delivery. *Chem Commun (Camb)* **48**, 8706-8708, doi:10.1039/c2cc33472k (2012).

162   Namiki, Y., Namiki, T., Yoshida, H., Ishii, Y., Tsubota, A., Koido, S., Nariai, K., Mitsunaga, M., Yanagisawa, S., Kashiwagi, H., Mabashi, Y., Yumoto, Y., Hoshina, S., Fujise, K. & Tada, N. A novel magnetic crystal–lipid nanostructure for magnetically guided in vivo gene delivery. *Nature Nanotechnology* **4**, 598, doi:10.1038/nnano.2009.202 (2009).

163   Cho, Y.-S., Yoon, T.-J., Jang, E.-S., Soo Hong, K., Young Lee, S., Ran Kim, O., Park, C., Kim, Y.-J., Yi, G.-C. & Chang, K. Cetuximab-conjugated magneto-fluorescent silica nanoparticles for in vivo colon cancer targeting and imaging. *Cancer Letters* **299**, 63-71, doi:https://doi.org/10.1016/j.canlet.2010.08.004 (2010).

164   Medarova, Z., Pham, W., Farrar, C., Petkova, V. & Moore, A. In vivo imaging of siRNA delivery and silencing in tumors. *Nature Medicine* **13**, 372, doi:10.1038/nm1486 (2007).

165   Kumar, M., Yigit, M., Dai, G., Moore, A. & Medarova, Z. Image-guided breast tumor therapy using a small interfering RNA nanodrug. *Cancer Res* **70**, 7553-7561, doi:10.1158/0008-5472.CAN-10-2070 (2010).

166   Li, L., Liu, T., Fu, C., Tan, L., Meng, X. & Liu, H. Biodistribution, excretion, and toxicity of mesoporous silica nanoparticles after oral administration depend on their shape. *Nanomedicine* **11**, 1915-1924, doi:10.1016/j.nano.2015.07.004 (2015).

167   Chauhan, S., Manivasagam, G., Kumar, P. & Ambasta, R. K. Cellular Toxicity of Mesoporous Silica Nanoparticle in SHSY5Y and BMMNCs Cell. *Pharm Nanotechnol* **6**, 245-252, doi:10.2174/2211738506666181031160108 (2018).

168   Murugadoss, S., Lison, D., Godderis, L., Van Den Brule, S., Mast, J., Brassinne, F., Sebaihi, N. & Hoet, P. H. Toxicology of silica nanoparticles: an update. *Arch Toxicol* **91**, 2967-3010, doi:10.1007/s00204-017-1993-y (2017).

169   Fu, C., Liu, T., Li, L., Liu, H., Chen, D. & Tang, F. The absorption, distribution, excretion and toxicity of mesoporous silica nanoparticles in mice following different exposure routes. *Biomaterials* **34**, 2565-2575, doi:https://doi.org/10.1016/j.biomaterials.2012.12.043 (2013).

170   Florea, B. I., Meaney, C., Junginger, H. E. & Borchard, G. Transfection efficiency and toxicity of polyethylenimine in differentiated Calu-3 and nondifferentiated COS-1 cell cultures. *AAPS PharmSci* **4**, E12, doi:10.1208/ps040312 (2002).

171   Xia, T., Kovochich, M., Liong, M., Meng, H., Kabehie, S., George, S., Zink, J. I. & Nel, A. E. Polyethyleneimine coating enhances the cellular uptake of mesoporous silica nanoparticles and allows safe delivery of siRNA and DNA constructs. *ACS Nano* **3**, 3273-3286, doi:10.1021/nn900918w (2009).

172   Li, X., Xie, Q. R., Zhang, J., Xia, W. & Gu, H. The packaging of siRNA within the mesoporous structure of silica nanoparticles. *Biomaterials* **32**, 9546-9556, doi:10.1016/j.biomaterials.2011.08.068 (2011).

173   Ashley, C. E., Carnes, E. C., Phillips, G. K., Padilla, D., Durfee, P. N., Brown, P. A., Hanna, T. N., Liu, J., Phillips, B., Carter, M. B., Carroll, N. J., Jiang, X., Dunphy, D. R., Willman, C. L., Petsev, D. N., Evans, D. G., Parikh, A. N., Chackerian, B., Wharton, W., Peabody, D. S. & Brinker, C. J. The targeted delivery of multicomponent cargos to cancer cells by nanoporous particle-supported lipid bilayers. *Nat Mater* **10**, 389-397, doi:http://www.nature.com/nmat/journal/v10/n5/abs/nmat2992.html#supplementary-information (2011).

174   Liu, J., Stace-Naughton, A., Jiang, X. & Brinker, C. J. Porous Nanoparticle Supported Lipid Bilayers (Protocells) as Delivery Vehicles. *Journal of the American Chemical Society* **131**, 1354-1355, doi:10.1021/ja808018y (2009).

175   Sun, J., Jakobsson, E., Wang, Y. & Brinker, C. Nanoporous Silica-Based Protocells at Multiple Scales for Designs of Life and Nanomedicine. *Life* **5**, 214-229 (2015).

176   Ashley, C. E., Carnes, E. C., Epler, K. E., Padilla, D. P., Phillips, G. K., Castillo, R. E., Wilkinson, D. C., Wilkinson, B. S., Burgard, C. A., Kalinich, R. M., Townson, J. L., Chackerian, B., Willman, C. L., Peabody, D. S., Wharton, W. & Brinker, C. J. Delivery of Small Interfering RNA by Peptide-Targeted Mesoporous Silica Nanoparticle-Supported Lipid Bilayers. *ACS Nano* **6**, 2174-2188, doi:10.1021/nn204102q (2012).

177   Canham, L. T. Silicon Quantum Wire Array Fabrication by Electrochemical and Chemical Dissolution. *Appl. Phys. Lett.* **57**, 1046-1048 (1990).

178   Gösele, U. & Lehmann, V. Light-emitting porous silicon. *Materials Chemistry and Physics* **40**, 253-259, doi:https://doi.org/10.1016/0254-0584(95)01493-4 (1995).

179   Gelloz, B. & Koshida, N. Long-lived blue phosphorescence of oxidized and annealed nanocrystalline silicon. *Applied Physics Letters* **94**, 201903, doi:10.1063/1.3140570 (2009).

180   Saar, A. *Photoluminescence from silicon nanostructures: The mutual role of quantum confinement and surface chemistry*. Vol. 3 (SPIE, 2009).

181   Sailor, M. J., Heinrich, J. L. & Lauerhaas, J. M. in *Studies in Surface Science and Catalysis* Vol. 103 (eds Prashant V. Kamat & Dan Meisel) 209-235 (Elsevier, 1997).

182   Serda, R. E., Godin, B., Blanco, E., Chiappini, C. & Ferrari, M. Multi-stage delivery nano-particle systems for therapeutic applications. *Biochim Biophys Acta* **1810**, 317-329, doi:10.1016/j.bbagen.2010.05.004 (2011).

183   Shen, H., Rodriguez-Aguayo, C., Xu, R., Gonzalez-Villasana, V., Mai, J., Huang, Y., Zhang, G., Guo, X., Bai, L., Qin, G., Deng, X., Li, Q., Erm, D. R., Aslan, B., Liu, X., Sakamoto, J., Chavez-Reyes, A., Han, H. D., Sood, A. K., Ferrari, M. & Lopez-Berestein, G. Enhancing chemotherapy response with sustained EphA2 silencing using multistage vector delivery. *Clin Cancer Res* **19**, 1806-1815, doi:10.1158/1078-0432.CCR-12-2764 (2013).

184   Tasciotti, E., Liu, X., Bhavane, R., Plant, K., Leonard, A. D., Price, B. K., Cheng, M. M.-C., Decuzzi, P., Tour, J. M., Robertson, F. & Ferrari, M. Mesoporous silicon particles as a multistage delivery system for imaging and therapeutic applications. *Nature Nanotechnology* **3**, 151, doi:10.1038/nnano.2008.34 (2008).

185   Chiappini, C., De Rosa, E., Martinez, J. O., Liu, X., Steele, J., Stevens, M. M. & Tasciotti, E. Biodegradable silicon nanoneedles delivering nucleic acids intracellularly induce localized in vivo neovascularization. *Nat Mater* **14**, 532-539, doi:10.1038/nmat4249 (2015).

186   Hasanzadeh Kafshgari, M., Alnakhli, M., Delalat, B., Apostolou, S., Harding, F. J., Makila, E., Salonen, J. J., Kuss, B. J. & Voelcker, N. H. Small interfering RNA delivery by polyethylenimine-functionalised porous silicon nanoparticles. *Biomater Sci* **3**, 1555-1565, doi:10.1039/c5bm00204d (2015).

187   Joo, J., Kwon, E. J., Kang, J., Skalak, M., Anglin, E. J., Mann, A. P., Ruoslahti, E., Bhatia, S. N. & Sailor, M. J. Porous silicon-graphene oxide core-shell nanoparticles for targeted delivery of siRNA to the injured brain. *Nanoscale Horiz* **1**, 407-414, doi:10.1039/C6NH00082G (2016).

188   Mann, A. P., Scodeller, P., Hussain, S., Joo, J., Kwon, E., Braun, G. B., Mölder, T., She, Z.-G., Kotamraju, V. R., Ranscht, B., Krajewski, S., Teesalu, T., Bhatia, S., Sailor, M. J. & Ruoslahti, E. A peptide for targeted, systemic delivery of imaging and therapeutic compounds into acute brain injuries. *Nature Communications* **7**, 11980, doi:10.1038/ncomms11980 (2016).

189   Kim, B. & Sailor, M. J. Synthesis, Functionalization, and Characterization of Fusogenic Porous Silicon Nanoparticles for Oligonucleotide Delivery. *J Vis Exp*, doi:10.3791/59440 (2019).

190   Maeda, H., Nakamura, H. & Fang, J. The EPR effect for macromolecular drug delivery to solid tumors: Improvement of tumor uptake, lowering of systemic toxicity, and distinct tumor imaging in vivo. *Adv Drug Deliv Rev* **65**, 71-79, doi:10.1016/j.addr.2012.10.002 (2013).

191   Wilhelm, S., Tavares, A. J., Dai, Q., Ohta, S., Audet, J., Dvorak, H. F. & Chan, W. C. W. Analysis of nanoparticle delivery to tumours. *Nature Reviews Materials* **1**, 16014, doi:10.1038/natrevmats.2016.14 (2016).

192   Liu, X., Jiang, J., Ji, Y., Lu, J., Chan, R. & Meng, H. Targeted drug delivery using iRGD peptide for solid cancer treatment. *Mol Syst Des Eng* **2**, 370-379, doi:10.1039/C7ME00050B (2017).

193   Agemy, L., Kotamraju, V. R., Friedmann-Morvinski, D., Sharma, S., Sugahara, K. N. & Ruoslahti, E. Proapoptotic peptide-mediated cancer therapy targeted to cell surface p32. *Mol Ther* **21**, 2195-2204, doi:10.1038/mt.2013.191 (2013).

194   Rosenblum, D., Joshi, N., Tao, W., Karp, J. M. & Peer, D. Progress and challenges towards targeted delivery of cancer therapeutics. *Nat Commun* **9**, 1410, doi:10.1038/s41467-018-03705-y (2018).

195   Bazak, R., Houri, M., El Achy, S., Kamel, S. & Refaat, T. Cancer active targeting by nanoparticles: a comprehensive review of literature. *J Cancer Res Clin Oncol* **141**, 769-784, doi:10.1007/s00432-014-1767-3 (2015).

196   Chu, T. C., Twu, K. Y., Ellington, A. D. & Levy, M. Aptamer mediated siRNA delivery. *Nucleic Acids Res* **34**, e73, doi:10.1093/nar/gkl388 (2006).

197   Dong, J., Cao, Y., Shen, H., Ma, Q., Mao, S., Li, S. & Sun, J. EGFR aptamer-conjugated liposome-polycation-DNA complex for targeted delivery of SATB1 small interfering RNA to choriocarcinoma cells. *Biomed Pharmacother* **107**, 849-859, doi:10.1016/j.biopha.2018.08.042 (2018).

198   Kim, M. W., Jeong, H. Y., Kang, S. J., Jeong, I. H., Choi, M. J., You, Y. M., Im, C. S., Song, I. H., Lee, T. S., Lee, J. S., Lee, A. & Park, Y. S. Anti-EGF Receptor Aptamer-Guided Co-Delivery of Anti-Cancer siRNAs and Quantum Dots for Theranostics of Triple-Negative Breast Cancer. *Theranostics* **9**, 837-852, doi:10.7150/thno.30228 (2019).

199   Kruspe, S. & Giangrande, P. H. Aptamer-siRNA Chimeras: Discovery, Progress, and Future Prospects. *Biomedicines* **5**, doi:10.3390/biomedicines5030045 (2017).

200   McNamara, J. O., 2nd, Andrechek, E. R., Wang, Y., Viles, K. D., Rempel, R. E., Gilboa, E., Sullenger, B. A. & Giangrande, P. H. Cell type-specific delivery of siRNAs with aptamer-siRNA chimeras. *Nat Biotechnol* **24**, 1005-1015, doi:10.1038/nbt1223 (2006).

201   Sivakumar, P., Kim, S., Kang, H. C. & Shim, M. S. Targeted siRNA delivery using aptamer-siRNA chimeras and aptamer-conjugated nanoparticles. *Wiley Interdiscip Rev Nanomed Nanobiotechnol* **11**, e1543, doi:10.1002/wnan.1543 (2019).

202   Wilner, S. E. & Levy, M. Synthesis and Characterization of Aptamer-Targeted SNALPs for the Delivery of siRNA. *Methods Mol Biol* **1380**, 211-224, doi:10.1007/978-1-4939-3197-2_18 (2016).

203   Ni, S., Liu, Y., Tang, Y., Chen, J., Li, S., Pu, J. & Han, L. GABAB receptor ligand-directed trimethyl chitosan/tripolyphosphate nanoparticles and their pMDI formulation for survivin siRNA pulmonary delivery. *Carbohydr Polym* **179**, 135-144, doi:10.1016/j.carbpol.2017.09.075 (2018).

204   Xu, X., Wu, J., Liu, Y., Saw, P. E., Tao, W., Yu, M., Zope, H., Si, M., Victorious, A., Rasmussen, J., Ayyash, D., Farokhzad, O. C. & Shi, J. Multifunctional Envelope-Type siRNA Delivery Nanoparticle Platform for Prostate Cancer Therapy. *ACS Nano* **11**, 2618-2627, doi:10.1021/acsnano.6b07195 (2017).

205   Xie, Y., Kim, N. H., Nadithe, V., Schalk, D., Thakur, A., Kilic, A., Lum, L. G., Bassett, D. J. P. & Merkel, O. M. Targeted delivery of siRNA to activated T cells via transferrin-polyethylenimine (Tf-PEI) as a potential therapy of asthma. *J Control Release* **229**, 120-129, doi:10.1016/j.jconrel.2016.03.029 (2016).

206   Zhang, W., Muller, K., Kessel, E., Reinhard, S., He, D., Klein, P. M., Hohn, M., Rodl, W., Kempter, S. & Wagner, E. Targeted siRNA Delivery Using a Lipo-Oligoaminoamide

Nanocore with an Influenza Peptide and Transferrin Shell. *Adv Healthc Mater* **5**, 1493-1504, doi:10.1002/adhm.201600057 (2016).

207   Lehner, R., Liu, K., Wang, X. & Hunziker, P. Efficient Receptor Mediated siRNA Delivery in Vitro by Folic Acid Targeted Pentablock Copolymer-Based Micelleplexes. *Biomacromolecules* **18**, 2654-2662, doi:10.1021/acs.biomac.7b00851 (2017).

208   Muller, K., Kessel, E., Klein, P. M., Hohn, M. & Wagner, E. Post-PEGylation of siRNA Lipo-oligoamino Amide Polyplexes Using Tetra-glutamylated Folic Acid as Ligand for Receptor-Targeted Delivery. *Mol Pharm* **13**, 2332-2345, doi:10.1021/acs.molpharmaceut.6b00102 (2016).

209   Thistlethwaite, J. R., Jr., Cosimi, A. B., Delmonico, F. L., Rubin, R. H., Talkoff-Rubin, N., Nelson, P. W., Fang, L. & Russell, P. S. Evolving use of OKT3 monoclonal antibody for treatment of renal allograft rejection. *Transplantation* **38**, 695-701 (1984).

210   Singh, S., Kumar, N. K., Dwiwedi, P., Charan, J., Kaur, R., Sidhu, P. & Chugh, V. K. Monoclonal Antibodies: A Review. *Curr Clin Pharmacol* **13**, 85-99, doi:10.2174/1574884712666170809124728 (2018).

211   Steinhauser, I., Spänkuch, B., Strebhardt, K. & Langer, K. Trastuzumab-modified nanoparticles: Optimisation of preparation and uptake in cancer cells. *Biomaterials* **27**, 4975-4983, doi:https://doi.org/10.1016/j.biomaterials.2006.05.016 (2006).

212   Baumer, S., Baumer, N., Appel, N., Terheyden, L., Fremerey, J., Schelhaas, S., Wardelmann, E., Buchholz, F., Berdel, W. E. & Muller-Tidow, C. Antibody-mediated delivery of anti-KRAS-siRNA in vivo overcomes therapy resistance in colon cancer. *Clin Cancer Res* **21**, 1383-1394, doi:10.1158/1078-0432.CCR-13-2017 (2015).

213   Miyake, N., Chikumi, H., Yamaguchi, K., Takata, M., Takata, M., Okada, K., Kitaura, T., Nakamoto, M. & Yamasaki, A. Effect of Cetuximab and EGFR Small Interfering RNA Combination Treatment in NSCLC Cell Lines with Wild Type EGFR and Use of KRAS as a Possible Biomarker for Treatment Responsiveness. *Yonago Acta Med* **62**, 85-93 (2019).

214   Attarwala, H. Role of antibodies in cancer targeting. *J Nat Sci Biol Med* **1**, 53-56, doi:10.4103/0976-9668.71675 (2010).

215   Nelson, A. L. Antibody fragments: hope and hype. *MAbs* **2**, 77-83, doi:10.4161/mabs.2.1.10786 (2010).

216   Di Paolo, D., Brignole, C., Pastorino, F., Carosio, R., Zorzoli, A., Rossi, M., Loi, M., Pagnan, G., Emionite, L., Cilli, M., Bruno, S., Chiarle, R., Allen, T. M., Ponzoni, M. & Perri, P. Neuroblastoma-targeted Nanoparticles Entrapping siRNA Specifically Knockdown ALK. *Molecular Therapy* **19**, 1131-1140, doi:https://doi.org/10.1038/mt.2011.54 (2011).

217   Laroui, H., Viennois, E., Xiao, B., Canup, B. S., Geem, D., Denning, T. L. & Merlin, D. Fab'-bearing siRNA TNFalpha-loaded nanoparticles targeted to colonic macrophages offer an effective therapy for experimental colitis. *J Control Release* **186**, 41-53, doi:10.1016/j.jconrel.2014.04.046 (2014).

218   Behlke, M. A. Progress towards *in Vivo* Use of siRNAs. *Molecular Therapy* **13**, 644-670, doi:10.1016/j.ymthe.2006.01.001 (2006).

219   Investigators, E. Use of a monoclonal antibody directed against the platelet glycoprotein IIb/IIIa receptor in high-risk coronary angioplasty. *N Engl J Med* **330**, 956-961, doi:10.1056/NEJM199404073301402 (1994).

220   Group, C. R., Martin, D. F., Maguire, M. G., Ying, G. S., Grunwald, J. E., Fine, S. L. & Jaffe, G. J. Ranibizumab and bevacizumab for neovascular age-related macular degeneration. *N Engl J Med* **364**, 1897-1908, doi:10.1056/NEJMoa1102673 (2011).

221   Sandborn, W. J., Feagan, B. G., Stoinov, S., Honiball, P. J., Rutgeerts, P., Mason, D., Bloomfield, R., Schreiber, S. & Investigators, P. S. Certolizumab pegol for the treatment of Crohn's disease. *N Engl J Med* **357**, 228-238, doi:10.1056/NEJMoa067594 (2007).

222   Laakkonen, P., Porkka, K., Hoffman, J. A. & Ruoslahti, E. A tumor-homing peptide with a targeting specificity related to lymphatic vessels. *Nat Med* **8**, 751-755, doi:10.1038/nm720 (2002).

223   Ruoslahti, E. Tumor penetrating peptides for improved drug delivery. *Adv Drug Deliv Rev* **110-111**, 3-12, doi:10.1016/j.addr.2016.03.008 (2017).

224   Ruoslahti, E. Peptides as targeting elements and tissue penetration devices for nanoparticles. *Adv Mater* **24**, 3747-3756, doi:10.1002/adma.201200454 (2012).

225   Sugahara, K. N., Teesalu, T., Karmali, P. P., Kotamraju, V. R., Agemy, L., Girard, O. M., Hanahan, D., Mattrey, R. F. & Ruoslahti, E. Tissue-penetrating delivery of compounds and nanoparticles into tumors. *Cancer Cell* **16**, 510-520, doi:10.1016/j.ccr.2009.10.013 (2009).

226   Hussain, S., Joo, J., Kang, J., Kim, B., Braun, G. B., She, Z. G., Kim, D., Mann, A. P., Molder, T., Teesalu, T., Carnazza, S., Guglielmino, S., Sailor, M. J. & Ruoslahti, E. Antibiotic-loaded nanoparticles targeted to the site of infection enhance antibacterial efficacy. *Nat Biomed Eng* **2**, 95-103, doi:10.1038/s41551-017-0187-5 (2018).

227   Ryvkin, A., Ashkenazy, H., Weiss-Ottolenghi, Y., Piller, C., Pupko, T. & Gershoni, J. M. Phage display peptide libraries: deviations from randomness and correctives. *Nucleic Acids Res* **46**, e52, doi:10.1093/nar/gky077 (2018).

228   Wu, C. H., Liu, I. J., Lu, R. M. & Wu, H. C. Advancement and applications of peptide phage display technology in biomedical science. *J Biomed Sci* **23**, 8, doi:10.1186/s12929-016-0223-x (2016).

229   Teesalu, T., Sugahara, K. N., Kotamraju, V. R. & Ruoslahti, E. C-end rule peptides mediate neuropilin-1-dependent cell, vascular, and tissue penetration. *Proc Natl Acad Sci U S A* **106**, 16157-16162, doi:10.1073/pnas.0908201106 (2009).

230   Feron, O. Tumor-penetrating peptides: a shift from magic bullets to magic guns. *Sci Transl Med* **2**, 34ps26, doi:10.1126/scitranslmed.3001174 (2010).

231 Hoffman, J. A., Giraudo, E., Singh, M., Zhang, L., Inoue, M., Porkka, K., Hanahan, D. & Ruoslahti, E. Progressive vascular changes in a transgenic mouse model of squamous cell carcinoma. *Cancer Cell* **4**, 383-391 (2003).

232 Uchida, M., Kosuge, H., Terashima, M., Willits, D. A., Liepold, L. O., Young, M. J., McConnell, M. V. & Douglas, T. Protein cage nanoparticles bearing the LyP-1 peptide for enhanced imaging of macrophage-rich vascular lesions. *ACS Nano* **5**, 2493-2502, doi:10.1021/nn102863y (2011).

233 Ellerby, H. M., Arap, W., Ellerby, L. M., Kain, R., Andrusiak, R., Rio, G. D., Krajewski, S., Lombardo, C. R., Rao, R., Ruoslahti, E., Bredesen, D. E. & Pasqualini, R. Anti-cancer activity of targeted pro-apoptotic peptides. *Nat Med* **5**, 1032-1038, doi:10.1038/12469 (1999).

234 Kwon, E. J., Skalak, M., Lo Bu, R. & Bhatia, S. N. Neuron-Targeted Nanoparticle for siRNA Delivery to Traumatic Brain Injuries. *ACS Nano* **10**, 7926-7933, doi:10.1021/acsnano.6b03858 (2016).

235 Fu, A., Zhang, M., Gao, F., Xu, X. & Chen, Z. A novel peptide delivers plasmids across blood-brain barrier into neuronal cells as a single-component transfer vector. *PLoS One* **8**, e59642, doi:10.1371/journal.pone.0059642 (2013).

236 Vives, E., Brodin, P. & Lebleu, B. A truncated HIV-1 Tat protein basic domain rapidly translocates through the plasma membrane and accumulates in the cell nucleus. *J Biol Chem* **272**, 16010-16017 (1997).

237 Madani, F., Lindberg, S., Langel, U., Futaki, S. & Graslund, A. Mechanisms of cellular uptake of cell-penetrating peptides. *J Biophys* **2011**, 414729, doi:10.1155/2011/414729 (2011).

238 Varkouhi, A. K., Scholte, M., Storm, G. & Haisma, H. J. Endosomal escape pathways for delivery of biologicals. *Journal of Controlled Release* **151**, 220-228, doi:https://doi.org/10.1016/j.jconrel.2010.11.004 (2011).

239 Donahue, N. D., Acar, H. & Wilhelm, S. Concepts of nanoparticle cellular uptake, intracellular trafficking, and kinetics in nanomedicine. *Advanced Drug Delivery Reviews*, doi:https://doi.org/10.1016/j.addr.2019.04.008 (2019).

240 Tangsangasaksri, M., Takemoto, H., Naito, M., Maeda, Y., Sueyoshi, D., Kim, H. J., Miura, Y., Ahn, J., Azuma, R., Nishiyama, N., Miyata, K. & Kataoka, K. siRNA-Loaded Polyion Complex Micelle Decorated with Charge-Conversional Polymer Tuned to Undergo Stepwise Response to Intra-Tumoral and Intra-Endosomal pHs for Exerting Enhanced RNAi Efficacy. *Biomacromolecules* **17**, 246-255, doi:10.1021/acs.biomac.5b01334 (2016).

241 Futaki, S., Masui, Y., Nakase, I., Sugiura, Y., Nakamura, T., Kogure, K. & Harashima, H. Unique features of a pH-sensitive fusogenic peptide that improves the transfection efficiency of cationic liposomes. *The Journal of Gene Medicine* **7**, 1450-1458, doi:10.1002/jgm.796 (2005).

242   Kakudo, T., Chaki, S., Futaki, S., Nakase, I., Akaji, K., Kawakami, T., Maruyama, K., Kamiya, H. & Harashima, H. Transferrin-modified liposomes equipped with a pH-sensitive fusogenic peptide: an artificial viral-like delivery system. *Biochemistry* **43**, 5618-5628, doi:10.1021/bi035802w (2004).

243   Parente, R. A., Nir, S. & Szoka, F. C., Jr. Mechanism of leakage of phospholipid vesicle contents induced by the peptide GALA. *Biochemistry* **29**, 8720-8728 (1990).

244   Lee, J., Kim, J., Jeong, M., Lee, H., Goh, U., Kim, H., Kim, B. & Park, J. H. Liposome-based engineering of cells to package hydrophobic compounds in membrane vesicles for tumor penetration. *Nano Lett* **15**, 2938-2944, doi:10.1021/nl5047494 (2015).

245   Dupont, E., Prochiantz, A. & Joliot, A. Penetratin story: an overview. *Methods Mol Biol* **683**, 21-29, doi:10.1007/978-1-60761-919-2_2 (2011).

246   Wojnilowicz, M., Glab, A., Bertucci, A., Caruso, F. & Cavalieri, F. Super-resolution Imaging of Proton Sponge-Triggered Rupture of Endosomes and Cytosolic Release of Small Interfering RNA. *ACS Nano* **13**, 187-202, doi:10.1021/acsnano.8b05151 (2019).

247   Benjaminsen, R. V., Mattebjerg, M. A., Henriksen, J. R., Moghimi, S. M. & Andresen, T. L. The possible "proton sponge " effect of polyethylenimine (PEI) does not include change in lysosomal pH. *Mol Ther* **21**, 149-157, doi:10.1038/mt.2012.185 (2013).

248   Bieber, T., Meissner, W., Kostin, S., Niemann, A. & Elsasser, H. P. Intracellular route and transcriptional competence of polyethylenimine-DNA complexes. *J Control Release* **82**, 441-454 (2002).

249   Godbey, W. T., Barry, M. A., Saggau, P., Wu, K. K. & Mikos, A. G. Poly(ethylenimine)-mediated transfection: a new paradigm for gene delivery. *J Biomed Mater Res* **51**, 321-328 (2000).

250   Tu, Y. & Kim, J.-s. A fusogenic segment of glycoprotein H from herpes simplex virus enhances transfection efficiency of cationic liposomes. *The Journal of Gene Medicine* **10**, 646-654, doi:10.1002/jgm.1184 (2008).

251   LeCher, J. C., Nowak, S. J. & McMurry, J. L. Breaking in and busting out: cell-penetrating peptides and the endosomal escape problem. *Biomol Concepts* **8**, 131-141, doi:10.1515/bmc-2017-0023 (2017).

252   Jiao, C. Y., Delaroche, D., Burlina, F., Alves, I. D., Chassaing, G. & Sagan, S. Translocation and endocytosis for cell-penetrating peptide internalization. *J Biol Chem* **284**, 33957-33965, doi:10.1074/jbc.M109.056309 (2009).

253   Saar, K., Lindgren, M., Hansen, M., Eiríksdóttir, E., Jiang, Y., Rosenthal-Aizman, K., Sassian, M. & Langel, Ü. Cell-penetrating peptides: A comparative membrane toxicity study. *Analytical Biochemistry* **345**, 55-65, doi:https://doi.org/10.1016/j.ab.2005.07.033 (2005).

254   Kleusch, C., Hersch, N., Hoffmann, B., Merkel, R. & Csiszár, A. Fluorescent Lipids: Functional Parts of Fusogenic Liposomes and Tools for Cell Membrane Labeling and Visualization. *Molecules* **17**, doi:10.3390/molecules17011055 (2012).

255   Sokolov Iu, V. & Lishko, V. K. [Effect of bivalent cations and fusogenic factors on the interaction of liposomes with planar phospholipid bilayers]. *Ukr Biokhim Zh (1978)* **52**, 700-705 (1980).

256   Duzgunes, N., Wilschut, J., Fraley, R. & Papahadjopoulos, D. Studies on the mechanism of membrane fusion. Role of head-group composition in calcium- and magnesium-induced fusion of mixed phospholipid vesicles. *Biochim Biophys Acta* **642**, 182-195 (1981).

257   Blumenthal, R., Clague, M. J., Durell, S. R. & Epand, R. M. Membrane fusion. *Chem Rev* **103**, 53-69, doi:10.1021/cr000036+ (2003).

258   Allen, T. M., Hong, K. & Papahadjopoulos, D. Membrane contact, fusion, and hexagonal (HII) transitions in phosphatidylethanolamine liposomes. *Biochemistry* **29**, 2976-2985 (1990).

259   Martens, S. & McMahon, H. T. Mechanisms of membrane fusion: disparate players and common principles. *Nat Rev Mol Cell Biol* **9**, 543-556, doi:10.1038/nrm2417 (2008).

260   Koshkaryev, A., Piroyan, A. & Torchilin, V. P. Bleomycin in octaarginine-modified fusogenic liposomes results in improved tumor growth inhibition. *Cancer Lett* **334**, 293-301, doi:10.1016/j.canlet.2012.06.008 (2013).

261   Kolasinac, R., Kleusch, C., Braun, T., Merkel, R. & Csiszar, A. Deciphering the Functional Composition of Fusogenic Liposomes. *Int J Mol Sci* **19**, doi:10.3390/ijms19020346 (2018).

262   Garber, K. Alnylam terminates revusiran program, stock plunges. *Nat Biotechnol* **34**, 1213-1214, doi:10.1038/nbt1216-1213 (2016).

263   Snove, O., Jr. & Holen, T. Many commonly used siRNAs risk off-target activity. *Biochem Biophys Res Commun* **319**, 256-263, doi:10.1016/j.bbrc.2004.04.175 (2004).

264   Haussecker, D. The Business of RNAi Therapeutics in 2012. *Mol Ther Nucleic Acids* **1**, e8, doi:10.1038/mtna.2011.9 (2012).

265   Zhang, P., Xia, J. & Luo, S. Generation of Well-Defined Micro/Nanoparticles via Advanced Manufacturing Techniques for Therapeutic Delivery. *Materials (Basel)* **11**, doi:10.3390/ma11040623 (2018).

266   Jeevanandam, J., Barhoum, A., Chan, Y. S., Dufresne, A. & Danquah, M. K. Review on nanoparticles and nanostructured materials: history, sources, toxicity and regulations. *Beilstein J Nanotechnol* **9**, 1050-1074, doi:10.3762/bjnano.9.98 (2018).
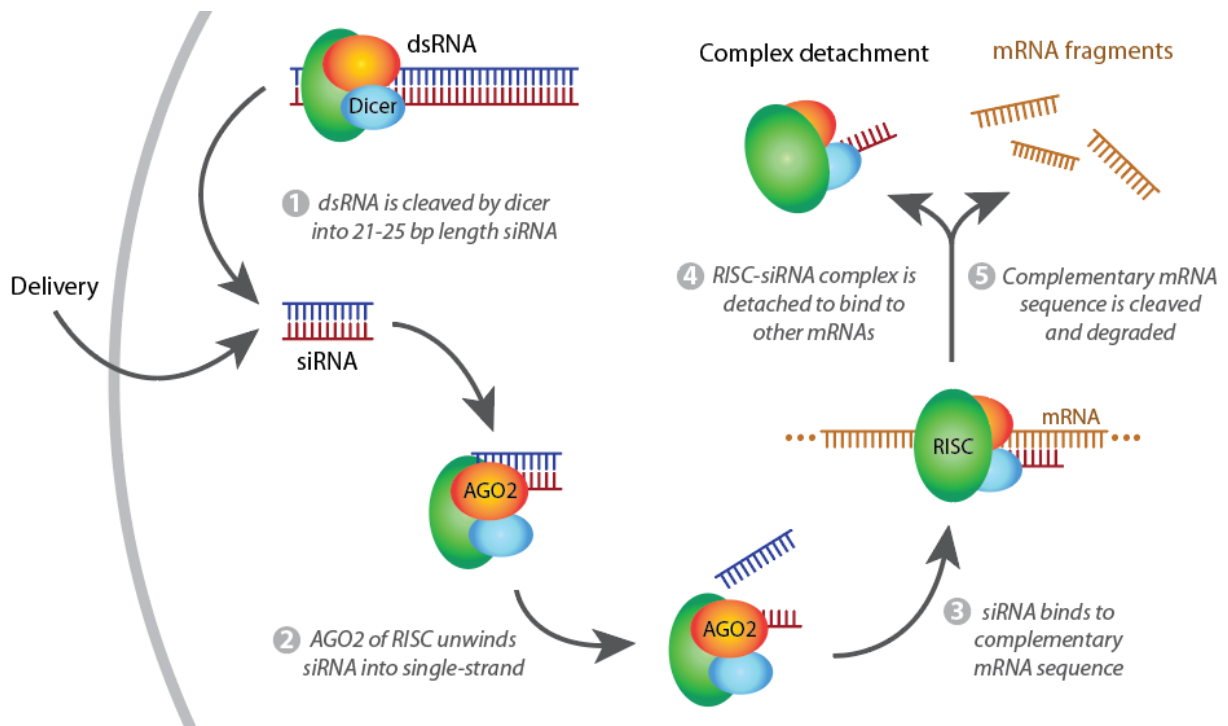
Figure 1.1. RNA interference mediated by siRNA.
(1) siRNA is either delivered exogenously or generated endogenously by the dicer (blue) of the RISC loading complex; (2) siRNA is unwound to a single-stranded form by the Argonaut 2 (AGO2; orange); (3) single-stranded siRNA activates the RISC into forming base-pairs between the siRNA and its complementary mRNA sequence; (4) the RISC-siRNA complex dissociates from the mRNA after cleavage of the complementary mRNA; (5) the cleaved mRNA sequence is fragmented for degradation. With degradation of the target mRNA sequence, the cell is unable to translate the sequence into protein synthesis.
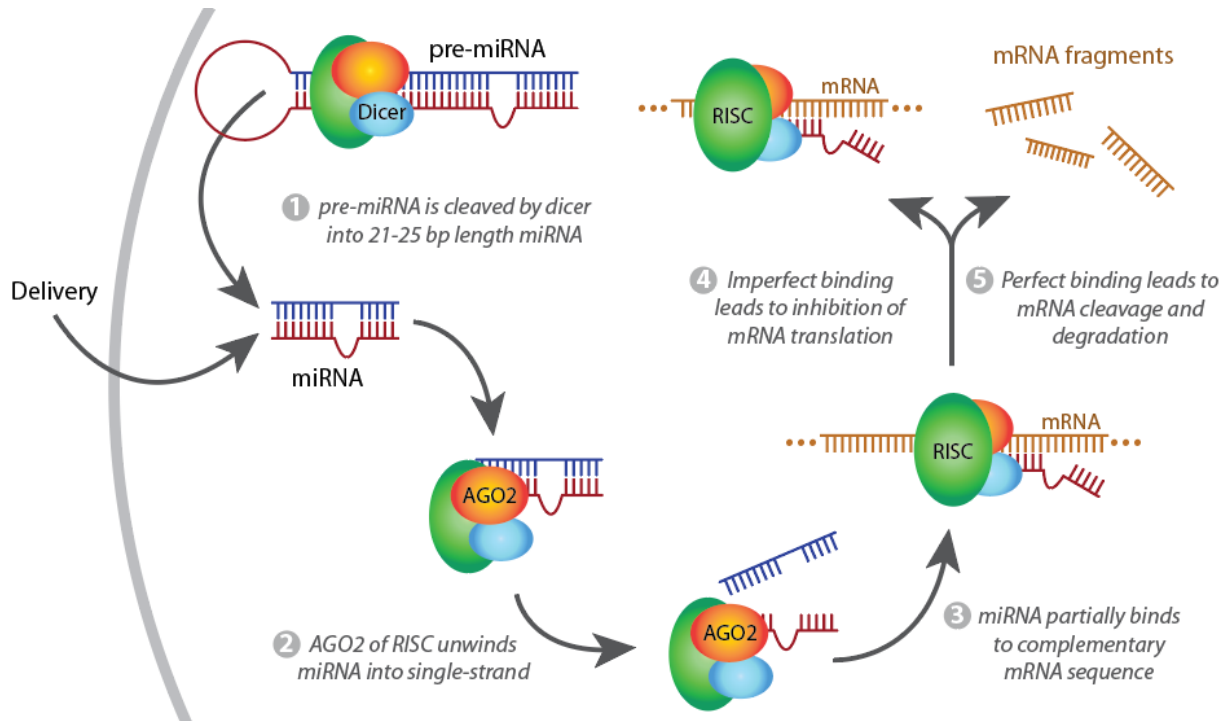
Figure 1.2. RNA interference mediated by miRNA.
(1) miRNA is either delivered exogenously or generated endogenously from the pre-miRNA by the dicer (blue) of the RISC loading complex; (2) miRNA is unwound to a single-stranded form by the Argonaut 2 (AGO2; orange); (3) single-stranded miRNA activates the RISC into forming base-pair between the siRNA and complementary mRNA sequence at the "seed sequence"; (4) with imperfect binding between the "seed sequence" and the complement mRNA, no cleavage occurs. Instead, the complex retains on the mRNA and protein translation is blocked; (5) with perfect binding between the "seed sequence" and the complement mRNA, the mRNA sequence is cleaved and fragmented for degradation. With degradation of the target mRNA sequence, the cell is unable to translate the sequence for protein synthesis.
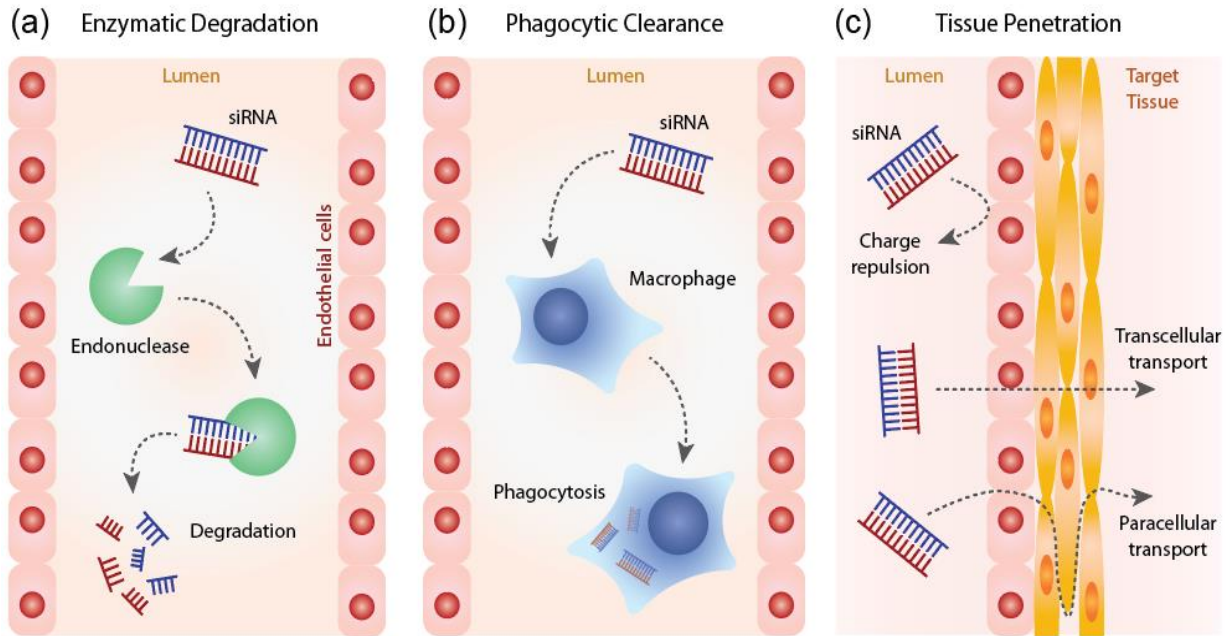
Figure 1.3. Extracellular barriers to RNAi therapy.
(a) Endonucleases degrade siRNA in circulation; (b) mononuclear phagocytic clearance of siRNA by macrophages of the major clearance organs remove siRNA from circulation; (c) tissue penetration of siRNA is hindered by charge repulsion between the anionic siRNA and the plasma membrane of endothelial cells, as well as tight junctions in selective regions (e.g. blood-brain-barrier) that require transcellular or paracellular transport to reach the target tissue.
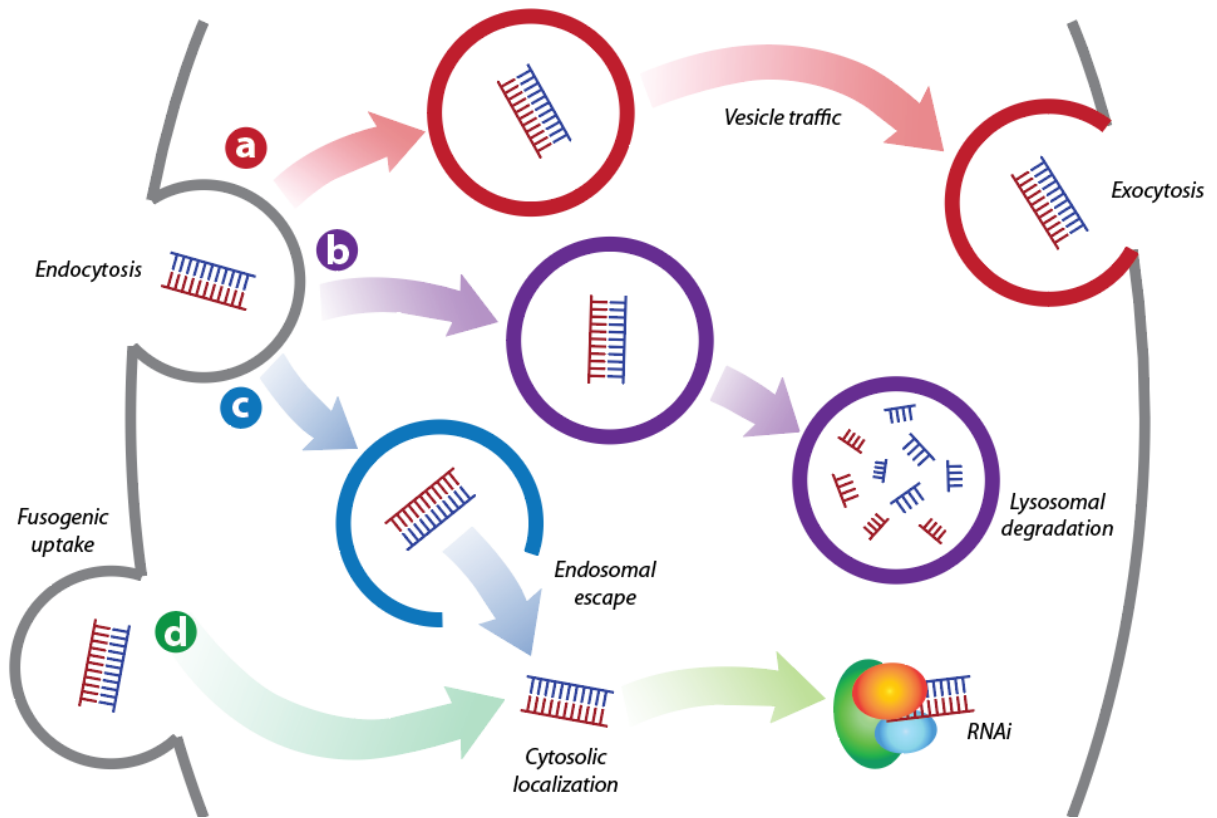
Figure 1.4. Intracellular barriers to RNAi therapy: endocytosis vs. fusogenic uptake.
(a) Endocytosis of siRNA, which eventually is excreted *via* vesicle trafficking and exocytosis; (b) Endocytosis of siRNA, which carries the siRNA through early to late endosomes, and lysosomes for acidification and degradation; (c) Endocytosis of siRNA, which escape from the early endosomes to undergo RNA interference (RNAi) within the cytoplasm; (d) Fusogenic uptake of siRNA that leads to immediate cytosolic localization and RNAi.
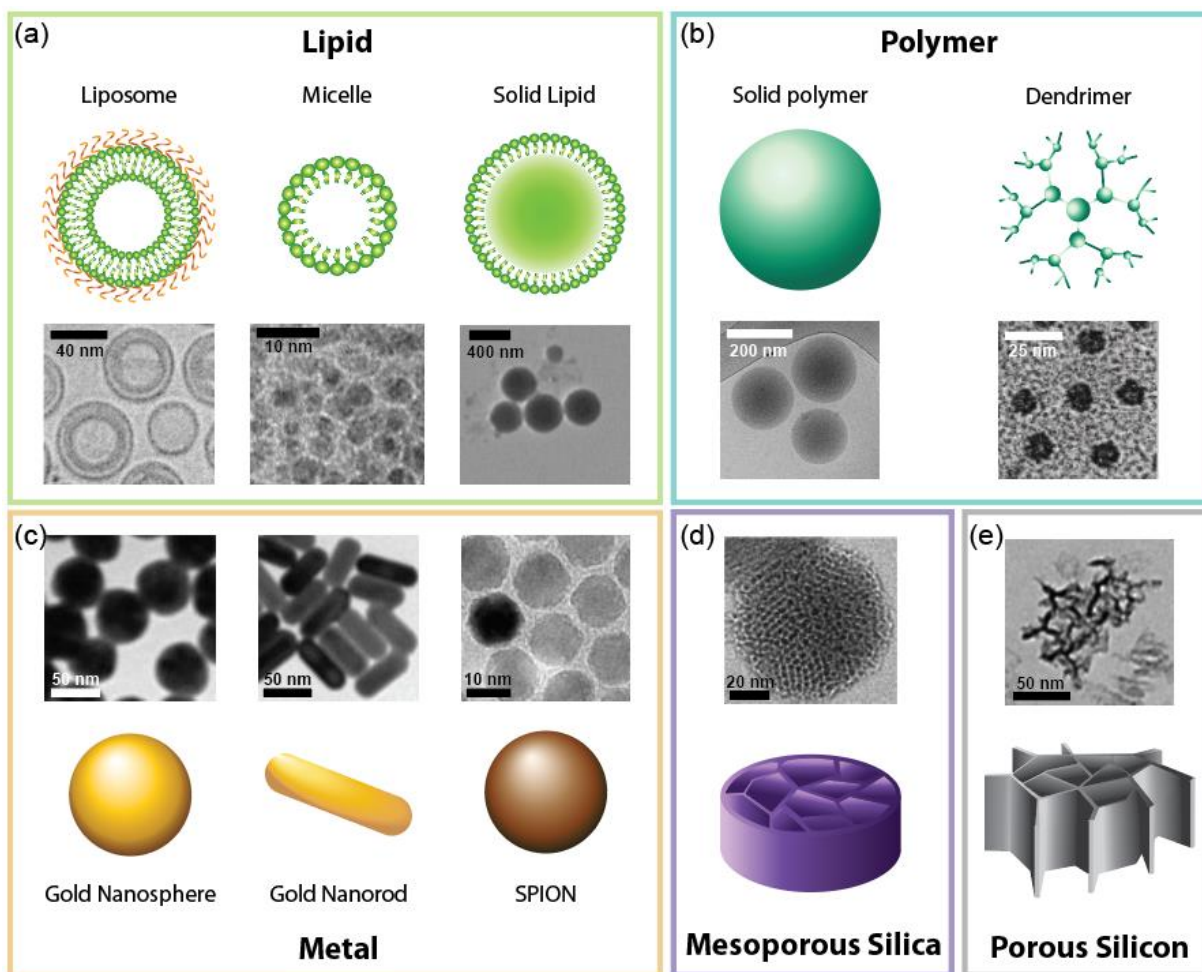
Figure 1.5. Schematic and electron micrograph images of each representative carrier system.
(a) Lipid-based nanoparticles are represented by PEGylated liposomes (cryo-electron micrograph adapted from [77], scale bar represents 40 nm); micelles (TEM adapted from [78]; scale bar represents 10 nm); and solid lipid nanoparticles (TEM of fluorescein-loaded SLNs adapted from [79], scale bar represents 400 nm); (b) polymeric nanoparticles are represented by solid polymeric nanoparticles (TEM image of PLGA particles adapted from [80], scale bar represents 200 nm); and dendrimers (TEM image of PAMAM dendrimers adapted from [81], scale bar represents 25 nm); (c) metallic nanoparticles are represented by gold nanospheres (TEM image adapted from [82], scale bar represents 50 nm); gold nanorods (TEM image adapted from [82], scale bar represents 50 nm); and superparamagnetic iron oxide nanoparticles (SPION; TEM image adapted from [83], scale bar represents 10 nm); (d) mesoporous silica particles are represented by a discoid particle (TEM image adapted from [84], scale bar represents 20 nm); (e) porous silicon (pSi) nanoparticles are represented by electrochemically etched silicon nanoparticle (scale bar represents 50 nm).

	In Vitro	In Vivo
Lipid	80.4 ± 13.8%	79.3 ± 15.2%
Polymer	64.6 ± 24.7%	61.5 ± 19.6%
Metal	72.3 ± 16.3%	54.7 ± 19.6%
Mesoporous silica (MSN)	75.7 ± 19.4%	63.2 ± 17.0%
Porous silicon (pSi)	75.6 ± 21.3%	80.4 ± 2.7%
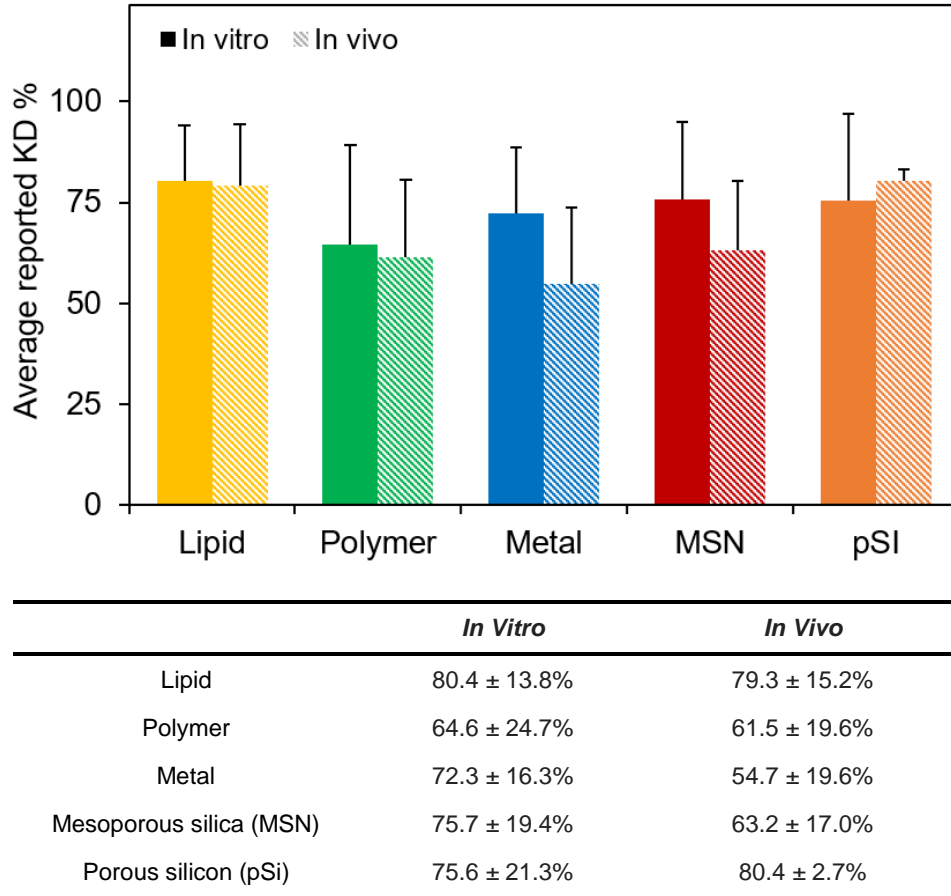
Figure 1.6. Comparison of reported *in vitro* and *in vivo* knockdown (KD) efficiencies across the literature, sorted by nanomaterial type.
The data are representative of results presented in 111 publications from 2008-2019 that quantitatively reported the gene silencing effect by their siRNA-loaded nano-carrier in the selected cell line and *in vivo* model. Bars represent standard deviation. It should be noted that the relative siRNA dose, potential cytotoxic effects, targeting efficiency, and therapeutic outcome are not represented nor normalized in the figure. The table details the average values and standard deviation.
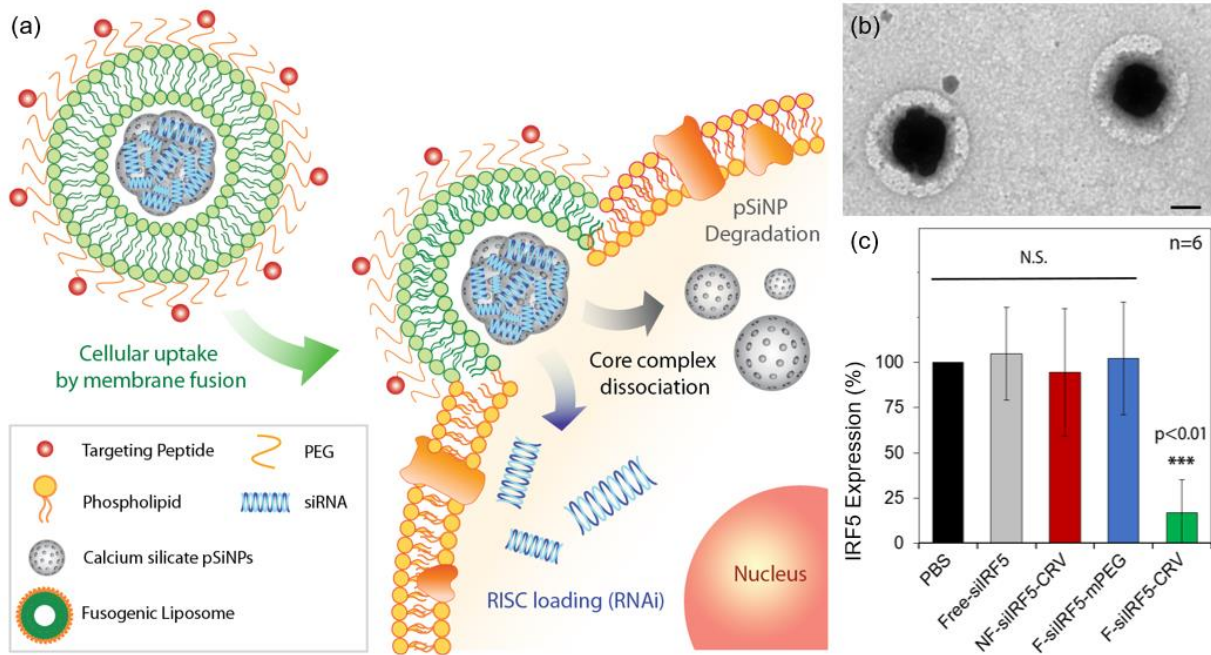
Figure 1.7. Fusogenic porous silicon nanoparticles (FNPs).
(a) Outline of the uptake mechanism for FNPs; (b) transmission electron microscope (TEM) image of FNPs; scale bar represents 100 nm; (c) *in vivo* gene silencing effect of FNPs delivering siRNA against *Irf5* gene to activated macrophages using the macrophage-targeting CRV peptide (F-siIRF5-CRV), in a mouse model of *S. aureus* pneumonia. Reproduced from[117].
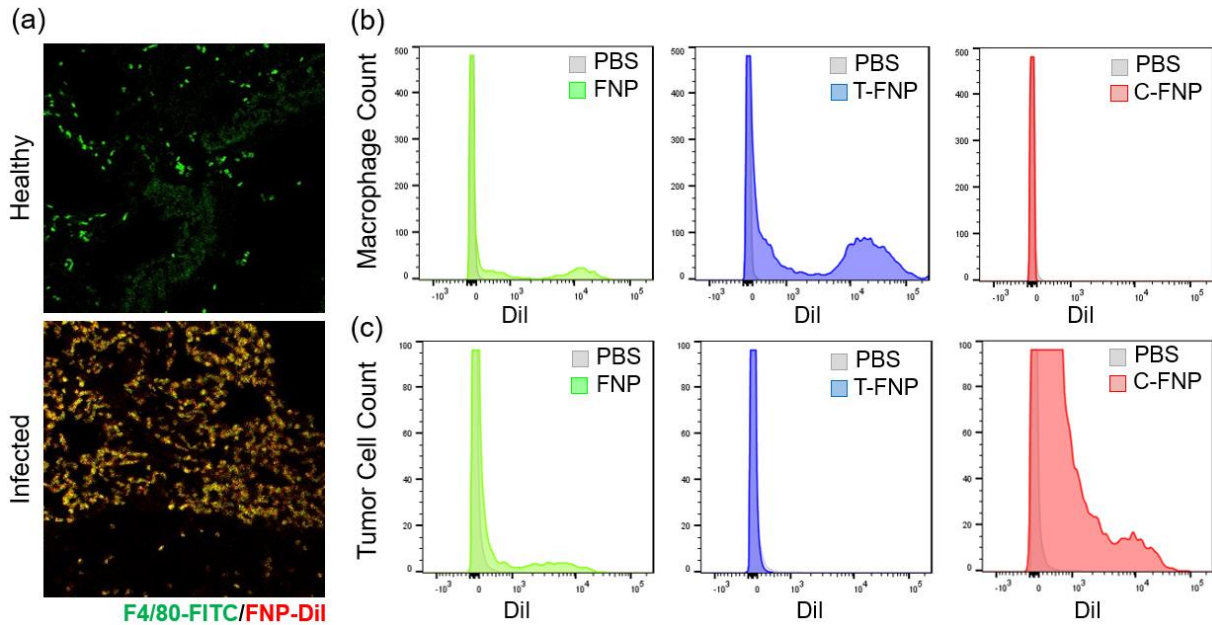
Figure 1.8. Peptide-mediated selective homing of fusogenic porous silicon nanoparticles (FNPs).
(a) Conjugation of the CRV peptide, which targets activated macrophages, to FNPs increases particle accumulation into activated macrophages in *S. aureus*-infected lungs, but not to inactive macrophages in healthy lungs; Adapted from[117]; (b) Conjugation of the LyP-1 peptide, which targets tumor-associated macrophages (TAMs), to the FNPs (T-FNPs) increases particle accumulation into TAMs in an ovarian peritoneal carcinomatosis xenograft model; (c) Conjugation of the iRGD peptide, which targets tumor cells, to the FNPs (C-FNPs) increases particle accumulation into tumor cells in an ovarian peritoneal carcinomatosis xenograft model. Reproduced with permission[118].
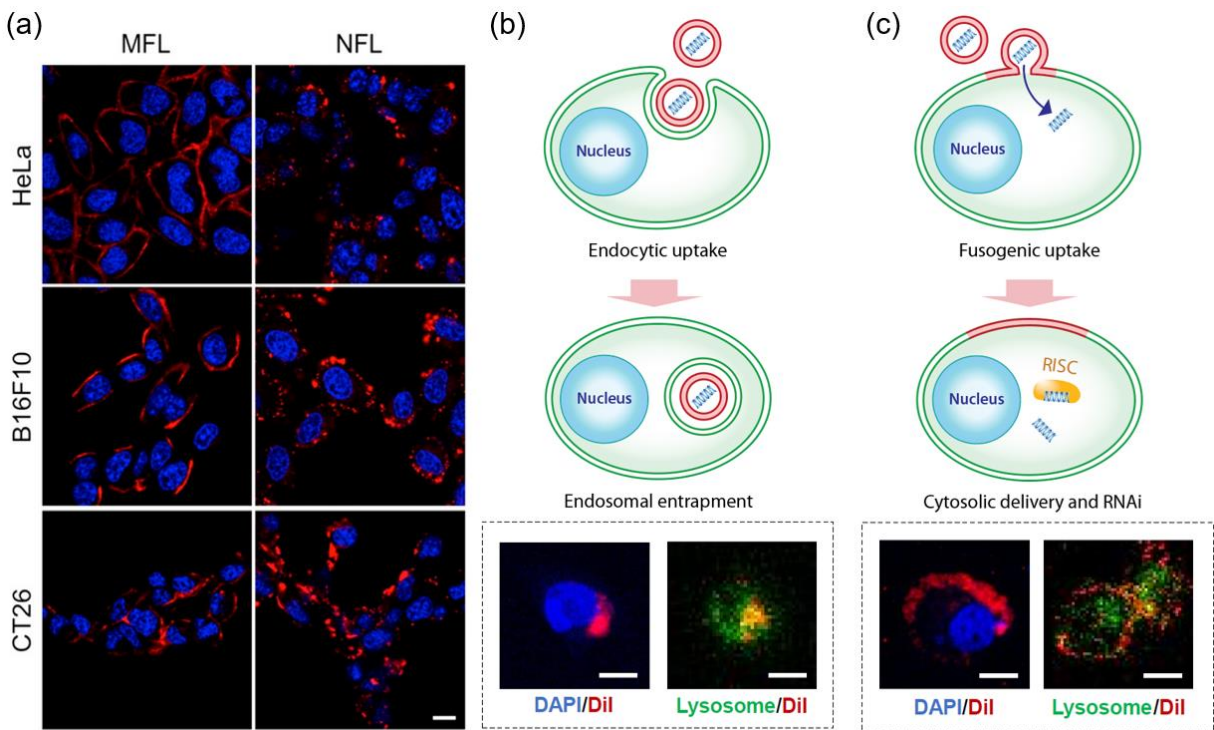
Figure 1.9. Fusogenic uptake bypasses endocytosis.
(a) Cell line-dependence of liposomal fusion to the plasma membrane by fusogenic liposome (MFL) versus endocytosis by non-fusogenic liposome (NFL) in HeLa, B16F10, and CT26 cell lines (scale bar represents 5 µm); Reprinted from [244] (copyright 2015, American Chemical Society); (b) schematic of endocytic uptake of Dil-loaded non-fusogenic liposome-coated pSiNPs (NNPs) with confocal microscopic image of CAOV-3 cells (scale bars represent 10 µm); (c) schematic of fusogenic uptake of Dil-loaded fusogenic liposome-coated pSiNPs (FNPs) with confocal microscopic image of CAOV-3 cells (scale bars represent 10 µm); Adapted from [189] (copyright 2019, J Vis Exp.).
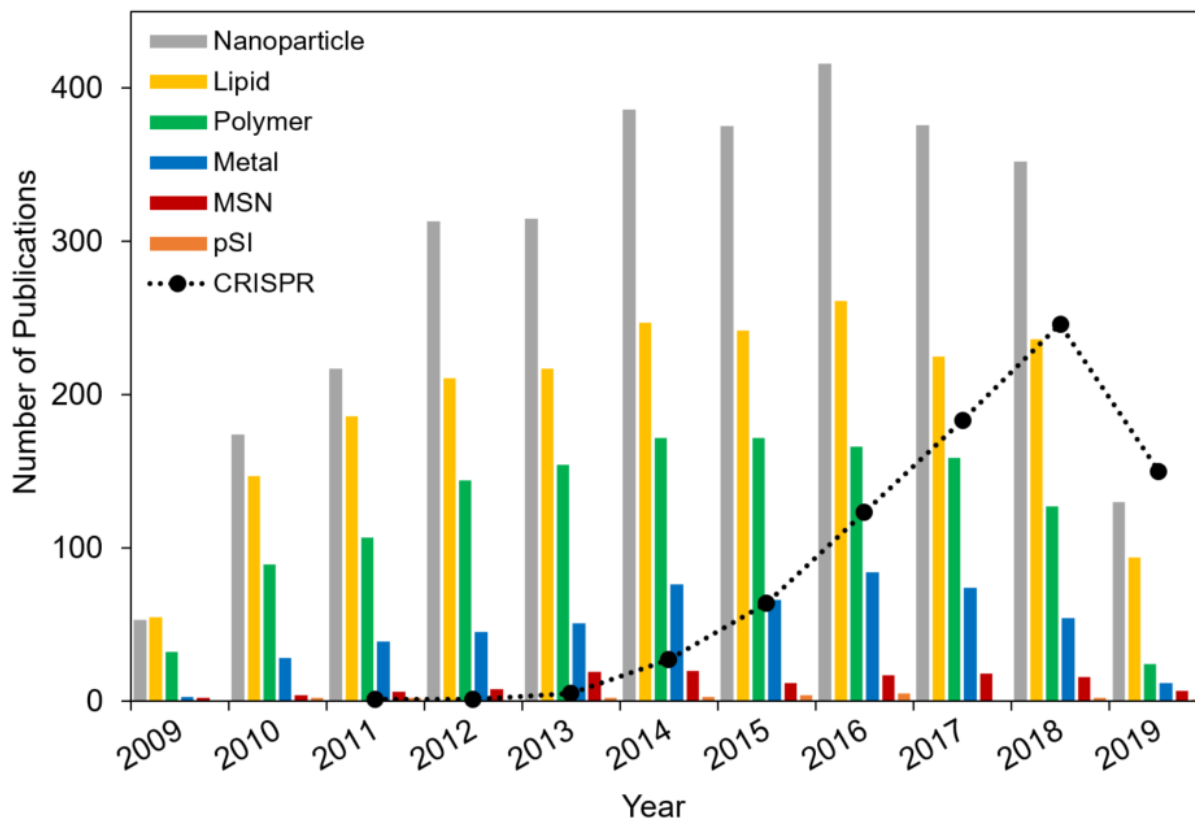
Figure 1.10. Publications on siRNA delivery systems from 2009-2019, identified via the PubMed search engine of the MEDLINE database.
Results for 'Nanoparticle' were obtained using query terms "siRNA + nanoparticle"; results for 'Lipid' were obtained using query terms "siRNA + liposome", "siRNA + lipid nanoparticle", and "siRNA + micelle"; results for 'Polymer' were obtained using query terms "siRNA + polymer nanoparticle"; results for 'Metal' were obtained using query terms "siRNA + metal nanoparticle", "siRNA + gold nanoparticle", and "siRNA + iron oxide nanoparticle"; results for 'MSN' were obtained using query terms "siRNA + mesoporous silica nanoparticle"; results for 'pSi' were obtained using query terms "siRNA + porous silicon"; and results for 'CRISPR' were obtained using query terms "CRISPR + delivery".

Table 1.1. Summary of gene editing tools that can be considered as potential payloads for delivery vehicles.
The tool is defined, the year it was discovered or first applied for gene editing is listed, and the mechanism by which it edits gene expression is described.

Payload	Definition	Year	Mechanism of Action
DNA/RNA			
cDNA	Complementary DNA; single-stranded DNA that is reverse-transcribed from mRNA (found naturally in retroviruses).	1970	cDNA is inserted into cyclic vectors that can self-replicate and potentially recombine into host DNA genome. Vectors with promoters drive transcription of the cDNA into mRNA for gene expression.
rDNA	Recombinant DNA; combination of more than one DNA sequence from plasmids of one or more species.	1972	When transfected in a plasmid, it can recombine into host DNA genome. Plasmids with promoters drive transcription of the cDNA into mRNA.
mRNA	Messenger RNA; single stranded sequence transcribed from DNA for protein translation.	1978	In the cytoplasm, the mRNA is translated into proteins for expression.
siRNA	Short interfering RNA; 21-25 bp sequence of double-stranded RNA (either artificially synthesized, or endogenous products dsRNA cleavage) that undergo RNAi.	2000	siRNA is bound by RISC and unwound into single-strands that bind to the complementary mRNA sequence. The pairing leads to cleavage at target sequence, and the cleaved mRNA is degraded and prevented from translation.
miRNA	MicroRNA; endogenous ~22 bp-long hairpin structure of non-coding sequence that regulates gene expression through RNAi.	1993	miRNA is cleaved by the dicer into a dsRNA (undergoing the same pathway thereof as siRNA). Alternatively, miRNAs bind to the mRNA and inhibit protein translation. Overall, miRNAs target wider range of mRNA targets than siRNA.
ASO	Anti-sense oligonucleotide; short single-stranded RNA complement to target mRNA.	1967	Binds to mRNA to inhibit protein translation.
Restriction Enzymes			
ZFN	Zinc Finger Nuclease; artificial restriction enzymes generated by fusing a zinc finger DNA-binding domain to a DNA-cleavage domain.	1994	DNA-binding domain is modified to a selective locus on the DNA sequence, and the DNA-cleavage domain cuts DNA to induce either: (1) gene knockout by NHEJ; or (2) gene insertion by HR when co-delivered with a DNA fragment.
TALEN	Transcription activator-like effector nuclease; restriction enzyme generated by fusing a TAL effector DNA-binding domain to a DNA-cleavage domain.	2010	DNA-binding domain is modified to a selective locus on the DNA sequence, and the DNA-cleavage domain cuts DNA to induce either: (1) gene knockout by NHEJ; or (2) gene insertion by HR when co-delivered with a DNA fragment.
CRISPR/Cas9	CRISPR is repeating DNA sequences in prokaryotic genome for recognizing DNA fragments; Cas9 is an enzyme that cleaves DNA that complement the CRISPR sequence.	2011	Guide RNA (gRNA) is modified to a selective locus on the DNA sequence, and the Cas9 may cut the DNA to induce either: (1) gene knockout by NHEJ; or (2) gene insertion by HR when co-delivered with a DNA fragment.

Table 1.2. Summary of technologies used for RNAi.
Representative publications are listed by the material type (Lipid, Polymer, Metal, Mesoporous Silica, and Porous Silicon), cell targeting moiety (Local: local administration; RES: uptake into clearance organs), strategy to overcome endocytosis, name of the gene silenced, the *in vivo* model used, and knockdown (KD) values (% relative mRNA expression compared to appropriate controls) as quantified and reported in the indicated references. NP stands for nanoparticle, NR stands for nanorod.

Delivery Vehicle	Cell Targeting	Endosome Strategy	Target Gene	Disease Model	*In vitro* KD	*In vivo* KD	Ref
Lipid							
Liposome	Local	-	Luc2p	Healthy	-	77%	85
Liposome	RES	-	Ssb	Healthy	-	87%	86
Liposome	Hyaluronic acid	Proton sponge + MMP2	HSP70	A549 xenograft	73.4%	54.8%	87
Lipoplex	RES	Endosome escape (DoGo3)	LxRalp ApoB	Healthy	75%	90%	88
Lipoplex	RES	-	GAPDH ApoB	Healthy	90%	90%	89
SNALP/LNP	-	-	Antitran sthyretin	Transthyretin amyloidosis	-	86.8%	90
SNALP/LNP	-	-	TTR	Healthy	-	80%	91
SNALP/LNP	-	-	PLK-1	Hepatic Neuro2a xenograft	-	58%	92
Polymer							
PEG NPs	-	-	Bcl2	SKOV3 xenograft	43%	62%	93
PEG-PTTMA-P(GMA-S-DMA)	-	Endosome escape (Proton sponge)	ApoB Scd-1	Healthy	95%	63-80%	94
Poly(amine-co-ester) NPs	RES	-	Nogo-B	Healthy	80%	60%	95
Chitosan NP	RES	-	GAPDH GFP	Healthy	75%	50%	96
Chitosan NP	RGD peptide	-	POSTN	A2780 orthotopic	-	80%	97
Cyclodextrin NP	hTf ligand	-	RRM2	human tumor	-	32-77%	98
Alkyl-PEI-IO NP	Local	Endosome escape (Proton sponge)	Luc	4T1-fluc xenograft	80%	30%	99
PEI-PEG lipid NP	-	Endosome escape (Proton sponge)	ICAM-2	Emphysema, lung primary, metastasis	85%	50-92%	100
Hyaluronic acid NP	Hyaluronic acid	Endosome escape (Proton sponge)	MDR	OVCAR8/AD R xenograft	-	75%	101

Table 1.2. Summary of technologies used for RNAi (continued).

Delivery Vehicle	Cell Targeting	Endosome Strategy	Target Gene	Disease Model	*In vitro* KD	*In vivo* KD	Ref
Metal							
PEI-AuNP	RGD peptide	-	Bcl-2	U87MG xenograft	78%	74.5%	[102]
PEI-HA-AuNP	Hyaluronic acid	Endosome escape (Proton sponge)	ApoB	Healthy	65%	80%	[103]
PLL-AuNP	Local	-	Luc	MDA-MD-231 (Luc)	86%	77%	[103]
AuNP	iRGD peptide	-	E6	HeLa-luc xenograft	50%	35%	[104]
AuNP	RGD peptide	TAT peptide	C-myc	Lung orthotopic	70%	65.2%	[105]
AuNR	CLPFFD peptide	-	PARP-1	Asphyxia	50%	30-50%	[106]
IONW-dendrimer	-	Endosome escape (Proton sponge)	EGFR	Transgenic glioblastoma	80%	60%	[107]
SPION	EPPT1 peptide	Endosome escape (polyarginine peptide)	PLK1	orthotopic pancreatic cancer	-	35%	[108]
PEI-SPION	galactose	Endosome escape (Proton sponge)	c-Met	Hepa1–6	50%	40%	[109]
Mesoporous Silica (MSN)							
PEI-MSN	-	Endosome escape (Proton sponge)	Pgp	MDR/MCF-7 xenograft	-	47%	[110]
Magnetic PEI-MSN	-	Endosome escape (KALA peptide)	VEGF	SKOV3 orthotopic	80%	60%	[111]
PEI-MSN-KALA	-	Endosome escape (KALA peptide)	VEGF	A549 xenograft	80%	48%	[112]
PEI-MSN	-	Endosome escape (Proton sponge)	TWIST1	MDA-MB-435S orthotopic	75%	90%	[113]
PEI-MSN-PEG	Trastuzumab	Endosome escape (Proton sponge)	PLK-1	LM2-/H2N metastasis	87%	84%	[114]
PEI-MSN-PEG	Trastuzumab	Endosome escape (Proton sponge)	HSP47; NOX4	HER2-positive breast cancer	95%	55%	[115]
PEI-MSN-PEG	Trastuzumab or Rituximab	Endosome escape (Proton sponge)	HER2	HCC1954 orthotopic	87%	58.6%	[116]

Table 1.2. Summary of technologies used for RNAi (continued).

Delivery Vehicle	Cell Targeting	Endosome Strategy	Target Gene	Disease Model	*In vitro* KD	*In vivo* KD	Ref
Porous Silicon (pSi)							
Fusogenic lipid-coated pSiNP	CRV peptide	Membrane fusion	IRF5	S. aureus pneumonia	96%	83%	[117]
Fusogenic lipid-coated pSiNP	iRGD peptide	Membrane fusion	REV3L	CAOV-3 IP xenograft	95%	76%	[118]
Fusogenic lipid-coated pSiNP	LyP-1 peptide	Membrane fusion	PI3Kg	CAOV-3 IP xenograft	85%	81%	[118]
PEI-pSiNP	-	-	MRP1	U87 xenograft	30%	82%	[119]
Lipid-pSiMP	-	-	EphA2	HeyA8 IP orthotopic	-	80%	[120]

Table 1.3. Summary of effective targeting peptides used for selective homing to different cell targets.
Name and amino acid sequence of the peptides are listed, and ordered by potential applications (cancer, bacterial infections, brain targeting, cell penetrating). Target cell types, the primary receptor, and mechanism of uptake (if known) are given.

Peptide	Target Tissue	Receptor	Mechanism	Refs
iRGD CRGDKGPDC	Tumor cells	$\alpha_v\beta_3$	**CendR:** RGD binds to $\alpha_v\beta_3$, cleavage at K, then RGDK binds to NRP1, then receptor-mediated endocytosis/transcytosis	[192,222, 223,225, 230]
CGKRK CGKRK	Tumor neovasculature	p32	Binds to p32, may then bind to NRD1, inducing cell penetrating properties that allow binding to mitochondria.	[193,224, 231]
LyP-1 CGNKRTRGC	Tumor lymphatics; Tumor cells; TAMs	p32	**CendR:** binds to p32, then KRT binds to NRP1 (and NRP2 in lymphatics), then receptor-mediated endocytosis/transcytosis	[223,232]
CRV CRVLRSGSC	Activated macrophages, TAMs	RXRB	Unknown (not CendR, not receptor-mediate endocytosis)	[117]
CARG CARGGLKSC	*S. aureus, MRSA* (+intracellular)	Unknown	Unknown	[226]
EKR EKRTKSRLM	*P. aeruginosa*	Unknown	Unknown	[226]
(KLAKKLAK)₂	Bacteria, mitochondria	Membrane (receptor unknown)	Pro-apoptotic (usually need another targeting peptide); permeabilizes mitochondrial membrane, and activates caspases to induce cell death by apoptosis	[233]
CAQK CAQK	Brain injury	Versican-(Hapln4)-tenascin-R complex	Perineuronal nets (PNN) complex in brain ECM is upregulated in brain injury. CAQK binds to PNNs. Exact uptake mechanism unknown	[188]
RVG YTIWMPENPR PGTPCDIFTN SRGKRASNG	Neuronal cells	Acetylcholine receptor	α7 subtype of nAchR-mediated transcytosis. GABA receptors, which are commonly found in neurons, glial cells, and brain capillary endothelial cells are also known to bind to RVG	[33,187,2 34,235]
TAT GRKKRRQRR RPQ	Plasma membrane	Heparan sulfate Proteo-glycans	Varying; different types of endocytotic pathways are involved in the uptake mechanism of TAT alone and when conjugated with the cargo molecules	[236,237]

Table 1.4. Summary of techniques used for endosomal escape or bypass in siRNA delivery.
Technique indicates the possible routes of endosomal escape or bypass by siRNA-delivery systems that have been presented in the literature. Example indicates molecules or structures that have been used to induce each technique. The hypothesized mechanism for each route of endosomal escape or bypass is given.

Technique	Example	Mechanism	Refs
Proton Sponge	PEI PAA Poly(L-histidine) Chloroquine PAsp(DET-CDM/DBCO)	Endosmolysis of vesicle; buffering molecule prevents pH drop in late endosome/lysosomes, and induces continuous influx of ions and water that eventually swells the vesicle for rupture.	138,139,144,240
Pore Formation	KALA peptide GALA peptide	Peptides engineered from innate bacterial pore-forming mechanisms or derived from fusion domains of viral proteins; peptides can embed into the cell membrane to create gaps in a pH-sensitive manner by causing membrane re-orientation to a more energetically favorable pore-form	111,112,238,241-243
Membrane Fusion	DOPE:DOTMA DMPC:DOTAP:DSPE-PEG	Fusogenic liposomes are composition-dependent, and undergo plasma membrane fusion to directly deposit its payload into the cytoplasm.	117,118,189,244
Cell Penetration	TAT peptide Penetratin peptide Pep14 peptide P1 peptide	Theorized to diffuse through the plasma membrane either with or without receptor binding. Different uptakes are shown by cell type and carrier type.	62,236-238,245

Table 1.5. siRNA formulations that have been, or are currently in clinical trials in the United States.
Trials are organized by the carrier material (SNALP/LNP, GalNAc-conjugates, Others, and No-carriers),
then by the year. 'Formulation' indicates the generic name of the tested drug, 'Gene' indicates the siRNA
target to be silenced, 'Disease' indicates the recruited patient conditions, 'Status' indicates the current
activity of the trials. Phases are indicated (P1: Phase 1; P2: Phase 2; and P3: Phase 3). ID number
indicated the NCT number designation from clinicaltrials.gov. Trials with active or recruiting status are
bolded.

Formulation	Gene	Disease	Phase	Status	Duration	ID Number
SNALP/LNP						
Patisiran (ALN-TTR02)	TTR	TTR-mediated amyloidosis		Approved		NCT02939820
CALAA-01	M2	Cancer; Solid tumor	P1	Terminated	2008-2012	NCT00689065
PRO-040201	ApoB	Hyper-cholesterolemia	P1	Terminated	2009-2010	NCT00927459
ALN-VSP02	KSP/VEGF	Solid Tumors	P1 P1	Completed Completed	2009-2011 2010-2012	NCT00882180 NCT01158079
TKM 080301	PLK-1	Cancer with hepatic metastases	P1 P1, P2 P1, P2	Completed Completed Completed	2011-2012 2010-2015 2014-2016	NCT01437007 NCT01262235 NCT02191878
ND-L02-s0201	HSP47	Fibrosis	P1 P2	Completed **Recruiting**	2013-2014 2018-2021	NCT01858935 NCT03538301
DCR-MYC	Myc	Solid tumors; Non-Hodgkins lymphoma, etc.	P1 P1, P2	Terminated Terminated	2014-2016 2015-2016	NCT02110563 NCT02314052
siRNA-EphA2-DOPC	EphA2	Advanced cancers	P1	**Recruiting**	2015-2020	NCT01591356
Fitusiran (ALN-AT3SC)	Antithrombin	Hemophilia A; Hemophilia B	P3 P3	**Recruiting** **Recruiting**	2018-2020 2018-2020	NCT03417102 NCT03417245
GalNAc-Conjugated siRNA						
Revusiran (ALN-TTRSC)	TTR	TTR-mediated amyloidosis	P2 P2 P3	Completed Completed Completed	2014-2015 2014-2017 2014-2017	NCT01981837 NCT02292186 NCT02319005
Inclisiran (ALN-PCSSC)	PCSK9	Hetero/homozygous familial hyper-cholesterolemia, etc.	P1 P2 P2 P3	Completed Completed Completed **Recruiting**	2014-2016 2016-2017 2016-2018 2019-2023	NCT02227459 NCT02597127 NCT02963311 NCT03814187
Givosiran (ALN-AS1)	ALAS1	Acute intermittent porphyria	P1 P1, P2 P3 -	Completed **Active** **Active** Terminated	2015-2017 2016-2020 2017-2021 2018-2019	NCT02452372 NCT02949830 NCT03338816 NCT03547297
Lumasiran (ALN-GO1)	Glycolate oxidase (GO)	Primary hyperoxaluria type 1	P1, P2 P3 P3	Completed **Recruiting** **Recruiting**	2016-2019 2018-2024 2019-2024	NCT02706886 NCT03681184 NCT03905694
DCR-PHXC-101	LDHA	Primary hyperoxaluria	P1	**Active**	2017-2019	NCT03392896

Table 1.5. siRNA formulations that have been, or are currently in clinical trials in the United States (continued).

Formulation	Gene	Disease	Phase	Status	Duration	ID Number
Other Carriers						
siG12D LODER (Polymer)	KRASG12D	Pancreatic cancer	P1 P2	Completed Recruiting	2011-2013 2018-2020	NCT01188785 NCT01676259
STP705 (Polymer)	TGF-β1 COX-2	Hypertrophic scar	P1, P2	**Recruiting**	2017-2018	NCT02956317
iExosomes (Exosome)	KrasG12D	Pancreatic cancer	P1	**Active**	2019-2019	NCT03608631
No Carriers						
Bevasiranib (Cand5)	VEGF-A	AMD	P1 P2 P2 P3	Completed Completed Completed Terminated	2004-2007 2006-2007 2005-2007 2007-2009	NCT00722384 NCT00306904 NCT00259753 NCT00499590
Sirna-027 (AGN211745)	VEGFR-1	AMD	P1, P2 P2	Completed Terminated	2004-2007 2007-2009	NCT00363714 NCT00395057
ALN-RSV01	RSV-N	Respiratory syncytial virus infections	P2 P2 P2	Completed Completed Completed	2007-2007 2008-2009 2010-2012	NCT00496821 NCT00658086 NCT01065935
PF-04523655 (PF-655)	RTP801	Diabetes complications	P1 P2 P2 P2	Completed Terminated Completed Completed	2007-2010 2008-2011 2009-2011 2012-2013	NCT00725686 NCT00701181 NCT00713518 NCT01445899
I5NP	p53	Acute renal failure	P1 P1 P1, P2	Completed Terminated Completed	2007-2010 2008-2010 2008-2014	NCT00554359 NCT00683553 NCT00802347
TD101	K6a	Pachyonychia congenita	P1	Completed	2008-2008	NCT00716014
QPI-1007	CASP2	Optic neuropathy; glaucoma	P1 P2 P2, P3	Completed Completed **Recruiting**	2010-2013 2013-2015 2015-2020	NCT01064505 NCT01965106 NCT02341560
Bamosiran (SYL040012)	β2-AR	Glaucoma; Ocular hypertension	P2	Completed	2014-2016	NCT02250612

Chapter 1, in full, has been submitted for publication of the material as it may appear in **Kim, B.**, Park, J., Sailor, M.J., Rekindling RNAi Therapy: Materials Design Requirements for In Vivo siRNA Delivery. *Adv Mater.* Submitted. The author of this dissertation was the primary author of the material.

Chapter 2:

Synthesis of Fusogenic Porous Silicon Nanoparticles

2.1   Abstract

With the advent of gene therapy, the development of an effective in vivo nucleotide-payload delivery system has become of parallel import. Fusogenic porous silicon nanoparticles (F-pSiNPs) have recently demonstrated high in vivo gene silencing efficacy due to its high oligonucleotide loading capacity and unique cellular uptake pathway that avoids endocytosis. The synthesis of F-pSiNPs is a multi-step process that includes: (1) loading and sealing of oligonucleotide payloads in the silicon pores; (2) simultaneous coating and sizing of fusogenic lipids around the porous silicon cores; and (3) conjugation of targeting peptides and washing to remove excess oligonucleotide, silicon debris, and peptide. The particle's size uniformity is characterized by dynamic light scattering, and its core-shell structure may be verified by transmission electron microscopy. The fusogenic uptake is validated by loading a lipophilic dye, 1,1'-dioctadecyl-3,3,3',3'-tetramethylindocarbocyanine perchlorate (DiI), into the fusogenic lipid bilayer and treating it to cells in vitro to observe for plasma membrane staining versus endocytic localizations. The targeting and in vivo gene silencing efficacies were previously quantified in a mouse model of Staphylococcus aureus pneumonia, in which the targeting peptide is expected to help the F-pSiNPs to home to the site of infection. Beyond its application in S. aureus infection, the F-pSiNP system may be used to deliver any oligonucleotide for gene therapy of a wide range of diseases, including viral infections, cancer, and autoimmune diseases.

2.2   Introduction

Gene therapy modulates specific gene expression to obtain a therapeutic outcome. Numerous tools for gene modulation have been discovered and studied, including ribonucleic acid interference (RNAi) using oligonucleotides (e.g., short interfering RNA (siRNA)[1,2], microRNA (miRNA)[3,4]), DNA plasmids[5,6], nucleases (e.g., zinc finger, TALENS)[7,8], and

CRISPR/Cas9 systems[9,10]. While each tool's mechanism of action differs, all of the tools must reach the cell's cytoplasm or the nucleus to be active. As such, while these tools have proven to induce significant effect in modulating gene expression in vitro, the in vivo efficacy suffers from extracellular and intracellular obstacles. Due to the fact that the tools are of biological origin, many enzymes and clearance systems exist in our body that have the ability to degrade or remove the foreign molecules[11]. Even in the case that the tools reach the target cell, they suffer from endocytosis; a mode of cellular uptake that encapsulates and traps the tools in acidic stomach-like vesicles that degrade or expel the tools out of the cell. In fact, studies have shown that lipid nanoparticles are endocytosed via macropinocytosis, from which approximately 70% of the siRNA are exocytosed from the cells within 24h of uptake[12,13]. The majority of the remaining siRNA are degraded through the lysosomal pathway, and ultimately only 1-2% of the siRNA that initially enters the cell with the nanoparticles achieve endosomal escape to potentially undergo RNAi[13,14].

We have recently developed fusogenic porous silicon nanoparticles (F-pSiNPs) that have an siRNA-loaded core composed of porous silicon nanoparticles, and a fusogenic lipid shell[15]. The F-pSiNPs present three major advantages over other conventional oligonucleotide delivery systems: (1) a fusogenic lipid coating which enables the particles to bypass endocytosis and deliver the entire payload directly in the cell cytoplasm (versus the 1-2% achieved by endocytosed particles[13,14]) (**Fig 2.1**); (2) high mass loading of siRNA in the pSiNPs (>20 wt% compared to 1-15 wt% by conventional systems)[15], which rapidly degrade in the cytoplasm (once the core particles shed the lipid coating via fusogenic uptake) to release the siRNA; and (3) targeting peptide conjugation for selective homing to desired cell types in vivo.

The F-pSiNP system has demonstrated significant gene silencing efficacy (>95% in vitro; >80% in vivo) and subsequent therapeutic effect in a fatal mouse model of *S. aureus* pneumonia; the results of which were published previously[15]. However, the complex structure of

the F-pSiNP system requires delicate handling and fine-tuned optimization to generate uniform and stable nanoparticles. Thus, the purpose of this work is to present a thorough protocol, as well as optimization strategies for the synthesis, functionalization, and characterization of F-pSiNPs to be used in targeted delivery of siRNAs for potent gene silencing effect.

2.3   Synthesis of porous silicon nanoparticles

Always use caution when working with hydrofluoric acid (HF). Follow all safety guides according to its safety data sheet (SDS), handle any HF-containing chemicals in a fume hood, and wear appropriate personal protective equipment (PPE; double gloves with butyl gloves on the outside, butyl apron with lab coat underneath, face shield with safety goggles underneath). All universities and R&D labs require specific training on HF safety prior to usage. Do not attempt to work with HF without pre-approval of your local lab safety coordinator, as additional safety measures not described here are required.

2.3.1. Preparation of the etching solutions

To make the 3:1 HF solution for etching, fill a plastic graduated cylinder with 30 mL of aqueous 48% HF and 10 mL of absolute ethanol (EtOH). The solution must be contained in high density plastics (e.g., HDPE), as the HF dissolves glass. To make a 1:29 HF solution for lift-off, fill a plastic graduated cylinder with 1 mL of aqueous 48% HF and 29 mL of absolute ethanol. The solution must be contained in high density plastics (e.g., HDPE), as the HF dissolves glass. Make the 1 M KOH solution in 10% EtOH for excess pSi.

2.3.2. Setting up the etch cell

In a Teflon etch cell with a 8.6 cm^2 etch well (area is calculated by measuring the

diameter of the silicon surface available for etching within the O-ring, and calculating the area by

$A = \pi r^2$), place in descending order (**Fig 2.2a**): (1) the Teflon cell top; (2) an O-ring; (3) a quarter

piece of the single crystal (1 0 0)-oriented p++-type silicon wafer cut into quarters (using a

diamond cutter); (4) aluminum foil; and (5) the Teflon cell base with screws gently tightened to

prevent leakage. Fill the well with EtOH. Take a wipe and insert into the crevice between the

Teflon cell top and base. If the wipe is dry upon removal, the etch cell is sealed. If wet, the cell is

leaking, and tighten the screws further until sealed.

2.3.3. Electropolishing the silicon wafer

Bring the assembled etch cell into a fume hood. Fill the well with 10 mL of 3:1 HF

solution. Connect the positive lead to the aluminum foil (electrode) from the etch cell and

connect the negative lead to the platinum coil (counter-electrode) immersed in the 3:1 HF

solution of the etch cell to complete the circuit (**Fig 2.2b**). Run a constant current at 50 mA cm^{-2}

for 60 s. Once etch is finished, remove the cell from the circuit, and rinse out the 3:1 HF

carefully using a syringe. Rinse with EtOH three times. Dissolve away the etched layer by filling

the well slowly with 10 mL of 1 M KOH. Wait until the bubbling subsides. Finally, rinse out the

KOH with water three times, and then with EtOH three times.

2.3.4. Electrochemically etching porous layers into silicon wafer

Run an alternating current of a square waveform, with lower current density of 50

mA/cm^2 for 0.6 s and high current density of 400 mA/cm^2 for 0.36 s repeated for 500 cycles.

Once etch is finished, remove the cell from the circuit, and rinse out the 3:1 HF carefully using a

syringe. Rinse with EtOH three times.

2.3.5. Lifting-off the porous layer from the silicon wafer

Fill the well with 10 mL of 1:29 HF solution. Run a constant of 3.7 mA/cm^2 for 250 s. Once etch is finished, remove the cell from the circuit. The pSi layer may have visible ripples indicating detachment from the crystalline silicon wafer. Gently wash out the 1:29 HF solution and rinse with EtOH three times, then with water three times. Using a pipette tip, firmly crack the circumference of the pSi layer for complete detachment. Using EtOH, collect the pSi fragments (chips) from the Teflon etch cell into a weighing boat. Transfer the chips to a glass vial. The pSi chips may be kept at room temperature in EtOH for over 6 months for storage. Dissolve away any remaining porous silicon on the wafer by filling the well slowly with 10 mL of 1 M KOH. Wait until the bubbling subsides. Rinse out the KOH with water three times, and then with EtOH three times. Repeat until the entire wafer thickness has been etched.

2.3.6. Sonicating porous layers for nanoparticle formation

Replace the solvent of the glass vial containing pSi chips from EtOH to 2 mL of DI water. Firmly close the cap, and seal using parafilm. Place the glass vial in a sonicator bath and suspended such that the volume of pSi chips is completely submerged below the surface. Sonicate for 12 h at 35 kHz and RF power of 48W. To prevent significant water loss during sonication, place a volumetric flask filled with water, inverted so that the opening of the flask touches the surface of the water bath. Place the glass vial on a flat surface for 1 h to allow larger particles to settle at the bottom. Collect the supernatant using a pipette; the suspension contains sub-100 nm pSiNPs.

2.4 Preparation of fusogenic lipid film

In a fume hood, make 10 mg/mL stocks of lipids by hydrating DMPC, DSPE-PEG-MAL and DOTAP lipids in chloroform. These stock solutions may be kept at -20 °C for up to 6 months under tight parafilm seal.

76

The fusogenic composition is made of the lipids, DMPC, DSPE-PEG, and DOTAP, at the molar ratio of 76.2:3.8:20 and 96.2:3.8:0, respectively. In a glass vial, mix 72.55 µL of DMPC, 15.16 µL of DSPE-PEG, and 19.63 µL of DOTAP by pipetting. Optionally for fluorescent labelling of the lipid coating, additionally add 20 µL of DiI dissolved in EtOH at a concentration of 1 mg/mL. Place the vial in a fume hood with a loose cap to allow the chloroform to evaporate overnight. The dried film will be a cloudy hard gel-like substance at the bottom of the vial.

2.5   Loading and sealing of siRNA in pSiNPs

To prepare the calcium chloride stock, dissolve 1.11 g of $CaCl_2$ in 10 mL of RNAse-free water to make a 2 M $CaCl_2$ solution. Centrifuge the solution at > 10,000 x g for 1 min to settle the aggregates and collect the supernatant using a pipette. Alternatively, filter the solution through a 0.22 µm filter. Hydrate or dilute the siRNA to 150 µM in RNAse-free water to make the siRNA loading stock. This stock solution may be aliquoted and kept frozen at -20 °C for at least 30 days given that it does not undergo frequent freeze-thaw cycles.

Prepare an iced sonication bath. Under 15 min ultrasonication, gently pipette 150 µL of siRNA and 700 µL of 2 M $CaCl_2$ into 150 µL of pSiNP. Make sure to leave the lid of the microcentrifuge tube open for gas generation. Remove the tube containing 1 mL of siRNA-loaded calcium coated pSiNPs from the sonicator.

2.6   Coating siRNA-loaded pSiNPs with fusogenic lipids

Fill a wide beaker with DI water. Soak 1 polycarbonate membrane (200 nm pores), and 4 filter supports by floating them on water surface. Assemble the liposome extrusion kit by following manufacturer's instructions. Hydrate the dried lipid film in the glass vial with 1 mL of of siRNA-loaded calcium coated pSiNPs obtained from step 3.3.3. Pipette until all lipids film have

lifted from the bottom of the vial and have mixed into a cloudy homogenous solution. Place a magnetic stirring bar in the glass vial, and place the vial onto a hot plate to heat the particles to 40 °C (or high enough above the lipids' phase transformation temperature to maintain the lipids in the more fluidic liquid crystal phase) while magnetically stirring the solution for 20 min.

Aspirate the 1 mL of lipid-coated pSiNP-siRNA solution in the extrusion syringe. Insert an empty syringe on one side of the extruder, and the filled syringe on the other end. Begin extrusion by pushing the piston in slowly to push the particles from one syringe, through the polycarbonate membrane, and into the other. Repeat 20 times. If the piston is stuck, the filter and membrane may be clogged. Disassemble the extruder and replace the membrane and filter supports. If the problem persists, dilute the particles until clogging is manageable. Collect the extruded particles into a microcentrifuge tube.

2.7   Conjugation of targeting peptides

Prepare the peptide stock with a 1 mg/mL peptide concentration in RNAse-free water. In the microcentrifuge tube containing fusogenic lipid-coated pSiNPs, add 100 µL of the 1 mg/mL peptide stock and pipet gently. Keep the tube static at room temperature for 20 min (alternatively, > 2 h at 4 °C). To remove excess peptide or siRNA and other excipients, wash in a 30 kDa centrifugal filter by spinning at 5,000 x g at 25 °C for 1 h. Centrifuge twice more with 1 mL of PBS under the same setting. Resuspend the final peptide-conjugated fusogenic lipid-coated pSiNPs in PBS at the desired concentration. The particles can now be aliquoted and frozen at -80 °C for storage of at least 30 days.

2.8   Representative Results

A successful synthesis of fusogenic pSiNPs should produce a homogenous, slightly opaque solution (**Fig 2.3a**). Failure to optimize the ratio and concentration of pSiNPs : siRNA : CaCl$_2$ may lead to aggregation upon loading (**Fig 2.3b**). As the particles are extruded through 200 nm membranes, the average hydrodynamic diameter of the fusogenic pSiNPs measured by DLS should be approximately 200 nm, and the average zeta-potential approximately +7 mV as shown in **Figure 2.4**. After surface modification with targeting peptides, the overall diameter should be increased to be under 230 nm, and the average zeta-potential decreased down to -3.4 mV[15]. Any extensive deviation from the extrusion size is indicative of failed extrusion ($d_{particle}$ >> $d_{extrusion}$), or failed loading ($d_{particle}$ << $d_{extrusion}$). Aggregations may also be quantified using DLS. Moreover, the frozen aliquots must be thawed only once, as repeated freeze-thaw cycles disrupt the lipid membrane and intraparticular fusion and aggregation (**Fig 2.4**). As **Figure 2.4a** shows, fusogenic pSiNPs may be stored for 30 days and thawed without causing structural changes. However, repeated freeze-thaw cycles of a single aliquot cause severe aggregation (d >> 1,000 nm) and within 4 days of the daily cycle (**Fig 2.4b**), thus it is advised that the particles be aliquoted to single-use volumes.

Fusion may be confirmed by labelling the fusogenic lipids with the lipophilic DiI (Step 2.2.2), and observing the in vitro localization using confocal microscopy. **Figure 2.1d** shows successful fusion, where the fusogenic pSiNP's lipids transfer the DiI to the plasma membrane and are localized independent of lysosomes. Unsuccessful fusion will show the DiI localization within the cell's cytoplasm and colocalization with lysosomes (**Fig 2.1c**).

2.9   Discussion and Conclusions

Synthesis of porous silicon nanoparticles is shown in **Figure 2.5**. The critical step in the synthesis of fusogenic pSiNPs is in the loading step (step 3). If the fusogenic nanoparticles are aggregating post-synthesis (**Fig 2.3**), the reason may be due to the following: (1) calcium

chloride stock was not homogenously prepared, thus step 3.1.2 must be carefully followed or refined; or (2) the ratio of pSiNP : siRNA : $CaCl_2$ or the concentration of one or more of the three components may not be optimal. Re-optimization starting from the $CaCl_2$ concentration is suggested (e.g., altering from 2 M to 1 M or 3 M). Moreover, it is important to make sure that the $CaCl_2$ is from the same vendor, as we found that the same chemical from different vendors resulted in lower pH at the loading step, and subsequent failure to load the siRNA. The pSiNPs may also be concentrated, diluted, or further degraded prior to the loading process by leaving the particles suspended in the RNAse-free water for 2 days after step 1.6.6.

Post-loading, the lipid coating often leads to difficulty in extrusion due to the concentration or density of the particles. If the extrusion membrane is clogged, forcing the extrusion may rip the membrane. Upon clogging, disassemble the extruder, and replace the membrane and the supports with a new set if the loss from clogging is small. If the loss is great, then dilute the particle suspension, and sonicate for 30 s prior to extrusion. If the problem persists, re-optimization of pSiNP size and loading ratio to minimize aggregates is advised. Lastly, we suggest filtering the particle suspension through a 0.22 µm-pore filter to eliminate any contaminants or aggregates prior to cell or animal treatment. Filtering is especially advised if the particles were synthesized in a non-sterile environment, or after thawing a frozen aliquot of the particles.

The fusogenicity of the particles may be validated by confocal microscopy (as shown in **Fig 2.1c, d**), and by transmission electron microscopy of the cells treated with the particles to observe for lipid-shed porous silicon cores in the cytoplasm[15].

The fusogenic pSiNPs and its synthesis protocol have a few limitations. For in vitro gene silencing applications, the presented fusogenic pSiNPs have proven to induce >90% knockdown efficiency in a range of cell lines at the 100 nM dose; including the Neuro-2a mouse neuroblastoma cell line, the CAOV-3 human ovarian cancer cell line, and the notoriously

difficult-to-transfect RAW 264.7 mouse macrophage cell line. However, we have observed >50% knockdown efficiency at as low as 25 nM dose, which was comparable to that of Lipofectamine. While cationic lipids must be used minimally to reduce cytotoxic effect, we have previously demonstrated its safety at a lipid dose of as high as 1 mg[15]. For in vivo gene silencing applications, the fusogenic pSiNPs are limited by selectivity. As the cationic lipids electrostatically attract to any cell membrane, the particles must be used as a local therapeutic, or be surface modified with a targeting moiety (e.g., peptides, antibodies, etc.). The synthesis protocol for fusogenic pSiNPs is currently optimized and limited for siRNA delivery only. The same method has been verified to successfully load miRNA, and is hypothesized to be able to load mRNA, cDNA, and other larger nucleotide payloads, but these have yet to be optimized.

The presented work makes a significant contribution to the field of gene therapy. The standard benchmark for in vitro gene silencing is the Lipofectamine 2000. We have demonstrated that the fusogenic pSiNPs can induce knockdown effect of comparable, if not higher, efficiencies[15]. The major advantage of the fusogenic pSiNPs over Lipofectamine 2000 is its ability to be used for in vivo applications with systemic injections. While other agents, such as Invivofectamine 3.0, have been commercialized for in vivo uses, they are only suitable for liver delivery, and require chemically modified siRNAs (with or without overhangs, or in locked nucleic acid (LNA) structure) to increase stability and specificity.[16-18] However, the fusogenic pSiNPs can be modified post-synthesis to conjugate targeting moieties with simple thiol-maleimide chemistry, wherein a thiol group in the targeting peptide (which carries an extra cysteine for this purpose) binds a double-bonded carbon in the maleimide ring at the end of PEGylated lipids in the fusogenic coating. Moreover, the high mass loading and delivery efficacy to the cell cytoplasm minimizes the necessity for intracellular specificity and attains strong gene silencing effect with non-modified siRNAs[15]. One drawback of the fusogenic pSiNPs is that the synthesis protocol is a multi-day process that is more complex than the commercially available

transfection agents. However, while the benchmark products must be freshly prepared prior to transfection to obtain the best results, the fusogenic pSiNPs may be aliquoted and frozen for at least 30 days without diminishing the knockdown efficiency.

Future applications for this method include optimization for loading and delivery of larger nucleic acid payloads, such as mRNAs and cDNAs. Additionally, delivery of the CRISPR/Cas9 protein-sgRNA complex, or a cocktail of the Cas9 mRNA and sgRNA, is also a development option, as the system is optimal for loading anionic payloads. Overall, the F-pSiNP system is a modular nanoplatform for gene therapy to treat diseases beyond infections, including viral infections, cancer, and autoimmune diseases.

2.10   References

1   Ryther, R. C. C., Flynt, A. S., Phillips Iii, J. A. & Patton, J. G. siRNA therapeutics: big potential from small RNAs. *Gene Therapy.* **12** 5, (2004).

2   Scherman, D., Rousseau, A., Bigey, P. & Escriou, V. Genetic pharmacology: progresses in siRNA delivery and therapeutic applications. *Gene Therapy.* **24** 151, (2017).

3   Broderick, J. A. & Zamore, P. D. MicroRNA therapeutics. *Gene Therapy.* **18** 1104, (2011).

4   Geisler, A. & Fechner, H. MicroRNA-regulated viral vectors for gene therapy. *World Journal of Experimental Medicine.* **6** (2), 37-54, (2016).

5   Williams, P. D. & Kingston, P. A. Plasmid-mediated gene therapy for cardiovascular disease. *Cardiovascular Research.* **91** (4), 565-576, (2011).

6   Ferreira, G. N. M., Monteiro, G. A., Prazeres, D. M. F. & Cabral, J. M. S. Downstream processing of plasmid DNA for gene therapy and DNA vaccine applications. *Trends in Biotechnology.* **18** (9), 380-388, (2000).

7   Shim, G. *et al.* Therapeutic gene editing: delivery and regulatory perspectives. *Acta Pharmacologica Sinica.* **38** 738, (2017).

8   Carlson, D. F., Fahrenkrug, S. C. & Hackett, P. B. Targeting DNA With Fingers and TALENs. *Molecular Therapy - Nucleic Acids.* **1**, (2012).

9   Dai, W.-J. *et al.* CRISPR-Cas9 for in vivo Gene Therapy: Promise and Hurdles. *Molecular Therapy - Nucleic Acids.* **5** e349, (2016).

10   Adli, M. The CRISPR tool kit for genome editing and beyond. *Nature Communications.* **9** (1), 1911, (2018).

11   Houseley, J. & Tollervey, D. The Many Pathways of RNA Degradation. *Cell.* **136** (4), 763-776, (2009).

12   Sahay, G. *et al.* Efficiency of siRNA delivery by lipid nanoparticles is limited by endocytic recycling. *Nature Biotechnology.* **31** (7), 653-658, (2013).

13   Wang, Y. & Huang, L. A window onto siRNA delivery. *Nature Biotechnology.* **31** (7), 611-612, (2013).

14   Gilleron, J. *et al.* Image-based analysis of lipid nanoparticle-mediated siRNA delivery, intracellular trafficking and endosomal escape. *Nature Biotechnology.* **31** (7), 638-646, (2013).

15   Kim, B. *et al.* Immunogene therapy with fusogenic nanoparticles modulates macrophage response to Staphylococcus aureus. *Nature Communications.* **9** (1), 1969, (2018).

16   Zhang, X. *et al.* Targeted Disruption of G_0/G_1 Switch Gene 2 Enhances Adipose Lipolysis, Alters Hepatic Energy Balance, and Alleviates High-Fat Diet–Induced Liver Steatosis. *Diabetes.* **63** (3), 934-946, (2014).

17   Schlosser, K., Taha, M., Deng, Y. & Stewart, D. J. Systemic delivery of MicroRNA mimics with polyethylenimine elevates pulmonary microRNA levels, but lacks pulmonary selectivity. *Pulmonary Circulation.* **8** (1), 2045893217750613, (2018).

18   Komarov, A. P. *et al.* Functional genetics-directed identification of novel pharmacological inhibitors of FAS- and TNF-dependent apoptosis that protect mice from acute liver failure. *Cell Death & Disease.* **7** e2145, (2016).

2.11   Figures and Tables
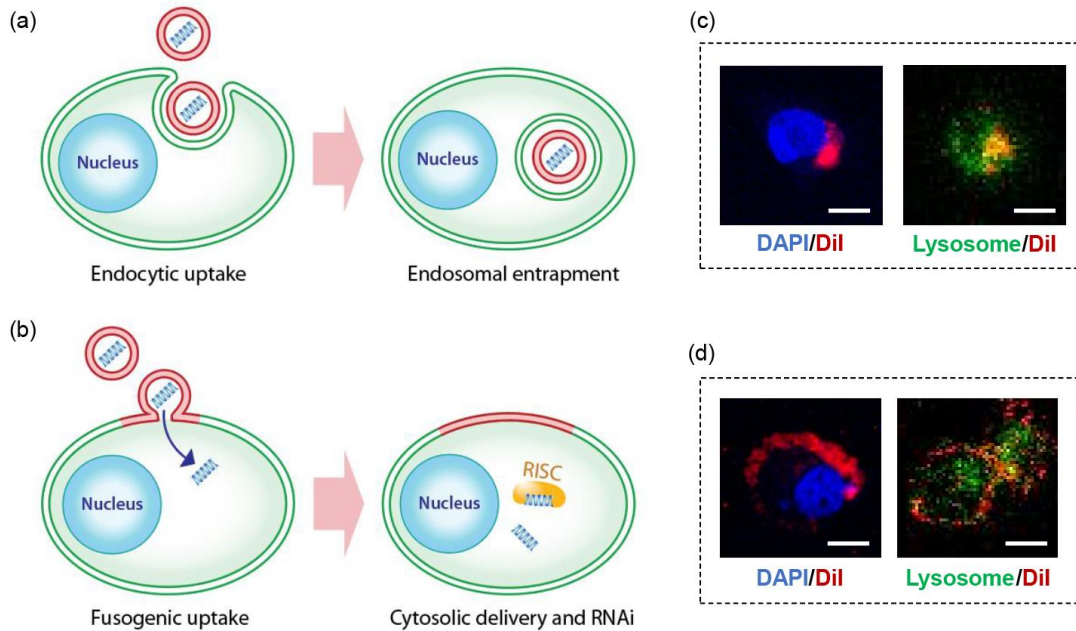
Figure 2.1. Fusogenic porous silicon nanoparticle system (F-pSiNP).
(a) Schematic showing endocytic uptake of conventional nanoparticles and subsequent endosomal entrapment. (b) Schematic showing fusogenic uptake of the F-pSiNPs and subsequent cytosolic delivery of the siRNA payload. (c) Confocal microscopic image of a CAOV-3 cell that has endocytosed non-fusogenic pSiNPs that were loaded with DiI lipophilic dye. CAOV-3 cells were grown to 80% confluence in a 6 well-plate, and treated with 10 µL of nanoparticles, and incubated at 37 °C in 5% CO_2 for 15 min. The cells were fixed in 1% paraformaldehyde to be mounted on glass slides with DAPI, dried and kept in the dark until examined by confocal microscopy. (D) Confocal microscopic image of a CAOV-3 cell that has taken up fusogenic pSiNPs that were loaded with DiI lipophilic dye. Cells were pre-stained with LysoTracker Green for 1 h at 37 °C in 5% CO_2 according to manufacturer's instructions. The cells were then washed PBS three times, and were treated with 10 µL of DiI-loaded particles for 15 min. The cells were washed with PBS three times to remove any particles that were not taken up, and the wells were filled with 1 mL of PBS and immediately taken for live-cell imaging by confocal microscopy; DAPI represents nuclear stain and Lysosome represents lysosomal staining by LysoTracker Green; scale bar represents 10 µm.
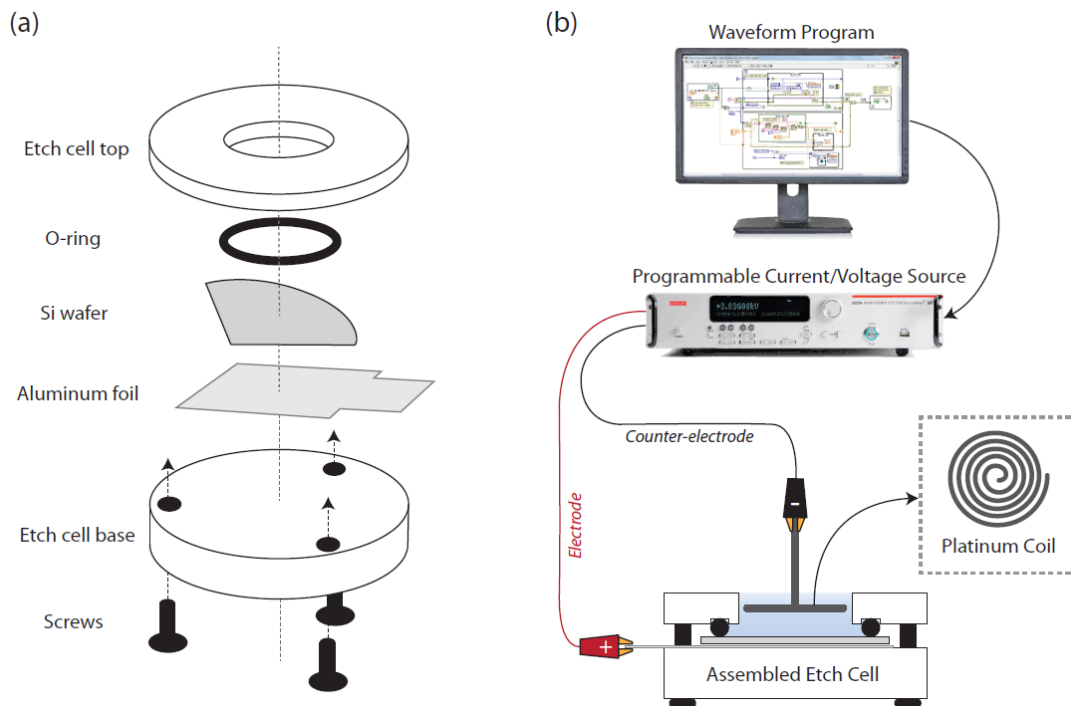
Figure 2.2. Etch cell setup.
(**a**) Schematic showing etch cell components and assembly order; and (**b**) diagram of setup for electrochemical etching of silicon.
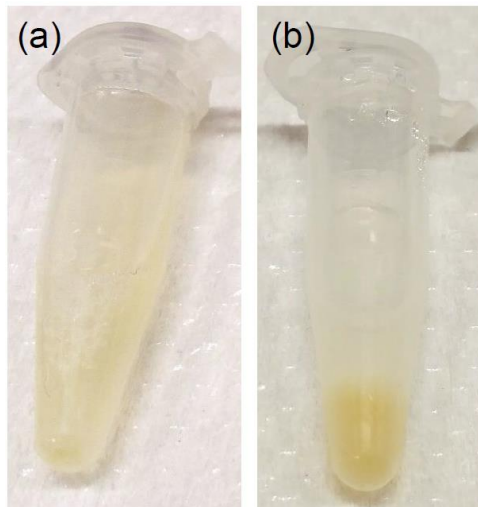
Figure 2.3. Photograph of final F-pSiNP product.
(**a**) Successful synthesis showing homogenous and cloudy solution; (**b**) unsuccessful synthesis showing aggregation of particles (yellow).
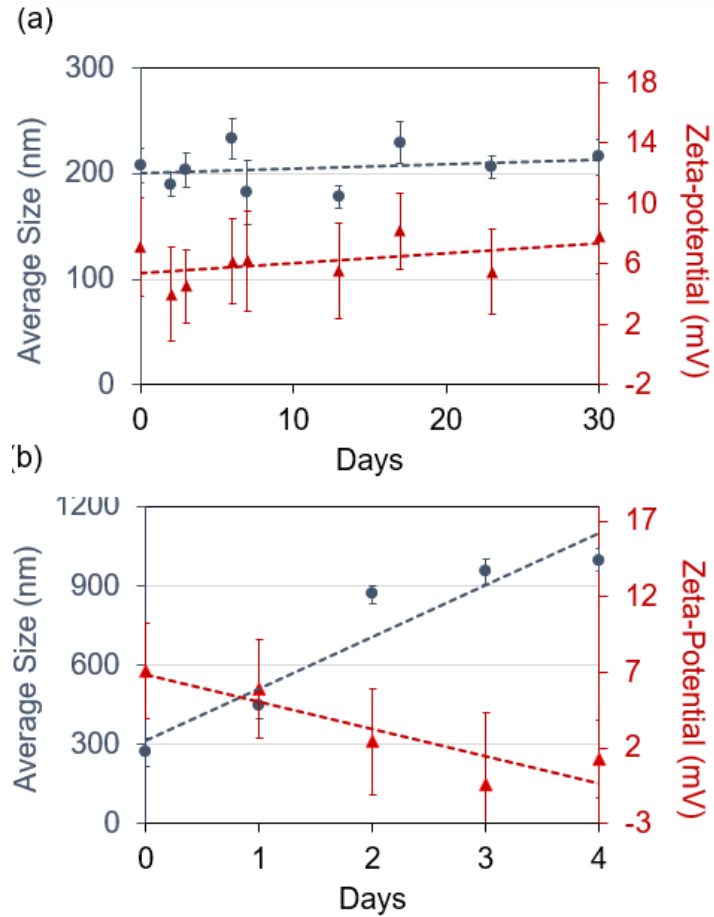
Figure 2.4. Repeated freeze-thaw cycle of fusogenic pSiNPs cause aggregation.
(**a**) Average size and zeta-potential of fusogenic pSiNPs remains steady for 30 days when thawed once post-freezing; (**b**) Average size and zeta-potential of the fusogenic pSiNPs shows signs of aggregation and loss of structural integrity within 4 days after undergoing daily freeze-thaw cycles. Error bars represent standard deviation (n = 5).
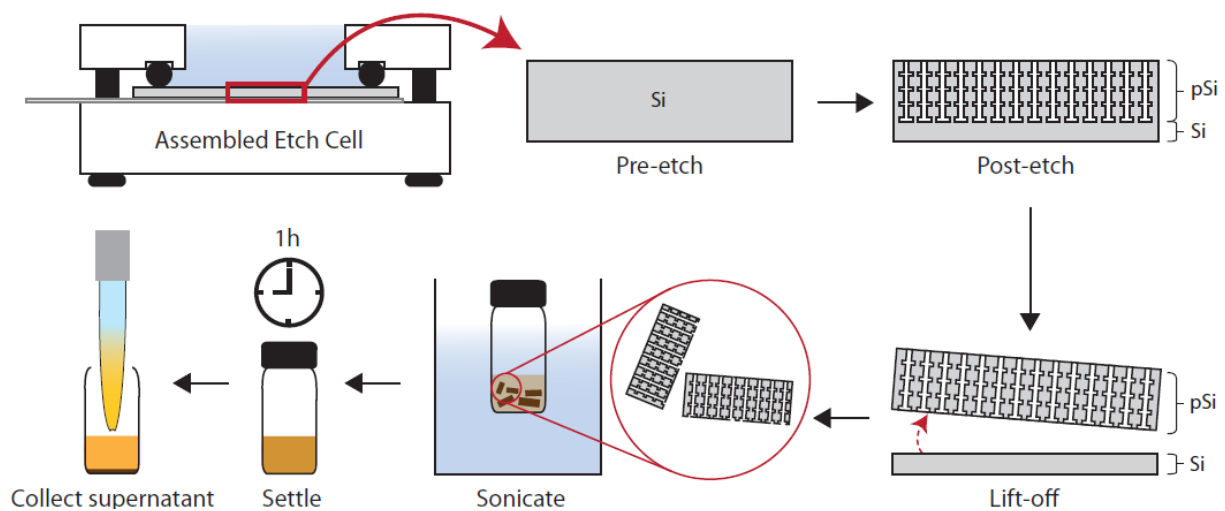
Figure 2.5. Diagram of porous silicon nanoparticle synthesis.
Schematic showing electrochemical etching of silicon wafe, lift-off of the porous layer, sonication of the porous layer into particles, and collection of porous silicon nanoparticles.

Chapter two is, in full, a reprint (with co-author permission) of the material as it appears in the following publication: **Kim, B.**, Sailor, M.J. Synthesis, Functionalization, and Characterization of Fusogenic Porous Silicon Nanoparticles for Oligonucleotide Delivery. *J. Vis. Exp.* (146), e59440, doi:10.3791/59440 (2019). The author of this dissertation is the primary author of this manuscript.

Chapter 3:

Properties and Mechanism of Fusogenic Porous Silicon Nanoparticles

3.1   Materials and Methods

Materials. Highly boron-doped p-type silicon wafers (~1 mΩ-cm resistivity, polished on the (100) face) were obtained from Virginia Semiconductor, Inc or Siltronix, Inc. Hydrofluoric acid (48% aqueous, ACS grade) was obtained from Fisher Scientific. Anhydrous calcium chloride was obtained from Spectrum Chemicals (Gardena, CA). Deionized (18 mΩ) water was used for all aqueous dilutions. For lipids, 1,2-dimyristoyl-sn-glycero-3-phosphocholine (DMPC), 1,2-distearoyl-sn-glycero-3-phosphoethanolamine-N-[methoxy(polyethylene glycol)-2000], (DSPE-mPEG), 1,2-distearoyl-sn-glycero-3-phosphoethanolamine-N-[maleimide(polyethylene glycol)-2000] (DSPE-PEG-maleimide), and 1,2-dioleoyl-3-trimethylammonium-propane (DOTAP) were purchased from Avanti Polar Lipids (Alabaster, AL) and stored at -4ºC. The fluorescent lipophilic dyes 1,1'-dioctadecyl-3,3,3',3'-tetramethylindocarbocyanine perchlorate (DiI) and 3,3'-dioctadecyloxacarbocyanine perchlorate (DiO) were obtained from Life Technologies, and Lipofectamine® 2000 transfection reagent was obtained from Thermo Fisher Scientific. Custom siRNA against luciferase (siLuc) was purchased from Dharmacon (Lafayette, CO), and primers were purchased from IDT DNA (San Diego, CA). Silencer ® Pre-designed siRNA encoding for PI3Kγ (siPI3Kγ; sequence: GGACCACGAGAGUGUGUUCtt) was purchased from Life Technologies, and siGENOME Human REV3L siRNA (siREV3L; sequence: CUGCAGAGAGAAUAACCCUGAdTdT) was purchased from Dharmacon. The siRNAs against *Cav1* (10297), *Cltc* (107565), *Rac1* (120601), *Rab11* (122729), *Rab5a* (120371), *Stx6* (121571), *T-snare* (127901), *Rab27b* (120374) were purchased from Thermo Fisher Scientific (Waltham, MA). Targeting peptides (LyP-1 and iRGD) were custom synthesized by CTC Scientific (Sunnyvale, CA). For *in vitro* studies, J774a.1 cells were purchased from ATCC (Manassas, VA) within 6 months prior to all experiments. DMEM cell media was purchased from GE Healthcare Life Sciences (HyClone, Pittsburg, PA), with supplemental fetal bovine serum (HyClone, Pittsburg, PA) and penicillin/streptomycin (HyClone, Pittsburg, PA). The Cell counting kit-8

(CCK-8) was purchased from Dojindo Molecular Technologies, Inc. (Rockville, MD). Corning Matrigel Membrane Matrix was purchased from Fisher Scientific. Six week-old female athymic nu/nu mice were purchased from Envigo (Placentia, CA).

Preparation of porous silicon nanoparticles. Porous silicon (pSi) samples were prepared by electrochemical etching of silicon wafers in an electrolyte consisting of 3:1 (v:v) of 48% aqueous HF:ethanol (CAUTION: HF is highly toxic and proper care should be exerted to avoid contact with skin or lungs). A silicon working electrode with an exposed area of 8.6 cm^2 was contacted on the back side with aluminum foil and mounted in a Teflon cell. The silicon wafer was then anodized in a two-electrode configuration with a platinum counter electrode, by applying an alternating current of square waveform, with lower current density of 50 mA/cm^2 for 0.6s and high current density of 400 mA/cm^2 for 0.36s, repeated for 500 cycles. The resulting porous layer was lifted off by application of a constant current density of 3.7 mA/cm^2 for 250s in a 1:20 (v:v) of 48% aqueous HF:ethanol solution. The porous layer (0.8 mg) was immersed in RNAse-free water (2 mL) and subjected to ultrasonic fracture (50T ultrasonic bath, VWR International) for 12h to generate the porous silicon (pSi) nanoparticles. Fluorescent dye and siRNA payloads were loaded into the pSi nanoparticles by calcium ion-induced precipitation of calcium silicate as described previously.[1] The oligonucleotide payload was hydrated in RNAse-free water to generate a 20 μM solution. 150 μL of siRNA was pipetted gently into a solution prepared from 150 μL of the pSiNP dispersion and 700 μL of 2M calcium chloride and the mixture was subjected to ultrasonication for 15 min. We used siREV3L (GAG AGU ACC UCC AGA UUU A), siPI3Kg (GGA CCA CGA GAG UGU GUU Ctt) and siLuc (CUU ACG CUG AGU ACU UCG A) for all relevant experiments.

Fusogenic coating. Fusogenic (FNP) and non-fusogenic (NNP) coatings were prepared from DMPC, DSPE-PEG, and DOTAP at molar ratios of 76.2:3.8:20 and 96.2:3.8:20, respectively. The lipid films were prepared by evaporating the organic solvent, with 725.5 μg of

DMPC, 151.6 µg of DSPE-PEG (methoxy or maleimide terminated), and 196.3 µg of DOTAP (fusogenic coating, F, used to prepare fusogenic nanoparticles, or FNPs) or 916.0 µg of DMPC and 151.6 µg of DSPE-PEG (methoxy or maleimide terminated) (non-fusogenic coating, NF, used to prepare non-fusogenic nanoparticles, or NNPs). To incorporate lipophilic DiI into the films, we added 26.3 µg of DiI (1.25 mg/ml in 100% ethanol) to the preparation. The films were then hydrated with the payload-containing pSiNP solution and prepared by film hydration/extrusion: the pSi-hydrated lipid was heated to 40ºC with constant magnetic stirring for 20 min. Then the mixture was extruded through a 200 nm polycarbonate membrane 20 times. Targeting peptides (iRGD and LyP-1) was conjugated to maleimide-terminated PEG by mixing 100 µL of 1 mg/mL of the peptide (in deionized water) in 1 mL of 1 mg/mL (by lipid mass) of the liposomal pSi construct overnight at 4ºC. Particles were washed three times at each step by centrifugation in a Microcon-30kDa Centrifugal Filter Unit (EMD Millipore) by spinning at 5,000g at 25ºC. The loaded siRNA concentration was quantified by NanoDrop 2000 spectrophotometer (Thermo Fisher Scientific, ND-2000).

The alternative formulations to the fusogenic nanoparticles were synthesized in the exact same manner as the fusogenic nanoparticles, albeit with different lipid compositions in the coating. In the DSPC particle, the composition was DSPC:DOTAP:DSPE-PEG at molar ratio of 76.2:3.8:20; in the DLPC particle, the composition was DLPC:DOTAP:DSPE-PEG at molar ratio of 76.2:3.8:20; in the DOTMA particle, the composition was DMPC:DOTMA:DSPE-PEG at molar ratio of 76.2:3.8:20; and in the non-PEGylated particle, the composition was DMPC:DOTAP at molar ratio of 76.2:20. Again, we added 26.3 µg of DiI (1.25 mg/mL in 100% ethanol) to incorporate lipophilic DiI into the films. All lipids were mixed at concentration of 10 mg/mL and the organic solvent was evaporated. The films were then hydrated with a solution of the payload-containing pSiNPs and prepared by the same abovementioned film hydration/extrusion method.

Nanoparticle size and zeta-potential were measured by dynamic light scattering (DLS, Zetasizer ZS90, Malvern Instruments), and structural morphology was visualized with a JEOL 1200 EX II TEM. Samples were prepared by dropping 5 uL of the sample on the TEM grid, drying off excess solvent after 1 min, and dropping 5 μL of uranyl acetate for negative staining.

In vitro **siRNA release.** Porous silicon core nanoparticles without lipid coating (pSiNPs), FNPs, and NNPs containing 11.9 μg of siPI3Kγ were incubated at 37˚C in 400 μL of PBS. The particles were removed from incubation and centrifuged in a Microcon-30kDa Centrifugal Filter Unit (EMD Millipore) by spinning at 5,000g at 25ºC for 30 min. The released siRNA concentration was quantified by measuring the supernatant in NanoDrop 2000 spectrophotometer (Thermo Fisher Scientific, ND-2000). Upon removal of the supernatant, 400 μL of fresh PBS was used to resuspend the particle pellets. The particles were kept in the incubator until each time point when the above measurement steps were repeated. The total siRNA release was summed up and averaged over six independent trials.

Cell culture. CAOV-3 human ovarian adenocarcinoma and J774a.1 murine macrophage lines were cultured in DMEM supplemented with 10% FBS and 1% penicillin/streptomycin, and were incubated at 37ºC in 5% CO_2.

Confocal microscopy. All confocal microscopy images are representative of at least three independent trials and of at least 1×10^6 cells per slide. Fusion of DiI-loaded or siRNA-loaded particles was observed by seeding 0.3×10^6 cells on top of 22 mm round coverslips (BD Biocoat Collagen Coverslip, 22 mm) in a 6-well plate, growing to 80% confluence, and treating the cells with 10 μL of nanoparticles. The particle-treated CAOV-3 cells were incubated at 37℃ in 5% CO_2 for 15 min, whereas the particle-treated J774a.1 cells were incubated for 5 min. After incubation, the cells were washed in PBS three times to remove any particles that were not taken up. The cells were fixed in 1% paraformaldehyde (PFA, Santa Cruz Biotechnology) for 10

min at 4˚C, then washed with PBS three times. The coverslips were mounted on glass slides with ProLong® Diamond Antifade Mountant with DAPI (Life Technologies), dried and kept in the dark until examined by confocal microscopy (Zeiss LSM 710 NLO).

For studies involving lysosome staining, 0.3×10^6 cells were seeded on 35 mm petri dishes, and grown to 80% confluence. The cells were pre-stained with LysoTracker Green (Thermo Fisher Scientific) for 1h at 37ºC in 5% CO_2 according to manufacturer's instructions. The cells were then washed with PBS three times, and then treated with 10 μL of DiI-loaded particles for 15 min (CAOV-3) or 5 min (J774a.1) at 37℃ in 5% CO_2. The cells were washed with PBS three times to remove any particles that were not taken up, and the wells were filled with 1 mL of PBS and immediately subjected to live-cell imaging by confocal microscopy (Zeiss LSM 710 NLO). Pearson's correlation coefficient (PCC) for co-localization was calculated using the Coloc2 plugin from the ImageJ software package (NIH). At least ten representative images were analyzed to obtain the average coefficient.

For imaging porous silicon core nanoparticles or Cy3-tagged siIRF5 as a model siRNA, 0.3×10^6 cells were seeded on 35 mm petri dishes, and grown to 80% confluence. The cells were treated with 10 μL of DiO-loaded fusogenic or non-fusogenic particles with either Cy3-tagged or non-tagged siIRF5-loaded pSiNP cores for 15 min at 37℃ in 5% CO_2. The cells were washed with PBS three times to remove any particles that were not taken up, then fixed in 1% paraformaldehyde (PFA, Santa Cruz Biotechnology) for 10 min at 4˚C, then washed with PBS three times. The coverslips were mounted on glass slides with ProLong® Diamond Antifade Mountant with DAPI (Life Technologies), dried and kept in the dark until examined by confocal microscopy (Zeiss LSM 710 NLO). For Cy3 imaging, $\lambda_{ex} = 550$ nm and $\lambda_{em} = 580\text{-}630$ nm band-pass was used, and for pSiNP imaging, $\lambda_{ex} = 370$ nm and $\lambda_{em} = 650$ nm long-pass was used.

***In vitro* biomarker studies.** For the mechanistic studies involving cellular uptake and intracellular trafficking of the DiI-stained lipids on the fusogenic nanoparticles, we seeded 6-well plates with 0.3 x 10^6 CAOV-3 cells on top of coverslips. At 70% confluence, we transfected the cells with 100 pmol of siRNAs (against Cav1*, Cltc, Rac1, Rab11, Rab5a, Stx6, T-snare, or Rab27b*) and 5 µL of Lipofectamine 2000 transfection agent per well, as per the manufacturer's instructions. The cells were incubated with the transfectant for 4h at 37˚C in 5% CO_2, then washed three times with PBS. The wells were replaced with 2 mL of fresh DMEM supplemented with 10% FBS and 1% penicillin/streptomycin, and further incubated for 48h. The cells were then treated with 10 µL of nanoparticles and incubated at 37°C in 5% CO_2 for 15 min, then washed with PBS three times, then fixed, dried, and mounted with DAPI as described above. For experiments with lysosome staining, the cells were stained with LysoTracker Green for 1h at 37ºC in 5% CO_2 according to the manufacturer's instructions, prior to particle treatment and live-cell imaging by confocal microscopy.

To determine the exocytosis pathway for fusogenic nanoparticles, we used a transwell culture system. We seeded 0.1 x 10^6 CAOV-3 cells in the top well, and placed them on top of an empty 6-well plate, and 0.3 x 10^6 CAOV-3 cells on coverslips were seeded in another 6-well plate to serve as the lower well post-inhibition. At 60% confluence, we treated the cells in the top wells with 10 µM of Bisindolymaleimide I (BIM I), or 10 µM of GW4869 for 24h at 37ºC in 5% CO_2, or 100 pmol of siRNA against *Rab27b* with 5 µL of Lipofectamine 2000 for 4h at 37ºC in 5% CO_2, then washed with PBS three times to be further incubated for 48h. Post-inhibition of exocytosis, the cells were treated with particles (10 µL) for 30 min at 37ºC in 5% CO_2, then washed with PBS three times. The top wells were then transferred to the lower wells in the 6-well plate with CAOV-3 cultured on the coverslips with fresh DMEM supplemented with 10% FBS and 1% penicillin/streptomycin, and further incubated for 48h. The lower well cells were

washed with PBS three times, fixed and mounted with DAPI and analyzed by confocal microscopy as described above.

For all particle uptake quantifications, we used Image J software to quantify the brightness and area taken up by the DiI signals for each condition. The values were averaged over 12 measurements per 10 representative images taken per well. Statistics were performed using Student's paired t-test with α-level of 0.05.

Statistics. All statistical analyses were performed using single way ANOVA and post hoc comparisons using Tukey's HSD test at $p < 0.05$, unless otherwise stated. Power analysis was performed to estimate the total mouse sample size required for the tumor growth and survival studies using the GPower 3.1 software. The analysis was performed using *a priori*, ANOVA: repeated measures, between factors, as the study looks at tumor growth by each therapeutic formulation over time. Based on a published study[2] (N=32), where the fusogenic nanoparticles were intravenously injected for siRNA knockdown in Balb/C mice with bacterial infection, the effect size (ES) was calculated to be 11.5, thus set to 'large' (0.40) in the software's parameter settings. With α error probability of 0.05 and Power of 0.80, 5 test groups, 15 measurements (for tumor size), and correlation of 0.3, we determined that a sample size of 35 mice was adequate for the experiments investigating the therapeutic efficacy of the formulations.

3.2   Structure and composition of fusogenic nanoparticles (FNPs)

The FNPs (**Fig 3.1a**) consisted of a porous silicon nanoparticle core loaded with siRNA (pSiNP), and a fusogenic lipid coating decorated with pendant targeting peptides. The porous silicon nanoparticle cores were prepared by electrochemical etch of silicon wafers, and the

siRNA payload was loaded into the nanoparticle with the assistance of calcium ion as previously described[13,14]. The calcium ion serves two functions in this preparation. First, it acts to neutralize the negative charge of the silicon oxide surface of the pSiNP and the negative charge of the nucleic acid[15], in a role similar to that played by the cationic polymers or lipids commonly deployed in nucleic acid delivery systems[9,16-23]. Second, partial dissolution of the silicon skeleton during the loading procedure generates silicic acid that then forms a precipitate with Ca (II) ions, generating a calcium silicate phase that effectively seals the nanostructure and traps the nucleic acid payload. This sealing chemistry is remarkably efficient in that it can load up to 25% nucleic acid by mass; in the present case the mass loading of siRNA was 10% (defined as mass of siRNA loaded relative to mass of siRNA-containing nanoparticle). The nanoparticle was then coated with the fusogenic lipid coating and the targeting peptide of interest was coupled to the PEG component of this coat *via* a terminal maleimide group; for non-targeted particles we used PEG with a methoxy terminus (mPEG). The overall hydrodynamic diameter of the resulting FNPs was 170 nm, and the zeta potential was +9 mV when mPEG was used. For the formulations that contained a peptide targeting group, the zeta potential was closer to neutral (**Table 3.1**). The siRNA-loaded particles were stable when stored at -80°C for > 1 month with no loss of functionality[14].

3.3　　Factors favoring cellular membrane fusion vs. endocytosis

The lipids that comprised the fusogenic coating were selected based on the known ability of liposomes with the composition used to fuse with the cellular membrane and avoid endocytosis[9,10,24,25]; we assumed that the composition would behave similarly if the final liposomal construct contained a core of solid nanoparticles. Each lipid component plays a role in plasma membrane fusion (**Table 3.2**)[10]. First, DMPC is the major structural component, with a

phase transition temperature (24˚C) below the physiological temperature (37˚C). This property allows the lipids to be in a fluidic liquid crystal phase (L_α) *in vivo*, which is the phase to which endogenous extracellular vesicles transition when fusing[26]. We selected DSPC (T_{ph}= 55˚C) and DLPC (T_{ph}= -2˚C) as alternative lipids to test for the importance of lipid phase in the fusion process. Second, cationic DOTAP serves to attract the negatively charged plasma membrane; another widely used cationic lipid, DOTMA, was selected as an alternative. The key difference is that, while DOTAP becomes completely protonated and more cationic at the physiologic pH of 7.4, DOTMA does not[26]. Finally, polyethylene glycol (PEG) is hypothesized to interact with cellular surface proteins in a manner akin to the endogenous SNARE proteins[27,28]. To test the influence of the PEG component, one alternative test formulation contained no PEGylated lipid.

The above formulations were used to probe the mechanism of cellular uptake *in vitro*, using CAOV-3 human ovarian adenocarcinoma cells. For these tests we used a methoxy group rather than a specific targeting peptide conjugated to the PEGylated lipid component. **Figures 3.1b-f** show confocal images of CAOV-3 cells treated with FNPs or with the alternative lipid compositions. When loaded with the lipophilic DiI fluorophore as a stain for the lipid membrane, FNPs demonstrated fusion and transfer of DiI into the plasma membrane (**Fig 3.1b**). When the cells were stained with LysoTracker Green, we observed minimal co-localization between the DiI lipid stain and the lysosomes (Pearson's correlation coefficient, or PCC = 0.08), indicating that the FNPs did not undergo endocytosis. However, when we replaced the DMPC component with DSPC (which has a higher T_{ph} and is in the L_β gel phase at 37°C), we observed endocytosis and co-localization between the lysosomes and the lipid stain (PCC= 0.51; **Fig 3.1c**). On the other hand, when DLPC (which has lower T_{ph} and is in the L_α liquid crystalline phase at 37°C) was used, we observed an overall lower level of DiI loading into the particle coating (data not shown). This result can be ascribed to the lower stability of the particles, as the DLPC lipids are expected to remain in a more fluidic state at during particle synthesis and at

physiologic temperature due to their low phase transition temperature (T_{ph}= -2°C). Despite the lower degree of dye loading, membrane fusion was still observed, although the formulation showed substantial co-localization between the lysosomes and the lipid stain compared with the FNP formulation (PCC=0.20; **Fig 3.1d**). Taken together, the data indicate that the fluidity of the lipid is important for effective membrane fusion; if the lipid is in the more rigid gel phase it is readily endocytosed and if it is in a more fluid state the entire construct is less stable during synthesis.

Next, we observed the uptake of particles where DOTAP was replaced by DOTMA. Due to the decrease in degree of protonation of the lipid, the overall zeta potential of the final particle was less positive. As a result, there was a marked reduction in particle uptake, although the particles that were taken up underwent fusion, as determined by the relatively low degree of co-localization observed between the lysosomes and the lipid stain (PCC= 0.14; **Fig 3.1e**). Thus, consistent with much prior work, the higher positive charge facilitates uptake and fusion due to the electrostatic attraction between the cationic FNPs and the anionic plasma membrane[29,30].

Finally, the formulation lacking DSPE-PEG was observed to have a high degree of co-localization between the lysosomes and the lipid stain suggesting extensive endocytosis (PCC=0.46; **Fig 3.1f**). As has been described previously for PEGylated nanoparticles and akin to the endogenous SNARE mechanism[27,28], the data are consistent with the hypothesis that PEG assists in dehydrating the gap between the fusogenic lipid coating on the nanoparticle and the plasma membrane on the cell, making lipid fusion energetically and structurally favorable.

From the above studies we can conclude that there are at least three factors favoring fusion of the FNPs with the plasma membrane: (1) a substantial portion (>70% molar ratio) of the composition must have a moderately low phase transition point near room temperature; (2)

the overall zeta potential of the lipid composition must be cationic (~10 mV); and (3) PEG or an equivalent dehydrating agent must be present in the lipid formulation.

3.4   Cellular uptake of FNPs

We next investigated the impact of inhibition of the major endocytic pathway mediators[3,4] — caveolin (*Cav1*), clathrin (*Cltc*), and macropinocytosis (*Rac1*) — on cellular uptake of FNPs **(Fig 3.2, pathway #1)**. The degree of uptake of the FNPs was compared to a non-fusogenic nanoparticle construct (NNPs; identical structure as FNPs, but with a lipid coating that is not fusogenic, see Methods section). The data are shown in **Fig 3.3a** and the corresponding confocal images are shown in **Fig 3.4**. For all three markers, we found that while non-fusogenic nanoparticles showed a significant decrease in uptake, the fusogenic nanoparticles were taken up at levels equivalent to the non-transfected control, and at significantly higher quantities than the NNPs (paired t-test; p= 0.024 (*Cav1*); = 0.031 (*Cltc*); and = 0.002 (*Rac1*)). Thus, we conclude that fusogenic FNPs are taken up *via* pathways that are independent of endocytosis.

In order to determine whether specific biological markers and pathways exert influence on the fusogenic uptake of the FNPs, other major markers of cellular uptake and metabolism of lipids were studied (**Fig 3.2**). A summary of the pathways investigated is given in the table shown in **Fig 3.2**.

After validating that FNPs are taken up through fusogenic uptake in CAOV-3 cells in a manner that is independent of the major endocytosis pathways (clathrin-, caveolin-mediated uptake, or macropinocytosis), we next asked whether fusogenic uptake of FNPs is dependent on other major markers of cellular traffic of lipids.

We studied *Rab11* and *Rab5A* markers, which regulate intracellular vesicle traffic (**Fig 3.2, pathway #2**), and investigated their impact on the uptake pathway of DiI-loaded FNPs (**Fig 3.5a**) and quantified the uptake (**Fig 3.5b**). While *Rab5A* is often found on early endosomes, *Rab11* is primarily found in recycling endosomes.[1-3] When we silenced *Rab5A* or *Rab11*, we observed fusogenic uptake of FNPs, as evidenced by the lack of co-localization between the DiI and the lysosomes. As *Rab5A* silencing depletes early endosomes and decreases endocytosis[4], and *Rab11* silencing prevents accumulation of recycling endosomes within the cell[1-3]; thus we confirmed that fusogenic delivery is independent of endocytic pathways and that it does not share the same intracellular fate as endocytosed materials.

On the other hand, we observed strong differences when we silenced *Stx6*, *T-snare*, and *Rab27b* to deplete intracellular vesicle fusion (**Fig 3.2, pathway #3**). Inhibition of these markers induced colocalization between DiI and lysosomes, although the reason for the endocytosis of FNPs remains unclear. One conjecture is that inhibition of endogenous fusion mechanisms locks the plasma membrane in the rigid L_β gel phase, preventing fusion with intra- and extracellular vesicles and particles. One common observation across all vesicle traffic and fusion markers was that their silencing reduced the overall particle uptake (**Fig 3.5b**), which is consistent with the literature on these markers.[5,6]

Lastly, we studied the exocytosis markers (**Fig 3.2, pathway #4**) using a transwell system. Based on literature reports, fusogenic liposomes may be recycled into microvesicles or exosomes.[7] Therefore, we inhibited exocytosis using chemical inhibitors (bisindolymaleimide I, GW4869) or siRNA against *Rab27b* in the top well of cells, then treated the inhibited cells with DiI-loaded FNPs or NNPs. We quantified the amount of DiI transferred from the top well of cells to the lower well of naïve cells (**Fig 3.6a**) using confocal microscopic images (**Fig 3.6b**).

Rab27b regulates trafficking of multivesicular endosomes (MVEs; intracellular vesicles that are excreted as exosomes).[8,9] When *Rab27b* was silenced, we observed decrease in the transfer of lipophilic DiI from the top to lower well of cells in both fusogenic and non-fusogenic particle treatments. This observation correlates with literature, which found that *Rab27b* silencing directs MVEs to the perinuclear region, and away from the plasma membrane and excretion.[9] The second inhibitor, bisindolymaleimide I (BIM I), is a protein kinase C inhibitor that prevents phosphorylation of t-SNARE and suppresses intracellular vesicle fusion to the plasma membrane for excretion.[10-13] When this excretion pathway was blocked, both FNPs and NNPs decreased transfer of the lipophilic payload from the top to lower well of cells. Lastly, GW4869 blocks neutral sphingomyelinase from activating the inward budding and excretion of MVEs; although the specific role of sphingomyelinase in exosomal secretion remains unclear.[14-16] When cells were treated with GW4869, NNPs showed decrease in the lipophilic DiI transfer to the lower wells. However, FNPs maintained the DiI transfer level compared to the control, and attained significantly higher transfer rate than the NNPs (paired t-test; p= 0.005). Thus, we conclude that payloads from fusogenic particles are likely excreted in protein kinase C- and *Rab27b*-dependent, but sphingomyelinase-independent manner (**Fig 3.2, pathway #4**).

Particles loaded with calcein as a model payload for siRNA were also treated to cells in the transwell, and while the lower chamber cells of NNP-treated transwell showed no signal, that of the FNP-treated transwell showed highly diluted calcein signal in the cytoplasm (data not shown), which correlates with literature.[21] **Fig 3.7** shows that targeting peptides are transferred with the lipophilic DiI payload regardless of the particle uptake pathway (fusogenic vs. non-fusogenic) in the upper chamber of cells, as the the FAM-conjugated peptide and DiI signals were found to co-localize in the cytoplasm of the cells cultured in the lower chamber of the transwell.

Overall, we observed that FNPs were able to undergo fusogenic uptake in a manner independent of the major known endocytosis or vesicle traffic pathways, but their uptake was highly dependent on mediators of intracellular vesicle fusion. It should be stressed that these results remain primarily phenomenological, because while the biological mechanism of these proteins on a molecular scale are elucidated (*e.g.* SNARE protein interaction), the interactions between the selected pathways and lipid dynamics are not known at this time, and there may be additional cellular uptake pathways as yet unidentified. However the data clearly show that the FNPs enter the cell in a manner that bypasses endocytosis.

3.5   Intracellular fate of FNP components

We evaluated the fate of the three major components of the FNP platform: (1) the fusogenic lipid coating; (2) the porous silicon nanoparticles in the core; and (3) the siRNA payload. We started with the hypothesis that the particles dissolve and release their siRNA payload upon shedding their lipid coats. Porous silicon nanoparticles that lacked a lipid coating (pSiNPs) dissolved and released 70% of their siRNA payload within the first 30 min of incubation in PBS at 37°C, and 90% was released within 6 h (**Figure 3.3b**). In contrast, the lipid-coated nanoparticles (either FNPs or NNPs) released very little (5%) siRNA in the first 30 min, and only 25% was released in 24 h. The particles released ~75% of their total siRNA payload after 168 h (7 days) of incubation, a factor of >300 fold slower than what was observed for the particles without a lipid coat. Complete release from the lipid-coated nanoparticles was achieved by 336 h (14 days). Thus, the lipid coating substantially impedes porous silicon dissolution and siRNA release under physiological conditions. This is a striking result considering the substantial leakage that is typically observed from conventional liposomal formulations that contain an aqueous core[31-34], and illustrates the advantage of locking the otherwise highly soluble siRNA payload into a solid core[35-37].

105

We next tracked the intracellular fate of the components, using CAOV-3 cells in a series of *in vitro* experiments. Cells were treated with DiO-loaded fusogenic (FNP; **Fig 3.3c**) or non-fusogenic (NNP; **Fig 3.3d**) lipid-coated pSiNPs that contained an siRNA payload. DiO is a lipophilic green fluorescent dye, used here to track the lipid component of the FNPs, and the siRNA was tracked with a pendant red Cy3 tag. The pSiNPs were tracked using their intrinsic red to NIR photoluminescence, which derives from quantum-confined silicon[38]. This provided a direct measure of the extent of dissolution of the silicon nano-carrier, as the photoluminescence disappears when the nanoparticles dissolve[39]. The FNPs showed clear dispersion of the Cy3-tagged siRNA in the cell cytosol post-fusion, whereas the DiO affiliated with the lipid components was retained in the cell membrane (**Fig 3.3c**). A similar experiment was performed using an siRNA payload without the red Cy3 tag and monitoring the red emission from the pSiNPs. Signals from the pSiNPs, readily observable in cell-free media, were not visible after fusion with the cells (**Fig 3.3d**). This indicates that the nano-carrier was rapidly degraded upon encounter with the cells, presumably a result of shedding of its fusogenic lipid coating. In contrast, signals from the pSiNPs were prominent in cells treated with non-fusogenic NNPs (**Fig 3.3d**), which enter the cell *via* endocytosis. The non-fusogenic NNPs showed strong co-localization of the red pSiNP signal with the DiO signal from the lipid, indicating that the lipid coat around the pSiNPs was retained upon endocytosis (**Fig 3.3d**). In separate experiments the DiO signal was found to co-localize with the Cy3 signal from a suitably labeled siRNA payload, showing that the endocytosed NNPs were not able to release the siRNA payload into the cytosol. These data support the mechanism given in **Fig 3.1a**, in which the fusogenic coating is shed upon encounter with the cell membrane, and the pSiNPs carrying their siRNA payload are delivered directly into the cellular cytoplasm. Once they lose their protective lipid coating, the pSiNPs dissolve rapidly, releasing their siRNA payload. When a non-fusogenic coating is used, the particles become endocytosed, which permits the lipid coat to remain intact and prevents

pSiNP degradation and siRNA release. Thus, the conditional shedding of the lipid coating around the pSiNP core *via* fusogenic uptake is critical to cytosolic release of siRNA.

3.6   Discussion and Conclusions

A primary goal of this study was to understand the mechanism by which the FNPs operate. We showed that the lipid composition has a direct influence on its behavior, and that a combination of properties (fluidity, cationic charge, and PEGylation) allows for plasma membrane fusion and endocytic bypass. Biological inhibitor studies showed that FNPs behave independent of typical endocytic pathways and intracellular vesicle traffic markers. However, vesicle fusion and certain exocytosis pathways were found to influence the fate of FNPs. The exact mechanism by which the fusogenic coating interacts with these markers remains to be seen, as the extent of existing knowledge regarding these cellular pathways is limited.

3.7 References

1   Kang, J. *et al.* Self-Sealing Porous Silicon-Calcium Silicate Core–Shell Nanoparticles for Targeted siRNA Delivery to the Injured Brain. *Adv. Mater.* **28**, 7962-7969, doi:10.1002/adma.201600634 (2016).

2   Kang, J. *et al.* Self-Sealing Porous Silicon-Calcium Silicate Core-Shell Nanoparticles for Targeted siRNA Delivery to the Injured Brain. *Adv Mater* **28**, 7962-7969, doi:10.1002/adma.201600634 (2016).

3   Kim, B. & Sailor, M. J. Synthesis, Functionalization, and Characterization of Fusogenic Porous Silicon Nanoparticles for Oligonucleotide Delivery. *JoVE*, e59440, doi:doi:10.3791/59440 (2019).

4   Choi, E., Lee, J., Kwon, I. C. & Kim, S. Cumulative directional calcium gluing between phosphate and silicate: A facile, robust and biocompatible strategy for siRNA delivery by amine-free non-positive vector. *Biomaterials*, doi:/10.1016/j.biomaterials.2019.04.006 (2019).

5   Hasanzadeh Kafshgari, M. *et al. Oligonucleotide delivery by chitosan-functionalized porous silicon nanoparticles.* Vol. 8 (2015).

6   Ozpolat, B., Sood, A. K. & Lopez-Berestein, G. Liposomal siRNA nanocarriers for cancer therapy. *Adv Drug Deliv Rev* **66**, 110-116, doi:10.1016/j.addr.2013.12.008 (2014).

7   Ashley, C. E. *et al.* Delivery of Small Interfering RNA by Peptide-Targeted Mesoporous Silica Nanoparticle-Supported Lipid Bilayers. *ACS Nano* **6**, 2174-2188, doi:Doi 10.1021/Nn204102q (2012).

8   Basha, G. *et al.* Influence of cationic lipid composition on gene silencing properties of lipid nanoparticle formulations of siRNA in antigen-presenting cells. *Mol Ther* **19**, 2186-2200, doi:10.1038/mt.2011.190 (2011).

9   Meng, H. A. *et al.* Engineered Design of Mesoporous Silica Nanoparticles to Deliver Doxorubicin and P-Glycoprotein siRNA to Overcome Drug Resistance in a Cancer Cell Line. *ACS Nano* **4**, 4539-4550, doi:10.1021/nn100690m (2010).

10   Woodrow, K. A. *et al.* Intravaginal gene silencing using biodegradable polymer nanoparticles densely loaded with small-interfering RNA. *Nat Mater* **8**, 526-533, doi:10.1038/nmat2444 (2009).

11   Oh, Y. K. & Park, T. G. siRNA delivery systems for cancer treatment. *Adv Drug Deliv Rev* **61**, 850-862, doi:10.1016/j.addr.2009.04.018 (2009).

12   Howard, K. A. Delivery of RNA interference therapeutics using polycation-based nanoparticles. *Adv Drug Deliv Rev* **61**, 710-720, doi:10.1016/j.addr.2009.04.001 (2009).

13   Zhang, S., Zhao, B., Jiang, H., Wang, B. & Ma, B. Cationic lipids and polymers mediated vectors for delivery of siRNA. *J Control Release* **123**, 1-10, doi:10.1016/j.jconrel.2007.07.016 (2007).

14   Lee, J. *et al.* Liposome-based engineering of cells to package hydrophobic compounds in membrane vesicles for tumor penetration. *Nano Lett* **15**, 2938-2944, doi:10.1021/nl5047494 (2015).

15   Kim, B. *et al.* Immunogene therapy with fusogenic nanoparticles modulates macrophage response to Staphylococcus aureus. *Nat Commun* **9**, 1969, doi:10.1038/s41467-018-04390-7 (2018).

16   Kim, J., Santos, O. A. & Park, J. H. Selective photosensitizer delivery into plasma membrane for effective photodynamic therapy. *J Control Release* **191**, 98-104, doi:10.1016/j.jconrel.2014.05.049 (2014).

17   Balazs, D. A. & Godbey, W. Liposomes for Use in Gene Delivery. *Journal of Drug Delivery* **2011**, doi:10.1155/2011/326497 (2011).

18   Lentz, B. R. Polymer-induced membrane fusion: potential mechanism and relation to cell fusion events. *Chem Phys Lipids* **73**, 91-106 (1994).

19   Dennison, S. M., Bowen, M. E., Brunger, A. T. & Lentz, B. R. Neuronal SNAREs do not trigger fusion between synthetic membranes but do promote PEG-mediated membrane fusion. *Biophys J* **90**, 1661-1675, doi:10.1529/biophysj.105.069617 (2006).

20   Sun, J., Jakobsson, E., Wang, Y. & Brinker, C. Nanoporous Silica-Based Protocells at Multiple Scales for Designs of Life and Nanomedicine. *Life* **5**, 214-229 (2015).

21   Liu, J., Stace-Naughton, A., Jiang, X. & Brinker, C. J. Porous Nanoparticle Supported Lipid Bilayers (Protocells) as Delivery Vehicles. *Journal of the American Chemical Society* **131**, 1354-1355, doi:10.1021/ja808018y (2009).

22   Gilleron, J. *et al.* Image-based analysis of lipid nanoparticle-mediated siRNA delivery, intracellular trafficking and endosomal escape. *Nature biotechnology* **31**, 638-646, doi:10.1038/nbt.2612 (2013).

23   Sahay, G. *et al.* Efficiency of siRNA delivery by lipid nanoparticles is limited by endocytic recycling. *Nature biotechnology* **31**, 653-658, doi:10.1038/nbt.2614 (2013).

24   Grosshans, B. L., Ortiz, D. & Novick, P. Rabs and their effectors: achieving specificity in membrane traffic. *Proc Natl Acad Sci U S A* **103**, 11821-11827, doi:10.1073/pnas.0601617103 (2006).

25   Campa, C. C. & Hirsch, E. Rab11 and phosphoinositides: A synergy of signal transducers in the control of vesicular trafficking. *Adv Biol Regul* **63**, 132-139, doi:10.1016/j.jbior.2016.09.002 (2017).

26   Takahashi, S. *et al.* Rab11 regulates exocytosis of recycling vesicles at the plasma membrane. *J Cell Sci* **125**, 4049-4057, doi:10.1242/jcs.102913 (2012).

27   Chen, P.-I., Kong, C., Su, X. & Stahl, P. D. Rab5 isoforms differentially regulate the trafficking and degradation of epidermal growth factor receptors. *The Journal of biological chemistry* **284**, 30328-30338, doi:10.1074/jbc.M109.034546 (2009).

28   Jae, N., McEwan, D. G., Manavski, Y., Boon, R. A. & Dimmeler, S. Rab7a and Rab27b control secretion of endothelial microRNA through extracellular vesicles. *FEBS Lett* **589**, 3182-3188, doi:10.1016/j.febslet.2015.08.040 (2015).

29   Ostrowski, M. *et al.* Rab27a and Rab27b control different steps of the exosome secretion pathway. *Nat Cell Biol* **12**, 19-30; sup pp 11-13, doi:10.1038/ncb2000 (2010).

30   Liu, X., Heidelberger, R. & Janz, R. Phosphorylation of syntaxin 3B by CaMKII regulates the formation of t-SNARE complexes. *Mol Cell Neurosci* **60**, 53-62, doi:10.1016/j.mcn.2014.03.002 (2014).

31   Malmersjo, S. *et al.* Phosphorylation of residues inside the SNARE complex suppresses secretory vesicle fusion. *EMBO J* **35**, 1810-1821, doi:10.15252/embj.201694071 (2016).

32   Chung, S. H., Polgar, J. & Reed, G. L. Protein kinase C phosphorylation of syntaxin 4 in thrombin-activated human platelets. *J Biol Chem* **275**, 25286-25291, doi:10.1074/jbc.M004204200 (2000).

33   Kosgodage, U. S., Trindade, R. P., Thompson, P. R., Inal, J. M. & Lange, S. Chloramidine/Bisindolylmaleimide-I-Mediated Inhibition of Exosome and Microvesicle Release and Enhanced Efficacy of Cancer Chemotherapy. *Int J Mol Sci* **18**, doi:10.3390/ijms18051007 (2017).

34   Essandoh, K. *et al.* Blockade of exosome generation with GW4869 dampens the sepsis-induced inflammation and cardiac dysfunction. *Biochim Biophys Acta* **1852**, 2362-2371, doi:10.1016/j.bbadis.2015.08.010 (2015).

35   Menck, K. *et al.* Neutral sphingomyelinases control extracellular vesicles budding from the plasma membrane. *J Extracell Vesicles* **6**, 1378056, doi:10.1080/20013078.2017.1378056 (2017).

36   Trajkovic, K. *et al.* Ceramide triggers budding of exosome vesicles into multivesicular endosomes. *Science* **319**, 1244-1247, doi:10.1126/science.1153124 (2008).

37   Kube, S. *et al.* Fusogenic Liposomes as Nanocarriers for the Delivery of Intracellular Proteins. *Langmuir* **33**, 1051-1059, doi:10.1021/acs.langmuir.6b04304 (2017).

38   Ozpolat, B., Sood, A. K. & Lopez-Berestein, G. Liposomal siRNA nanocarriers for cancer therapy. *Adv. Drug Deliv. Rev.* **66**, 110-116, doi:10.1016/j.addr.2013.12.008 (2014).

39   Kraft, J. C., Freeling, J. P., Wang, Z. & Ho, R. J. Y. Emerging Research and Clinical Development Trends of Liposome and Lipid Nanoparticle Drug Delivery Systems. *J. Pharm. Sci.* **103**, 29-52, doi:10.1002/jps.23773 (2014).

40   Allen, T. M. & Cullis, P. R. Liposomal drug delivery systems: From concept to clinical applications. *Adv. Drug Deliv. Rev.* **65**, 36-48, doi:10.1016/j.addr.2012.09.037 (2013).

41   Jiang, W., Lionberger, R. A. & Yu, L. X. In vitro and in vivo characterizations of PEGylated liposomal doxorubicin. *Bioanalysis* **3**, 333-344, doi:DOI: 10.4155/bio.10.204 (2011).

42   Russell, L. M., Hultz, M. & Searson, P. C. Leakage kinetics of the liposomal chemotherapeutic agent Doxil: The role of dissolution, protonation, and passive transport, and implications for mechanism of action. *Journal of Controlled Release* **269**, 171-176, doi:https://doi.org/10.1016/j.jconrel.2017.11.007 (2018).

43   Hasan, W. *et al.* Delivery of Multiple siRNAs Using Lipid-Coated PLGA Nanoparticles for Treatment of Prostate Cancer. *Nano Lett.* **12**, 287-292, doi:Doi 10.1021/Nl2035354 (2012).

44   Park, J.-H. *et al.* Biodegradable luminescent porous silicon nanoparticles for in vivo applications. *Nature Mater.* **8**, 331-336, doi:DOI: 10.1038/NMAT2398 (2009).

45   Jin, Y. *et al.* Tracking the Fate of Porous Silicon Nanoparticles Delivering a Peptide Payload by Intrinsic Photoluminescence Lifetime. *Adv. Mater.* **30**, 1802878, doi:doi:10.1002/adma.201802878 (2018).

3.8   Figures and Tables

(a)

(b)

Lipid Comp.	**FNP** DMPC:DOTAP:PEG	**DSPC**:DOTAP:PEG	**DLPC**:DOTAP:PEG	DMPC:**DOTMA**:PEG	DMPC:DOTAP
T_{ph}	24°C	55°C	-2°C	24°C	24°C
ζ	+12.1 mV	+6.0 mV	+16.7 mV	+2.7 mV	+30.1 mV
PCC	0.08	0.51	0.20	0.14	0.46
DAPI/DiI	(b)	(c)	(d)	(e)	(f)
DiI/Lyso					
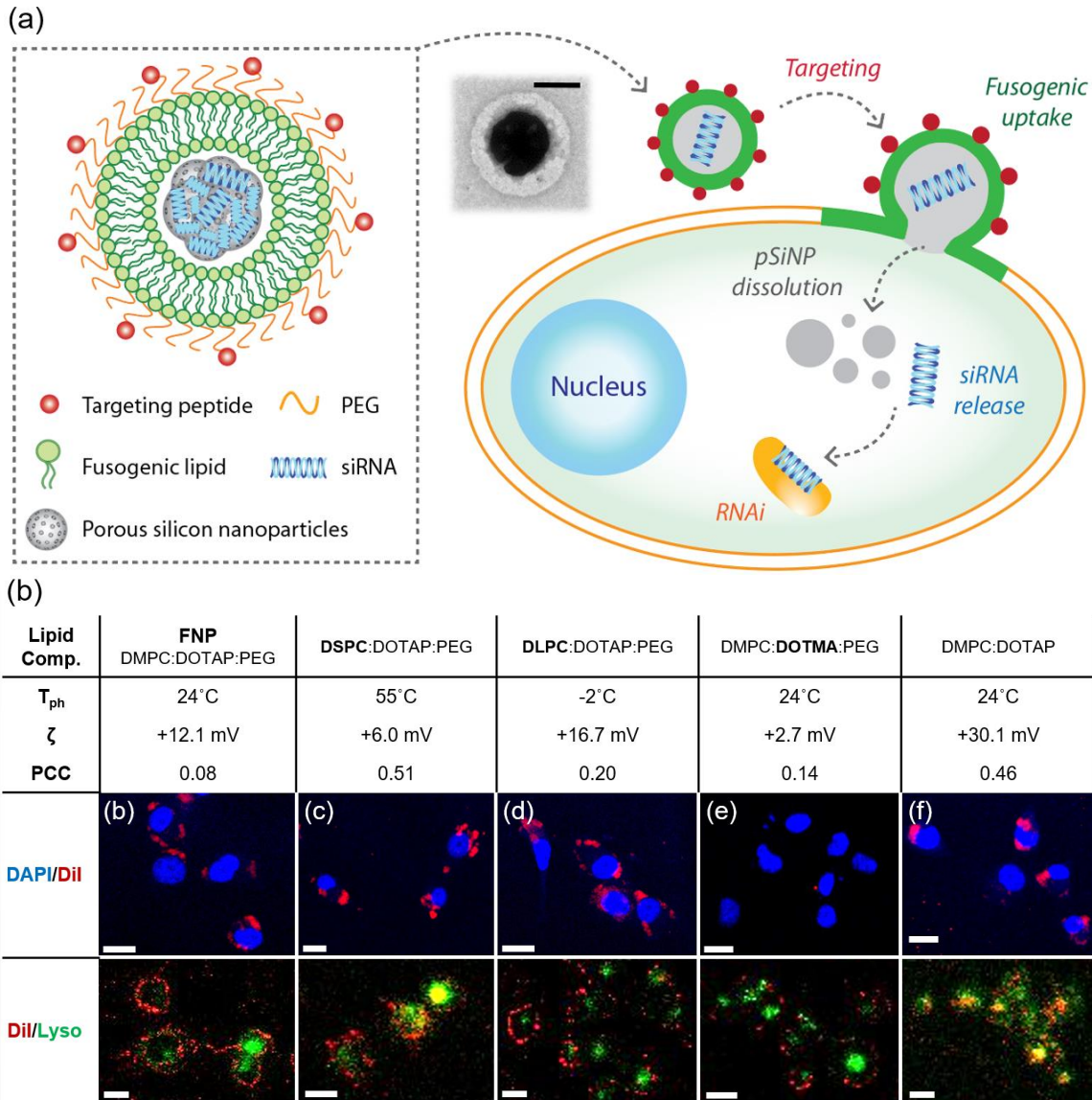
Figure 3.1. Fusogenic nanoparticles (FNPs) are able to deliver payloads directly into the cytoplasm by fusion with the cellular plasma membrane.
(a) Schematic of FNP structure and hypothesized uptake pathway in cells. pSiNP stands for porous silicon nanoparticles, siRNA represents a double stranded RNA construct, RNAi stands for ribonucleic acid interference, and PEG is a polyethylene glycol oligomer. Inset shows transmission electron microscope image of FNPs with 2% uranyl acetate negative staining. Scale bar represents 100 nm; **(b-f)** confocal microscope images showing the effect of replacing various lipid constituents on the ability of the nano-constructs to infiltrate CAOV-3 cells: **(b)** FNPs, the optimized lipid formulation used in this study; **(c)** DMPC replaced with DSPC; **(d)** DMPC replaced with DLPC; **(e)** DOTAP replaced with DOTMA; and **(f)** elimination of DSPE-PEG. For these experiments no targeting peptide was used; instead, the terminus of the PEGylated lipid component was methoxy (mPEG) rather than a peptide. All formulations contained the DiI membrane dye in the lipid coat, and cells were stained with either DAPI nuclear stain or the LysoTracker Green lysosomal compartment stain ("Lyso"). Scale bar represents 10 µm.
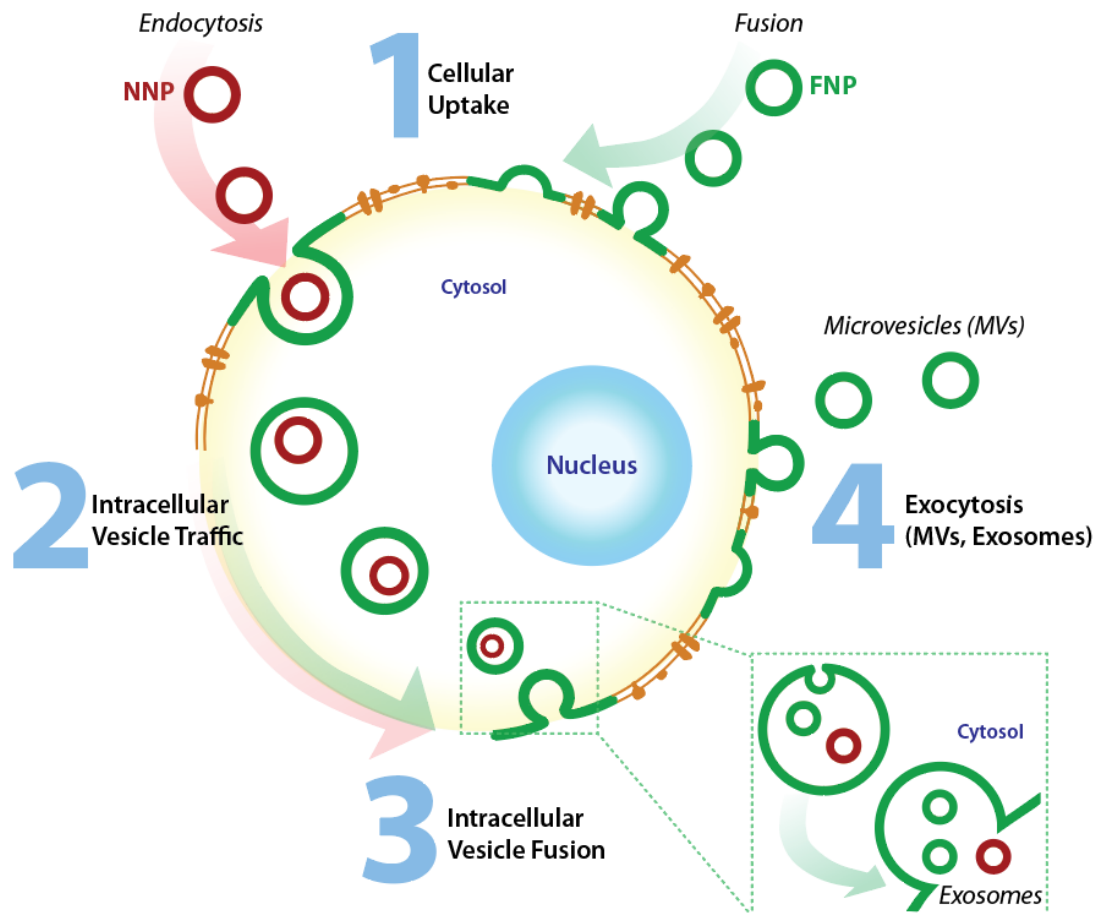
Target gene	Pathway	Fusion (Y/N)	Uptake
Cltc	Uptake	Y	Normal
Cav1	Uptake	Y	Normal
Rac1	Uptake	Y	Normal
Rab5a	Vesicle traffic	Y	Reduced
Rab11	Vesicle traffic	Y	Reduced
Stx6	Vesicle fusion	N	Reduced
T-snare	Vesicle fusion	N	Reduced
Rab27b	Vesicle fusion	N	Reduced
Inhibitor	**Pathway**	**Transfer**	
Bisindolymaleimide I	Exocytosis	Reduced	
GW4869	Exocytosis	Normal	
Rab27b	Exocytosis	Reduced	

Figure 3.2. Schematic showing the summary of cellular pathways and markers, and their influence on uptake of FNPs.

For each pathway 1-4, the relevant genes that were inhibited are listed in red, as well as in the table. The resulting effect the marker downregulation had on the FNPs is listed as Y (fusogenic uptake) or N (endocytic uptake), and the extent of the effect is listed in the Uptake column. Thus in Pathway 1 (Endocytosis), when expression of the endocytosis marker "Clathrin (cltc)" was inhibited, the FNPs were still observed to fuse ("Y"), and the cellular uptake was the same as for control cells where clathrin expression was not inhibited ("Normal"). The Transfer column indicates the extent of dye uptake in the cells of the lower chamber in a transwell system, when the exocytosis from cells in the upper chamber was inhibited.
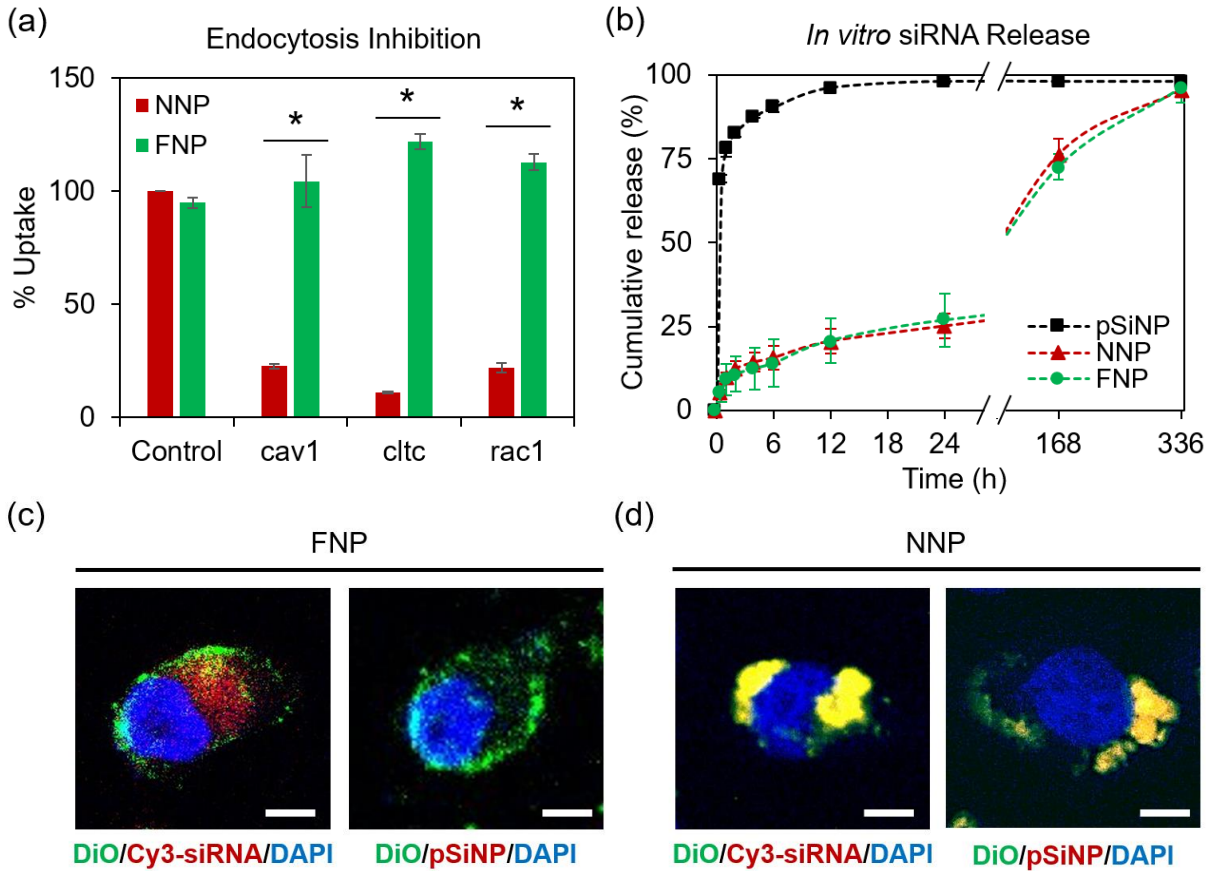
Figure 3.3. Lipid coating of FNPs protect siRNAs from leakage, and allow for cytosolic release upon fusion and pSiNP degradation.
(a) Uptake quantification of DiI-loaded FNPs and NNPs administered to CAOV-3 cells that were depleted of major markers of endocytosis (*cav1, cltc, rac1*); **(b)** *in vitro* cumulative release over time of siPI3Kγ from pSiNPs (porous silicon nanoparticles loaded with siPI3Kγ without lipid coating), NNPs (non-fusogenic nanoparticles loaded with siPI3Kγ), and FNPs (fusogenic nanoparticles loaded with siPI3Kγ). Cumulative release measured by siRNA absorbance measured in the supernatant after centrifugal separation of nanoparticles. Error bars represent n=6; **(c)** confocal microscope images of CAOV-3 cells treated with FNPs. Left panel shows cells treated with FNPs loaded with lipophilic DiO (green) in the lipid shell and cy3-siIRF5 (red) in the porous silicon core. Right panel shows cells treated with FNPs loaded with lipophilic DiO (green) and (non-labeled) siIRF5-loaded porous silicon core (red indicates intrinsic photoluminescence from the Si core); **(d)** confocal microscope images of CAOV-3 cells treated with NNPs. Left panel shows cells treated with NNPs loaded with lipophilic DiO (green) in the lipid shell and cy3-siGFP (red) in the porous silicon core, and right panel shows cells treated with NNPs loaded with lipophilic DiO (green) and siGFP-loaded porous silicon core (red indicates intrinsic photoluminescence from the Si core). Error bars represent standard deviation of n=6; Scale bar represents 5 μm.
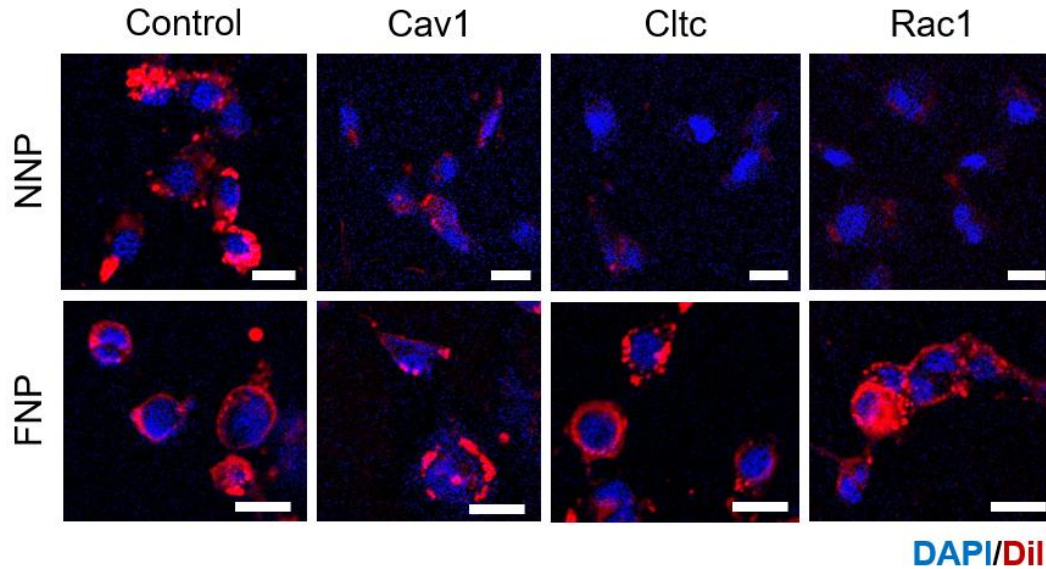
Figure 3.4. Confocal microscope images of CAOV-3 cells that were depleted of major markers of endocytosis (*cav1, cltc, rac1*)

Post depletion, cells were treated with DiI-loaded FNPs and NNPs. FNPs are full fusogenic nanoparticles, consisting of porous Si nanoparticles loaded with an irrelevant siRNA via calcium silicate chemistry and coated with the fusogenic lipid (DMPC:DSPE-PEG:DOTAP, molar ratio 76.2:3.8:20). The PEGylated lipid component contained a methoxy terminus rather than a specific targeting peptide. NNPs are non-fusogenic nanoparticles, prepared identically to the FNPs except using a "conventional" lipid formula of DMPC and DSPE-PEG in the mole ratio 96.2:3.8. Cells were stained with DAPI nuclear stain. Scale bar represents 10 µm.
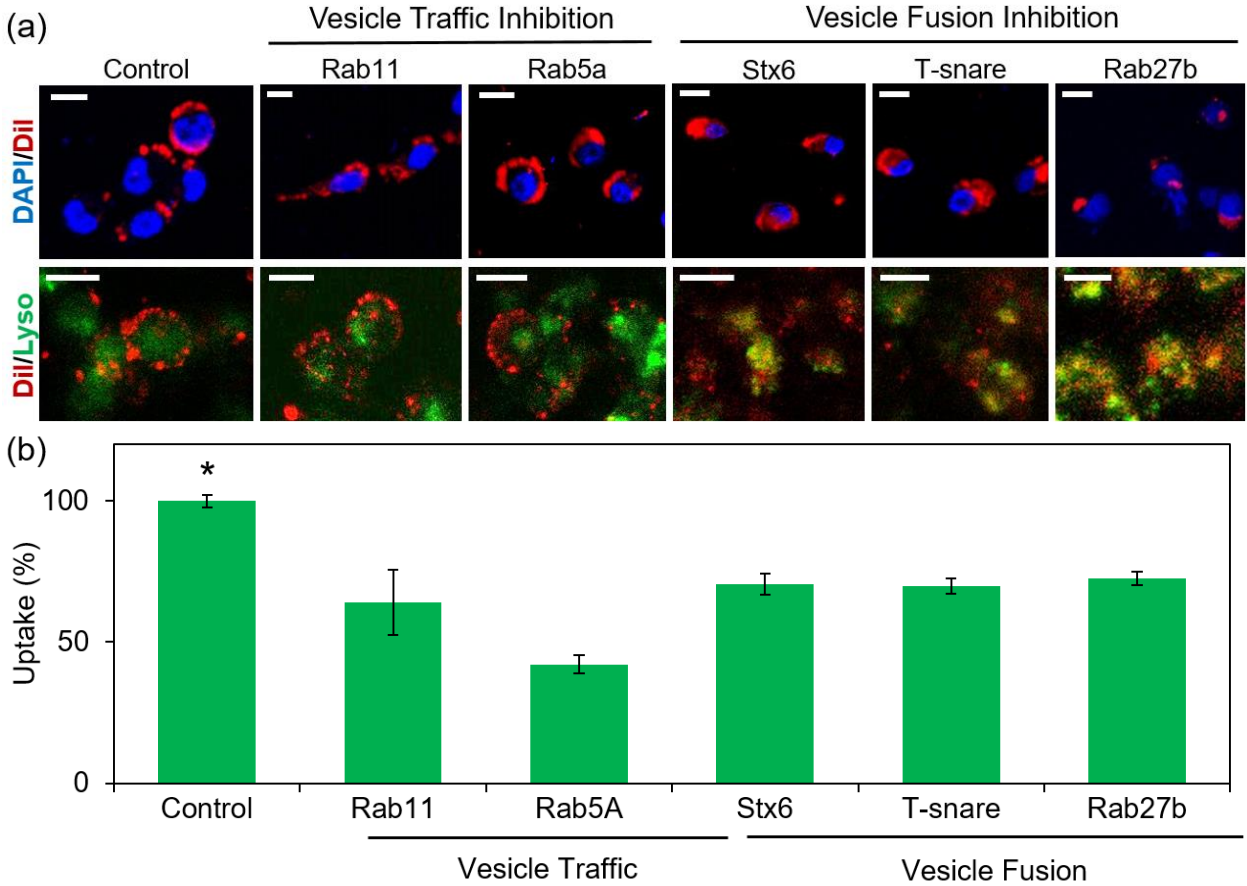
Figure 3.5. CAOV-3 cells that were depleted of major markers of vesicle traffic markers (*rab11, rab5a*) or vesicle fusion markers (*stx6, t-snare, rab27b*).
(a) Confocal microscope images of CAOV-3 cells depleted of vesicle traffic markers (*rab11, rab5a*) or vesicle fusion markers (*stx6, t-snare, rab27b*). Cells were treated with DiI-loaded FNPs and stained with either DAPI nuclear stain (top row) or the LysoTracker Green lysosomal compartment stain (bottom row). Scale bar represents 10 μm; (b) Image J quantification of DiI fluorescence signal found in CAOV-3 cells that were treated with DiI-loaded FNPs. The cells were depleted of vesicle traffic markers (*rab11, rab5a*) or vesicle fusion markers (*stx6, t-snare, rab27b*) prior to particle treatment. Bars represent standard deviation with n=6. * represents significant difference of $p < 0.05$ based on One-way ANOVA with Tukey's HSD test.
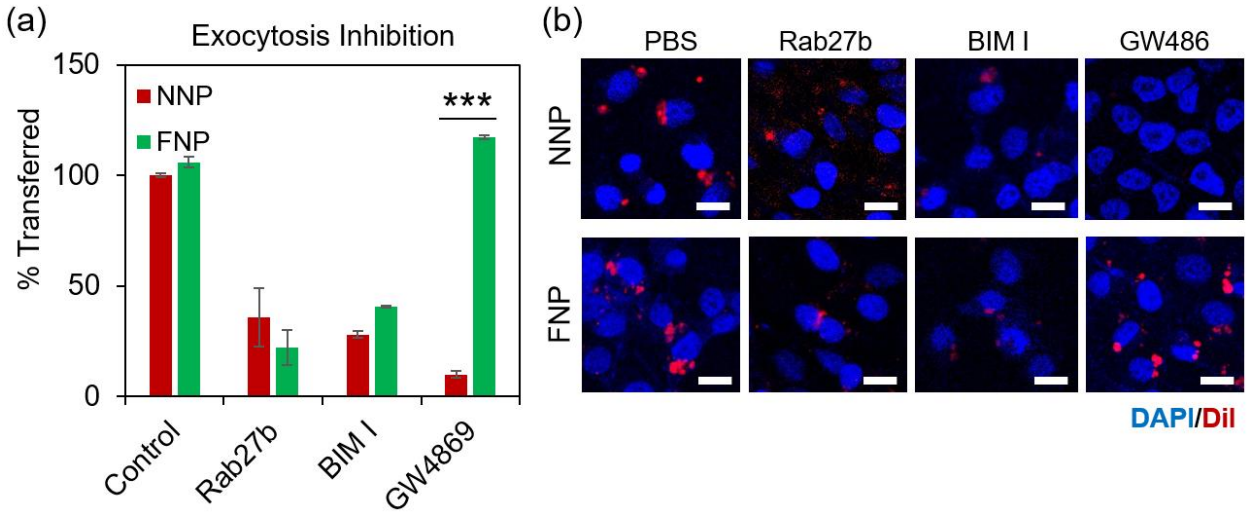
Figure 3.6. Analysis of particle intercellular transfer by exocytosis.
(a) Quantification of transfer of the DiI signal into the lower chamber of a transwell system from the upper chamber containing CAOV-3 cells. Exocytosis was inhibited in the cells in the upper chamber by depletion of *rab27b* or by treatment with bisindolylmaleimide I (BIM I) or with GW4869. Bars represent standard deviation with n=10. *** represents paired t-test with p<0.05; (b) Confocal microscopic images of CAOV-3 cells in the lower chamber of transwell system. Exocytosis was inhibited in the upper chamber cells by depletion of *rab27b* or treatment of bisindolymaleimide I (BIM I) or GW4869. The upper chamber cells were then treated with DiI-loaded NNPs (top row) or FNPs (bottom row). Red DiI signals represent transfer of the dye delivered in the upper chamber to the lower chamber through exocytosis. Cells were stained with DAPI nuclear stain. Scale bar represents 10 μm.
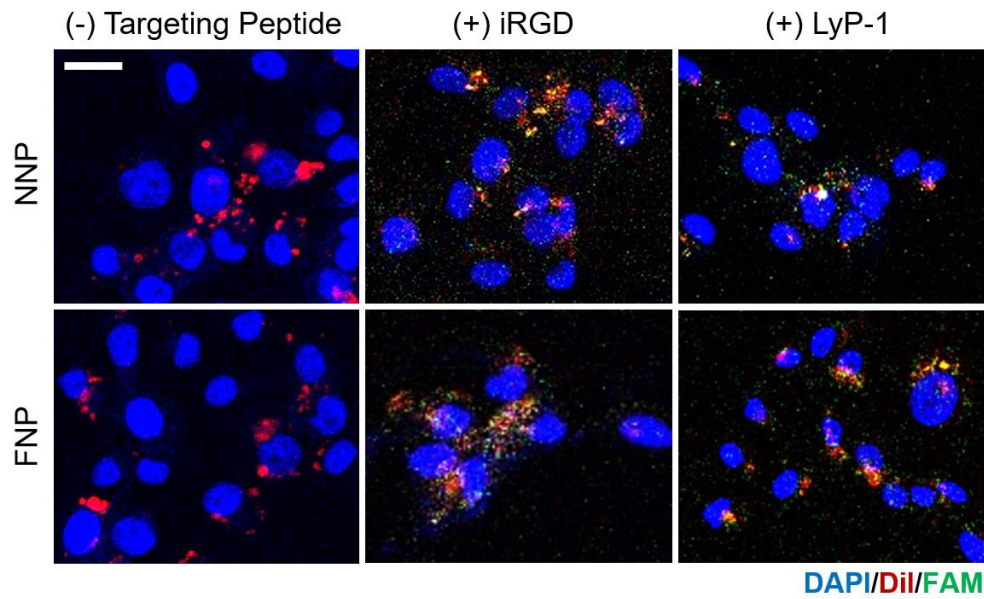
Figure 3.7. Confocal microscopic images of CAOV-3 cells (left and center columns) and J774a.1 macrophage cells (right column) in the lower chamber of transwell system.
The upper chamber cells were treated with DiI-loaded NNPs (top row) or FNPs (bottom row) that were conjugated with FAM-tagged iRGD or LyP-1 targeting peptides. Red DiI and green FAM signals represent transfer of the dyes delivered in the upper chamber to the lower chamber through exocytosis. Cells were stained with DAPI nuclear stain. Scale bar represents 10 μm.

Table 3.1. Hydrodynamic diameter and zeta potential of the particle formulations measured by dynamic light scattering (DLS).
Data is representative of n=8. pSiNP represents the nanoparticle consisting of a porous silicon nanoparticle framework that was then loaded with the siRNA payload through the agency of calcium ion-silicate precipitation. The resulting pSiNP consisted of a porous silicon framework with a silicon oxide skin, and the siRNA (approximately 10% by mass) was resident in the pores along with a calcium silicate binder. The synthesis of this particle is described in the methods section. FNP represents the above pSiNP nanoparticles coated with the fusogenic lipid, but with no targeting peptide attached to the PEGylated lipid component of the lipid (PEGylated lipid in the FNP construct contained a methoxy group on the distal end of the PEG). The fusogenic lipid composition is given in Table 3. The T-FNP and C-FNP constructs contained iRGD or Lyp-1 peptides, respectively, grafted to the distal end of the PEG *via* maleimide coupling chemistry.

Particle	Size (nm)	Zeta-potential (mV)
pSiNP	57.9 ± 14.3	-23.2 ± 3.7
FNP	171.9 ± 12.3	9.1 ± 0.8
T-FNP	207.9 ±18.7	-3.6 ± 1.2
C-FNP	208.5 ± 17.1	-1.7 ± 0.6

Table 3.2. Composition of nanoparticles and hypothesized roles of lipid components.
Composition of the fusogenic and non-fusogenic nanoparticles in terms of molar ratio. Hypothesized role of each lipid and the alternative lipid used as a replacement in the mechanistic studies is indicated.

Lipid Composition (Molar Ratio)			
	DMPC	**DOTAP**	**DSPE-PEG**
Fusogenic	76.2	20	3.8
Non-fusogenic	96.2	0	3.8
Hypothesized Role	• Low phase transition temperature (T_{ph}= 24°C) • Allows for liquid crystal phase in physiological conditions	• Cationic lipid for attraction to plasma membrane	• For dispersion and stealth • Hypothesized to act as a bridge linker akin to v-SNARE
Alternative Lipid	• DSPC (T_{ph}= 55°C) • DLPC (T_{ph}= -2°C)	• DOTMA	• No PEG

Chapter three, in full, has been submitted for publication of the material as it may appear in **Kim, B.**, Varner, J.A., Howell, S.B., Ruoslahti, E., Sailor, M.J. Securing the Payload, Finding the Cell, Avoiding the Endosome: Peptide-Targeted, Fusogenic Porous Silicon Nanoparticles for More Effective Delivery of siRNA Therapies. *Adv Mater.* Submitted. The author of this dissertation was the primary author of the material.

Chapter 4:

Fusogenic Porous Silicon Nanoparticles for Combination Therapy in

Peritoneal Carcinomatosis of Ovarian Cancer

4.1   Abstract

Despite the promise of RNAi therapeutics, the delivery of oligonucleotides selectively to diseased tissues in the body, and specifically to the cellular location in the tissues needed to provide optimal therapeutic outcome, remains a significant challenge. Here we identify key material properties and biological mechanisms for delivery of siRNAs to effectively silence target-specific cells in vivo. Using porous silicon nanoparticles as the siRNA host, tumor-targeting peptides for selective tissue homing, and fusogenic lipid coatings to induce fusion with the plasma membrane, we show that the uptake mechanism can be engineered to be independent of common receptor-mediated endocytosis pathways. We provide two examples demonstrating the potential broad clinical applicability of this concept in a mouse model of peritoneal carcinomatosis of ovarian cancer: silencing of cancer chemoresistance by inhibition of the Rev3l subunit of the DNA repair polymerase Pol ζ; and suppressing cancer immunity by reprogramming tumor-associated macrophages into a pro-inflammatory state.

4.2   Introduction

Of the ~100 FDA-approved anticancer drugs,[1] about 40% are cytotoxic agents and 60% are inhibitors of oncogenic pathways.[1] As the discovery of key oncogenic markers and pathways has progressed, siRNAs have emerged as a promising class of drugs to transiently silence oncogenic mutations. Despite the tremendous worldwide effort expended in the development of siRNA-based therapeutics over more than 15 years, substantial challenges have limited their clinical translation. The first siRNA-based drug was approved only in the last year, and that only for treatment of a rare hereditary disease[2]; there is currently no approved cancer therapeutic based on siRNA. A primary obstacle in this endeavor has been the lack of

delivery vehicles that can overcome *in vivo* clearance and cellular degradation via endocytosis[3-5].

One of the early proposed solutions to the problem of endocytosis and subsequent lysosomal degradation of siRNA was delivery *via* fusogenic liposomes[6]. Fusogenic liposomes directly fuse with the cell membrane, bypassing endocytotic uptake pathways[7,8]. While they have shown promise as delivery vehicles for RNAi therapeutics[9], liposomes suffer from a generally low capacity for nucleic acid therapeutics[10] and leakage of their payloads either in storage or *in vivo*[11]. We recently demonstrated a delivery system that harnessed a fusogenic lipid, which employed a solid porous silicon nanoparticle (pSiNP) core. The system capitalized on the relatively high loading of siRNA[12] into pSiNPs that can be accomplished via a calcium ion precipitation strategy[13], which stabilized the siRNA payload and minimized leakage. When grafted with the appropriate homing peptide, the fusogenic nanoparticles (FNPs) showed a strong *in vivo* gene silencing effect specific to macrophages[10]. While it showed good efficacy against a *S. aureus* lung infection model, the mechanism of cellular penetration and trafficking was not established, and the applicability of this approach to other cell types and diseases remained unclear. Here, we evaluate the mechanism of action of the FNPs, and conclude that it is generalizable to other cell types, provided the targeting peptide is sufficiently specific. We then validate its clinical applicability as a platform technology by demonstrating two separate siRNA therapeutics against peritoneal carcinomatosis of ovarian cancer, intercepting two very different oncogenic pathways: (1) a cancer cell-targeting fusogenic nanoparticle (C-FNP) that sensitizes cells to platinum (Pt)-based chemotherapy by suppressing their DNA repair machinery; and (2) a tumor-associated macrophage (TAM)-targeting fusogenic nanoparticle (T-FNP) that reprograms the immune system to enhance T-cell infiltration and downregulate immunosuppression.

4.3   Materials and Methods

Materials. Highly boron-doped p-type silicon wafers ($\sim$1 mΩ-cm resistivity, polished on the (100) face) were obtained from Virginia Semiconductor, Inc or Siltronix, Inc. Hydrofluoric acid (48% aqueous, ACS grade) was obtained from Fisher Scientific. Anhydrous calcium chloride was obtained from Spectrum Chemicals (Gardena, CA). Deionized (18 mΩ) water was used for all aqueous dilutions. For lipids, 1,2-dimyristoyl-sn-glycero-3-phosphocholine (DMPC), 1,2-distearoyl-sn-glycero-3-phosphoethanolamine-N-[methoxy(polyethylene glycol)-2000], (DSPE-mPEG), 1,2-distearoyl-sn-glycero-3-phosphoethanolamine-N-[maleimide(polyethylene glycol)-2000] (DSPE-PEG-maleimide), and 1,2-dioleoyl-3-trimethylammonium-propane (DOTAP) were purchased from Avanti Polar Lipids (Alabaster, AL) and stored at -4°C. The fluorescent lipophilic dyes 1,1'-dioctadecyl-3,3,3',3'-tetramethylindocarbocyanine perchlorate (DiI) was obtained from Life Technologies, and Lipofectamine® 2000 transfection reagent was obtained from Thermo Fisher Scientific. Custom siRNA against luciferase (siLuc) was purchased from Dharmacon (Lafayette, CO), and primers were purchased from IDT DNA (San Diego, CA). Silencer ® Pre-designed siRNA encoding for PI3Kγ (siPI3Kγ; sequence: GGACCACGAGAGUGUGUUCtt) was purchased from Life Technologies, and siGENOME Human REV3L siRNA (siREV3L; sequence: CUGCAGAGAGAAUAACCCUGAdTdT) was purchased from Dharmacon. Targeting peptides (LyP-1 and iRGD) were custom synthesized by CTC Scientific (Sunnyvale, CA). For *in vitro* studies, J774a.1 cells were purchased from ATCC (Manassas, VA) within 6 months prior to all experiments. DMEM cell media was purchased from GE Healthcare Life Sciences (HyClone, Pittsburg, PA), with supplemental fetal bovine serum (HyClone, Pittsburg, PA) and penicillin/streptomycin (HyClone, Pittsburg, PA). The Cell counting kit-8 (CCK-8) was purchased from Dojindo Molecular Technologies, Inc. (Rockville, MD). Corning Matrigel Membrane Matrix was purchased from Fisher Scientific. Six week-old female athymic nu/nu mice were purchased from Envigo (Placentia, CA).

Preparation of porous silicon nanoparticles. Porous silicon (pSi) samples were prepared by electrochemical etching of silicon wafers in an electrolyte consisting of 3:1 (v:v) of 48% aqueous HF:ethanol (CAUTION: HF is highly toxic and proper care should be exerted to avoid contact with skin or lungs). A silicon working electrode with an exposed area of 8.6 cm^2 was contacted on the back side with aluminum foil and mounted in a Teflon cell. The silicon wafer was then anodized in a two-electrode configuration with a platinum counter electrode, by applying an alternating current of square waveform, with lower current density of 50 mA/cm^2 for 0.6s and high current density of 400 mA/cm^2 for 0.36s, repeated for 500 cycles. The resulting porous layer was lifted off by application of a constant current density of 3.7 mA/cm^2 for 250s in a 1:20 (v:v) of 48% aqueous HF:ethanol solution. The porous layer (0.8 mg) was immersed in RNAse-free water (2 mL) and subjected to ultrasonic fracture (50T ultrasonic bath, VWR International) for 12h to generate the porous silicon (pSi) nanoparticles. Fluorescent dye and siRNA payloads were loaded into the pSi nanoparticles by calcium ion-induced precipitation of calcium silicate as described previously.[1] The oligonucleotide payload was hydrated in RNAse-free water to generate a 20 µM solution. 150 µL of siRNA was pipetted gently into a solution prepared from 150 µL of the pSiNP dispersion and 700 µL of 2M calcium chloride and the mixture was subjected to ultrasonication for 15 min. We used siREV3L (GAG AGU ACC UCC AGA UUU A), siPI3Kg (GGA CCA CGA GAG UGU GUU Ctt) and siLuc (CUU ACG CUG AGU ACU UCG A) for all relevant experiments.

Fusogenic coating. Fusogenic (FNP) and non-fusogenic (NNP) coatings were prepared from DMPC, DSPE-PEG, and DOTAP at molar ratios of 76.2:3.8:20 and 96.2:3.8:20, respectively. The lipid films were prepared by evaporating the organic solvent, with 725.5 µg of DMPC, 151.6 µg of DSPE-PEG (methoxy or maleimide terminated), and 196.3 µg of DOTAP (fusogenic coating, F, used to prepare fusogenic nanoparticles, or FNPs) or 916.0 µg of DMPC and 151.6 µg of DSPE-PEG (methoxy or maleimide terminated) (non-fusogenic coating, NF,

used to prepare non-fusogenic nanoparticles, or NNPs). To incorporate lipophilic DiI into the films, we added 26.3 µg of DiI (1.25 mg/ml in 100% ethanol) to the preparation. The films were then hydrated with the payload-containing pSiNP solution and prepared by film hydration/extrusion: the pSi-hydrated lipid was heated to 40ºC with constant magnetic stirring for 20 min. Then the mixture was extruded through a 200 nm polycarbonate membrane 20 times. Targeting peptides (iRGD and LyP-1) was conjugated to maleimide-terminated PEG by mixing 100 µL of 1 mg/mL of the peptide (in deionized water) in 1 mL of 1 mg/mL (by lipid mass) of the liposomal pSi construct overnight at 4ºC. Particles were washed three times at each step by centrifugation in a Microcon-30kDa Centrifugal Filter Unit (EMD Millipore) by spinning at 5,000g at 25ºC. The loaded siRNA concentration was quantified by NanoDrop 2000 spectrophotometer (Thermo Fisher Scientific, ND-2000).

Cell culture. CAOV-3 human ovarian adenocarcinoma and J774a.1 murine macrophage lines were cultured in DMEM supplemented with 10% FBS and 1% penicillin/streptomycin, and were incubated at 37ºC in 5% CO_2.

Confocal microscopy. All confocal microscopy images are representative of at least three independent trials and of at least 1×10^6 cells per slide. Fusion of DiI-loaded or siRNA-loaded particles was observed by seeding 0.3×10^6 cells on top of 22 mm round coverslips (BD Biocoat Collagen Coverslip, 22 mm) in a 6-well plate, growing to 80% confluence, and treating the cells with 10 µL of nanoparticles. The particle-treated CAOV-3 cells were incubated at 37℃ in 5% CO_2 for 15 min, whereas the particle-treated J774a.1 cells were incubated for 5 min. After incubation, the cells were washed in PBS three times to remove any particles that were not taken up. The cells were fixed in 1% paraformaldehyde (PFA, Santa Cruz Biotechnology) for 10 min at 4˚C, then washed with PBS three times. The coverslips were mounted on glass slides with ProLong® Diamond Antifade Mountant with DAPI (Life Technologies), dried and kept in the dark until examined by confocal microscopy (Zeiss LSM 710 NLO).

***In vitro* siRNA silencing.** *In vitro* knockdown efficiencies of the nanoformulations were quantified using two-step quantitative real-time reverse transcription polymerase chain reaction (qRT-PCR, Roche LightCycler 96).

For the dose-response of the siRNA against *Rev3l* (siREV3L), we seeded 0.25 x 10^6 CAOV-3 cells per well in a 24 well-plate. At 50% confluence, we treated the cells at 0, 0.5, 2.5, 5, 12.5, 25, 50, and 100 nM siREV3L doses of Lipofectamine, fusogenic nanoparticles (FNPs) and non-fusogenic nanoparticle (NNPs). While the Lipofectamine formulations were incubated for 4h, the FNPs and NNPs were treated for 1h, then washed with PBS three times. The wells were replaced with fresh DMEM supplemented with 10% FBS and 1% penicillin/streptomycin, and further incubated for 48h. Post-incubation, the cell media was removed, and RNA was purified using the QIAshredder and RNeasy Mini Kit (Qiagen, Valencia, Ca). cDNA was transcribed from the purified RNA using the BIORAD iScript cDNA Synthesis Kit and heat-treated in the Eppendorf Vapo.protect Mastercycler thermal cycler. cDNA was mixed with REV3L primers, or the control HPRT primers (REV3L forward: AGGACTCGAAGTCACCTATGC; REV3L reverse: AGAGGTAACCCCAGGAATGC; HPRT forward: GTCAACGGGGGACATAAAAG; HPRT reverse: CAACAATCAAGACATT-CTTTCCA) and iQ SYBR Green Supermix according to the manufacturer's instructions. RT-PCR analysis was performed in BIORAD 96-well white Multiplate PCR Plates using the Roche LightCycler 96. The quantification was performed at n=8 and in RNAse- and DNAse-free laminar flow hood dedicated to RNA work.

For quantification of *in vitro* knockdown efficiency of siRNA against PI3Kγ (siPI3Kγ), we seeded 0.25 x 10^6 J774a.1 cells per well in a 24-well plate. At 50% confluence, we treated the cells at 50 and 100 nM siPI3Kγ doses of Lipofectamine, fusogenic nanoparticles (FNPs) and non-fusogenic nanoparticle (NNPs). The transfection and qRT-PCR protocol were identical to

the dose-response study described above, with primers for PI3Kγ (PI3Kγ forward: GGCTCAAAGAAAAATCCCCTA; PI3Kγ reverse: AGCCTGCACAGGAATAAACAA).

Cell viability assay. Cell viability was determined by seeding 96 well-plates with 0.01 x 10^6 CAOV-3 or J774a.1 cells per well. At 50% confluence, we treated each well at the 50 nM siRNA dose of Lipofectamine (0.25 µL per well), FNPs, FNPs loaded with siLuc, NFPs, or PBS as the control group. The formulations were incubated for 1h (4h for Lipofectamine group) at 37ºC in 5% CO_2, then washed with PBS three times and further incubated for 48h. The CCK-8 cytotoxicity assay was performed according to manufacturer's instructions. In brief, the CAOV-3 cells were treated with 10 µL of the CCK-8 solution per well, and incubated for 2h. The absorbance at 450 nm was measured using the UV-Vis microplate reader for quantification of cell viability. The cell viability was averaged over 10 wells per group, and normalized to the viability of the PBS control treatment group. Single-way ANOVA was used with α-level of 0.01 to determine significant differences between the formulations.

For the *in vitro* cDDP-siREV3L interaction study, we seeded a 96 well-plate with 0.01 x 10^6 CAOV-3 cells per well. At 50% confluence, we treated each well at the 50 nM siRNA dose of Lipofectamine (0.25 µL per well), FNPs, FNPs loaded with siLuc, NFPs, or PBS as the control group. The formulations were incubated for 1h (4h for Lipofectamine group) at 37ºC in 5% CO_2, then washed with PBS three times and further incubated for 48h. Post-transfection, the media was removed, and the cells were treated with increasing doses of cDDP (0, 0.01, 0.1, 1, 10, 25, 50, and 100 µg/mL in PBS) per treatment group. The cells were incubated with cDDP for 24h at 37ºC in 5% CO_2, then washed with PBS three times. The CCK-8 cytotoxicity was assay was used as described above to quantify the cell viability of each treatment group at the treated cDDP doses. Cell viability for the 0 µg/mL cDDP treatment in the PBS control group was used as the normalization control, and each result was averaged over 10 independent trials. The IC_{50} of each treatment was extrapolated from the results.

Mouse Model. Ovarian cancer xenografts were established in athymic nude mice (6-8 week old, female) by subcutaneously injecting 5×10^6 CAOV-3 cells in PBS and Matrigel media mixed at 1:1 ratio. For the peritoneal carcinomatosis model, we performed intraperitoneal injection of 3×10^6 CAOV-3 cells in PBS. All animals for the *in vivo* studies were handled, anesthetized, and euthanized according to the Institutional Animal Care and Use Committee (IACUC) guidelines. All animal experiments were performed independent of each other with different cohorts of mice.

Statistics. All statistical analyses were performed using single way ANOVA and post hoc comparisons using Tukey's HSD test at $p < 0.05$, unless otherwise stated. Power analysis was performed to estimate the total mouse sample size required for the tumor growth and survival studies using the GPower 3.1 software. The analysis was performed using *a priori*, ANOVA: repeated measures, between factors, as the study looks at tumor growth by each therapeutic formulation over time. Based on a published study[2] (N=32), where the fusogenic nanoparticles were intravenously injected for siRNA knockdown in Balb/C mice with bacterial infection, the effect size (ES) was calculated to be 11.5, thus set to 'large' (0.40) in the software's parameter settings. With α error probability of 0.05 and Power of 0.80, 5 test groups, 15 measurements (for tumor size), and correlation of 0.3, we determined that a sample size of 35 mice was adequate for the experiments investigating the therapeutic efficacy of the formulations.

Biosafety of fusogenic nanoparticles. For *in vivo* biosafety evaluation, healthy athymic nu/nu mice were intravenously injected with T-FNP or C-FNP at 100 µmol/kg lipid, corresponding to 62.5 µg/kg siRNA, and 641 µg/kg pSi in 100 µL PBS. After 24h circulation, the mice were sacrificed under deep isofluorane anesthesia (no response to toe pinch) by cardiac perfusion, and brain, heart, lungs, liver, kidneys, and spleen were harvested. Organs were fixed immediately in 4% PFA, and sent to the University of California, San Diego (UCSD)'s histology

130

core to be paraffinized and sectioned for hematoxylin and eosin (H&E) staining. The stained slides were histopathologically evaluated by Dr. Kent Osborn (Associate Director, Animal Care Program, UCSD).

Nanoparticle biodistribution. After establishment of the tumor mouse model, the tumor nodules were allowed to grow for 3 weeks. The mice were then IP injected with PBS, FNP, T-FNP, or C-FNP formulations loaded with DiI at 100 μmol/kg lipid corresponding to 641 μg/kg pSi in 100 μL PBS. After 1h or 24h, the mice were sacrificed by perfusion, and the major organs (heart, lungs, liver, spleen, kidneys) and the tumor nodules were harvested and immediately fixed in 4% PFA. The organs were imaged for DiI fluorescence using an IVIS 200 imaging system (Perkin-Elmer) with 0.1s exposure time and excitation/emission filters set at 500/520 nm. The DiI accumulation was quantified based on five mouse images per formulation and time group using Image J analysis. The quantified uptake was statistically analyzed using one-way ANOVA with Tukey's post hoc analysis. The same experiment was performed with xenograft mice by intravenous injection of the particles.

Flow Cytometry. After establishment of the mouse tumor model, the tumor nodules were allowed to grow for 3 weeks. The mice were then IP injected with PBS, FNP, T-FNP, C-FNP, or a 50:50 cocktail mix of T-FNP and C-FNP formulations loaded with DiI (peptides were tagged with FAM) at 100 μmol/kg lipid corresponding to 641 μg/kg pSi in 100 μL PBS. After 24h, the mice were sacrificed for macrophage and tumor collection. First, we performed intraperitoneal lavage using 3-5 mL of 4% PFA in a 20G syringe. After aspirating cells from the peritoneal cavity, we opened up the cavity for tumor nodule collection. We then homogenized the tumor nodules for further cell separation. Both the lavage and tumor homogenates were treated with Dead Cell Removal MicroBeads (Miltenyi Biotec) for magnetic separation on an LS column according to the manufacturer's instructions. The collected cells were then treated with Anti-F4/80 microbeads (Miltenyi Biotec) for magnetic separation on an LS column according to

the manufacturer's instructions to collect only the macrophages. The macrophages from the lavage and tumor homogenates, as well as the tumor cells were run through a LSRFortessa flow cytometer (BD Biosciences) to analyze the number of cells containing either the particles' DiI signals (ex: 561 nm/50 mW; em: 582/15 nm) or the peptides' FAM signals (ex: 488 nm/50 mW; em: 510/25 nm). The results were analyzed and presented using FlowJo v10 software (FlowJo, LLC).

In vivo **siRNA silencing.** After establishment of the mouse tumor model, the tumor nodules were allowed to grow for 3 weeks. The mice were then IP injected with PBS, T-FNP or C-FNP at 100 µmol/kg lipid, corresponding to 62.5 µg/kg siRNA, and 641 µg/kg pSi in 100 µL PBS. After 48h, the mice were sacrificed for macrophage and tumor collection. First, we performed intraperitoneal lavage using 3-5 mL of 4% PFA in a 20G syringe. After aspirating cells from the peritoneal cavity, we opened up the cavity for tumor nodule collection. We then homogenized the tumor nodules for further cell separation. Both the lavage and tumor homogenates were treated with Dead Cell Removal MicroBeads (Miltenyi Biotec) for magnetic separation on an LS column according to the manufacturer's instructions. The collected cells were then treated with Anti-F4/80 microbeads (Miltenyi Biotec) for magnetic separation on an LS column according to the manufacturer's instructions to collect only the macrophages. The macrophages from the lavage and tumor homogenates, as well as the tumor cells were collected by centrifugation post-magnetic separation by centrifugation at 300g for 5 min at 4°C.

The degree of knockdown of *Pi3kγ* in the macrophages and of *Rev3l* in the tumor cells was quantified using two-step qRT-PCR (Roche LightCycler 96). The cells were lysed for RNA purification using QIAshredder and RNeasy Mini Kit (Qiagen, Valencia, Ca). cDNA was transcribed from the purified RNA using the BIORAD iScript cDNA Synthesis Kit and heat-treated in the Eppendorf Vapo.protect Mastercycler thermal cycler. cDNA was mixed with PI3Kγ primers for macrophages and REV3L primers for the tumor cells, with HPRT primers as control

for both cells (PI3Kγ forward: GGCTCAAAGAAAAATCCCCTA; PI3Kγ reverse:

AGCCTGCACAGGAATAAACAA; REV3L forward: TGAGTTCAAATTTGGCTGTACCT; REV3L

reverse: TCTAGTCTTCAAAATTTCTTCAAGCA; HPRT forward:

GTCAACGGGGGACATAAAAG; HPRT reverse: CAACAATCAAGACATTCTTTCCA) and iQ

SYBR Green Supermix according to the manufacturer's instructions. qRT-PCR analysis was

performed in BIORAD 96-well white Multiplate PCR Plates using the Roche LightCycler 96. The

quantification was performed at n=6 and in a RNAse- and DNAse-free laminar flow hood

dedicated to RNA work. Relative knockdown was statistically evaluated using one-way ANOVA

with Tukey's HSD post-hoc analysis.

In vivo **therapeutic efficacy of fusogenic nanoparticles.** After establishment of the

mouse tumor model, the tumor nodules were allowed to grow for 1 week. The mice were then IP

injected with PBS, cDDP (2 mg/kg), 1:1 cocktail of cDDP (2 mg/kg) with T-FNP, 1:1 cocktail of

cDDP (2 mg/kg) with C-FNP, or a 1:1:1 cocktail of cDDP (2 mg/kg) with T-FNP and C-FNP at

70.2 µmol/kg lipid, corresponding to 36.1 µg/kg siRNA, and 451 µg/kg pSi in 100 µL PBS. The

mice were IP injected with 2 mg/kg of cDDP every 3 days, and the T- and C-FNP formulations

every 7 days. After 30 days, the mice were sacrificed and opened for tumor nodule collection.

The number of tumor nodules were counted and the size of tumor nodules were measured on

the longest dimension using a caliper. The results were analyzed by one-way ANOVA with

Tukey's HSD post-hoc analysis.

4.4   *In vitro* validation of FNPs for therapeutic applications

In order to evaluate whether or not the FNPs offer a generalizable solution for siRNA

therapies, we evaluated two different approaches (**Fig 4.1a**): a chemosensitizing siRNA (C-

FNPs) that inhibits the DNA repair mechanism in cancer cells, and an immunosuppressing

siRNA (T-FNPs) that reprograms tumor-associated macrophages to enhance the immune system's ability to clear these aberrant cells. We selected the first therapeutic (C-FNPs) to sensitize cancer cells to cisplatin, as Pt-resistant or Pt-refractory ovarian cancer is seen in over 70% of patients at advanced stages; chemoresistant tumors cause high morbidity, and has been an unsolved problem for over two decades[40-42]. Cisplatin crosslinks cellular DNA which trigger apoptosis in the absence of adequate DNA repair[43]. Cancer cells that can repair the modified DNA well exhibit chemoresistance[42,44]. While key predictors of Pt-drug response have been identified[42,44], there is no preventative measure against the development of resistance, or reliable strategy to induce chemosensitivity. To this end, we chose to deliver siRNA against *Rev3l* (subunit of DNA repair polymerase, Pol ζ) to disable a component of the DNA repair pathway known to enhance chemosensitivity in the CAOV-3 human ovarian adenocarcinoma[45-48]. For this model we specifically targeted the FNPs to ovarian cancer cells using the iRGD peptide (**Table 1.1**)[49].

The second therapeutic tested (T-FNPs) was designed to reprogram tumor-associated macrophages (TAMs) to inhibit their oncogenic pathways[50-56]. PI3kγ is a key regulator of immunosuppression, and its downregulation has shown benefits in increasing both CD8+ T-cell recruitment to the tumor and sensitivity of immunosuppressive myeloid cells to checkpoint inhibitors[57-60]. In order to target TAMs selectively, we used the LyP-1 peptide (**Table 1.1**), which homes to TAMs and tumor-associated lymphatic vessels[61-64]. The LyP-1-conjugated FNPs were loaded with siRNA against *Pi3kγ*, with the goal of eliciting tumoricidal behavior in TAMs.

First, we verified that FNPs retained their fusogenic nature after conjugation with targeting peptides (**Fig 4.1b**). For both CAOV-3 cancer cells and J774a.1 macrophages, FNPs without targeting peptides successfully fused with the plasma membrane. In CAOV-3 cells treated with iRGD-conjugated, DiI-loaded nanoparticles (C-FNPs), we saw uniform distribution of the DiI signals on the cell plasma membrane indicating successful fusion, and the FAM-

tagged iRGD peptides segregated into the cytoplasm. We saw the same trend in J774a.1 cells when the Lyp-1-conjugated, DiI-loaded nanoparticles (T-FNPs) were used, indicative of successful fusion to this macrophage cell line. The insertion of the iRGD or Lyp-1 targeting peptides into the cytosol of their respectively targeted cells is consistent with the established CendR mechanism[65] where the peptide initially binds to the target receptor to undergo peptide cleavage, then transfers to a secondary receptor to undergo receptor-mediated endocytosis (**Table 1.1**)[63-68]. In some of the cells, co-localization between the DiI and the FAM-LyP-1 peptides on the plasma membrane was observed, suggestive of the intermediate stage prior to migration of the peptide to its secondary receptor. Based on these results, we believe that fusion occurs immediately after the peptide binds to its primary cellular receptor, and that by the time the peptide transfers to its secondary receptor, fusogenic uptake has occurred. This hypothesis is further supported by experiments with non-fusogenic constructs; in that case both C-NNPs and T-NNPs were endocytosed, and their DiI and FAM-peptide signals were strongly co-localized within the cell cytoplasm. Thus, the FNPs retain their ability to fuse with cellular membranes even when a cell-specific targeting peptide is deployed on the exterior of the nanoparticle's lipid membrane.

Next, we determined the efficiency of knockdown of the *Rev3l* gene target in CAOV-3 cancer cells (**Fig 4.1c**) that could be achieved using the cancer cell-targeting iRGD peptide. Both fusogenic and non-fusogenic nanoparticles (C-FNPs and C-NNPs) were compared. We serially diluted the siRNA dose starting from a maximum dose of 100 nM, based on previous work (FNPs attained >95% relative knockdown efficiency in RAW264.7 macrophages at this concentration of siRNA)[10]. The dose-response curve for C-FNPs was similar to that of Lipofectamine (Lf), and over 90% knockdown efficiency was attained with a dose of 50 nM siRNA. In contrast, C-NNPs reached a plateau of only ~50% knockdown efficiency under similar conditions.

We next compared the efficiency of silencing of *Pi3kγ* in J774a.1 cells (**Fig 4.1d**), using the macrophage-targeting LyP-1 peptide on the fusogenic or non-fusogenic nanoparticles (T-FNPs or T-NNPs). Based on the above results from the cancer cell studies, we selected 50 and 100 nM siRNA doses. When the fusogenic T-FNPs were used, both 50 nM and 100 nM doses were able to induce significantly higher knockdown of *Pi3kγ* compared with the non-fusogenic T-NNPs (p <0.01) or with Lipofectamine (p<0.05), based on **One-way ANOVA** ([$F_{(6, 36)}$=113.6, p=1.9x10^{-21}]) and Tukey HSD test. Although J774a.1 is a difficult cell line to transfect[69,70], T-FNPs were able to attain approximately 75% knockdown efficiency at 50 nM of siRNA, and 85% at 100 nM of siRNA.

The chemosensitizing effect of the *Rev3l* siRNA payload was evaluated using the C-FNPs. We pre-transfected the CAOV-3 tumor cells with siREV3L formulations, then treated the cells with increasing concentrations of cisplatin (cDDP; 0-100 μg/mL). **Fig 4.1e** shows the dose-response curve of cDDP in transfected cells, and **Fig 4.2** shows the IC$_{50}$ values quantified from the dose-response data. While the IC$_{50}$ of cDDP in cells treated with PBS or sham siRNA-loaded C-FNP (C-FNP/siLuc) were 72.1 μg/mL and 74.9 μg/mL, respectively, the IC$_{50}$ in non-fusogenic C-NNP and Lipofectamine (Lf) treatments decreased to 54 μg/mL and 50.6 μg/mL, respectively. However, C-FNPs induced a greater increase in cDDP-sensitivity, with IC$_{50}$ of only 29.9 μg/mL, which was significantly lower than all other transfectant groups (p<0.004). Thus, transfection with 50 nM siREV3L using C-FNPs was able to increase the susceptibility of CAOV-3 cells to a dose of cDDP that was more than two-fold lower than what was needed in the absence of *Rev3l* silencing.

4.5 Biosafety, biodistribution, and selective targeting of FNPs

Prior to therapeutic application, we verified the biosafety of C- and T-FNPs. **Figures 4.3a and b** show cytotoxicity assays of the formulations in CAOV-3 and J774a.1 cells, respectively. At an siRNA dose of 50 nM, neither the targeting peptide-conjugated FNPs nor the siRNA against *Rev3l* and *Pi3kγ* induced any *in vitro* cytotoxicity. Moreover, hematoxylin and eosin (H&E) stains of the major organs in healthy mice intravenously injected with T-FNPs or C-FNPs showed normal morphology and no lesions (**Fig 4.4**).

Next, we looked at biodistribution of the FNPs in a mouse model of peritoneal carcinomatosis, established by intraperitoneal (IP) injection of CAOV-3 human ovarian adenocarcinoma cells. We allowed the tumor nodules grow for 3 weeks, then IP injected PBS, non-conjugated FNPs, T-FNPs, or C-FNPs loaded with lipophilic DiI. We harvested the major organs and the largest tumor nodules at 1h and 24h post-injection and assayed for DiI signal localizations. Fluorescence imaging revealed that the DiI-loaded particles were localized primarily in the tumor nodules regardless of the accumulation time (**Fig 4.5a, b**). Both T-FNPs and C-FNPs showed significant increase in tumor accumulation from 1h to 24h ($p<0.01$ for T-FNPs; $p<0.05$ for C-FNPs), and both formulations accumulated in the tumor more effectively than the PBS and non-targeted FNP groups ($p<0.05$ for T-FNPs; $p<0.01$ for C-FNPs).

A second mouse model was established as a xenograft tumor model by subcutaneously injecting CAOV-3 cells with matrigel. As the CAOV-3 line has difficulty forming xenografts, tumor masses were <5 mm^3 in size[71]. When the therapeutic formulations were intravenously injected, a similar biodistribution trend was seen in the xenograft model as was seen with the local IP injection in peritoneal carcinomatosis model: primary accumulation in tumors, increased DiI accumulation from 1h to 24h of circulation, and superior tumor homing by T- and C-FNPs compared to non-targeted FNPs (**Fig 4.6**).

Flow cytometry was used to quantify cell-specificity of T- and C-FNPs. We IP injected PBS, non-targeted FNPs, T-FNPs, C-FNPs, and a 50:50 cocktail of C- and T-FNPs, and waited

24h prior to sample collection. Immune cells were collected by intraperitoneal lavage and the tumor nodules were harvested and homogenized. Macrophages from both the lavage and homogenized tumor nodules were eluted by magnetic separation using Anti-F4/80 beads. The purified macrophages (**Fig 4.5c-f**) and the homogenized tumor nodules (after extraction of macrophages, **Fig 4.5g-j**) were subjected to flow cytometry analysis, detecting the DiI signal channel. The non-targeted FNPs showed minimal homing to either macrophages (4.19%; **Fig 4.5c**) or tumor cells (1.13%; **Fig 4.5g**). In contrast, the T-FNPs (which deployed the TAM-homing LyP-1 peptide) successfully homed to macrophages (21.40%; **Fig 4.5d**) and not to the macrophage-free tumor nodule cells (0.01%; **Fig 4.5h**). Conversely, C-FNPs (which deployed the tumor cell-homing iRGD peptide) did not bind to macrophages (0.00%; **Fig 4.5e**) while it strongly accumulated in tumor cells (6.79%; **Fig 4.5i**). When co-injected, the T-FNPs and C-FNPs homed to both macrophages (29.6%; **Fig 4.5f**) and tumor nodules (11.2%; **Fig 4.5j**). Observing the FAM signal channel on FAM-conjugated targeting peptides showed a similar trend of selective targeting (**Fig 4.7**), and the accumulation ratios are reported in **Table 4.1**. Thus, we confirmed that pendant homing peptides can effectively target FNPs to their intended cells.

4.6   *In vivo* therapeutic efficacy of FNPs

With the ability of the peptide-conjugated FNPs to selectively target cells *in vivo* established, we next evaluated if FNPs could induce significant gene silencing *in vivo.* After 3 weeks of tumor growth, we IP injected PBS, T-FNPs, or C-FNPs. After 24h, we quantified gene expression using the quantitative reverse transcription polymerase chain reaction (qRT-PCR) on macrophages and tumor cells (**Figs 4.8a and b**).

The TAM-targeting T-FNPs loaded with siRNA against *Pi3kγ* were able to induce 81%

knockdown efficiency in the macrophages, while the chemo-sensitizing C-FNPs loaded with

siRNA against *Rev3l* had no effect (**Fig 4.8a**). Conversely, in tumor cells the C-FNPs induced a

silencing efficiency for *Rev3l* expression by 76%, while T-FNPs showed no effect (**Fig 4.8b**).

Thus, only targeted FNPs with siRNA appropriate for the cell type were able to induce a potent

in vivo gene silencing effect, and there were no detectable off-target effects.

Lastly, we conducted combination therapy experiments, using cisplatin (cDDP) with: (1)

immunotherapy by reprogramming macrophages to their tumoricidal phenotype (using T-FNPs);

and (2) gene therapy by sensitizing cancer cells to cDDP (using C-FNPs). A week after tumor

model establishment, we IP injected PBS, cDDP at 2 mg/kg, a cocktail of cDDP and T-FNPs, a

co-injection of cDDP and C-FNPs, or a co-injection of cDDP, T-FNPs, and C-FNPs. Cisplatin

was injected once every three days at the 2 mg/kg dose, and the T- and C-FNP formulations

were injected once a week, based on literature protocols[72].

After 30 days of treatment, **Fig 4.8c** shows that while cDDP treatment alone was able to

reduce the tumor nodule count by half, the difference was not statistically significant from the

PBS control. However, combination treatment of cDDP with T-FNPs, cDDP with C-FNPs, and

all three together (cDDP with T-FNPs and C-FNPs) significantly reduced the total number of

tumor nodules (One-way ANOVA, $[F_{(4,30)}=64.7, p=2.5 \times 10^{-14}]$, Tukey's HSD $p<0.05$). In

particular, the group given cDDP with both T-FNPs and C-FNPs was significantly more effective

than cDDP with only C-FNPs ($p=0.019$), and showed a notable trend compared with the cDDP

and T-FNP group ($p=0.051$). Size distribution of tumor nodules showed similar findings (**Fig

4.8d**). While the PBS control group had a wide size distribution range of nodules from 1.3-9.4

mm, we saw a small decrease with the cDDP-only treatment group (2.2-7.4 mm), and a greater

decrease in the groups given either cDDP + T-FNP (1.3-4.4 mm), or cDDP + C-FNP (1.4-6.2

mm). Remarkably, the triple combination (cDDP + T-FNP + C-FNP) showed complete

elimination of detectable tumors in 6 of the 7 members of the treatment group; the seventh member of this group presented with only a single nodule with a size of 2.8 mm.

The above results demonstrated the utility of the FNP platform for siRNA-based treatment--in the form of immunotherapy and gene therapy. They further showed that combination therapy to target multiple aspects of cancer can yield an improved therapeutic outcome relative to singular chemotherapy.

4.7   Discussion and Conclusions

The fusogenic porous silicon nanoparticles (FNPs) demonstrated three materials aspects that are crucial for effective siRNA-mediated gene therapy. First, peptide targeting moieties enabled the FNPs to selectively home to and transfect the desired cell target; in this work we focused on cancer cell types (tumor associated macrophages and tumor cells) and we previously demonstrated that another peptide can home FNPs to and transfect macrophages[10], establishing this as a relatively general approach. Second, effective delivery of the gene payload to the interior of the cell was afforded by the fusogenic lipid coating, which allowed the nanoparticles to avoid the endocytosis pathway. The fusogenic nature of these lipid coatings enabled a third crucial aspect: the specific, triggered release of the nucleic acid payload. The lipid stabilized the calcium silicate nanoparticle chemistry until cellular fusion had stripped the lipids, at which point rapid dissolution of the porous silicon nanoparticle ensued such that free siRNA was released into the cytosol. A strong gene silencing effect was observed both *in vitro* (> 90%) and *in vivo* (> 80%), which compares favorably to the average of 57.4 ± 21% *in vitro* (N=54) and 55.0 ± 17% *in vivo* (N=13) for gene therapy found across the literature[73].

A primary goal of this study was to understand the mechanism by which the FNPs operate. We showed that the lipid composition has a direct influence on its behavior, and that a

140

combination of properties (fluidity, cationic charge, and PEGylation) allows for plasma membrane fusion and endocytic bypass. Biological inhibitor studies showed that FNPs enter cells independently of typical endocytic pathways and intracellular vesicle traffic routes. However, vesicle fusion and certain exocytosis pathways were found to influence the fate of FNPs. The exact mechanism by which the fusogenic coating interacts with these pathways remains to be studied, as the extent of existing knowledge regarding these cellular pathways is limited.

The general nature of this approach was established and exemplified using two therapeutic formulations: (1) gene therapy (C-FNPs) to sensitize cancer cells to chemotherapy; and (2) immunotherapy (T-FNPs) to polarize macrophages toward the tumorigenic M2 phenotype. Each used a different targeting peptide for cell specificity and a different siRNA to program the desired genetic outcome. Combining homing specificity with high *in vivo* gene knockdown capabilities, the system showed a strong synergy in combination with a first-line chemotherapeutic, cisplatin, that showed significant reduction (and in some cases, complete elimination) of tumors in an ovarian cancer mouse model.

4.8   References

1   Sun, J. *et al.* A systematic analysis of FDA-approved anticancer drugs. *BMC Syst Biol* **11**, 87, doi:10.1186/s12918-017-0464-7 (2017).

2   Wood, H. FDA approves patisiran to treat hereditary transthyretin amyloidosis. *Nat Rev Neurol* **14**, 570, doi:10.1038/s41582-018-0065-0 (2018).

3   Gilleron, J. *et al.* Image-based analysis of lipid nanoparticle-mediated siRNA delivery, intracellular trafficking and endosomal escape. *Nature biotechnology* **31**, 638-646, doi:10.1038/nbt.2612 (2013).

4   Sahay, G. *et al.* Efficiency of siRNA delivery by lipid nanoparticles is limited by endocytic recycling. *Nature biotechnology* **31**, 653-658, doi:10.1038/nbt.2614 (2013).

5   Wang, Y. & Huang, L. A window onto siRNA delivery. *Nat Biotechnol* **31**, 611-612, doi:10.1038/nbt.2634 (2013).

6   Lewis, J. G. *et al.* A serum-resistant cytofectin for cellular delivery of antisense oligodeoxynucleotides and plasmid DNA. *Proc. Natl. Acad. Sci. U. S. A.* **93**, 3176-3181, doi:10.1073/pnas.93.8.3176 (1996).

7   Torchilin, V. P. Recent advances with liposomes as pharmaceutical carriers. *Nat Rev Drug Discov* **4**, 145-160, doi:10.1038/nrd1632 (2005).

8   Torchilin, V. P. Multifunctional, stimuli-sensitive nanoparticulate systems for drug delivery. *Nat Rev Drug Discov* **13**, 813-827, doi:10.1038/nrd4333 (2014).

9   Ozpolat, B., Sood, A. K. & Lopez-Berestein, G. Liposomal siRNA nanocarriers for cancer therapy. *Adv Drug Deliv Rev* **66**, 110-116, doi:10.1016/j.addr.2013.12.008 (2014).

10   Kim, B. *et al.* Immunogene therapy with fusogenic nanoparticles modulates macrophage response to Staphylococcus aureus. *Nat Commun* **9**, 1969, doi:10.1038/s41467-018-04390-7 (2018).

11   Russell, L. M., Hultz, M. & Searson, P. C. Leakage kinetics of the liposomal chemotherapeutic agent Doxil: The role of dissolution, protonation, and passive transport, and implications for mechanism of action. *J Control Release* **269**, 171-176, doi:10.1016/j.jconrel.2017.11.007 (2018).

12   Tanaka, T. *et al.* Sustained small interfering RNA delivery by mesoporous silicon particles. *Cancer Res* **70**, 3687-3696, doi:10.1158/0008-5472.CAN-09-3931 (2010).

13   Kang, J. *et al.* Self-Sealing Porous Silicon-Calcium Silicate Core-Shell Nanoparticles for Targeted siRNA Delivery to the Injured Brain. *Adv Mater* **28**, 7962-7969, doi:10.1002/adma.201600634 (2016).

14   Kim, B. & Sailor, M. J. Synthesis, Functionalization, and Characterization of Fusogenic Porous Silicon Nanoparticles for Oligonucleotide Delivery. *JoVE*, e59440, doi:doi:10.3791/59440 (2019).

15   Choi, E., Lee, J., Kwon, I. C. & Kim, S. Cumulative directional calcium gluing between phosphate and silicate: A facile, robust and biocompatible strategy for siRNA delivery by amine-free non-positive vector. *Biomaterials*, doi:/10.1016/j.biomaterials.2019.04.006 (2019).

16   Hasanzadeh Kafshgari, M. *et al. Oligonucleotide delivery by chitosan-functionalized porous silicon nanoparticles*. Vol. 8 (2015).

17   Ashley, C. E. *et al.* Delivery of Small Interfering RNA by Peptide-Targeted Mesoporous Silica Nanoparticle-Supported Lipid Bilayers. *ACS Nano* **6**, 2174-2188, doi:Doi 10.1021/Nn204102q (2012).

18   Basha, G. *et al.* Influence of cationic lipid composition on gene silencing properties of lipid nanoparticle formulations of siRNA in antigen-presenting cells. *Mol Ther* **19**, 2186-2200, doi:10.1038/mt.2011.190 (2011).

19   Meng, H. A. *et al.* Engineered Design of Mesoporous Silica Nanoparticles to Deliver Doxorubicin and P-Glycoprotein siRNA to Overcome Drug Resistance in a Cancer Cell Line. *ACS Nano* **4**, 4539-4550, doi:10.1021/nn100690m (2010).

20   Woodrow, K. A. *et al.* Intravaginal gene silencing using biodegradable polymer nanoparticles densely loaded with small-interfering RNA. *Nat Mater* **8**, 526-533, doi:10.1038/nmat2444 (2009).

21   Oh, Y. K. & Park, T. G. siRNA delivery systems for cancer treatment. *Adv Drug Deliv Rev* **61**, 850-862, doi:10.1016/j.addr.2009.04.018 (2009).

22   Howard, K. A. Delivery of RNA interference therapeutics using polycation-based nanoparticles. *Adv Drug Deliv Rev* **61**, 710-720, doi:10.1016/j.addr.2009.04.001 (2009).

23   Zhang, S., Zhao, B., Jiang, H., Wang, B. & Ma, B. Cationic lipids and polymers mediated vectors for delivery of siRNA. *J Control Release* **123**, 1-10, doi:10.1016/j.jconrel.2007.07.016 (2007).

24   Lee, J. *et al.* Liposome-based engineering of cells to package hydrophobic compounds in membrane vesicles for tumor penetration. *Nano Lett* **15**, 2938-2944, doi:10.1021/nl5047494 (2015).

25   Kim, J., Santos, O. A. & Park, J. H. Selective photosensitizer delivery into plasma membrane for effective photodynamic therapy. *J Control Release* **191**, 98-104, doi:10.1016/j.jconrel.2014.05.049 (2014).

26   Balazs, D. A. & Godbey, W. Liposomes for Use in Gene Delivery. *Journal of Drug Delivery* **2011**, doi:10.1155/2011/326497 (2011).

27   Lentz, B. R. Polymer-induced membrane fusion: potential mechanism and relation to cell fusion events. *Chem Phys Lipids* **73**, 91-106 (1994).

28   Dennison, S. M., Bowen, M. E., Brunger, A. T. & Lentz, B. R. Neuronal SNAREs do not trigger fusion between synthetic membranes but do promote PEG-mediated membrane fusion. *Biophys J* **90**, 1661-1675, doi:10.1529/biophysj.105.069617 (2006).

29   Sun, J., Jakobsson, E., Wang, Y. & Brinker, C. Nanoporous Silica-Based Protocells at Multiple Scales for Designs of Life and Nanomedicine. *Life* **5**, 214-229 (2015).

30   Liu, J., Stace-Naughton, A., Jiang, X. & Brinker, C. J. Porous Nanoparticle Supported Lipid Bilayers (Protocells) as Delivery Vehicles. *Journal of the American Chemical Society* **131**, 1354-1355, doi:10.1021/ja808018y (2009).

31   Kube, S. *et al.* Fusogenic Liposomes as Nanocarriers for the Delivery of Intracellular Proteins. *Langmuir* **33**, 1051-1059, doi:10.1021/acs.langmuir.6b04304 (2017).

32   Ozpolat, B., Sood, A. K. & Lopez-Berestein, G. Liposomal siRNA nanocarriers for cancer therapy. *Adv. Drug Deliv. Rev.* **66**, 110-116, doi:10.1016/j.addr.2013.12.008 (2014).

33   Kraft, J. C., Freeling, J. P., Wang, Z. & Ho, R. J. Y. Emerging Research and Clinical Development Trends of Liposome and Lipid Nanoparticle Drug Delivery Systems. *J. Pharm. Sci.* **103**, 29-52, doi:10.1002/jps.23773 (2014).

34   Allen, T. M. & Cullis, P. R. Liposomal drug delivery systems: From concept to clinical applications. *Adv. Drug Deliv. Rev.* **65**, 36-48, doi:10.1016/j.addr.2012.09.037 (2013).

35   Jiang, W., Lionberger, R. A. & Yu, L. X. In vitro and in vivo characterizations of PEGylated liposomal doxorubicin. *Bioanalysis* **3**, 333-344, doi:DOI: 10.4155/bio.10.204 (2011).

36   Russell, L. M., Hultz, M. & Searson, P. C. Leakage kinetics of the liposomal chemotherapeutic agent Doxil: The role of dissolution, protonation, and passive transport, and implications for mechanism of action. *Journal of Controlled Release* **269**, 171-176, doi:https://doi.org/10.1016/j.jconrel.2017.11.007 (2018).

37   Hasan, W. *et al.* Delivery of Multiple siRNAs Using Lipid-Coated PLGA Nanoparticles for Treatment of Prostate Cancer. *Nano Lett.* **12**, 287-292, doi:Doi 10.1021/Nl2035354 (2012).

38   Park, J.-H. *et al.* Biodegradable luminescent porous silicon nanoparticles for in vivo applications. *Nature Mater.* **8**, 331-336, doi:DOI: 10.1038/NMAT2398 (2009).

39   Jin, Y. *et al.* Tracking the Fate of Porous Silicon Nanoparticles Delivering a Peptide Payload by Intrinsic Photoluminescence Lifetime. *Adv. Mater.* **30**, 1802878, doi:doi:10.1002/adma.201802878 (2018).

40   Gore, M. E., Fryatt, I., Wiltshaw, E. & Dawson, T. Treatment of relapsed carcinoma of the ovary with cisplatin or carboplatin following initial treatment with these compounds. *Gynecol Oncol* **36**, 207-211 (1990).

41   Matsuo, K., Lin, Y. G., Roman, L. D. & Sood, A. K. Overcoming platinum resistance in ovarian carcinoma. *Expert Opin Investig Drugs* **19**, 1339-1354, doi:10.1517/13543784.2010.515585 (2010).

42   Morgan, R. D., Clamp, A. R., Evans, D. G. R., Edmondson, R. J. & Jayson, G. C. PARP inhibitors in platinum-sensitive high-grade serous ovarian cancer. *Cancer Chemother Pharmacol* **81**, 647-658, doi:10.1007/s00280-018-3532-9 (2018).

43   Siddik, Z. H. Cisplatin: mode of cytotoxic action and molecular basis of resistance. *Oncogene* **22**, 7265-7279, doi:10.1038/sj.onc.1206933 (2003).

44   da Cunha Colombo Bonadio, R. R., Fogace, R. N., Miranda, V. C. & Diz, M. Homologous recombination deficiency in ovarian cancer: a review of its epidemiology and management. *Clinics (Sao Paulo)* **73**, e450s, doi:10.6061/clinics/2018/e450s (2018).

45   Doles, J. *et al.* Suppression of Rev3, the catalytic subunit of Pol{zeta}, sensitizes drug-resistant lung tumors to chemotherapy. *Proc Natl Acad Sci U S A* **107**, 20786-20791, doi:10.1073/pnas.1011409107 (2010).

46   Jiang, H. G. *et al.* Knockdown of REV3 Synergizes with ATR Inhibition to Promote Apoptosis Induced by Cisplatin in Lung Cancer Cells. *J Cell Physiol*, doi:10.1002/jcp.25792 (2017).

47   Dai, C. H. *et al.* Co-inhibition of pol theta and HR genes efficiently synergize with cisplatin to suppress cisplatin-resistant lung cancer cells survival. *Oncotarget*, doi:10.18632/oncotarget.11214 (2016).

48   Wu, F., Lin, X., Okuda, T. & Howell, S. B. DNA Polymerase zeta regulates cisplatin cytotoxicity, mutagenicity and the rate of development of cisplatin resistance. *Cancer Res.* **64**, 8029-8035 (2004).

49   Sugahara, K. N. *et al.* A tumor-penetrating peptide enhances circulation-independent targeting of peritoneal carcinomatosis. *J Control Release* **212**, 59-69, doi:10.1016/j.jconrel.2015.06.009 (2015).

50   Coussens, L. M., Zitvogel, L. & Palucka, A. K. Neutralizing tumor-promoting chronic inflammation: a magic bullet? *Science* **339**, 286-291, doi:10.1126/science.1232227 (2013).

51   Germano, G. *et al.* Role of macrophage targeting in the antitumor activity of trabectedin. *Cancer Cell* **23**, 249-262, doi:10.1016/j.ccr.2013.01.008 (2013).

52   Mantovani, A., Bottazzi, B., Colotta, F., Sozzani, S. & Ruco, L. The origin and function of tumor-associated macrophages. *Immunol Today* **13**, 265-270, doi:10.1016/0167-5699(92)90008-U (1992).

53   Noy, R. & Pollard, J. W. Tumor-associated macrophages: from mechanisms to therapy. *Immunity* **41**, 49-61, doi:10.1016/j.immuni.2014.06.010 (2014).

54   Ries, C. H. *et al.* Targeting tumor-associated macrophages with anti-CSF-1R antibody reveals a strategy for cancer therapy. *Cancer Cell* **25**, 846-859, doi:10.1016/j.ccr.2014.05.016 (2014).

55   Williams, C. B., Yeh, E. S. & Soloff, A. C. Tumor-associated macrophages: unwitting accomplices in breast cancer malignancy. *NPJ Breast Cancer* **2**, doi:10.1038/npjbcancer.2015.25 (2016).

56   Mantovani, A., Marchesi, F., Malesci, A., Laghi, L. & Allavena, P. Tumour-associated macrophages as treatment targets in oncology. *Nature Reviews Clinical Oncology* **14**, 399, doi:10.1038/nrclinonc.2016.217 (2017).

57   Foubert, P., Kaneda, M. M. & Varner, J. A. PI3Kgamma Activates Integrin alpha4 and Promotes Immune Suppressive Myeloid Cell Polarization during Tumor Progression. *Cancer Immunol Res* **5**, 957-968, doi:10.1158/2326-6066.CIR-17-0143 (2017).

58   Kaneda, M. M. *et al.* PI3Kgamma is a molecular switch that controls immune suppression. *Nature* **539**, 437-442, doi:10.1038/nature19834 (2016).

59   Schmid, M. C. *et al.* Receptor tyrosine kinases and TLR/IL1Rs unexpectedly activate myeloid cell PI3kgamma, a single convergent point promoting tumor inflammation and progression. *Cancer Cell* **19**, 715-727, doi:10.1016/j.ccr.2011.04.016 (2011).

60   De Henau, O. *et al.* Overcoming resistance to checkpoint blockade therapy by targeting PI3Kgamma in myeloid cells. *Nature* **539**, 443-447, doi:10.1038/nature20554 (2016).

61   Uchida, M. *et al.* Protein cage nanoparticles bearing the LyP-1 peptide for enhanced imaging of macrophage-rich vascular lesions. *ACS Nano* **5**, 2493-2502, doi:10.1021/nn102863y (2011).

62   Scodeller, P. *et al.* Precision Targeting of Tumor Macrophages with a CD206 Binding Peptide. *Sci Rep* **7**, 14655, doi:10.1038/s41598-017-14709-x (2017).

63   Fogal, V., Zhang, L., Krajewski, S. & Ruoslahti, E. Mitochondrial/cell-surface protein p32/gC1qR as a molecular target in tumor cells and tumor stroma. *Cancer Res* **68**, 7210-7218, doi:10.1158/0008-5472.CAN-07-6752 (2008).

64   Laakkonen, P., Porkka, K., Hoffman, J. A. & Ruoslahti, E. A tumor-homing peptide with a targeting specificity related to lymphatic vessels. *Nat Med* **8**, 751-755, doi:10.1038/nm720 (2002).

65   Ruoslahti, E. Tumor penetrating peptides for improved drug delivery. *Adv Drug Deliv Rev* **110-111**, 3-12, doi:10.1016/j.addr.2016.03.008 (2017).

66   Feron, O. Tumor-penetrating peptides: a shift from magic bullets to magic guns. *Sci Transl Med* **2**, 34ps26, doi:10.1126/scitranslmed.3001174 (2010).

67   Liu, X. *et al.* Targeted drug delivery using iRGD peptide for solid cancer treatment. *Mol Syst Des Eng* **2**, 370-379, doi:10.1039/C7ME00050B (2017).

68   Sugahara, K. N. *et al.* Tissue-penetrating delivery of compounds and nanoparticles into tumors. *Cancer Cell* **16**, 510-520, doi:10.1016/j.ccr.2009.10.013 (2009).

69   Keller, A. A., Maess, M. B., Schnoor, M., Scheiding, B. & Lorkowski, S. Transfecting Macrophages. *Methods Mol Biol* **1784**, 187-195, doi:10.1007/978-1-4939-7837-3_18 (2018).

70   Maeß, M. B., Wittig, B. & Lorkowski, S. Highly efficient transfection of human THP-1 macrophages by nucleofection. *Journal of visualized experiments : JoVE*, e51960-e51960, doi:10.3791/51960 (2014).

71   Mitra, A. K. *et al.* In vivo tumor growth of high-grade serous ovarian cancer cell lines. *Gynecologic oncology* **138**, 372-377, doi:10.1016/j.ygyno.2015.05.040 (2015).

72   Bartlett, D. W. & Davis, M. E. Insights into the kinetics of siRNA-mediated gene silencing from live-cell and live-animal bioluminescent imaging. *Nucleic acids research* **34**, 322-333, doi:10.1093/nar/gkj439 (2006).

73   Draz, M. S. *et al.* Nanoparticle-mediated systemic delivery of siRNA for treatment of cancers and viral infections. *Theranostics* **4**, 872-892, doi:10.7150/thno.9404 (2014).

4.9   Figures and Tables
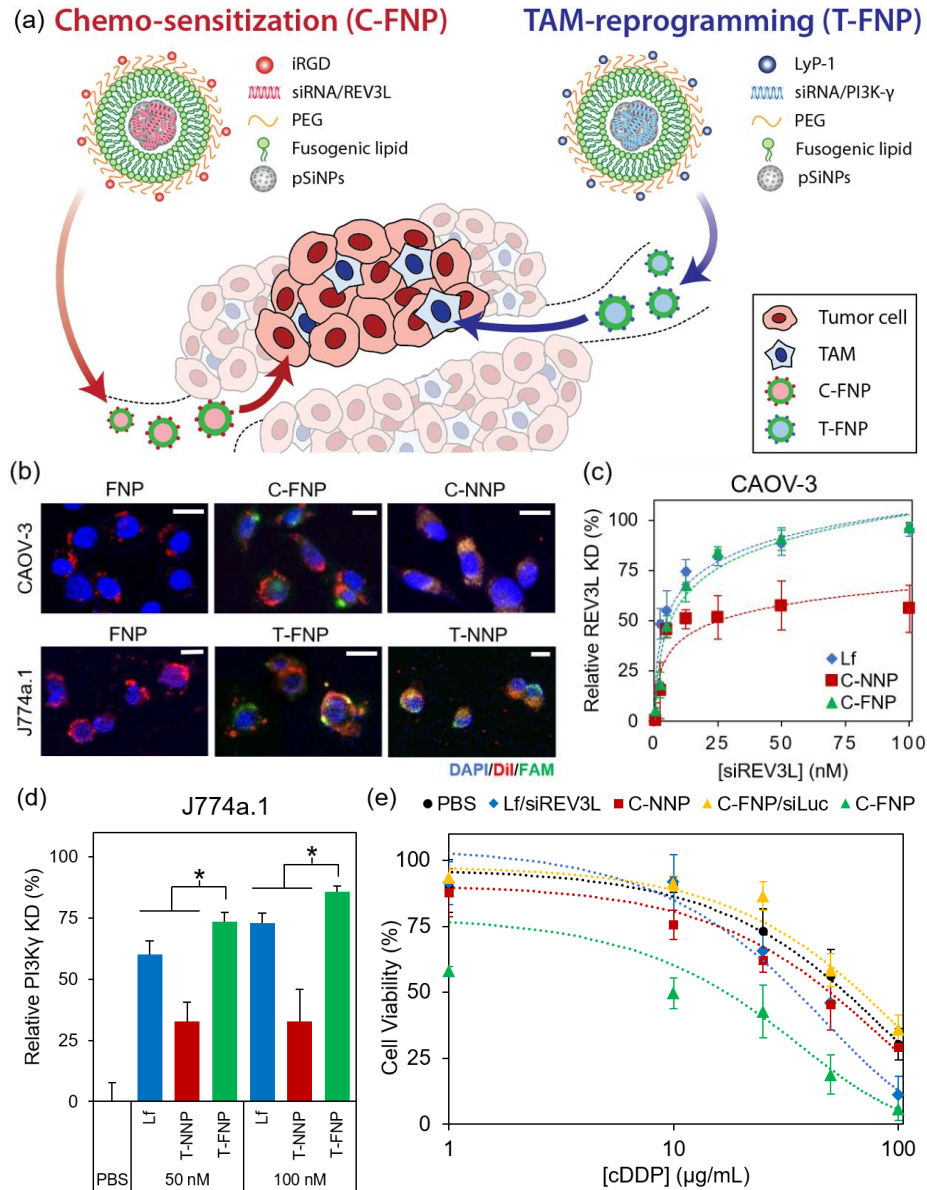
Figure 4.1. FNPs induce potent gene silencing effect *in vitro* and can sensitize cancer cells to chemotherapy.
(a) Intended mode of action of two model therapeutics; **(b)** confocal microscope images of CAOV-3 cancer cells (top row) and J774a.1 macrophages (bottom row) treated with DiI-loaded particles that were non-targeted (FNPs), targeted with iRGD (C-FNPs and C-NNPs) or with LyP-1 (T-FNPs and T-NNPs). The peptides were tagged with FAM (green) and nuclei were stained with DAPI (blue). Red channel is the DiI. Scale bar represents 10 μm; **(c)** dose-response curve of CAOV-3 cells treated with increasing doses of siRNA against *Rev3l* using Lipofectamine (Lf), C-NNPs, or C-FNPs. Bars represent standard deviation with n=8; **(d)** *Pi3kγ* knockdown quantification in J774a.1 macrophages treated 50 or 100 nM of siRNA against *Pi3kγ* using Lipofectamine (Lf), T-NNPs, or T-FNPs. Bars represent standard deviation with n=8. *represents p<0.05 using One-way ANOVA with Tukey HSD test; **(e)** chemo-sensitivity test in CAOV-3 cells with *Rev3l* silencing. Cells were treated with increasing doses of cisplatin (cDDP) as indicated. Bars represent standard deviation with n=10.

Transfectant	IC_{50} (µg/mL)
PBS	72.1 ± 2.4
Lf/siREV3L	50.6 ± 7.1
C-NNP	54.0 ± 9.3
C-FNP/siLuc	74.9 ± 5.1
C-FNP	29.9 ± 5.9
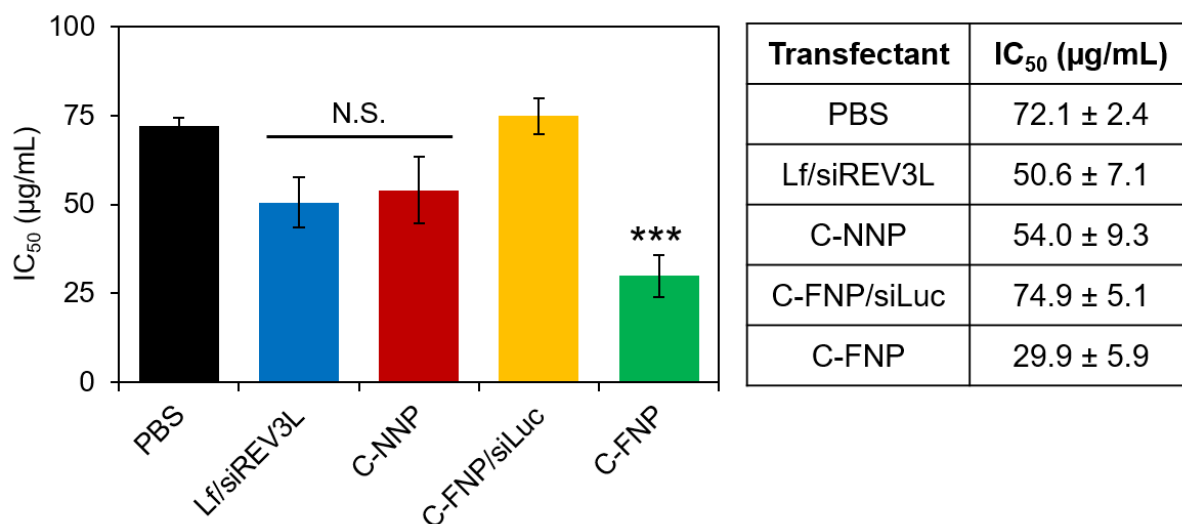
Figure 4.2. Quantified IC_{50} values of cDDP when treated to CAOV-3 cells that were pre-transfected

CAOV-3 cells were transfected with PBS, Lipofectamine 2000 with siREV3L (Lf/siREV3L), iRGD-conjugated non-fusogenic particles loaded with siRNA against *Rev3l* (C-NNPs), iRGD-conjugated fusogenic particles loaded with sham siRNA against luciferase (C-FNP/siLuc), or iRGD-conjugated fusogenic particles loaded with siRNA against *Rev3l* (C-FNP), with all formulations treated at 50 nM siRNA dose. Right table shows the average IC_{50} value with standard deviation in n=10. Bars also represent standard deviation with n=10; N.S. represents no significant difference, and *** represents p< 0.01 based on One-way ANOVA with Tukey's HSD post hoc analysis.
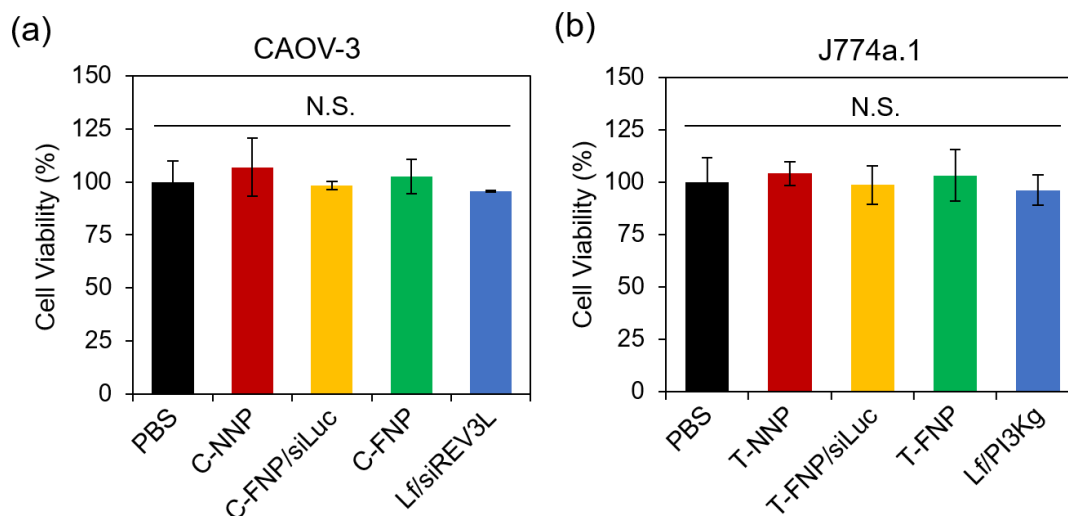
Figure 4.3. Cell viability assay of cells based on CCK-8 assay
(a) CAOV-3 cancer cells treated with PBS, iRGD-conjugated non-fusogenic particles loaded with siRNA against *Rev3l* (C-NNPs), iRGD-conjugated fusogenic particles loaded with sham siRNA against luciferase (C-FNP/siLuc), C-FNPs, and Lipofectamine treated with siRNA against *Rev3l* with all formulations treated at 50 nM siRNA dose; (b) J774a.1 macrophages treated with PBS, LyP-1-conjugated non-fusogenic particles loaded with siRNA against *Pi3kγ* (T-NNPs), LyP-1-conjugated fusogenic particles loaded with sham siRNA against luciferase (T-FNP/siLuc), T-FNPs, and Lipofectamine treated with siRNA against *Pi3kγ* with all formulations treated at 50 nM siRNA dose. Bars represent standard deviation with n=6. N.S. represents no significance based on One-way ANOVA.
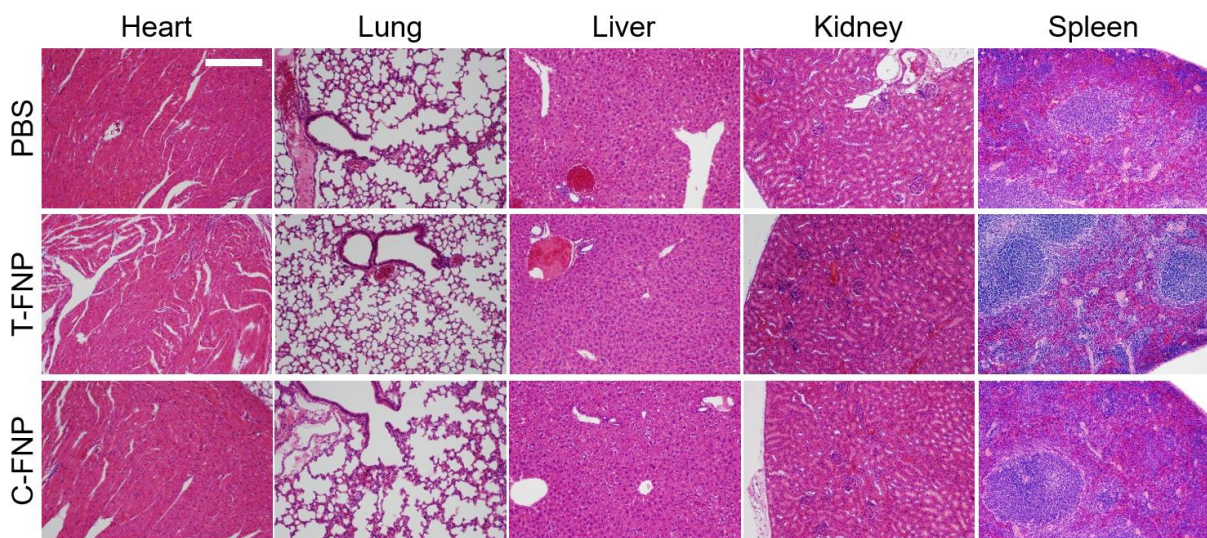
Figure 4.4. H&E stain of major organs harvested from healthy mice that were intravenously injected with formulations.

Mice was IV injected with PBS, LyP-1-conjugated fusogenic nanoparticles loaded with siRNA against *Pi3kγ* (T-FNPs), and iRGD-conjugated fusogenic nanoparticles loaded with siRNA against *Rev3l* (C-FNPs). Scale bar represents 200 µm.
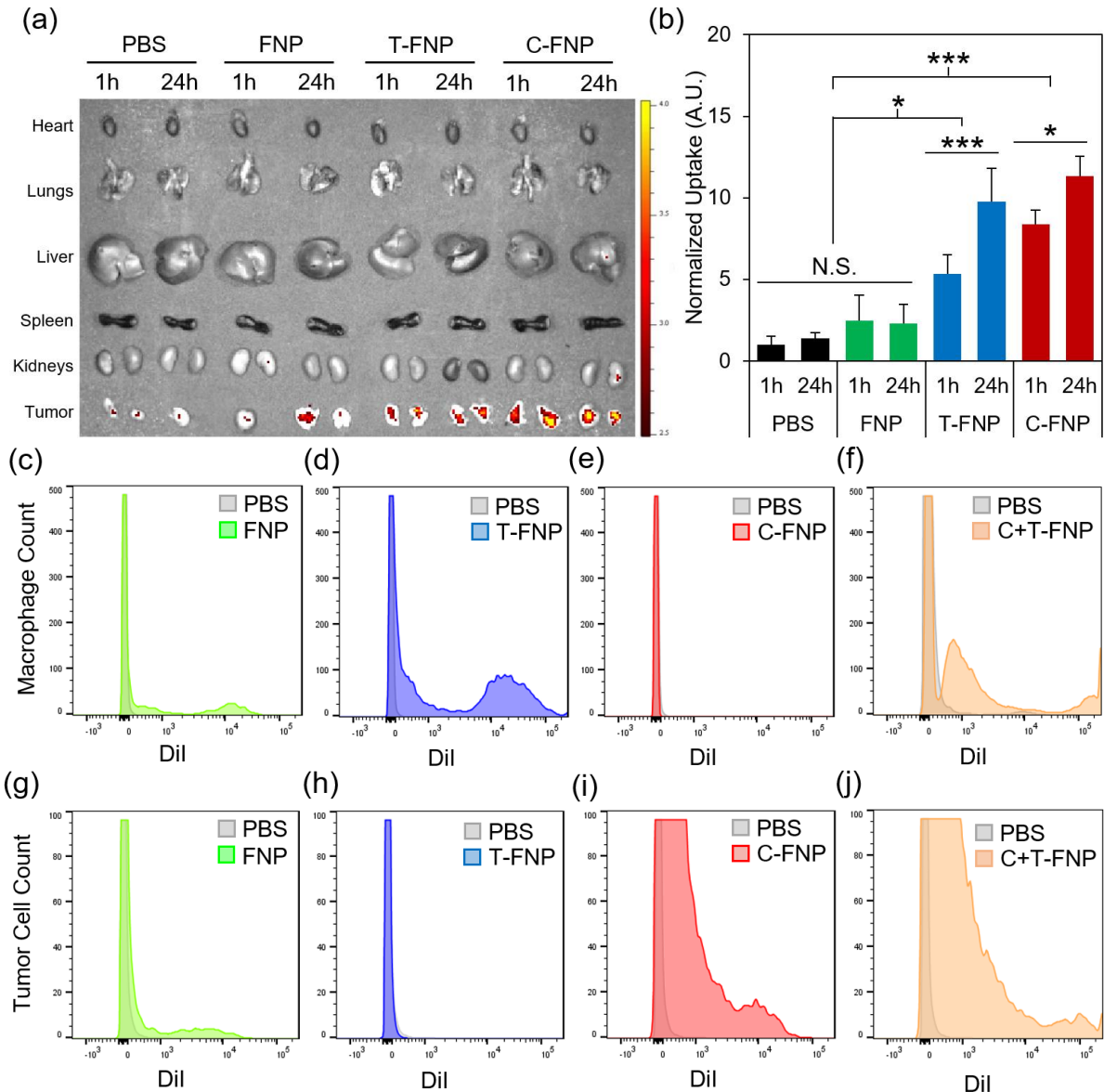
Figure 4.5. T- and C-FNPs selectively home to their target cells *in vivo* with minimal off-target accumulation.
(a) *ex vivo* IVIS 200 fluorescence images of organs harvested from mice bearing peritoneal carcinomatosis of CAOV-3 cells. Mice were IP-injected with PBS, DiI-loaded non-targeted FNPs, DiI loaded LyP-1 conjugated T-FNPs (fusogenic nanoparticles targeted to tumor associated macrophages, or TAMs, via the LyP-1 peptide), and DiI-loaded iRGD-conjugated C-FNPs (chemosensitizing fusogenic nanoparticles, targeted to tumor cells via the iRGD peptide) for 1h or 24h accumulation time. Image representative of n=5; **(b)** Image J quantification of DiI fluorescence signals from IVIS 200 images. Bars represent standard deviation with n=5. * represents One-way ANOVA with Tukey's HSD test with p<0.05, *** represents the same with p <0.01, and N.S. represents no significance; **(c-j)** DiI signal quantification using flow cytometry of macrophages purified from IP lavage fluid and tumor nodule homogenates **(c-f)**, or tumor cells **(g-j)** from the nodule homogenates. Samples were harvested from mice IP injected with DiI loaded FNPs, T-FNPs, C-FNPs, or a 1:1 cocktail of C- and T-FNPs. Data is representative of n=4.
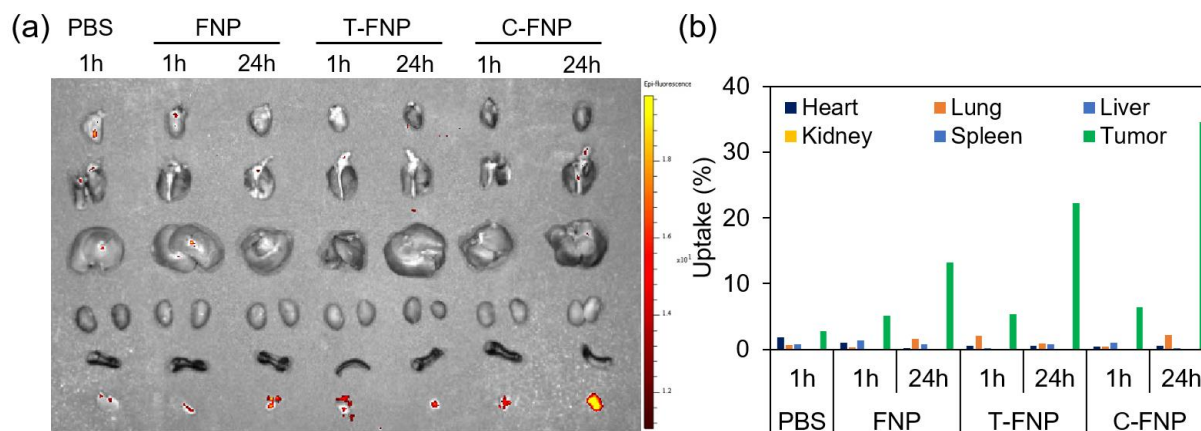
Figure 4.6. Biodistribution of formulations in major organs when intravenously injected in tumor xenograft models.
(a) *ex vivo* IVIS 200 fluorescence images of organs harvested from mice bearing xenograft of CAOV-3 cells on the flank. Mice were intravenously injected via tail-vein with PBS, DiI-loaded non-targeted FNPs, DiI loaded LyP-1 conjugated T-FNPs, and DiI-loaded iRGD-conjugated C-FNPs for 1h or 24h accumulation time; (b) Image J quantification of DiI fluorescence signals from IVIS 200.
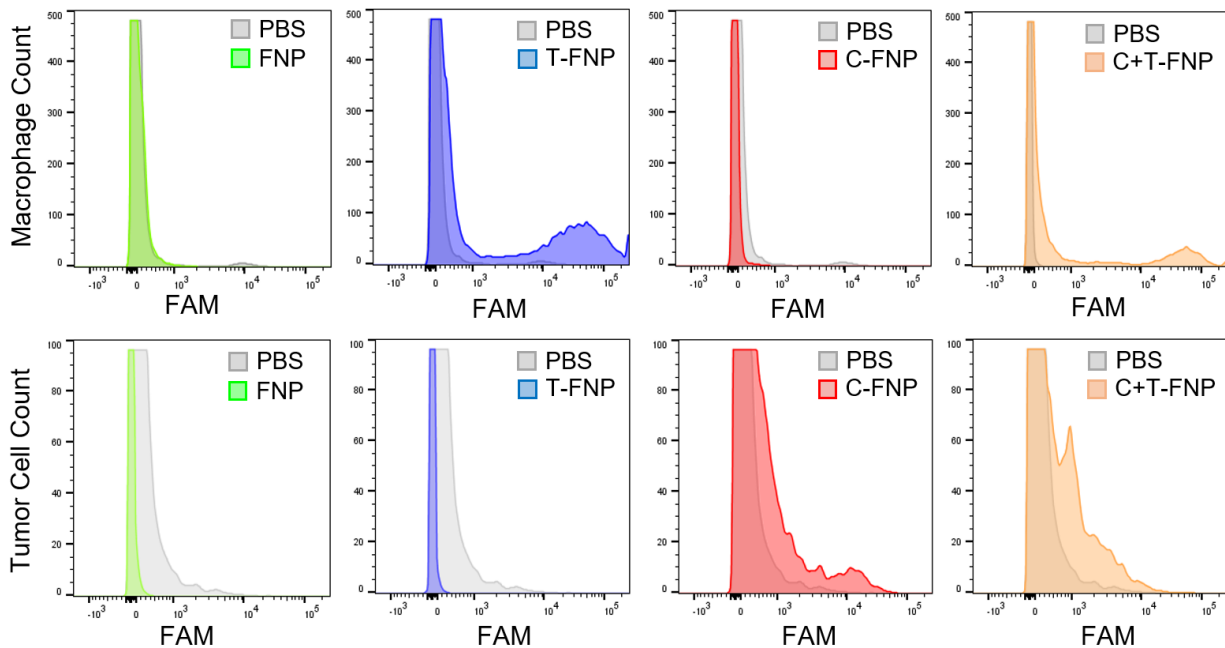
Figure 4.7. FAM signal quantification using flow cytometry.
Macrophages (top row) were purified from IP lavage fluid and tumor nodule homogenates, and tumor cells (bottom row) from the nodule homogenates. Samples were harvested from mice IP injected with FNPs, T-FNPs, C-FNPs, or a 1:1 cocktail of C- and T-FNPs, using FAM-tagged targeting peptides. Data is representative of n=4.
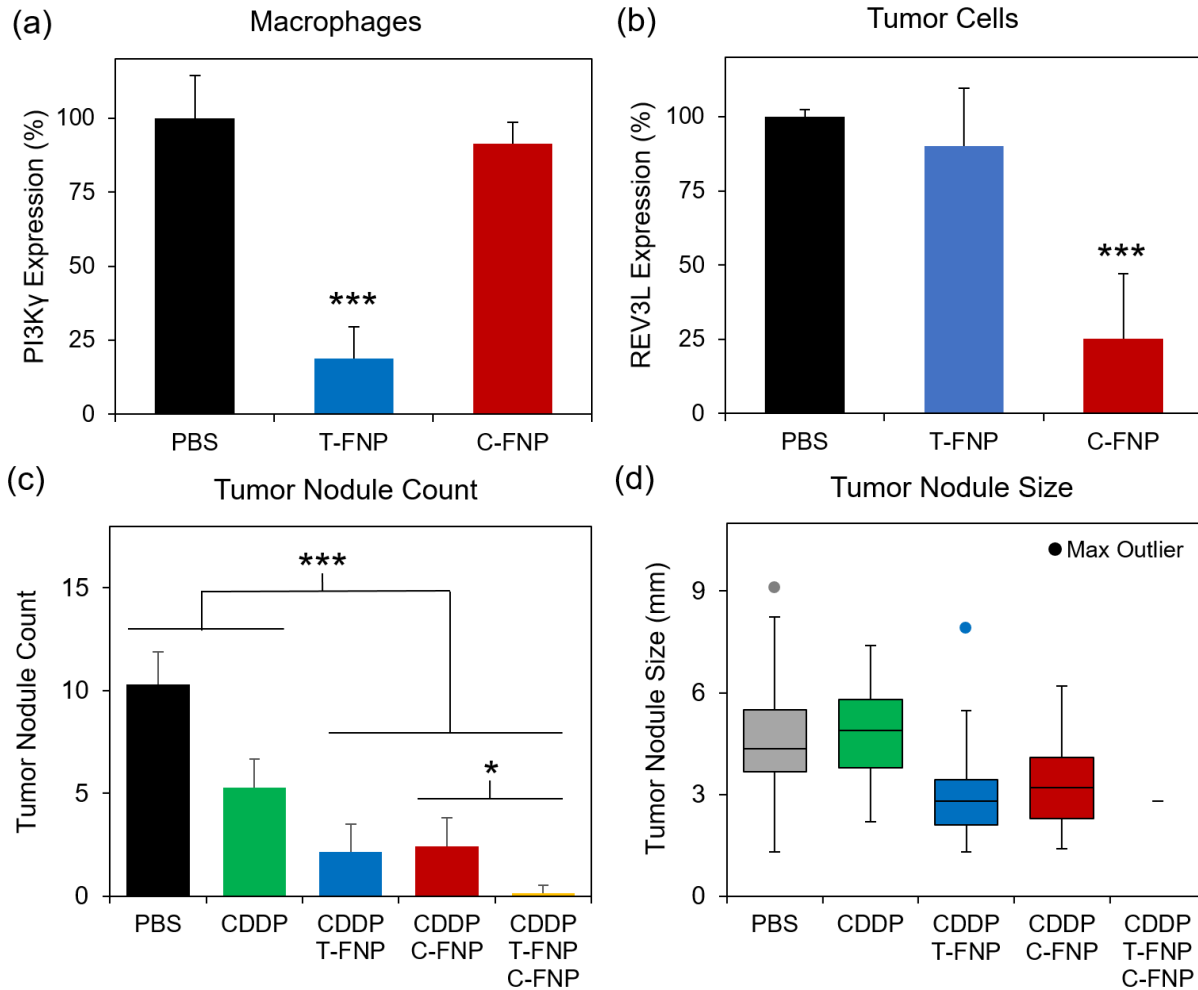
Figure 4.8. T- and C-FNPs are effective as immuno- and gene therapy formulations for combination treatment with chemotherapy.

(a) *Pi3kγ* expression quantified in macrophages purified from IP lavage fluid and tumor nodule homogenates using qRT-PCR. Mice bearing CAOV-3 human ovarian adenocarcinoma tumors were IP injected with PBS, LyP-1 conjugated FNPs carrying siRNA against *Pi3kγ* (T-FNP), or iRGD conjugated FNPs carrying siRNA against *Rev3l* (C-FNP). Bars represent standard deviation with n=6. *** represents One-way ANOVA with Tukey's HSD test with $p < 0.01$; **(b)** *Rev3l* expression quantified in tumor cells from tumor nodule homogenates using qRT-PCR. Mice were IP injected with PBS, T-FNP, or C-FNP. Bars represent standard deviation with n=6. *** represents One-way ANOVA with Tukey's HSD test with $p < 0.01$; **(c)** number of tumor nodules found in mice peritoneum after 30 days of treatment with PBS, cisplatin (cDDP) at 2 mg/kg, 1:1 cocktail of cDDP with T-FNPs, 1:1 cocktail of cDDP with C-FNPs, or 1:1:1 cocktail of cDDP, T-FNPs, and C-FNPs. Bars represent standard deviation with n=7. * represents One-way ANOVA with Tukey's HSD test with $p < 0.05$, and *** represents the same with $p < 0.01$; **(d)** size distribution of tumor nodules found mice from (c). Bars and boxes represent each quartile and dots represent outliers, with $n_{PBS} = 72$, $n_{cDDP} = 37$, $n_{cDDP+T-FNP} = 15$, $n_{cDDP+C-FNP} = 17$, and $n_{cDDP+T-FNP+C-FNP} = 1$.

155

Table 4.1. Percentage of cells with fluorophore signals as measured by flow cytometry.

	FNP	T-FNP	C-FNP	C+T-FNP
Dil Signal				
Macrophage	4.19%	21.4%	0.00%	29.6%
Tumor	1.13%	0.01%	6.79	11.2%
FAM Signal				
Macrophage	0.45%	22.6%	0.14%	7.44%
Tumor	0.01%	0.00%	4.28%	5.36%

Chapter four, in full, has been submitted for publication of the material as it may appear in **Kim, B.**, Varner, J.A., Howell, S.B., Ruoslahti, E., Sailor, M.J. Securing the Payload, Finding the Cell, Avoiding the Endosome: Peptide-Targeted, Fusogenic Porous Silicon Nanoparticles for More Effective Delivery of siRNA Therapies. *Adv Mater.* Submitted. The author of this dissertation was the primary author of the material.

Chapter 5:

Fusogenic Porous Silicon Nanoparticles for Immunotherapy against

Staphylococcus aureus Infection

5.1   Abstract

With the increased incidence of side effects and pathogen resistance encountered with small molecule antibiotics, there is rising focus on immunogene therapy to augment the immune system's own efforts to clear the infection and accelerate healing. A major obstacle to in vivo gene delivery is that the primary uptake pathway, cellular endocytosis, results in extracellular excretion and lysosomal degradation of genetic material. Herein, we present a nanosystem that bypasses endocytosis to achieve potent gene knockdown efficacy. Using a porous silicon nanoparticle containing of an outer sheath of homing peptides and fusogenic liposome, an oligonucleotide payload is selectively targeted to macrophages and directly introduced into the cytosol. Highly effective knockdown of the pro-inflammatory macrophage marker, IRF5, enhances the clearance capability of the macrophages and dramatically improves survival in a mouse model of Staphyloccocus aureus-induced pneumonia.

5.2   Introduction

Deep-tissue Staphyloccocus aureus (Staph. aureus) infection remains one of the most difficult therapeutic challenges today. Staph. aureus is a gram positive bacterium that predominantly infects the skin, and the respiratory system causing pneumonia; the local infections can become systemic in the most serious form of Staphylococcal disease, sepsis[1]. At high levels of bacterial burden in the lungs, Staphyloccocal pneumonia becomes fatal due to two major factors: (1) pathogenic activity by Staph. aureus, and (2) prolonged inflammation caused by the body's immune system. The acute inflammatory response at the site of an infection involves the secretion of cytokines by alveolar macrophages, recruiting polymorphonuclear neutrophils (PMNs) and monocytes from circulation that differentiate into macrophages[2]. Alveolar inflammation causes extensive bleeding and exudation that slow down

159

vascular flow and impede breathing[2,3], and prolonged excretion of inflammatory cytokines drastically lowers the chances of recovery[3]. Although the immediate inflammatory response to Staphylococcal pneumonia is necessary for rapid elimination of the threat, it must be balanced with anti-inflammatory and tissue-reparative actions to maintain lung homeostasis[4].

Due to toxic side effects of small molecule antibiotics such as vancomycin[5] and the emergence of strains resistant to these therapeutics[2], there is increasing emphasis on therapies that can harness the immune system to treat bacterial infections[6-9]. Macrophages are one potential target for these therapies due to their dual role as inflammatory, immune stimulatory phagocytes (M1 macrophages) and as anti-inflammatory phagocytes (M2 macrophages) associated with bacterial phagocytosis and tissue repair functions[10-15]. Inflammatory M1 macrophages are marked by the IRF5 gene, which upregulates TNF-α, IL-1, IL-6, IL-15, IL-18, IL-23, and downregulates anti-inflammatory cytokines such as IL-10[10,12-15]. Knockdown of the IRF5 gene in the early stages of Staphylococcal pneumonia can curtail prolonged inflammation by preventing the excretion of inflammatory cytokines, allowing the immune system to focus on bacterial clearance and tissue recovery[10,15,16].

Despite much effort, the *in vivo* knockdown of genes has seen limited success. Naked RNA has a very short half-life *in vivo*, thus various types of nanoparticle delivery vehicles have been employed to protect the oligonucleotide and deliver it intracellularly[17-19]. The most common means of delivery is with lipid nanoparticles[20], and these have been observed to be readily endocytosed by the cell, leading to extracellular excretion of 70% of the siRNA payload, with the remaining siRNA undergoing lysosomal degradation. Typically only 1-2% of administered siRNA escapes early endosomal uptake to potentially undergo RNA interference (RNAi)[21-23]. In order to increase the quantity of RNA delivered, polymeric and related hybrid nanoparticles have been engineered with cationic polyethylenimine (PEI) components. While it increases the carrying capacity of the nanoparticles, PEI displays undesirable cytotoxicity[24,25]. Certain lipid

constituents, such as dioleoylphosphatidylethanolamine (DOPE) or 1,2-dioleoyl-3-

trimethylammonium-propane (DOTAP), impart a fusogenic nature to liposomes that allows them

to fuse with the cellular membrane, mitigating toxicity and enhancing cellular delivery of genes[26-29]. With certain PEGylated lipid compositions, fusogenic liposomes have been shown to bypass

endocytosis altogether, much like the endogenous SNARE-mediated vesicular uptake

mechanism[30,31].

Although cellular penetration is important, gene therapeutics must also reach the

appropriate cell to be effective[18,19,32-34]. Here we present a solution to these problems that uses

nanoparticles containing a targeting peptide specific for activated macrophages and a fusogenic

liposomal coating (F-pSi). Membrane fusion allows for the direct release of hydrophilic payloads

from the core of the nanoparticle directly into the cell cytoplasm, the transfer of hydrophobic

molecules from the liposomal bilayer to the cell membrane bilayer, and the transfer of moieties

conjugated on the outer surface of lipid coat (antibodies, small molecules, peptides, etc.) to the

cell membrane. By avoiding endocytosis entirely, the fusogenic coating allows for much higher

probability of siRNAs to reach the perinuclear region to undergo RNAi. More details are

presented in the Discussion. In addition, in place of conventional peptide-based and polymeric

nanoparticles (ie. protamine, poly-L-lysine, and PEI) we use porous silicon nanoparticles

(pSiNPs), which have been shown to be an effective gene delivery vehicle[35]. The pSiNPs are

with a calcium silicate trapping chemistry[36] that can load and protect high quantities of siRNA

without the use of cytotoxic polymer stabilizers. We employ siRNA against the IRF5 gene in

order to inhibit the inflammatory phenotype of macrophages and favor phagocytotic function.

We find that these macrophage-targeting F-pSi hybrid nanoparticles yield high siRNA

knockdown efficiency *in vitro* and provide exceptionally strong therapeutic efficacy against a

Staph. aureus pneumonia infection model in mice, affording full recovery from a lethal dose.

This study represents the first successful *in vivo* demonstration of gene silencing for

immunotherapy of deep-tissue infection, with strong implications for treatment of increasingly antibiotic-resistant bacterial infections.

5.3   Materials and Methods

Materials. Highly boron-doped p-type silicon wafers (~1 mΩ-cm resistivity, polished on the (100) face) were obtained from Virginia Semiconductor, Inc or Siltronix, Inc. Hydrofluoric acid (48% aqueous, ACS grade) was obtained from Fisher Scientific. Anhydrous calcium chloride was obtained from Spectrum Chemicals (Gardena, CA). Deionized (18 mΩ) water was used for all aqueous dilutions. For lipids, 1,2-dimyristoyl-sn-glycero-3-phosphocholine (DMPC), 1,2-distearoyl-sn-glycero-3-phosphoethanolamine-N-[methoxy(polyethylene glycol)-2000, Avanti Polar Lipids] (DSPE-mPEG), 1,2-distearoyl-sn-glycero-3-phosphoethanolamine-N-[maleimide(polyethylene glycol)-2000] (DSPE-PEG-maleimide), and 1,2-dioleoyl-3-trimethylammonium-propane (DOTAP) were purchased from Avanti Polar Lipids (Alabaster, AL) and stored at -4ºC. Fluorescent dyes Calcein (Sigma-Aldrich) and hydrophobic 1,1'-Dioctadecyl-3,3,3',3'-Tetramethylindocarbocyanine Perchlorate (DiI, Life Technologies) were used, and Lipofectamine® 2000 Transfection Reagent was obtained from Thermo Fisher Scientific. Custom siRNAs were purchased from Dharmacon (Lafayette, CO), and primers were purchased from IDT DNA (San Diego, CA). Macrophage-targeting peptide (CRV) was identified by Dr. Erkki Ruoslahti's group at Sanford-Burnham-Prebys Medical Discovery Center (SBPMDI, CA) and custom synthesized by CTC Scientific (Sunnyvale, CA). For *in vitro* studies, Raw 264.7 and J774a.1 cells were purchased from ATCC (Manassas, VA) within 6 months prior to all experiments. DMEM cell media was purchased from GE Healthcare Life Sciences (HyClone, Pittsburg, PA), with supplemental fetal bovine serum (HyClone, Pittsburg, PA) and penicillin/streptomycin (HyClone, Pittsburg, PA). Staphylococcus aureus subsp. aureus

Rosenbach (ATCC® 25923™) was purchased from ATCC (Manassas, VA) within 6 months prior to all experiments, and 6 week-old male Balb/C were purchased from Envigo (Placentia, CA).

Preparation of porous silicon nanoparticles. Porous silicon (pSi) samples were prepared by electrochemical etching of silicon wafers in an electrolyte consisting of 3:1 (v:v) of 48% aqueous HF:ethanol (CAUTION: HF is highly toxic and proper care should be exerted to avoid contact with skin or lungs). A silicon working electrode with an exposed area of 8.6 cm^2 was contacted on the back side with aluminum foil and mounted in a Teflon cell. The silicon wafer was then anodized in a two-electrode configuration with a platinum counter electrode, by applying an alternating current of square waveform, with lower current density of 50 mA/cm^2 for 0.6s and high current density of 400 mA/cm^2 for 0.36s repeated for 500 cycles. Then the porous layer is lifted off by etching at a constant current density of 3.7 mA/cm^2 for 250s in a 1:20 (v:v) of 48% aqueous HF:ethanol solution, to be sonicated in deionized water for 12h into nanoparticles. Fluorescent dye and siRNA payloads were loaded into the pSi nanoparticles by pore sealing by calcium silicate formation; the calcium silicate sealing chemistry has demonstrated high efficiency in loading anionic payloads previously[36]. Calcein was dissolved in PBS at 100 mM. 150 uL of calcein was pipetted gently with 150 uL of pSiNP and 700 uL of 3M calcium chloride under ultrasonication for 15 min. For siRNA loading, we used siIRF5 (IRF5, sense 5'-dTdT-CUG CAG AGA AUA ACC CUG A-dTdT-3' and antisense 5'-dTdT UCA GGG UUA UUC UCU GCA G dTdT-3') and siLuc (luciferase, 5′-CUU ACG CUG AGU ACU UCG A dTdT-3′ and antisense 5′-UCG AAG UAC UCA GCG UAA G dTdT-3′). siRNA was dissolved in RNAse-free water to 150 µM and loaded into pSi at the same volume ratio and process as calcein loading with only RNAse-free water used as solvent.

Liposomal coating. Fusogenic coating (F) and non-fusogenic coating (NF) were prepared from DMPC, DSPE-PEG, and DOTAP at the molar ratio of 76.2:3.8:20 and 96.2:3.8:0,

respectively. The lipid films were prepared by evaporating the organic solvent, with 725.5 µg of

DMPC, 151.6 µg of DSPE-PEG (methoxy or maleimide terminated), and 196.3 µg of DOTAP (F)

or 916.0 µg of DMPC and 151.6 µg of DSPE-PEG (methoxy or maleimide terminated) (NF). The

DiI-incorporated films were added with 26.3 µg of DiI (1.25 mg/ml in 100% ethanol). The films

were then hydrated with payload-pSi solution and prepared by film hydration/extrusion; the pSi-

hydrated lipid was heated to 40ºC with constant magnetic stirring for 10 min. Then the mixture

was extruded through 200 nm polycarbonate membrane 20 times. CRV was conjugated to

maleimide-terminated PEG by mixing 100 uL of 1 mg/mL CRV (in deionized water) in 1 mg/ml of

the liposomal pSi (by lipid mass) overnight at 4ºC. Particles were washed three times at each

step by centrifugation in Microcon-30kDa Centrifugal Filter Unit (EMD Millipore) by spinning at

5000g at 25ºC. The loaded siRNA concentration was quantified by NanoDrop 2000

spectrophotometer (Thermo Fisher Scientific, ND-2000) after each step of particle formation by

checking the ultraviolet absorption of the supernatant and pellet of each wash. Nanoparticle size

and zeta-potential were measured by dynamic light scattering (DLS, Zetasizer ZS90, Malvern

Instruments), and structural morphology were visualized by JEOL 1200 EX II TEM and FEI

Tecnai Spirit G2 BioTWIN TEM. Samples were prepared by dropping 5 uL of the sample on the

TEM grid, drying off excess solvent after 1 min, and dropping 5 uL of uranyl acetate for negative

staining. Particle physiostability was observed by storing the formulations in PBS, refrigerated at

4ºC and measuring the hydrodynamic diameter every day for the first week, then every 7 days

for a total of 4 weeks. The experiment was replicated 3 times and averaged.

Macrophage-targeting peptide (CRV) identification. Phage display screening was

carried out as previously described[54]. Briefly, the macrophage cell line used here was J774A.1,

a mouse monocyte/macrophage cell line isolated from ascites of female animals bearing

reticulum cell sarcoma. A T7 phage library displaying 9-residue cyclic peptides (CX7C, two

terminal Cysteine residues form a disulfide bond to render peptide cyclic; X being random amino

acid) was used for screening. J774A.1 cells (2.5×10^5) were first incubated with 5×10^{10} pfu

(plaque-forming unit) inactivated phages displaying the sequence, RPARPAR, for one hour at

4°C. RPARPAR is a prototypic CendR (C-end Rule) peptide that will bind to a known receptor,

neuropilin-1 (NRP1)[55]. Here, RPARPAR phages were inactivated for their infection ability by UV

exposure before incubation with cells, and the pre-incubation of RPARPAR phage was to

exclude all NRP1-binding peptide sequences. Next, 5×10^9 pfu CX7C library was incubated with

cells for another hour at 4°C. Phage tittering and subsequent rounds of enrichment were carried

out according to our established protocol[54]. After three rounds of biopannings, the peptide

sequences between two terminal Cysteine were determined using next generation sequencing

performed by the DNA analysis core facility at Sanford Burnham Prebys Medical Discovery

Institute.

Peptide binding to cells. FAM-X-CRV (X being one copy of 6-aminohexanoic acid

linker) and biotin-X-CRV were synthesized by Lifetein, LLC (Hillsborough, NJ). The control

peptides used here included GGSGGSKG and ARA peptide[56]. Cells were incubated on rotator

with indicated peptides at a final concentration of 10 µM in the solution of DMEM plus 1% BSA.

For competition study, biotin-X-CRV was added to a final concentration of 500 µM together with

FAM-X-CRV (10 µM final). After 1 h at 4°C, cells were washed 3 times with PBS followed by

flow cytometry analysis.

Affinity Chromatography. The membrane proteins of Raw264.7 cells were isolated

using Mem-PER Plus membrane protein extraction kit (Thermo Fisher Scientific) according to

the manufacturer's instruction. Affinity chromatography was then performed with a protocol

adapted from our previous report[54]. Briefly, biotin-X-CRV was first immobilized onto streptavidin

coated magnetic beads (Thermo Fisher Scientific), then incubated with the membrane protein

extracts of Raw264.7 cells at 4°C overnight. After two times of washing with PBS, beads were

first incubated with GGSGGSKG peptide (a final concentration of 1 mM) at 4°C for 3 h, to elute

those nonspecifically bound proteins. Lastly, beads were incubated twice with FAM-CRV (a final concentration of 2 mM) at 4°C (2 h each time), to elute those proteins specially bound to CRV. The elutes from GGSGGSKG (control peptide) and FAM-CRV were collected and subjected to mass spectrometry analysis by the mass spectrometry core facility at Sanford Burnham Prebys Medical Discovery Institute.

Bacterial culture. All bacterial work was performed in an approved BSL-2 facility with a clean hood. Staphylococcus aureus was cultured by incubating 50 uL of bacteria in 10 mL of the brain heart infusion broth (Fisher Scientific) for 16h in a shaking incubator at 37ºC and shaking at 200 RPM with the cap loose. The culture was re-introduced to the lag phase from the stationary phase by sub-culturing 10 uL of bacteria in fresh 5 mL of brain heart infusion broth for 2h in a shaking incubator at 37ºC and shaking at 200 RPM with the cap loose.

Cell culture. Raw 264.7 and J774a.1 macrophage cell lines were cultured in DMEM supplemented with 10% FBS and 1% penicillin/streptomycin. All cells were incubated at 37ºC in 5% CO_2.

Fusion of DiI-loaded or calcein-loaded nanoformulations were tested by seeding 6-well plates with 0.3 x 10^6 cells on top of 22 mm round coverslips (BD Biocoat Collagen Coverslip, 22 mm), growing to 80% confluence overnight, and treating the cells with the nanoparticles at 1 mg lipid dose. The formulations without CRV-conjugations were incubated at 37℃ in 5% CO_2 for 10 min, whereas the formulations with CRV-conjugation were incubated for 5 min. Calcein-loaded particles were incubated for 10 min after cells were pre-treated with 500 nM of LysoTracker Red DND-99 (Thermo Fisher Scientific) for 1h at 37ºC in 5% CO_2. The non-fusogenic particles generally demonstrate higher uptake (approximately 3x) into cells relative to the fusogenic particles. For clearer visualization of the LysoTracker, the dose of F-pSi-Cal NF-pSi-Cal was decreased to 0.3 mg lipid dose. After incubation, the cells were washed in PBS three times to remove any particles that were not taken up. The cells were fixed in 1% paraformaldehyde

(PFA, Santa Cruz Biotechnology) for 10 min, then washed with PBS three times. The coverslips were mounted on glass slides with ProLong® Diamond Antifade Mountant with DAPI (Life Technologies), dried and kept in the dark until examined by confocal microscopy (Zeiss LSM 710 NLO). Pearson's correlation coefficient for co-localization was calculated using the Coloc2 plugin from ImageJ. At least ten representative images were analyzed to obtain the average coefficient.

For transmission electron microscopy of cells, particles were introduced to the Raw 264.7 and J774a.1 cells under the same conditions as above, and cells were fixed with glutaraldehyde overnight before being stained with osmium and uranyl acetate during embedding, and with lead on the TEM grids. The samples were viewed using a JEOL 1200 EX II TEM instrument.

In vitro **knockdown.** *In vitro* knockdown efficiencies of the nanoformulations were quantified using two-step quantitative real-time reverse transcription polymerase chain reaction (qRT-PCR, Roche LightCycler 96). Raw 264.7 cells were seeded on a 6-well plate at 3 x 10^5 cells per well and grown to 80% confluency overnight. The cells were incubated with the desired nanoformulations at 0.2 nmol of siRNA in 2 mL of media (100 nM siRNA). 48h post-incubation, the cell media was removed, and RNA was purified using the QIAshredder and RNeasy Mini Kit (Qiagen, Valencia, Ca). cDNA was transcribed from the purified RNA using the BIORAD iScript cDNA Synthesis Kit and heat-treated in the Eppendorf Vapo.protect Mastercycler thermal cycler. cDNA was mixed with IRF5 primers, or the control HPRT primers (IRF5 forward: AATACCCCACCACCTTTTGA; IRF5 reverse: TTGAGATCCGGGTTTGAGAT; HPRT forward: GTCAACGGGGGACATAAAAG; HPRT reverse: CAACAATCAAGACATT-CTTTCCA) and iQ SYBR Green Supermix according to the manufacturer's instructions. RT-PCR analysis was performed in the BIORAD 96-well white Multiplate PCR Plates using the Roche LightCycler 96. The quantification was performed at n=6 and in RNAse- and DNAse-free laminar flow hood

dedicated to RNA work. Relative knockdown was statistically evaluated using one-way ANOVA with Tukey's HSD post-hoc analysis.

Cell viability assay. Raw 264.7 and J774a.1 macrophages were cultured in 6-well plates on top of 22 mm round coverslips (BD Biocoat) to 80% confluency from seeding density of 3×10^5 cells/well. The cells were incubated for 1h with nanoparticle formulations containing 0.5 mg and 1 mg total lipid mass. After incubation, cells were washed three times with PBS. Molecular Probes LIVE/DEAD Cell Viability/Cytotoxicity Kit (Thermo Fisher Scientific) uses calcein AM for live cell uptake ($\lambda_{ex}/\lambda_{em}$ = 494/517 nm), and ethidium homodimer-1 (EthD-1) for dead cell infiltration ($\lambda_{ex}/\lambda_{em}$ = 528/617 nm). The probes were treated and incubated with cells according to the manufacturer's instructions. Briefly, probe stock was composed of 60 μL of 2 mM EthD-1, and 15 μL of 4 mM calcein AM in 30 mL fresh DMEM, and each cell well was incubated with 2 mL of the probe stock for 30 min at room temperature in the dark. The cells were then washed with PBS three times, fixed with 1% PFA and mounted on glass slides. The slides were dried and imaged using confocal microscopy (Zeiss LSM 710 NLO), and the calcein AM/EthD-1 fluorescence signals were quantified using ImageJ at n=20. The cell viability was statistically evaluated using one-way ANOVA. For fluorescence plate reader validation, the same experiment was conducted in a 96-well plate with seeding density of 6,000 cells/well in 200 μL media and probe treatment. After 30 min room-temperature incubation in the dark, the fluorescence was read in a Gemini XPS spectrofluorometer (Molecular Devices) at n=8 per group. The quantified viability was normalized to the PBS control treatment.

Biosafety of fusogenic nanoparticles. All animals for all the *in vivo* studies were handled, anesthetized, and euthanized according to the Institutional Animal Care and Use Committee (IACUC) guidelines. All animal experiments were performed independent of each other with different cohorts of mice. For *in vivo* biosafety validation, healthy Balb/C mice were intravenously injected with F-sIRF5-CRV at 23.2 µmol/kg lipid, corresponding to 69 µg/kg

siRNA, and 0.3 mg/kg pSi in 100 μL PBS. After 24h circulation, the mice were sacrificed under deep isofluorane anesthesia (no response to toe pinch) by cardiac perfusion, and brain, heart, lungs, liver, kidneys, and spleen were harvested. Organs were fixed immediately in 4% PFA, and sent to the University of California, San Diego (UCSD)'s histology core to be paraffinized and sectioned for hematoxylin and eosin (H&E) staining. The stained slides were histopathologically evaluated by Dr. Kent Osborn (Associate Director, Animal Care Program, UCSD).

In vivo **infection model.** After 16h incubation in brain heart infusion broth, 10 uL Staph. aureus was sub-cultured in 5 mL of fresh broth for 2h to reach growth phase. The optical density at 600 nm was measured using a cuvette spectrometer with the broth set as the blank. Five mL of bacterial culture at $OD_{600} \approx 0.32$ was centrifuged, the bacteria were washed by centrifugation in PBS three times, and re-suspended in 200 μL of PBS for inoculation. The Staph. aureus pneumonia animal model was established in 6-8 week old male Balb/C mice by intratracheal catheter injection of approximately 1×10^7 CFU of bacteria in 10 μL of PBS. All treatment-injections were performed 24h after inoculation of the bacteria.

Biodistribution of CRV. Three healthy and infected (24h post-infection) mice were intravenously injected with CRV tagged with 5'6-FAM dye in 100 μL PBS at a concentration of 1 mg/mL. Organs were harvested after 1h circulation and fixed in 4% PFA. Organs were sent to the UCSD histology core to be paraffinized, sectioned, and stained with DAPI nuclei stain and F4/80-AF555 macrophage marker for immunofluorescence analysis under the Zeiss LSM 710 NLO confocal microscope with single photon laser (for excitation of DiI, calcein, LysoTracker Red) and Mai-Tai Laser HB (690-1020nm) (for two-photon excitation of DAPI).

Nanoparticle biodistribution. 8-week old male Balb/C mice were intratracheally infected as described. 24h post-infection, infected and healthy mice were intravenously injected

with siIRF5-loaded fusogenic pSiNPs with or without CRV-conjugation, at 23.2 µmol/kg lipid, corresponding to approximately 69 µg/kg siRNA, and 0.3 mg/kg pSi 100 µL in PBS. The DiI-loaded particle localization was visualized using the IVIS 200 (Perkin Elmer) with 0.12s exposure time on the DsRed excitation and emission filters. Both healthy and infected animals were sacrificed and harvested for organs 24h post-infection, with additional 1h-post treatment analyses for infected animals injected with the fusogenic nanoparticle formulations. ImageJ was used to quantify the fluorescence of each organ, and averaged over the three mice per group. Infected lung homing was further validated using fluorescence activated cell sorting (FACS). 24h post-infection, mice were intravenously injected with calcein-loaded non-fusogenic particles with MPT, fusogenic particles without CRV, and fusogenic particles with CRV at 23.2 µmol/kg lipid, corresponding to 69 µg/kg siRNA, and 0.3 mg/kg pSi in 100 µL PBS. 1h post-injection, the mice were sacrificed by cardiac perfusion with PBS. The harvested lungs were homogenized and the homogenates were processed with the LSR Fortessa FACS instrument, and analyzed using the FlowJo software (FlowJo, LLC). For immunofluoresce microscopy of infected lungs, mice were intravenously injected 24h post-infection with DiI-loaded formulations of non-fusogenic and fusogenic particles (without siRNA) conjugated with CRV, and were sacrificed for lung harvest and fixation in 4% PFA at 24h post-injection. The fixed lungs were paraffinized and sectioned and stained with FITC-labelled F4/80 macrophage marker. The sections were observed under Zeiss LSM 710 NLO confocal microscope for DiI and FITC localizations.

In vivo therapeutic efficacy of fusogenic nanoparticles. 8 week-old male Balb/C mice were intratracheally infected as described. Twenty-four hours post-infection, infected mice were intravenously injected with 100 µL of PBS or siIRF5-loaded fusogenic pSiNPs conjugated with CRV at 23.2 µmol/kg lipid, corresponding to 69 µg/kg siRNA, and 0.3 mg/kg pSi in 100 µL PBS. PBS-injected mouse was harvested for the lungs _ad mortem_ (24h post-injection), whereas nanoformulation-injected mouse was sacrificed and harvested for the lungs 3 days post-

injection. Additionally, lungs from healthy mouse and infected mouse with no injection, at 24h post-infection, were harvested. All organs were immediately fixed in 4% PFA to be sent to the UCSD histology core for paraffinization, sectioning, and H&E staining. The stained sections were histopathologically evaluated by Dr. Kent Osborn (Associate Director, Animal Care Program, UCSD).

To confirm clearance of bacteria from lungs, the number of colony-forming units (CFU) of Staph. aureus was determined from titering of lung homogenates. 24h post-infection, mice were intravenously injected with 100 μL of PBS, non-fusogenic particles with siIRF5 and CRV conjugation, fusogenic particles with sham siRNA (siLuc, luciferase encoding siRNA) conjugated with CRV, or fusogenic particles with siIRF5 and CRV conjugation at 23.2 μmol/kg lipid, corresponding to 69 μg/kg siRNA, and 0.3 mg/kg pSi in 100 μL PBS. Healthy mice with no injection were also observed. At days 2, 3, 4, and 8 post-infection, mice were sacrificed for lung harvest. Due to factors that may affect the bacteria count on the day of the therapeutics injection, day 1 (ie. variations in before vs. after injection, the number of hours post-injection, etc.), we began the count at day 2. In cases where mice succumbed to infection prior to the time-points, the lungs were harvested *ad mortem*. The lungs were weighed, gently washed in PBS, and then homogenized. The homogenates were serially diluted to a dilution factor of 10^7, plated on agar-coated petri dishes and incubated at 37ºC overnight. The Staph. aureus colonies were counted n=4 for each dilution factor, and divided by the lung mass. The average CFU/g was quantified using counts from 4 plates at equivalent dilution factors from 2 mice (n = 4 plates x 2 mice = 8).

Finally, a survival challenge was performed with infected mice, who were intravenously injected 24h post-infection with the treatment compounds. Each group had 8 mice, which were blindly observed daily for survival. Moribund mice that showed signs of expiring within 5h were

sacrificed according to the IACUC guidelines. The resulting data were statistically evaluated using single way ANOVA and post hoc comparisons using Tukey's HSD test at $p < 0.05$.

In vivo IRF5 knockdown efficiency. 8 week-old male Balb/C mice were intratracheally infected as described above. Twenty-four hours post-infection, infected mice were intravenously injected with 100 μL of PBS or siIRF5-loaded fusogenic and non-fusogenic pSiNPs with or without CRV at 23.2 μmol/kg lipid, corresponding to 69 μg/kg siRNA, and 0.3 mg/kg pSi in 100 μL PBS. Twenty-four hours post-injection and circulation, mice were sacrificed for brochoalveolar lavage (BAL). BAL was performed by intratracheal instillation of a mouse catheter, with a suture tied around the trachea to prevent leakage. 1 mL of PBS was injected into the lungs through the catheter, and aspirated back out. The process was repeated three times to collect up to 2.5 mL of the BAL fluid. Lungs were also harvested after completion of the BAL procedure.

Cells from the BAL fluid were collected by centrifugation at 350g for 10 min at room temperature. The supernatant was removed, and the cell pellets were washed with PBS once by centrifugation at 350g for 10 min at room temperature. Prior to qRT-PCR processing, the cell pellets were kept dry at -80ºC. Harvest lungs were weighed and homogenized, 30 mg of the homogenates were isolated for qRT-PCR processing and stored at -80ºC.

The *in vivo* knockdown of IRF5 was quantified using two-step quantitative real-time reverse transcription polymerase chain reaction (qRT-PCR, Roche LightCycler 96). The cell pellets or the lung homogenates were lysed and RNA was purified using the QIAshredder and RNeasy Mini Kit (Qiagen, Valencia, Ca). cDNA was transcribed from the purified RNA using the BIORAD iScript cDNA Synthesis Kit and heat-treated in the Eppendorf Vapo.protect Mastercycler thermal cycler. cDNA was mixed with IRF5 primers, or the control HPRT primers (IRF5 forward: AATACCCCACCACCTTTTGA; IRF5 reverse: TTGAGATCCGGGTTTGAGAT; HPRT forward: GTCAACGGGGGACATAAAAG; HPRT reverse: CAACAATCAAGACATT-

CTTTCCA) and iQ SYBR Green Supermix according to the manufacturer's instructions. qRT-PCR analysis was performed in the BIORAD 96-well white Multiplate PCR Plates using the Roche LightCycler 96. The quantification was performed at n=6 and in RNAse- and DNAse-free laminar flow hood dedicated to RNA work. Relative knockdown was statistically evaluated using one-way ANOVA with Tukey's HSD post-hoc analysis.

5.4   Synthesis of fusogenic liposome-coated pSiNPs

The siRNA carrier consisted of porous silicon (pSi) nanoparticles, prepared by electrochemical etch of single-crystal silicon wafers and ultrasonic fracture of the resulting porous layers into nanoparticles. siRNA and hydrophilic fluorescent dye payload were loaded into the porous nanoparticles by subjecting the payload and the pSi nanoparticles to ultrasound in an aqueous solution of calcium chloride[36]. Fusogenic liposomes were synthesized using the established film hydration method[30,31], and were coated around the payload-loaded pSi nanoparticles by co-extrusion through 200 nm polycarbonate membranes (**Fig 5.1b**). The fusogenic (F) feature of the liposomes is derived from a controlled ratio of structural, cationic, and PEGylated lipid components[30,31] (**Table 5.1**). Control non-fusogenic (NF) nanoparticles were prepared using the structural and PEGylated lipids, but without the cationic component—yielding a more conventional liposome. Dynamic light scattering (DLS) and microscopic data of the F-pSi confirmed an average hydrodynamic diameter of approximately 190 nm with a distribution range of 100-400 nm, with a cationic surface charge of ~10 mV (**Table 5.2**). The F-pSi formulations were physically stable in deionized water for up to 28 days at 4°C (**Fig 5.2**). The loading efficiency of the siRNA payload was approximately 25 wt%, substantially larger than the 1-14 wt% achieved with other reported oligonucleotide-loaded nanoplatforms, such as lipid-based nanoparticles and mesoporous Si-polymer hybrid systems (**Table 5.3**). Notably,

particles with sizes comparable to those used in the study (200 nm) display oligonucleotide loadings of less than 5 wt%.

5.5   Fusion and intracellular delivery of fusogenic pSiNPs *in vitro*

Nanoparticles were loaded with the hydrophilic dye calcein in the pSi core or with the lipophilic dye DiI in the lipid leaflets to evaluate differences in intracellular localization and to infer uptake pathway. Calcein was chosen as the model-siRNA payload (**Fig 5.3a**), because it shares two key characteristics with oligonucleotides: (i) it is anionic, and (ii) it is membrane-impermeable. The lipophilic DiI was chosen to track fusogenic uptake, because the hydrophobic molecule localizes in lipid bilayers (**Fig 5.3a**)[37]. In the event of fusogenic uptake, DiI would be expected to diffuse from the liposomal bilayer of the nanoparticle into the plasma membrane, whereas non-fusogenic uptake would result in endocytosis and localization in the cytoplasm.

Confocal microscopy revealed that the F-pSi formulation fused with the plasma membrane of cultured J774A.1 murine macrophages and delivered the payload into the cytoplasm. The F-pSi formulation that contained DiI in the liposomal coating transferred this lipophilic dye to the cell membrane (**Fig 5.3b**), confirming fusion, whereas the F-pSi formulation that contained calcein in the nanoparticle interior dispersed this hydrophilic dye throughout the cytoplasm (**Fig 5.3c**). Control experiments performed using non-fusogenic (NF) nanoparticles resulted in an overall lower uptake, and the DiI signal from NF formulation were found to be concentrated within the cytoplasm (**Fig 5.3e**). That these nanoparticles were associated with intracellular endosomes/lysosomes was confirmed using LysoTracker Red stain (**Fig 5.3c, f**). By contrast, fusogenic nanoparticles showed dispersed calcein signals that did not co-localize with lysosomal compartments. The F-pSi attained an average Pearson's correlation coefficient (PCC) = 0.04 ± 0.03, whereas the NF-pSi attained an average PCC = 0.59 ± 0.18. The two

values are significantly different by T-test ($p = 2 \times 10^{-6}$), validating the lysosomal compartmentalization of the NF-pSi formulation.

The ability of the nanoparticles to be selectively targeted to the macrophages was tested using a peptide selected in a phage library screen[38,39] for cultured J774A.1 murine macrophages (**Fig 5.4a**). This peptide, denoted as CRV, is a 9-amino acid peptide (sequence CRVLRSGSC) made cyclic by a disulfide bond between the side chains of the two cysteine residues. CRV labeled with a 5-FAM dye (FAM-CRV) showed a higher binding ability than control peptides to J774A.1 and Raw 264.7 macrophages (**Fig 5.4b**). Biotin labeled CRV was able to significantly reduce the binding of FAM-CRV to the macrophages (**Fig 5.4c**). All these results suggest that CRV peptide specifically binds to macrophages.

To permit coupling to the NPs, the peptide was modified by adding a third cysteine through a 6-aminohexanoic acid linker and labeled with a 5-FAM dye to track by fluorescence. The 3-cysteine peptide was attached to the PEG head of a minor fraction of the lipids *via* maleimide coupling chemistry. A fusogenic formulation containing CRV, the DiI membrane dye, and pSi nanoparticles (F-DiI-CRV) showed strong co-localization of the DiI and FAM signals at specific points on the cell membrane (**Fig 5.3d**), suggesting that the CRV anchors the particles to its specific macrophage membrane receptors to allow localized fusion. The data are more consistent with a membrane fusion mechanism rather than endocytosis; substantial endocytosis would be expected to lead to increased DiI signals from the cell cytoplasm. We note that CRVs appeared to expedite the fusion process, as only half the incubation time was needed to achieve a comparable level of fusion. In contrast, the non-fusogenic NF-DiI-CRV (**Fig 5.3g**) displayed a cellular distribution similar to NF-DiI-mPEG, a non-fusogenic formulation that contained mPEG (methoxy polyethylene glycol) in place of the targeting peptide-conjugated PEG (**Fig 5.3e**). The CRV-FAM and DiI signals co-localized in clusters within the cytoplasm,

indicative of endosomal and lysosomal compartmentalization. These results indicate the targeting peptide is permissive for either cell entry pathway.

TEM results (**Fig 5.3h-j**) verify the different uptake pathways between fusogenic and non-fusogenic formulations. While the targeted non-fusogenic particles demonstrated macropinocytosis, and were found to be localized in intracellular vesicles (**Fig 5.3i**), only the core pSi of the targeted fusogenic particles were found degrading in the cell cytoplasm (**Fig 5.3j**).

5.6   Cytotoxicity and *in vitro* knockdown efficacy of fusogenic pSiNPs

To test the hypothesis that the fusogenic pathway for uptake and direct cytoplasmic release of siRNA attains higher knockdown efficiency than the endosomal uptake route, we delivered siRNA encoding the IRF5 gene to cultured Raw 264.7 macrophage cells, and gene expression was analyzed by quantitative real-time PCR (qRT-PCR) (**Fig 5.5a**). Fusogenic nanoparticle formulations (F-siIRF5) delivering 200 nM siRNA demonstrated high knockdown efficiencies with or without an added CRV macrophage targeting peptide (96.4% and 96.6% respectively). Knockdown was comparable to that of the standard transfection agent, Lipofectamine (95.5%). The non-fusogenic formulation (NF-siIRF5-CRV) demonstrated only 42.9% knockdown with high standard deviation. The relatively high variance in this control is attributed to occasional incidences of endosomal escape[22]. Administration of free-siIRF5 achieved only 6.3% knockdown under similar conditions, statistically similar to the PBS control. The presence of CRVs on the particle surface had no adverse effect on the knockdown ability. These experiments established that the fusogenic coatings enable higher knockdown efficiency than a conventional liposomal coating, and that active targeting of the fusogenic formulations does not enhance gene silencing in the isolated cellular environment of the *in vitro* experiment,

likely because the long incubation period allowed the entry of non-targeted NP to catch up with the targeted NPs.

Assays of cell cytotoxicity and histological evaluations of major organs were performed to assess biosafety of the fusogenic nanoparticles and their siRNA payload. The primary concern with the fusogenic system is the insertion of the cationic lipid constituents into cell membranes, disrupting membrane charge homeostasis of cells. Two macrophage cell lines, J774a.1 and Raw 264.7, were incubated for 1h with nanoparticle formulations containing 0.5 mg and 1 mg total lipid mass. Calcein AM and ethidium homodimer-1 assays indicated >95% cell viability compared to the PBS-treated control for either fusogenic or non-fusogenic CRV-targeted nanoparticle constructs (**Fig 5.5b**). To test *in vivo* biosafety, healthy Balb/C mice were intravenously injected with the fusogenic, CRV-targeted nanoparticle construct (F-siIRF5-CRV) at doses corresponding to 23.2 μmol/kg lipid, corresponding to 24 μg/kg siRNA. After 24h circulation, the major organs were harvested and sectioned for H&E histopathological evaluation (**Fig 5.5c-h**). All major organs were found to be normal, though the liver showed minor incidental findings also seen in control mice.

5.7   Biodistribution of fusogenic pSiNPs targeted to infected lungs and macrophages

We established a Staph. aureus pneumonia animal model involving intratracheal injection of bacteria at a dose that was lethal to untreated mice within 2 days. First, we tested the homing ability of the CRV macrophage-targeting peptide in this model, using the "free" peptide not bound to any nanoparticle, but conjugated to a fluorescein (5-FAM) dye to allow tracking. Infected and healthy control mice (n=3 each) were intravenously injected with FAM-CRV 24h post-infection. Confocal immunofluorescence microscopy of organs harvested from the healthy animals showed signs of renal clearance but no selective homing to any of the

macrophage-heavy organs (**Fig. 5.6a**). However, the infected animals demonstrated clear evidence of selective homing, with CRV-FAM signals co-localizing with the F4/80-AF555 macrophage signals in the infected lungs. The peptides cleared primarily through the kidneys, with minor localizations seen in the spleen and liver. The results demonstrate the ability of the CRV peptide to home to macrophages in Staph. aureus-infected lungs.

Next, we tested the *in vivo* homing ability of the CRV when attached to the fusogenic nanoparticles. Mice were intravenously injected, 24h post-infection, with DiI-loaded F-siIRF5 nanoparticles coated with conjugated CRV peptide, and the *in vivo* biodistribution was tracked by immunofluorescence microscopy of organs harvested at 1h and 24h post-treatment. The quantified DiI fluorescence signal showed strong accumulation in the lungs after 1h, and it was still detected 24h post-treatment (**Fig. 5.6b**; **Fig 5.7** shows the representative images of the organs). Control experiments using the same nanoparticle construct but replacing the CRV-conjugated PEG with methoxylated PEG (F-DiI-mPEG) showed minimal accumulation in the lungs. The efficacy of lung homing was quantified by fluorescence-activated cell sorting (FACS), which showed that the CRV-conjugated fusogenic particles (F-DiI-CRV) homed to infected lungs with high selectivity (**Fig 5.8**). While the free-CRV peptide showed preferential clearance through the kidneys, the nanoparticles showed no elevated fluorescence over background autofluorescence signals in the kidneys, and substantially increased clearance through the liver. These results were similar for both the targeted and the untargeted fusogenic nanoparticle constructs, in both healthy and infected animals. The clearance data are consistent with the size limitations displayed by the organs of mononuclear phagocytic system (MPS); nanoparticles < 5.5 nm tend to be cleared by the kidneys, and nanoparticles show preferential clearance through the hepatobiliary system[40,41]. We note the CRV-conjugated nanoparticles showed substantially enhanced uptake in the spleen of infected animals relative to controls, which is

attributed to the splenic clearance and filtration of targeted macrophages that have phagocytosed senesced neutrophils and damaged cells from the infected lung.

We next studied the efficacy of CRV targeting and fusogenic uptake at the cellular level in the lungs using DiI-tagged nanoparticles. The lungs of healthy mice intravenously injected with targeted fusogenic nanoparticles (F-DiI-CRV) showed minimal recruitment of macrophages marked by F4/80-FITC, and no visible F-DiI-CRV accumulation (**Fig 5.6c**). Healthy lungs possess a baseline number of alveolar macrophages, with no significant recruitment of peripheral macrophages. However, the lungs of infected control mice (PBS injection at 24h post-infection) recruited a high number of macrophages, as expected of an inflammatory process (**Fig 5.6d**). The group of infected mice injected (24h post-infection) with non-fusogenic nanoparticles (NF-DiI-CRV) showed minimal co-localization of macrophages with DiI from these nanoparticles (**Fig 5.6e**). In marked contrast, infected lungs of mice injected with the targeted fusogenic nanoparticles (F-DiI-CRV) showed high accumulation of DiI signals, which were strongly co-localized with macrophage fluorescence signals (**Fig 5.6f**). Taken together, the results show that the combination of CRV-targeting and fusogenic uptake achieves strong homing to circulating macrophages recruited to infected lungs.

5.8   Efficacy of macrophage-targeted fusogenic pSiNPs delivering anti-inflammatory siIRF5 for treatment of Staph. aureus-infected mice

With the cellular fusion and *in vivo* homing capabilities established, we next evaluated the therapeutic efficacy of the fusogenic, siRNA-loaded, CRV-targeted nanosystem (F-siIRF5-CRV) against a lethal dose of Staph. aureus in the mouse pneumonia model. As discussed above, we chose to deliver siRNA against the IRF5 gene of macrophages, in order to suppress inflammatory cytokine excretion of macrophages[13] and enhance bacterial phagocytosis and

tissue repair[10,15,16]. We initially studied bacterial colonization and titers in the lungs of mice in 3 treatment groups: (i) Staph. aureus-infected mice with no treatment (lungs harvested at fatality) ; (ii) infected mice treated with PBS (lungs harvested at fatality within 24h post-treatment); and (iii) infected mice treated with F-siIRF5-CRV via tail vein injection (lungs harvested 3 days post-treatment). A section of a healthy lung is shown for comparison in **Figure 5.9a**. The infected mice, when untreated (**Fig 5.9b**) or treated with PBS only (**Fig 5.9c**), displayed overt signs of neutrophilic pneumonia associated with bacteria. Moreover, Staph. aureus leakage into the perilaryngeal muscles was observed in these untreated controls (**Fig 5.9b inset**), and gram-positive cocci were identified in the lungs of the PBS-injected group by Gram staining (**Fig 5.9c inset**). Three days after injection of the F-siIRF5-CRV therapeutic, the lungs of the infected mice displayed an appearance similar to healthy lungs, and no bacteria were detected in the Gram stains (**Fig 5.9d**).

We also quantified the bacterial population in the various treatment groups by preparing lung homogenates and counting the number of bacterial colonies obtained (**Fig 5.9e**). Healthy mice showed an average baseline count of approximately 10^3 CFU/g. Control groups of infected mice treated with PBS, with the non-fusogenic targeted nanoparticle formulation containing siIRF5 (NF-siIRF5-CRV), or with the fusogenic targeted nanoparticle containing siRNA against luciferase as a negative control for siIRF5 (F-siLuc-CRV), were all observed to carry bacterial burdens of $>10^{10}$ CFU/g and all cohorts perished within 3 days of infection. By contrast, infected mice treated with the fusogenic targeted nanoparticle delivering the siIRF5 therapeutic (F-siIRF5-CRV) demonstrated a notable decrease in titer starting 2 days post-infection, and titers reached the baseline count at 8 days post-infection.

To confirm that the therapeutic effect resulted from IRF5 knockdown, qRT-PCR was used to determine the relative *in vivo* knockdown efficiency in infected mice. Bronchoalveolar lavage (BAL) fluid collected from the lungs of infected mice was observed to have significantly

lower expression of IRF5 (17%) in mice injected with the CRV-conjugated fusogenic pSi nanoparticles relative to the PBS, free siIRF5, CRV-conjugated non-fusogenic pSi nanoparticles, and non-targeted fusogenic pSi nanoparticle controls (**Fig 5.10a**). However, the lung homogenates processed after removal of BAL fluid showed no significant difference in IRF5 expression between all groups (**Fig 5.10b**). BAL fluid in healthy mice consists of 98% macrophages[42], whereas infected mouse BAL fluid accumulates activated macrophages and neutrophils that are recruited during the initial stages of inflammation; by seven days post-infection, the BAL fluid comprises 38% macrophages, 56% neutrophils, and 6% lymphocytes[42]. As the BAL fluid was collected 48h post-infection and 24h post-therapeutic injection, the population is expected to be primarily macrophages. On the other hand, the lung homogenate is composed of epithelial, endothelial, and interstitial cells[43], with a small population of macrophages. Thus, we conclude that the CRV-conjugated fusogenic particles successfully homed to the activated macrophages of the infected lungs in a selective manner and silenced IRF5 gene expression.

In a separate experiment, mouse survival was dramatically improved with the F-siIRF5-CRV nanotherapeutic; 100% of the mice administered the formulation survived the lethal challenge and showed no apparent sequelae from the infection within a 4-day post-infection observation period (**Fig 5.9f**). Mice administered the NF-siIRF5-CRV, and mice administered the F-siLuc-CRV, with siLuc as a sham siRNA, showed limited survival, with a significantly lower average number of survival days compared to the F-siIRF5-CRV (one-way ANOVA, post hoc comparisons using Tukey's HSD test, **Fig 5.9g**). By comparison, the first-line antibiotic vancomycin gave only 30% survival rate in the same pneumonia model when intravenously administered at a 3 mg/kg (the published ED_{50} for vancomycin in mice is in the range 0.65-4 mg/kg[44,45]) single dose given one day post-infection[46].

5.9   Discussion and Conclusions

A primary role of the inflammatory response during bacterial infection is to recruit additional macrophages whose function ultimately shifts to bacterial phagocytosis and tissue repair [10-15]. However, an excessive inflammatory reaction can become septic, generating multi-organ failure and fatality [2,3]. This study harnessed siRNA targeting the IRF5 gene, a transcriptional regulator of the inflammatory M1 macrophage phenotype that is a key inductor of pro-inflammatory cytokines[11]. We hypothesized that effective silencing of this gene would suppress the inflammatory response and mitigate a lethal bacterial infection.

Silencing of IRF5 has not previously been tested as a means to slow or eliminate bacterial infections. A serious bacterial infection, such as the lethal *Staph. aureus* model studied here, requires an overwhelming and effective immune response. While IRF5 is an attractive target, it was not clear that a strong response could be achieved using gene therapy, which can be notoriously inefficient *in vivo* [47]. Achieving high *in vivo* knockdown efficiency has been a challenge due to passive clearance in circulation, and endocytic uptake that causes extracellular excretion or lysosomal degradation of the oligonucleotides [22,23]. In this work, we addressed these problem by incorporating three key features into the nanoparticle design: (i) a host pSi nanoparticle with high oligonucleotide loading efficiency and low systemic toxicity; (ii) a fusogenic lipid coating that effectively avoids endosomal uptake; and (iii) a targeting peptide that selectively homes the nanoparticles to macrophages.

The first new aspect of the present approach was the nanoparticle host for the RNAi therapeutic. The carrier was based on porous silicon, a drug delivery vehicle that has shown good biocompatibility [48-50] and an ability to load and protect sensitive therapeutics, such as proteins [51-53] and oligonucleotides [35,54,55]. We used a self-sealing chemistry that trapped the oligonucleotide payload within the nanoparticle in a calcium silicate matrix [36], loading a quantity

at least 2x greater than has been achieved with typical liposomal or related hybrid carriers (**Table 5.3**). The calcium silicate pSi nanoparticles follow the exact protocol as introduced in Kang et al. [56] In brief, large quantities of siRNA are loaded into pSi by precipitating a calcium silicate shell that simultaneously traps the payload. As the pSi matrix dissolves, the silicate product reacts with calcium (II) ion present in the $CaCl_2$ solvent, and forms Ca_2SiO_4 at the nanoparticle surface. To load siRNA, the oligonucleotide is added to the solvent to trap the molecules during the Ca_2SiO_4 shell formation. Between the presented work and the referenced formulation, the pSi chemistry and properties remain identical, with the exception of particle size (which was ~180 nm [56]). Thus the pore volume in the F-pSi system is also expected to decrease by approximately 80% (1.36 ± 0.03 to 0.29 ± 0.04 cm^3 g^{-1}) upon shell formation. In contrast to the referenced work, the small pSi nanoparticle sizes (68.1 ± 5.8 nm; **Table 5.2**) in the F-pSi system allows it to dissolve at a much accelerated rate under physiological conditions (pH 7.4, 37 °C). Moreover, the higher mass loading is important in minimizing the injected dose and maximizing gene silencing in the cells. Also, unlike the cationic polymer or oligomer stabilizers usually employed to increase loading of negatively charged oligonucleotide payloads, Ca^{2+} is an endogenous species that is essential for cellular function.

Second, we introduced a liposomal coating that protected the nanoparticle from premature degradation until cellular fusion. The coating contained a specific composition of lipids that favored fusion with the cellular membrane over endocytosis (**Fig 5.3b-g**). The fusogenic lipid coating was composed of pro-fusogenic lipids and moieties. DMPC is the major constitution that acts as the structural backbone of the liposome, with a relatively low phase transition temperature ($T_m = 24$ºC). The low transition temperature gives the L_α liquid crystal phase at room temperature and body temperature [57]. The L_α phase is the more fluidic, dynamic, and permeable structure that allows for the wide size range (100-400 nm) of extruded liposomal coatings and an easier fusion potential [58]. DOTAP is the cationic lipid essential for the

183

electrostatic attraction toward the anionic plasma membrane [59,60]. Lastly, PEGylated lipid was also found to be imperative in fusion [61]; though the exact mechanistic role of PEG is not yet known, it is hypothesized that PEG electrostatically binds water molecules to dehydrate the lipid head groups, which leads to structural asymmetry in the lipid alignment and drives double-leaflet to single-leaflet fusion as the energetically favorable route [62], similar to how SNARE proteins anchor and pull vesicles into merging with plasma membranes endogenously; in fact, neuronal SNAREs have been observed to promote PEG-mediated fusion [63]. The fusion pathway peeled off the protective liposomal coating, which enhanced the rate of dissolution of the pSi carrier and release of the RNA payload after the bare nanoparticle was inserted into the cytosol, giving substantially greater knockdown of IRF5 *in vitro* (**Fig 5.5a**).

Third, we used an activated macrophage-specific targeting peptide, which provided strong and selective homing to macrophages in infected lungs. The effectiveness of the targeting peptide in enhancing gene silencing was not apparent *in vitro* due to the high efficacy of the fusogenic coatings (**Fig 5.5a**). However, the targeting peptide was critical for effective homing to macrophages in infected lungs *in vivo*. The CRV-targeted nanoparticle constructs localized in infected and not healthy lungs (**Fig 5.6b, c, f**), whereas nanoparticles containing the sham targeting group showed little accumulation in either infected or healthy lungs (**Fig 5.6b**). Furthermore, the CRV-conjugated nanoparticles strongly co-localized with macrophages in infected lungs (**Fig 5.6f**).

The siRNA therapeutic chosen for this study focused on enhancing the macrophage response to an infection by selectively inhibiting a gene associated with inflammatory M1 macrophages. Macrophages are essential components of the innate immune system that are responsible for defense against a wide range of pathogens. On a cellular level, the alveolar macrophages respond to a challenge of infectious particles by secreting cytokines, including TNF-α, IL-1β, IL-6, IL-8, IL-12, and IL-23 to recruit polymorphonuclear neutrophils (PMNs),

which secrete additional cytokines. However, this prolonged excretion of inflammatory cytokines results in deleterious effects that drastically lower the chances of recovery [64]. In this study, we knockdown IRF5, a key pro-inflammatory marker of M1 inflammatory macrophages [11].

There are two leading hypotheses regarding the role of IRF5 in macrophages. The first is that knockdown of IRF5 in the M1 macrophage preserves its polarization, but eliminates pro-inflammatory factors [12]. It is known that knockdown of IRF5 inhibits the expression of TNF-α and other inflammatory markers of M1 (e.g. *IL12A and IL23A*[11]), lowering recruitment of Th1/Th17 and impeding inflammation. In addition, a decrease in the TLR-mediated induction of pro-inflammatory cytokines (including IL-6) leads to further decrease in inflammation [65]. The result of eliminating the action of IRF5 is an overall reduction in extended and damaging inflammation that occurs after initial leukocyte recruitment, preventing destruction of lung infrastructure and decreasing survival burden.

The second hypothesis is that IRF5 knockdown causes M1 macrophages to repolarize to the M2 phenotype, and become highly anti-inflammatory, yet strongly tissue-restorative [10]. In the M2 phenotype, IL-10 is upregulated and IL-12 is downregulated, the combination of which increases arginase-1 production to reduce nitrogen monoxide excretion and inflammation [10]. Moreover, the M2 macrophages are known to induce Th2 cytokine responses to mediate immune responses against extracellular bacteria and toxins [66]. Thus in the re-polarization model, knockdown of IRF5 induces both anti-inflammatory, tissue-regeneration and immune effects to reduce infection burden and inhibit sepsis. Either model supports the hypothesis that knockdown of IRF5 will improve healing of infections that induce an excessive inflammatory response. Indeed, *in vivo* silencing of IRF5 has been shown to reduce inflammation and accelerate tissue regeneration in mouse models of myocardial infarct and skin wounds [10]. The improved healing response was attributed to attenuation of M1 macrophage polarization, which

is typically the dominant macrophage phenotype in wounds shortly after injury. In these studies, the siRNA was delivered in a lipidoidal nanoparticle vehicle [67].

Finally, it should be pointed out that the substantially improved survival afforded by the targeted gene nano-therapeutic developed in this work relative to a standardized dose of vancomycin represents a significant finding. Vancomycin is a first-line antibiotic, which is prescribed at high dosage and prolonged administration when used to treat Staph. aureus infections [5]. Staph. aureus strains have a history of evolving antibiotic-resistance genes, such that we are currently facing vancomycin-intermediate (VISA) and -resistant (VRSA) strains that build strong peptidoglycan walls to bind and trap vancomycin, and inhibit its therapeutic action [2]. The IFR5 knockdown approach used here is unlikely to be susceptible to development of resistance.

Taken together, the combination of high payload capacity, fusogenic uptake, and macrophage-specific targeting yielded an IRF5-silencing construct that rescued all mice tested from a lethal dose of Staph. aureus, and that gave the immune system time to clear the bacteria and return the lungs of the infected animals to their normal, healthy state within seven days. The work reported here represents the first example of successful immunogene therapy against fatal deep-tissue infection. Because the therapy focuses on changing the host macrophage response to suppress excessive inflammatory stimuli and enhance the anti-bacterial macrophage activity through IFR5 silencing, rather than attacking a phenotypic characteristic of the pathogen, the approach should be applicable to a wide range of infections.

5.10 References

1   Bergstrom, B. *et al.* TLR8 Senses Staphylococcus aureus RNA in Human Primary Monocytes and Macrophages and Induces IFN-beta Production via a TAK1-IKKbeta-IRF5 Signaling Pathway. *J. Immunol.* **195**, 1100-1111, doi:10.4049/jimmunol.1403176 (2015).

2   Johnson, A. G., Ziegler, R. J. & Hawley, L. *Microbiology and Immunology.* 5th edn, (Lippincott Williams & Wilkins, 2010).

3   Monton, C. & Torres, A. Lung inflammatory response in pneumonia. *Monaldi. Arch. Chest Dis.* **53**, 56-63 (1998).

4   Moldoveanu, B. *et al.* Inflammatory mechanisms in the lung. *J. Inflamm. Res.* **2**, 1-11 (2009).

5   Davies, J. & Davies, D. Origins and evolution of antibiotic resistance. *Microbiol. Mol. Biol. Rev.* **74**, 417-433, doi:10.1128/MMBR.00016-10 (2010).

6   Song, E. H. *et al.* In vivo targeting of alveolar macrophages via RAFT-based glycopolymers. *Biomaterials* **33**, 6889-6897, doi:10.1016/j.biomaterials.2012.06.025 (2012).

7   Lee, W. H., Loo, C. Y., Traini, D. & Young, P. M. Nano- and micro-based inhaled drug delivery systems for targeting alveolar macrophages. *Expert. Opin. Drug. Deliv.* **12**, 1009-1026, doi:10.1517/17425247.2015.1039509 (2015).

8   Harvey, C. J. *et al.* Targeting Nrf2 signaling improves bacterial clearance by alveolar macrophages in patients with COPD and in a mouse model. *Sci. Transl. Med.* **3**, 78ra32, doi:10.1126/scitranslmed.3002042 (2011).

9   Burke, B., Sumner, S., Maitland, N. & Lewis, C. E. Macrophages in gene therapy: cellular delivery vehicles and in vivo targets. *J. Leukoc. Biol.* **72**, 417-428 (2002).

10 Courties, G. *et al.* In vivo silencing of the transcription factor IRF5 reprograms the macrophage phenotype and improves infarct healing. *J. Am. Coll. Cardiol.* **63**, 1556-1566, doi:10.1016/j.jacc.2013.11.023 (2014).

11 Eames, H. L. *et al.* KAP1/TRIM28: An inhibitor of IRF5 function in inflammatory macrophages. *Immunobiology* **217**, 1315-1324, doi:http://dx.doi.org/10.1016/j.imbio.2012.07.026 (2012).

12 Hall, J. L. & Wei, L.-N. Could Silencing IRF5 Improve Healing of a Myocardial Infarct Through the Reprogramming of the Macrophage Population? *J. Am. Coll. Cardiol.* **63**, 1567-1568, doi:10.1016/j.jacc.2013.11.024 (2014).

13 Krausgruber, T. *et al.* IRF5 promotes inflammatory macrophage polarization and TH1-TH17 responses. *Nat. Immunol.* **12**, 231-238, doi:http://www.nature.com/ni/journal/v12/n3/abs/ni.1990.html#supplementary-information (2011).

14   Takaoka, A. *et al.* Integral role of IRF-5 in the gene induction programme activated by Toll-like receptors. *Nature* **434**, 243-249, doi:10.1038/nature03308 (2005).

15   Weiss, M. *et al.* IRF5 controls both acute and chronic inflammation. *Proc. Natl. Acad. Sci. U.S.A.* **112**, 11001-11006, doi:10.1073/pnas.1506254112 (2015).

16   Leuschner, F. *et al.* Therapeutic siRNA silencing in inflammatory monocytes in mice. *Nat. Biotechnol.* **29**, 1005-1010, doi:10.1038/nbt.1989 (2011).

17   De Fougerolles, A., Vornlocher, H. P., Maraganore, J. & Lieberman, J. Interfering with disease: a progress report on siRNA-based therapeutics. *Nat. Rev. Drug Discov.* **6**, 443-453, doi:Doi 10.1038/Nrd2310 (2007).

18   Prabha, S. *et al.* RNA interference technology with emphasis on delivery vehicles-prospects and limitations. *Artif. Cell. Nanomed. Biotechnol.* **44**, 1391-1399, doi:10.3109/21691401.2015.1058808 (2016).

19   Kozielski, K. L., Rui, Y. & Green, J. J. Non-viral nucleic acid containing nanoparticles as cancer therapeutics. *Expert Opin. Drug Deliv.* **13**, 1475-1487, doi:10.1080/17425247.2016.1190707 (2016).

20   Allen, T. M. & Cullis, P. R. Liposomal drug delivery systems: From concept to clinical applications. *Adv. Drug Deliv. Rev.* **65**, 36-48, doi:10.1016/j.addr.2012.09.037 (2013).

21   Wang, Y. & Huang, L. A window onto siRNA delivery. *Nat. Biotechnol.* **31**, 611-612, doi:10.1038/nbt.2634 (2013).

22   Gilleron, J. *et al.* Image-based analysis of lipid nanoparticle-mediated siRNA delivery, intracellular trafficking and endosomal escape. *Nat. Biotechnol.* **31**, 638-646, doi:10.1038/nbt.2612 (2013).

23   Sahay, G. *et al.* Efficiency of siRNA delivery by lipid nanoparticles is limited by endocytic recycling. *Nat. Biotechnol.* **31**, 653-658, doi:10.1038/nbt.2614 (2013).

24   Xue, H. Y., Liu, S. & Wong, H. L. Nanotoxicity: a key obstacle to clinical translation of siRNA-based nanomedicine. *Nanomedicine* **9**, 295-312, doi:10.2217/nnm.13.204 (2014).

25   Godbey, W. T., Wu, K. K. & Mikos, A. G. Poly(ethylenimine)-mediated gene delivery affects endothelial cell function and viability. *Biomaterials* **22**, 471-480 (2001).

26   Marzban, E. *et al.* Optimizing the therapeutic efficacy of cisplatin PEGylated liposomes via incorporation of different DPPG ratios: In vitro and in vivo studies. *Colloids and Surfaces B-Biointerfaces* **136**, 885-891, doi:10.1016/j.colsurfb.2015.10.046 (2015).

27   Maruyama, K., Ishida, O., Takizawa, T. & Moribe, K. Possibility of active targeting to tumor tissues with liposomes. *Adv. Drug Deliv. Rev.* **40**, 89-102, doi:10.1016/s0169-409x(99)00042-3 (1999).

28   Filion, M. C. & Phillips, N. C. Toxicity and immunomodulatory activity of liposomal vectors formulated with cationic lipids toward immune effector cells. *Biochim. Biophys. Acta-Biomembr.* **1329**, 345-356, doi:10.1016/s0005-2736(97)00126-0 (1997).

29   Lewis, J. G. *et al.* A serum-resistant cytofectin for cellular delivery of antisense oligodeoxynucleotides and plasmid DNA. *Proc. Natl. Acad. Sci. U. S. A.* **93**, 3176-3181, doi:10.1073/pnas.93.8.3176 (1996).

30   Kim, J., Santos, O. A. & Park, J.-H. Selective photosensitizer delivery into plasma membrane for effective photodynamic therapy. *J. Control. Release* **191**, 98-104, doi:http://dx.doi.org/10.1016/j.jconrel.2014.05.049 (2014).

31   Lee, J. *et al.* Liposome-Based Engineering of Cells To Package Hydrophobic Compounds in Membrane Vesicles for Tumor Penetration. *Nano Lett.* **15**, 2938-2944, doi:10.1021/nl5047494 (2015).

32   Ren, Y., Hauert, S., Lo, J. H. & Bhatia, S. N. Identification and Characterization of Receptor-Specific Peptides for siRNA Delivery. *ACS Nano* **6**, 8620-8631, doi:10.1021/nn301975s (2012).

33   Daka, A. & Peer, D. RNAi-based nanomedicines for targeted personalized therapy. *Adv. Drug Deliv. Rev.* **64**, 1508-1521, doi:Doi 10.1016/J.Addr.2012.08.014 (2012).

34   Ashley, C. E. *et al.* Delivery of Small Interfering RNA by Peptide-Targeted Mesoporous Silica Nanoparticle-Supported Lipid Bilayers. *ACS Nano* **6**, 2174-2188, doi:Doi 10.1021/Nn204102q (2012).

35   Tanaka, T. *et al.* Sustained Small Interfering RNA Delivery by Mesoporous Silicon Particles. *Cancer Res.* **70**, 3687-3696, doi:10.1158/0008-5472.can-09-3931 (2010).

36   Kang, J. *et al.* Self-Sealing Porous Silicon-Calcium Silicate Core–Shell Nanoparticles for Targeted siRNA Delivery to the Injured Brain. *Adv. Mater.* **28**, 7962-7969, doi:10.1002/adma.201600634 (2016).

37   Honig, M. G. & Hume, R. I. Fluorescent carbocyanine dyes allow living neurons of identified origin to be studied in long-term cultures. *J. Cell Biol.* **103**, 171-187 (1986).

38   Teesalu, T., Sugahara, K. N. & Ruoslahti, E. in *Methods in Enzymology: Protein Engineering for Therapeutics, Vol 203, Pt B* Vol. 503 *Methods in Enzymology* (eds K. D. Wittrup & G. L. Verdine) 35-56 (2012).

39   Ruoslahti, E. Peptides as Targeting Elements and Tissue Penetration Devices for Nanoparticles. *Adv. Mater.* **24**, 3747-3756, doi:Doi 10.1002/Adma.201200454 (2012).

40   Choi, H. S. *et al.* Renal clearance of quantum dots. *Nat. Biotechnol.* **25**, 1165-1170, doi:10.1038/nbt1340 (2007).

41   De Jong, W. H. *et al.* Particle size-dependent organ distribution of gold nanoparticles after intravenous administration. *Biomaterials* **29**, 1912-1919, doi:10.1016/j.biomaterials.2007.12.037 (2008).

42   Sapru, K., Stotland, P. K. & Stevenson, M. M. Quantitative and qualitative differences in bronchoalveolar inflammatory cells in Pseudomonas aeruginosa-resistant and -

susceptible mice. *Clinical and Experimental Immunology* **115**, 103-109, doi:10.1046/j.1365-2249.1999.00762.x (1999).

43   Crapo, J. D., Barry, B. E., Gehr, P., Bachofen, M. & Weibel, E. R. Cell number and cell characteristics of the normal human lung. *Am Rev Respir Dis* **126**, 332-337, doi:10.1164/arrd.1982.126.2.332 (1982).

44   Knudsen, J. D., Fuursted, K., Raber, S., Espersen, F. & Frimodt-Moller, N. Pharmacodynamics of glycopeptides in the mouse peritonitis model of Streptococcus pneumoniae or Staphylococcus aureus infection. *Antimicrob Agents Chemother* **44**, 1247-1254 (2000).

45   Park, Y. S., Shin, W. S. & Kim, S. K. In vitro and in vivo activities of echinomycin against clinical isolates of Staphylococcus aureus. *J Antimicrob Chemother* **61**, 163-168, doi:10.1093/jac/dkm421 (2008).

46   Hussain, S., Joo, J., Kang, J., Kim, B., Braun, G.B., She, Z., Kim, D., Mann, A.P., Mölder, T., Teesalu, T., Carnazza, S., & Guglielmino, S., Sailor, M.J., and Ruoslahti, E. Enhanced antibacterial efficacy of antibiotic-loaded nanoparticles targeted to the site of infection. *Nat. Biomed. Eng.* (2017).

47   Krieg, A. M. Is RNAi Dead? *Mol. Therapy* **19**, 1001–1002, doi:10.1038/mt.2011.94 (2011).

48   Canham, L. T. in *Porous Silicon for Biomedical Applications Woodhead Publishing Series in Biomaterials* (ed H. A. Santos) 3-20 (2014).

49   Nakki, S. *et al.* Improved stability and biocompatibility of nanostructured silicon drug carrier for intravenous administration. *Acta Biomater.* **13**, 207-215, doi:10.1016/j.actbio.2014.11.019 (2015).

50   Gongalsky, M. B. *et al.* Porous silicon nanoparticles as biocompatible contrast agents for magnetic resonance imaging. *Appl. Phys. Lett.* **107**, doi:10.1063/1.4937731 (2015).

51   DeLouise, L. A. & Miller, B. L. Quantatitive assessment of enzyme immobilization capacity in porous silicon. *Anal. Chem.* **76**, 6915-6920, doi:10.1021/ac0488208 (2004).

52   Wu, C.-C., Hu, Y., Miller, M., Aroian, R. V. & Sailor, M. J. Protection and Delivery of Anthelmintic Protein Cry5B to Nematodes Using Mesoporous Silicon Particles. *ACS Nano* **9**, 6158–6167, doi:10.1021/acsnano.5b01426 (2015).

53   Andrew, J. S. *et al.* Sustained Release of a Monoclonal Antibody from Electrochemically Prepared Mesoporous Silicon Oxide. *Adv. Funct. Mater.* **20**, 4168–4174, doi:10.1002/adfm.201000907 (2010).

54   Salonen, J. in *Handbook of Porous Silicon*   (ed L..T. Canham) 909 (Springer, 2014).

55   Joo, J. *et al.* Porous Silicon-Graphene Oxide Core-Shell Nanoparticles for Targeted Delivery of siRNA to the Injured Brain. *Nanoscale Horiz.* **1**, 407-414, doi:10.1039/C6NH00082G (2016).

56   Kang, J. *et al.* Self-Sealing Porous Silicon-Calcium Silicate Core-Shell Nanoparticles for Targeted siRNA Delivery to the Injured Brain. *Adv Mater* **28**, 7962-7969, doi:10.1002/adma.201600634 (2016).

57   Rodgers, J. M., Sørensen, J., de Meyer, F. J. M., Schiøtt, B. & Smit, B. Understanding the Phase Behavior of Coarse-Grained Model Lipid Bilayers through Computational Calorimetry. *The Journal of Physical Chemistry B* **116**, 1551-1569, doi:10.1021/jp207837v (2012).

58   Mukai, M., Sasaki, Y. & Kikuchi, J. Fusion-triggered switching of enzymatic activity on an artificial cell membrane. *Sensors (Basel)* **12**, 5966-5977, doi:10.3390/s120505966 (2012).

59   Sun, J., Jakobsson, E., Wang, Y. & Brinker, C. Nanoporous Silica-Based Protocells at Multiple Scales for Designs of Life and Nanomedicine. *Life* **5**, 214-229 (2015).

60   Liu, J., Stace-Naughton, A., Jiang, X. & Brinker, C. J. Porous Nanoparticle Supported Lipid Bilayers (Protocells) as Delivery Vehicles. *Journal of the American Chemical Society* **131**, 1354-1355, doi:10.1021/ja808018y (2009).

61   Lee, J. *et al.* Liposome-Based Engineering of Cells To Package Hydrophobic Compounds in Membrane Vesicles for Tumor Penetration. *Nano Letters* **15**, 2938-2944, doi:10.1021/nl5047494 (2015).

62   Lentz, B. R. Polymer-induced membrane fusion: potential mechanism and relation to cell fusion events. *Chem Phys Lipids* **73**, 91-106 (1994).

63   Dennison, S. M., Bowen, M. E., Brunger, A. T. & Lentz, B. R. Neuronal SNAREs do not trigger fusion between synthetic membranes but do promote PEG-mediated membrane fusion. *Biophys J* **90**, 1661-1675, doi:10.1529/biophysj.105.069617 (2006).

64   Monton, C. & Torres, A. Lung inflammatory response in pneumonia. *Monaldi Arch Chest Dis* **53**, 56-63 (1998).

65   Juhas, U., Ryba-Stanislawowska, M., Szargiej, P. & Mysliwska, J. Different pathways of macrophage activation and polarization. *Advances in Hygiene and Experimental Medicine* **69**, 496-502, doi:10.5604/17322693.1150133 (2015).

66   Muraille, E., Leo, O. & Moser, M. Th1/Th2 Paradigm Extended: Macrophage Polarization as an Unappreciated Pathogen-Driven Escape Mechanism? . *Front. Immunol.* **5**, 603, doi:http://doi.org/10.3389/fimmu.2014.00603 (2014).

67   Akinc, A. *et al.* A combinatorial library of lipid-like materials for delivery of RNAi therapeutics. *Nat. Biotechnol.* **26**, 561-569, doi:Doi 10.1038/Nbt1402 (2008).

68   Auguste, D. T. *et al.* Triggered release of siRNA from poly(ethylene glycol)-protected, pH-dependent liposomes. *J. Control. Release* **130**, 266-274, doi:10.1016/j.jconrel.2008.06.004 (2008).

69   Basha, G. *et al.* Influence of cationic lipid composition on gene silencing properties of lipid nanoparticle formulations of siRNA in antigen-presenting cells. *Mol. Ther.* **19**, 2186-2200, doi:10.1038/mt.2011.190 (2011).

70   Akinc, A. *et al.* Targeted delivery of RNAi therapeutics with endogenous and exogenous ligand-based mechanisms. *Mol. Ther.* **18**, 1357-1364, doi:10.1038/mt.2010.85 (2010).

71   Akinc, A. *et al.* Development of lipidoid-siRNA formulations for systemic delivery to the liver. *Mol. Ther.* **17**, 872-879, doi:10.1038/mt.2009.36 (2009).

72   Xu, C.-f. & Wang, J. Delivery systems for siRNA drug development in cancer therapy. *Asian J. Pharmacol.* **10**, 1-12, doi:http://dx.doi.org/10.1016/j.ajps.2014.08.011 (2015).

73   Leung, A. K. *et al.* Lipid Nanoparticles Containing siRNA Synthesized by Microfluidic Mixing Exhibit an Electron-Dense Nanostructured Core. *J. Phys. Chem. C* **116**, 18440-18450, doi:10.1021/jp303267y (2012).

74   Zheng, Y. *et al.* A novel gemini-like cationic lipid for the efficient delivery of siRNA. *New J. Chem.* **38**, 4952-4962, doi:10.1039/C4NJ00531G (2014).

75   Hasan, W. *et al.* Delivery of Multiple siRNAs Using Lipid-Coated PLGA Nanoparticles for Treatment of Prostate Cancer. *Nano Lett* **12**, 287-292, doi:Doi 10.1021/Nl2035354 (2012).

76   Xia, T. A. *et al.* Polyethyleneimine Coating Enhances the Cellular Uptake of Mesoporous Silica Nanoparticles and Allows Safe Delivery of siRNA and DNA Constructs. *ACS Nano* **3**, 3273-3286, doi:10.1021/nn900918w (2009).

77   Bhattarai, S. R. *et al.* Enhanced Gene and siRNA Delivery by Polycation-Modified Mesoporous Silica Nanoparticles Loaded with Chloroquine. *Pharm. Res.* **27**, 2556-2568, doi:10.1007/s11095-010-0245-0 (2010).

78   Moller, K. *et al.* Highly efficient siRNA delivery from core-shell mesoporous silica nanoparticles with multifunctional polymer caps. *Nanoscale* **8**, 4007-4019, doi:10.1039/c5nr06246b (2016).

79   Shen, J. *et al.* Cyclodextrin and polyethylenimine functionalized mesoporous silica nanoparticles for delivery of siRNA cancer therapeutics. *Theranostics* **4**, 487-497, doi:10.7150/thno.8263 (2014).

80   Ashley, C. E. *et al.* Delivery of small interfering RNA by peptide-targeted mesoporous silica nanoparticle-supported lipid bilayers. *ACS Nano* **6**, 2174-2188, doi:10.1021/nn204102q (2012).

5.11   Figures and Tables
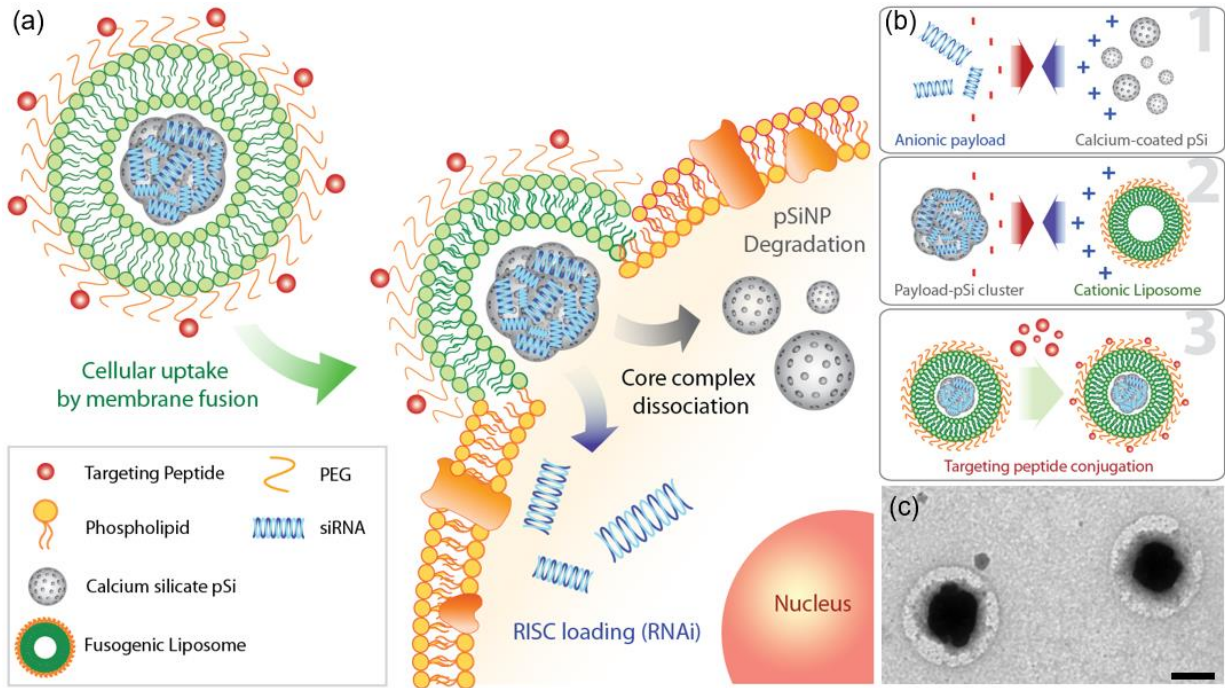
Figure 5.1. Mode of action, synthesis, and structure of the fusogenic particles
(**a**) Schematic showing mode of action of the fusogenic liposome-coated porous silicon NP (F-pSi). (**b**) Schematic showing nanoparticle synthesis, including (1) siRNA loading into the porous silicon nanoparticles and sealing by precipitation of calcium silicate; (2) coating of the nanoparticle clusters with cationic liposome; and (3) conjugation of targeting peptides to the liposomal exterior. (**c**) TEM image of final F-pSi constructs, showing cloudy liposomal coatings around dark and dense porous silicon-based cores. Imaged using JEOL 1200EX TEM. Negative staining by 2% phosphotungstic acid. Scale bar indicates 200 nm.
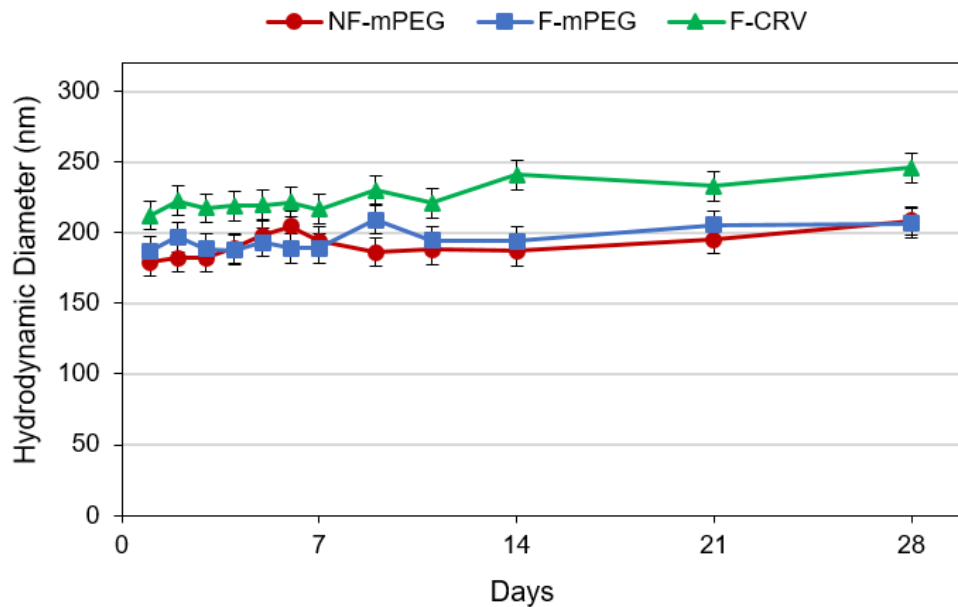
Figure 5.2. Nanoparticles demonstrate physical stability for up to 28 days in physiological salt solution.
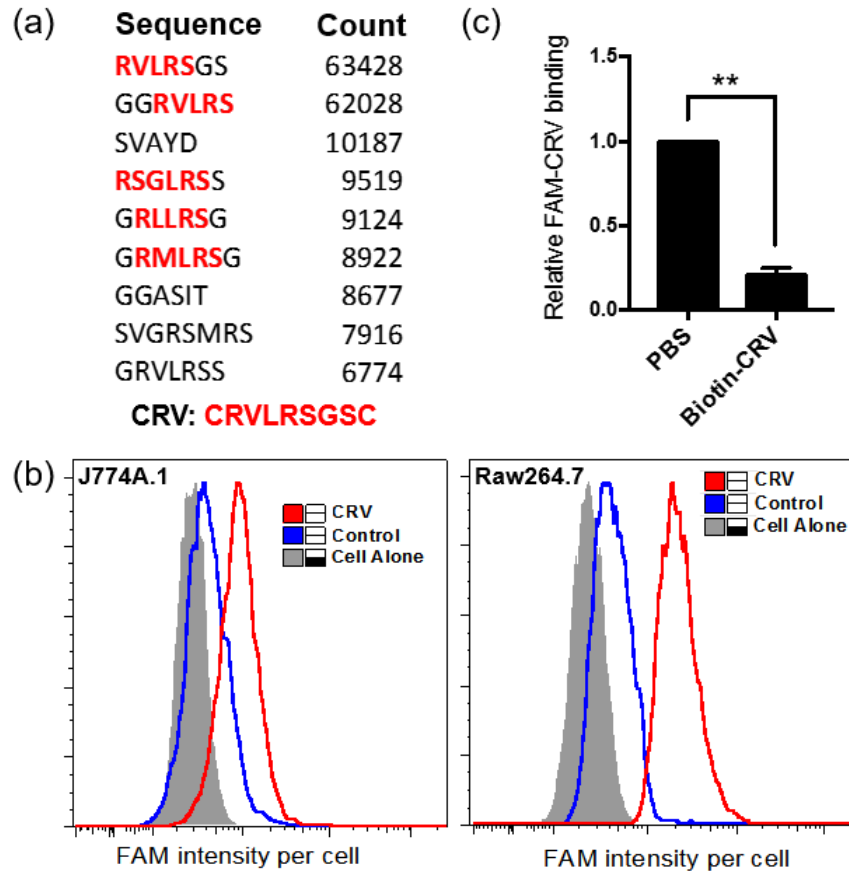28-day observation of average hydrodynamic diameter of fusogenic (F-mPEG) and non-fusogenic (NF-mPEG) porous silicon (pSi) nanoparticles, and CRV-conjugated fusogenic porous silicon nanoparticles (F-CRV) in aqueous phosphate-buffered saline (PBS) solution, measured by DLS. Bars indicate standard deviation, n=3.
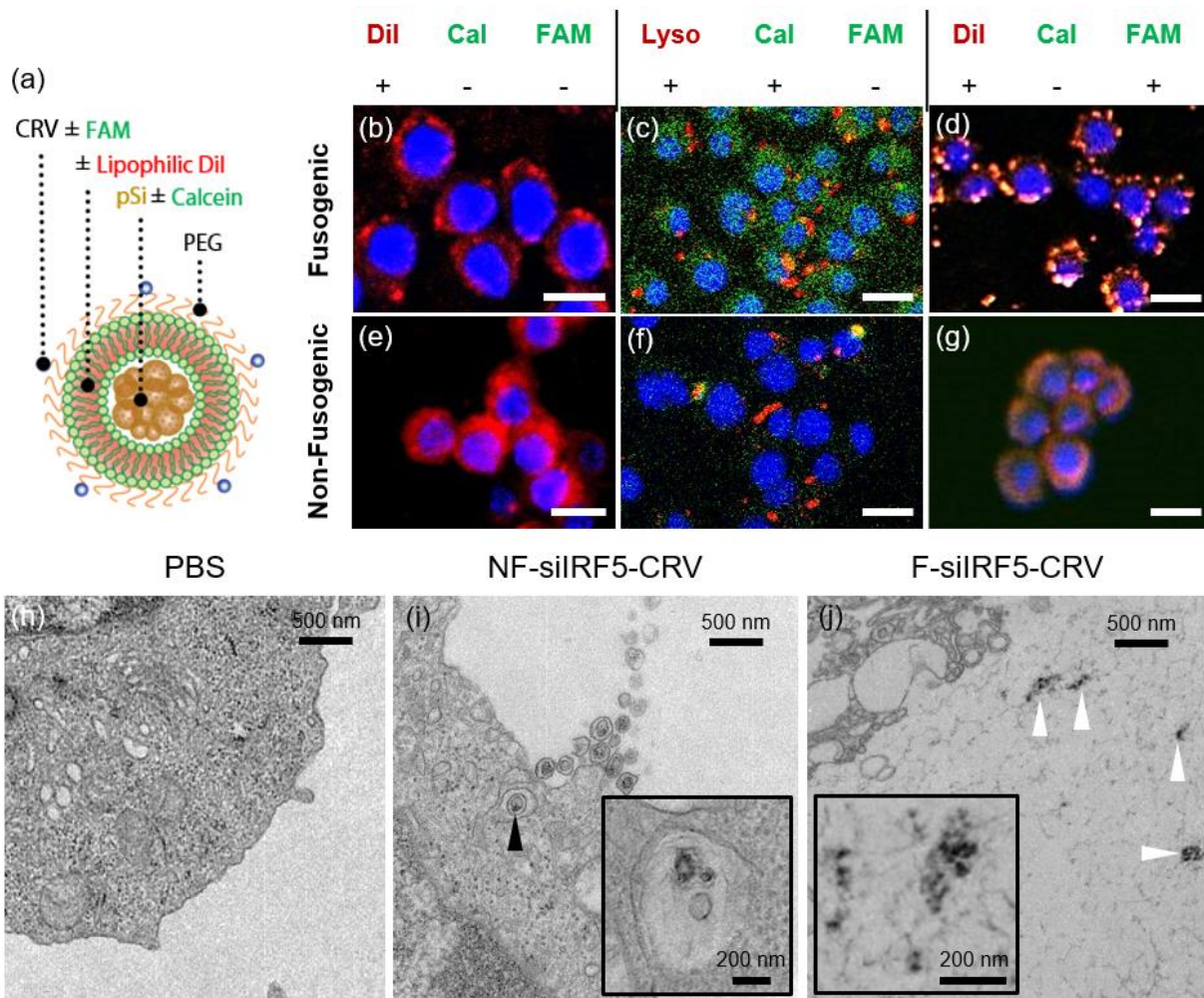
Figure 5.3. Fusion and intracellular delivery of Fusogenic particles *in vitro*.
(**a**) Particle schematic. CRV = macrophage targeting peptide, FAM = fluorescein label attached to targeting peptide, DiI = the hydrophobic carbocyanine membrane stain, pSi = porous Si nanoparticles, Calcein = anionic calcein fluorescent dye, PEG = polyethylene glycol. (**b-g**) Confocal microscope images of J771A.1 murine macrophage cells; (**b**) after 10 min incubation with DiI-loaded F-pSi nanoparticles; (**c**) after 1h incubation with Lysotracker Red and 10 min incubation with calcein-loaded F-pSi nanoparticles; (**d**) after 5 min incubation with CRV-FAM-conjugated, DiI-loaded F-pSi nanoparticles; (**e**) after 10 min incubation with DiI-loaded NF-pSi nanoparticles; (**f**) after 1h incubation with Lysotracker Red and 10 min incubation with calcein-loaded NF-pSi nanoparticles; (**g**) after 5 min incubation with CRV-FAM-conjugated, DiI-loaded NF-pSi nanoparticles. Blue is DAPI nuclear stain. (**h-j**) Transmission electron microscope (TEM) images of Raw 264.7 murine macrophage cells after 10 min incubation with nanoparticles. (**h**), cells treated with PBS (phosphate buffered saline) control show no signs of particles; (**i**) cells treated with nanoparticles containing a non-fusogenic lipid coating, siRNA against transcription factor IRF5, and the macrophage targeting peptide (NF-siIRF5-CRV) display evidence of pinocytotic uptake (arrowhead). Inset shows particles localized in vesicles (endosome/lysosome); (**j**) cells treated with nanoparticles containing fusogenic lipid coating, siRNA against transcription factor IRF5, and the macrophage targeting peptide (F-siIRF5-CRV) become localized in the cell cytoplasm. Scale bar represents 20 μm.

195

(a)

| Sequence	Count
RVLRSGS	63428
GG**RVLRS**	62028
SVAYD	10187
RSGLRSS	9519
G**RLLRS**G	9124
G**RMLRS**G	8922
GGASIT	8677
SVGRSMRS	7916
GRVLRSS	6774

CRV: **CRVLRSGSC**

Figure 5.4. Identification of CRV peptide and *in vitro* characterization of macrophage binding.
(a) Phage display using CX$_7$C library was performed on J774A.1 cells as described in Materials and Methods. The amino acid sequences between two Cysteine residues of the most abundant phages enriched after three rounds of biopannings, and their frequency, are shown here. A consensus motif, RVLRS, is highlighted here in red. (b) FAM-CRV, or a FAM labeled control peptide (ARA for J774A.1 cells; GGSGGSKG for Raw264.7 cells) was mixed with indicated cells for binding as described in Materials and Methods. At least three independent experiments were carried out, and the representative results are shown here. (c) FAM-CRV was mixed with PBS or biotin-CRV for competition of binding to J774A.1 cells as described in Materials and Methods. Error bars, SEM. **P<0.01 (Student's t-test).

196
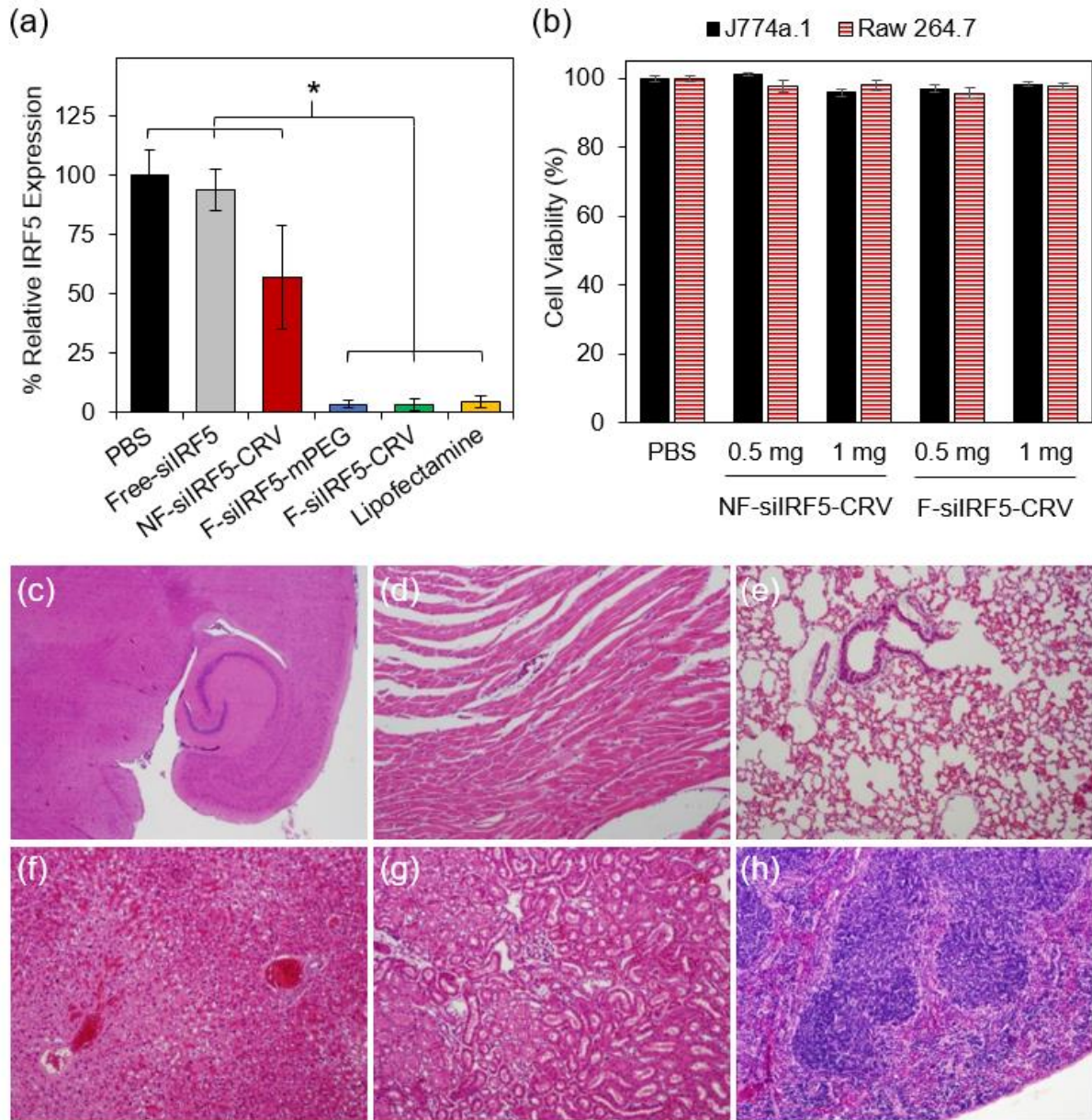
Figure 5.5. Gene knockdown *in vitro* and *in vivo* cytotoxicity of fusogenic porous Si nanoparticle constructs.

(a) siRNA knockdown results (*via* qRT-PCR) from Raw 264.7 macrophage cells incubated with nanoparticles for 24h. Error bars indicate standard deviation (n=6). The fusogenic formulations show substantial knockdown, comparable to standard lipofectamine transfection agent. No significant difference in knockdown efficiency is observed between the two fusogenic formulations (F-siIRF5-mPEG, F-siIRF5-CRV) and lipofectamine. * indicates significant difference (One-way ANOVA with Tukey's HSD post hoc test, p level <0.05, $F_{(5, 30)} = 28$, $p = 6.9 \times 10^{-10}$). **(b)** Viability of J774a.1 and Raw 264.7 macrophage cells after 1h incubation with NF-siIRF5-CRV and F-siIRF5-CRV nanoparticle constructs, containing 0.5 mg and 1 mg total mass of lipid as indicated. Error bar indicates standard deviation (n=6). ANOVA test found no statistical significance at $p < 0.01$; (c-h) H&E staining of major organs after 24h circulation of F-siIRF5-CRV via tail-vein injection (23.2 µmol/kg lipid, 24 µg/kg siRNA, 0.5 mg/kg pSi) in healthy Balb/C mice; **(c)** brain; **(d)** heart; **(e)** lung; **(f)** liver; **(g)** kidney; and **(h)** spleen.
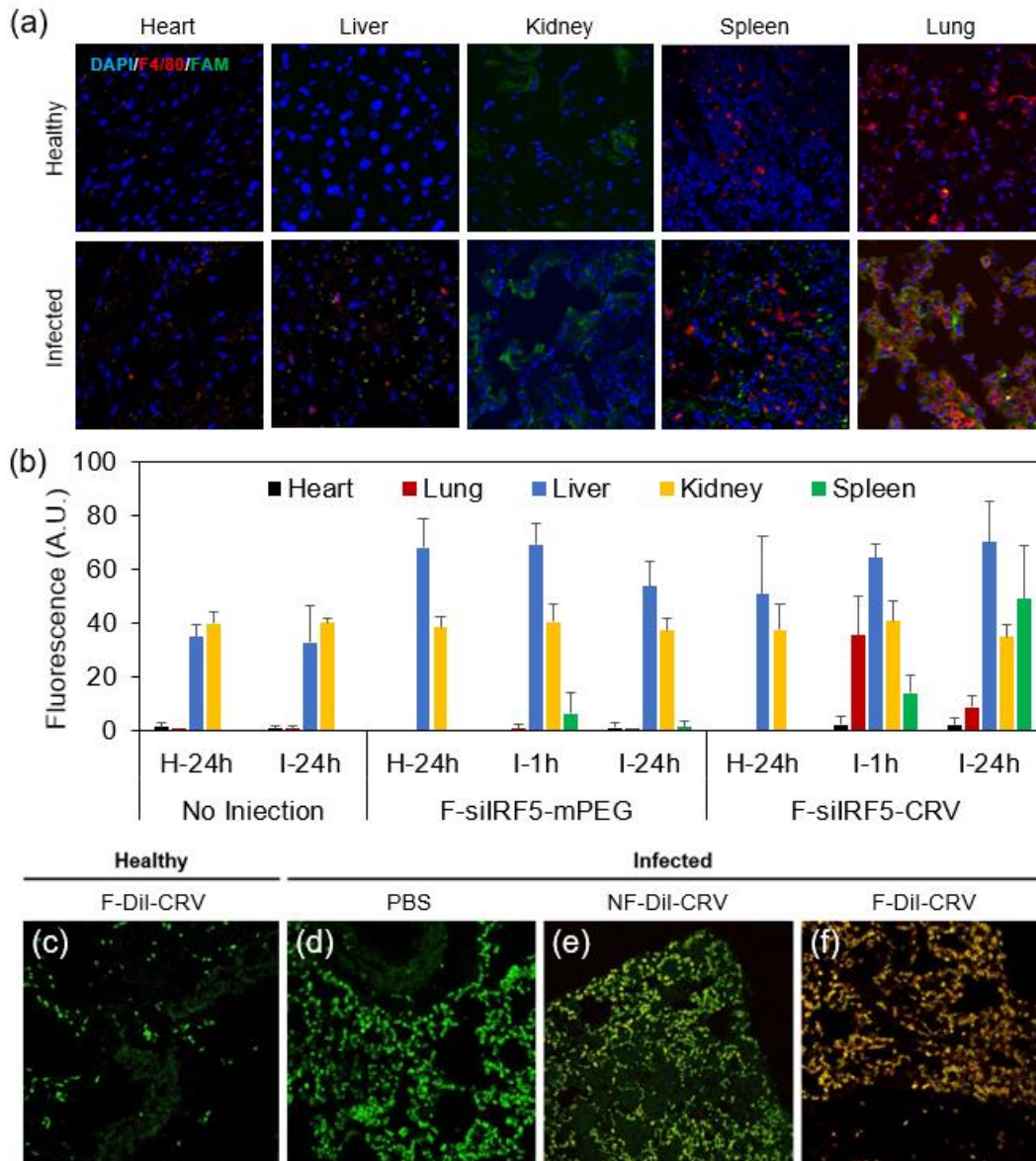
**Figure 5.6. Targeting peptide and fusogenic uptake enhances homing to infected lungs and macrophages.**
(**a**) Immunofluorescent sections of major organs of healthy and infected Balb/C mice injected with FAM CRV.peptide (green). Blue indicates cell nuclei stained with DAPI, red indicates macrophages marked by F4/80 antibody stain; (**b**) Quantified fluorescence signals (IVIS200) from organs of healthy and infected Balb/C mice injected with fusogenic nanoparticles containing DiI membrane stain and siIRF5 payload, with either a non-targeting (F-siIRF5-mPEG) or the CRV targeting group (F-siIRF5-CRV) at doses of 23.2 μmol/kg lipid, 24 μg/kg siRNA, 0.5 mg/kg pSi. 'H-24' indicates healthy organs harvested 24h post-treatment, 'I-1' indicates Balb/C organs of infected harvested 1h post-treatment, and 'I-24' indicates infected Balb/C organs 24h post-treatment. Bars indicate standard deviation. Data is representative of n=3, quantified by ImageJ analyses. (**c-f**) Confocal microscope images of DiI-loaded fusogenic and non-fusogenic nanoparticles homed to infected lung with CRV targeting peptide. The nanoparticles contained no siIRF5 payload; green indicates FITC-tagged rat anti-mouse F4/80 stain, red indicates lipophilic DiI; (**c**) lung of healthy mouse injected with F-DiI-CRV; (**d**) lung of infected mouse injected with PBS; (**e**) lung of infected mouse injected with NF-DiI-CRV; (**f**) lung of infected mouse injected with F-DiI-CRV. The data show DiI from the fusogenic, CRV-targeted nanoparticles is strongly co-localized with macrophages.

198
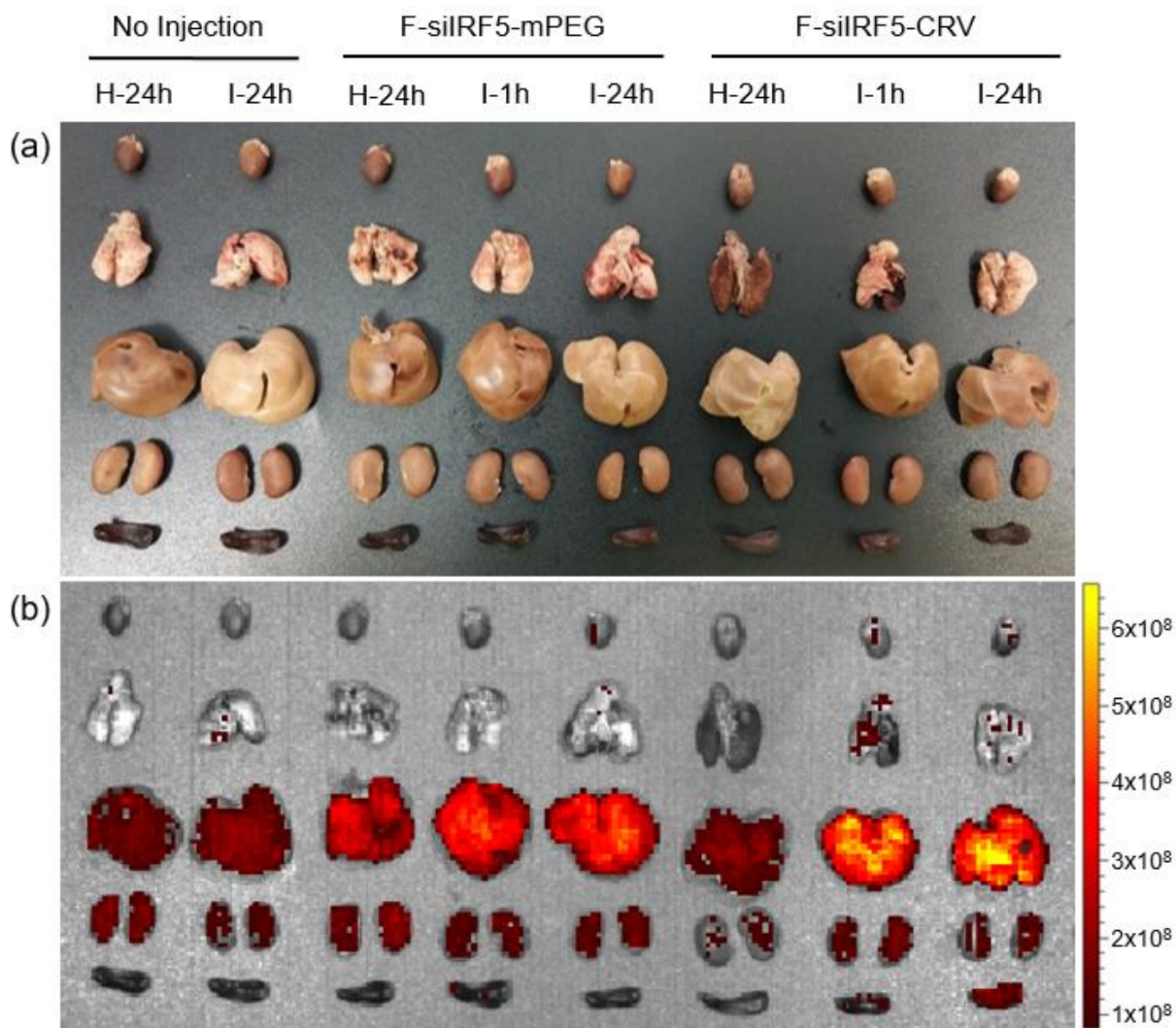
Figure 5.7. CRV-conjugated fusogenic particles show homing to infected lungs within 1h of intravenous injection.
Representative images of biodistribution of DiI-tagged fusogenic nanoparticles in healthy and infected Balb/C mice. (a) Photograph of harvested organs (top to bottom: heart, lungs, liver, kidneys, and spleen); (b) IVIS 200 fluorescence image of DiI-labeled fusogenic nanoparticle without CRV conjugation (F-siIRF5-mPEG) and fusogenic nanoparticle with CRV conjugation (F-siIRF5-CRV). 'H-24' indicates healthy Balb/C organs harvested 24h post-treatment, 'I-1' indicates organs harvested from infested mice 1h post-treatment, and 'I-24' indicates infected Balb/C organs 24h post-treatment. Data are representative of n=3. The images were quantified using ImageJ software, given in **Fig 5.6b**.
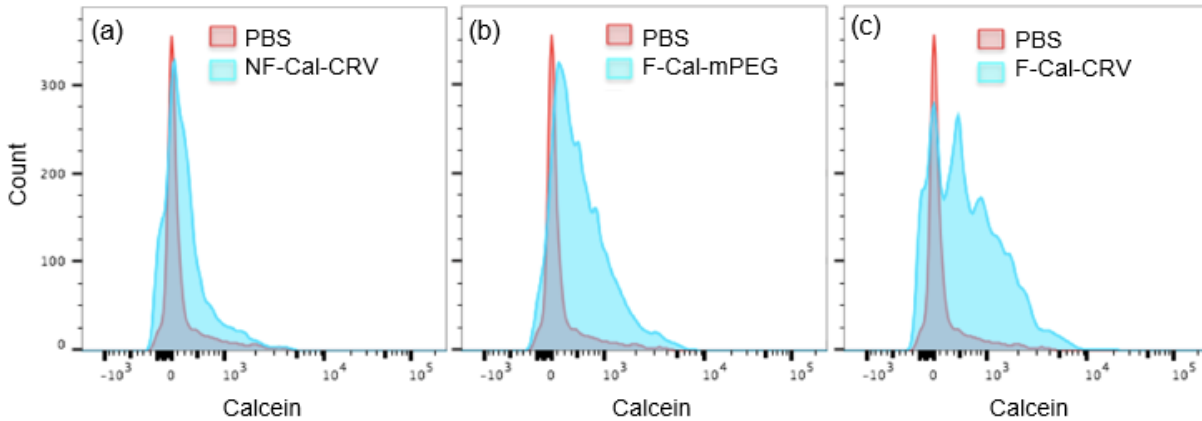
Figure 5.8. CRV-conjugation enhances selective homing to infected lungs.
FACS analyses of calcein accumulation in homogenized Staph. aureus-infected Balb/C lungs. (a) PBS vs. non-fusogenic particles loaded with calcein (Cal) and conjugated to targeting peptide (CRV); (b) PBS vs. fusogenic particles loaded with calcein without targeting peptide; (c) PBS vs. fusogenic particles loaded with calcein and conjugated to targeting peptide. These data validate the efficacy of CRV-conjugation. Infected Balb/C were intravenously injected with the indicated preparations. Lungs were harvested 1h post-injection and homogenized. The homogenates were analyzed by FACS for cellular accumulation of calcein-loaded particles. NF-Cal-CRV showed no visible difference in calcein signal compared to PBS-injected mice. Non-targeted F-Cal-mPEG showed a slight shift in the calcein signal toward higher values, but targeted F-Cal-CRV demonstrated a substantial peak shift toward a higher degree of fluorescence. The data demonstrate that CRV-conjugation to fusogenic particles enables homing to infected lungs.
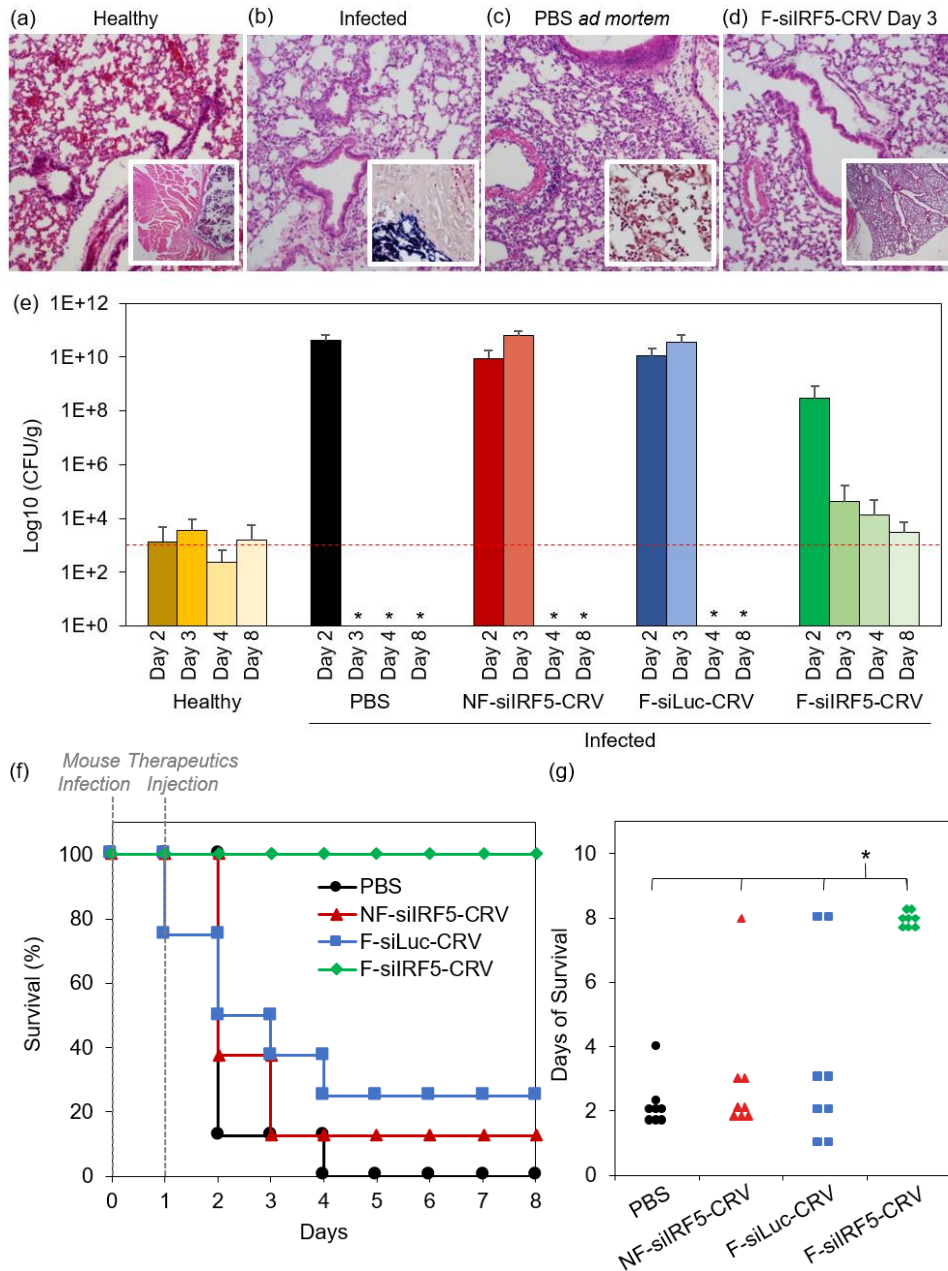
Figure 5.9. Macrophage-targeting fusogenic pSi nanoparticles loaded with anti-inflammatory siIRF5 effectively treats and causes recovery of infected mice.
(**a-d**) H&E stained sections of lungs subjected to histopathological analyses; (**a**) Lung of healthy mouse with no treatment (inset shows lower magnification); (**b**) Lung of infected mouse with no treatment (inset shows perilaryngeal muscle); (**c**) Lung of infected mouse *ad mortem* 24h post-PBS treatment (inset shows Gram stain); and (**d**) Lung of infected mouse treated with F-siIRF5-CRV at 3 days post-treatment (inset shows lower magnification); (**e**) Bacterial titer from lungs of mice injected with PBS, NF-siIRF5-CRV, F-siLuc-CRV, and F-siIRF5-CRV. Animals were infected on day 0 and therapeutic injections were on day 1. The dashed red line indicates the average CFU/g in healthy lungs. Error bars indicate standard deviation with n=8. * indicates *ad mortem*; no measurements due to death of all mice in the cohort. (**f**) Mouse survival post-therapeutic injection (at day 1). Each group has n=8 mice. (**g**) Average days of survival of mice from (**f**) post-infection (at day 0) and post-therapeutic injection (at day 1). One-way ANOVA with Tukey's HSD post hoc test (p level <0.05, $F_{(3, 28)}$ = 17, p = 1.77x10^{-6}) revealed significant difference between F-siIRF5-CRV and the three control groups.
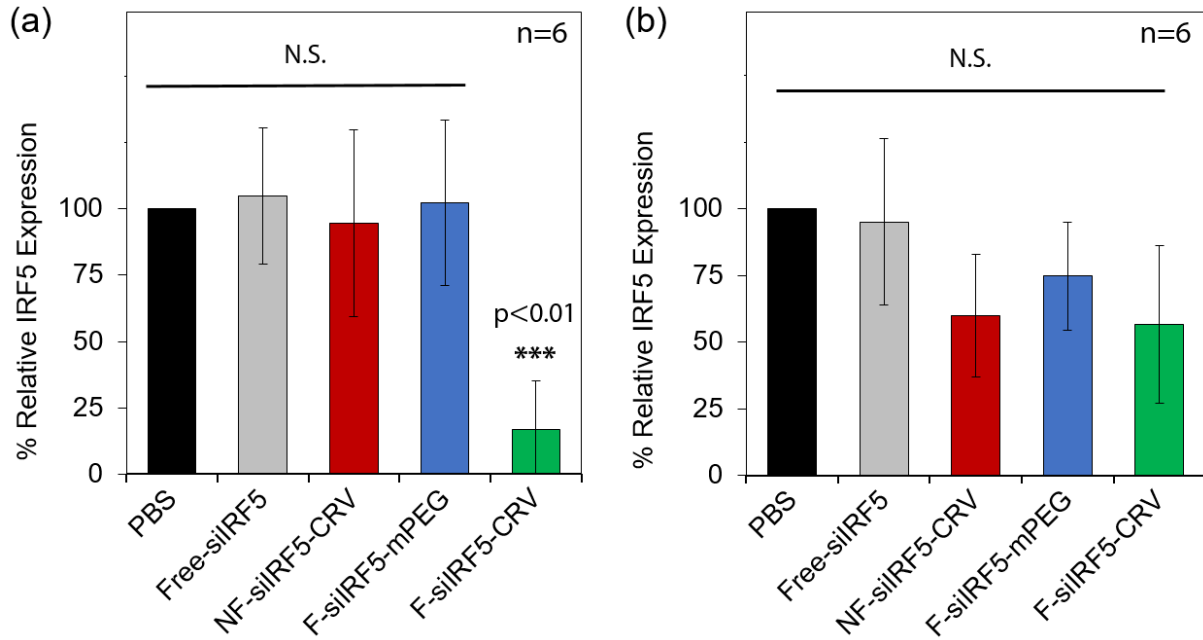
Figure 5.10. CRV-conjugated fusogenic pSi nanoparticles demonstrate effective knockdown of IRF5 in the BAL fluid of infected lungs *in vivo*.
(a) *in vivo* siRNA knockdown efficiency (via qRT-PCR) in BAL fluid collected from *Staph. aureus* infected Balb/C mice injected with formulations for 24h. Error bars indicate standard deviation (n=6). *** indicates significant difference (One-way ANOVA with Tukey's HSD post hoc test, p level <0.05, $F_{(5, 30)}$ = 26.5, p = 5.9×10^{-14}). **(b)** *in vivo* siRNA knockdown efficiency (via qRT-PCR) in lung homogenates from *Staph. aureus* infected Balb/C mice injected with nanoparticles for 24h. Error bars indicate standard deviation (n=6). N.S. indicates no significant difference.

Table 5.1. Lipid composition of fusogenic and non-fusogenic liposomal coatings expressed in molar ratio.
DMPC is 1,2-dimyristoyl-sn-glycero-3-phosphocholine, DSPE-PEG is 1,2-distearoyl-sn-glycero-3-phosphoethanolamine-N-[methoxy(polyethylene glycol)-2000] (DSPE-mPEG), or 1,2-distearoyl-sn-glycero-3-phosphoethanolamine-N-[maleimide(polyethylene glycol)-2000] (DSPE-PEG-maleimide), and DOTAP is 1,2-dioleoyl-3-trimethylammonium-propane.

Lipid Composition (Molar Ratio)		
DMPC	**DSPE-PEG**	**DOTAP**
Fusogenic 76.2	3.8	20
Non-fusogenic 96.2	3.8	0
Fusion mechanism • Major structural component • Low phase transition temperature allows for liquid crystal phase (essential phase for fusion) in physiological conditions	• For dispersion and stealth • Hypothesized to act as a bridge linker akin to SNARE • PEG-methoxy used for non-conjugated • PEG-maleimide used for targeting peptide conjugation	• Cationic lipid for fusion and attraction to plasma membrane

Table 5.2. Table of particle size and zeta-potential measured by DLS (n=3).
F-mPEG indicates fusogenic liposome-coated pSi nanoparticles without CRV conjugation; NF-mPEG indicates non-fusogenic liposome-coated pSi nanoparticles without CRV conjugation; F-CRV indicates fusogenic liposome-coated pSi nanoparticles with CRV conjugation; and NF-CRV indicates non-fusogenic liposome-coated pSi nanoparticles with CRV conjugation.

	Average Hydrodynamic Diameter (nm)	Zeta-Potential (mV)
Core pSiNPs	68.1 ± 5.8	-21.3 ± 1.0
Fusogenic (F-mPEG)	187.4 ± 5.2	9.8 ± 0.4
Non-fusogenic (NF-mPEG)	190.8 ± 4.7	-9.1 ± 1.8
Targeted Fusogenic (F-CRV)	225.0 ± 10.2	-3.4 ± 2.3
Targeted Non-fusogenic (NF-CRV)	229.2 ± 7.8	-10.8 ± 0.8

Table 5.3. siRNA loading efficiency by wt.% comparison between Fusogenic pSiNPs and conventional platforms compiled based on literature published from 2008-2016.

Particle	Size	siRNA Loading (wt. %)
Fusogenic liposome-coated pSiNP	190 nm	20-25%
Lipid-based Nanoparticles	50-200 nm	1-14%[†]
Mesoporous Silica-Polymer Hybrid NPs	60-200 nm	1-10%[‡]
[†] Comparable 200 nm particles had the lowest loading amounts (< 5 wt. %)[16,22,23,68-75]		
[‡] Comparable 200 nm particles had the lowest loading amounts (< 5 wt. %)[76-80]		

Chapter five is, in full, a reprint (with co-author permission) of the material as it appears in the following publication: **Kim, B.***, Pang, H.*, Kang, J., Park, J., Ruoslahti, E., Sailor, M.J. Immunogene therapy with fusogenic nanoparticles modulates macrophage response to Staphylococcus aureus. *Nat Commun*, (2018). The author of this dissertation is the primary author of this manuscript.

Chapter 6:

Fusogenic Porous Silicon Nanoparticles as a Wide-Spectrum

Immunotherapy against Bacterial Infections

6.1   Abstract

Bacterial infections are reemerging threats due to limited antibiotic options, and increasing developments of antibiotic resistance. In order to deter such mutations whilst minimizing the need to develop new pathogen-specific antibiotics, immunotherapy offers a wide-spectrum therapeutic. Herein, we present a fusogenic porous silicon nanoparticle that is targeted to activated macrophages and loaded with siRNA against *Irf5* to induce >80% gene silencing effect *in vivo* to inhibit excessive inflammatory response for increased therapeutic outcome. In order to demonstrate the versatility of the treatment, we use the fusogenic formulation to treat mice with: (1) muscle infection of methicillin-resistant *Staphylococcus aureus* (*MRSA*), which is an antibiotic-resistant Gram positive bacterium; and (2) lung infection of *Pseudomonas aeruginosa* (*P. aeruginosa*), which is Gram negative. We demonstrate that depletion of the *Irf5* in macrophages is able to significantly improve the therapeutic outcome of infected mice, regardless of the bacteria strain and type.

6.2   Introduction

Two decades since antibiotics development in the 1940s, antibiotic-resistant strains were first identified.[1] For the past 60 years, the numbers have been increasing since, while the number of effective antibiotics remain static.[2] While antibiotics development against Gram positive remain relatively diverse and fast-paced, the dual-walled nature of Gram negative bacteria make it much more difficult to develop countermeasures; while most existing antibiotics are able to penetrate through a single bacterial cell wall to induce its mechanism of action, they fail to breach the secondary wall that Gram negative bacteria carry.[3,4] While adjuvant therapies using peptide-based potentiators are under research, there is as of yet no solution to prevent

resistance development even in the event that the antibiotics are able to penetrate through to the cell body.

Moreover, the greater problem is that continuous development and exposure of new antibiotics will inevitably face resistance over time.[1] Thus, in order to minimize the need to develop new drugs for each new resistance from microbial evolutions, we are in need of a solution that is able to evolve alongside the bacteria. To this end, we decided develop an immunotherapy strategy against bacterial infections to harness the body's immune system, which is innately under constant evolution.

Immunotherapy has primarily been explored for treatments against cancer and autoimmune disorder treatments, but not for infections.[5] While pre-antibiotic era of treatments against bacterial infections involved transient anti-serum or lasting vaccine immunotherapy, more recent efforts solely involve monoclonal antibody therapy.[6-9] Moreover, the potential therapeutics still require pathogen-specific properties, and must be re-designed for different bacteria, and none have yet reached clinical trials despite showing promising results in research.

We present fusogenic porous silicon nanoparticles (F-pSiNPs/FNPs) which are (**Fig 1a**): (1) loaded with siRNA against the *irf5* gene, which encodes for pro-inflammatory signals in macrophages of the M1 phenotype; and (2) surface-conjugated with the CRV peptide (sequence: CRVLRSGSC), which targets activated macrophages in the inflammatory site. We have previously demonstrated that this therapeutic is able to completely recover mice infected with fatal *Staphylococcus aureus* pneumonia by RNAi-induced inhibition of excessive inflammatory response that contributes significantly to mortality.[10] Here, we aim to demonstrate the wide-spectrum property of this RNAi-mediated immunotherapy, as excessive immune response remains consistent regardless of the bacteria type. Among them are methicillin-resistant *Staph. aureus* (MRSA) and *Pseudomonas aeruginosa*, which contribute significantly to

the morbidity and mortality of hospital-acquired infections.[11,12] Thus, we apply the fusogenic pSiNPs in muscle infection of *MRSA* (strain: USA100) as a model antibiotic-resistant strain of bacteria, as well as in lung infection of *Pseudo. aeruginosa* (strain: PA01) as a model Gram negative bacteria (**Fig 1a**).

6.3   Materials and Methods

Materials. Highly boron-doped p-type silicon wafers (~1 mΩ-cm resistivity, polished on the (100) face) were obtained from Virginia Semiconductor, Inc or Siltronix, Inc. Hydrofluoric acid (48% aqueous, ACS grade) was obtained from Fisher Scientific. Anhydrous calcium chloride was obtained from Spectrum Chemicals (Gardena, CA). Deionized (18 mΩ) water was used for all aqueous dilutions. For lipids, 1,2-dimyristoyl-sn-glycero-3-phosphocholine (DMPC), 1,2-distearoyl-sn-glycero-3-phosphoethanolamine-N-[methoxy(polyethylene glycol)-2000, Avanti Polar Lipids] (DSPE-mPEG), 1,2-distearoyl-sn-glycero-3-phosphoethanolamine-N-[maleimide(polyethylene glycol)-2000] (DSPE-PEG-maleimide), and 1,2-dioleoyl-3-trimethylammonium-propane (DOTAP) were purchased from Avanti Polar Lipids (Alabaster, AL) and stored at -4ºC. Fluorescent dyes Calcein (Sigma-Aldrich) and hydrophobic 1,1'-Dioctadecyl-3,3,3',3'-Tetramethylindocarbocyanine Perchlorate (DiI, Life Technologies) were used, and Lipofectamine® 2000 Transfection Reagent was obtained from Thermo Fisher Scientific. Custom siRNAs were purchased from Dharmacon (Lafayette, CO), and primers were purchased from IDT DNA (San Diego, CA). Macrophage-targeting peptide (CRV) was identified by Dr. Erkki Ruoslahti's group at Sanford-Burnham-Prebys Medical Discovery Center (SBPMDI, CA) and custom synthesized by CTC Scientific (Sunnyvale, CA). For *in vitro* studies, Raw 264.7 and J774a.1 cells were purchased from ATCC (Manassas, VA) within 6 months prior to all experiments. DMEM cell media was purchased from GE Healthcare Life Sciences (HyClone, Pittsburg, PA), with supplemental fetal bovine serum (HyClone, Pittsburg, PA) and

penicillin/streptomycin (HyClone, Pittsburg, PA). Staphylococcus aureus subsp. aureus Rosenbach (ATCC® 25923™) was purchased from ATCC (Manassas, VA) within 6 months prior to all experiments, and 6 week-old male Balb/C were purchased from Envigo (Placentia, CA). Tobramycin was purchased from Sigma Aldrich (St. Louis, MO). Vancomycin was purchased from Cayman Chemical Company (Ann Arbor, MI).

Preparation of porous silicon nanoparticles. Porous silicon (pSi) samples were prepared by electrochemical etching of silicon wafers in an electrolyte consisting of 3:1 (v:v) of 48% aqueous HF:ethanol (CAUTION: HF is highly toxic and proper care should be exerted to avoid contact with skin or lungs). A silicon working electrode with an exposed area of 8.6 cm^2 was contacted on the back side with aluminum foil and mounted in a Teflon cell. The silicon wafer was then anodized in a two-electrode configuration with a platinum counter electrode, by applying an alternating current of square waveform, with lower current density of 50 mA/cm^2 for 0.6s and high current density of 400 mA/cm^2 for 0.36s repeated for 500 cycles. Then the porous layer is lifted off by etching at a constant current density of 3.7 mA/cm^2 for 250s in a 1:20 (v:v) of 48% aqueous HF:ethanol solution, to be sonicated in deionized water for 12h into nanoparticles. Fluorescent dye and siRNA payloads were loaded into the pSi nanoparticles by pore sealing by calcium silicate formation; the calcium silicate sealing chemistry has demonstrated high efficiency in loading anionic payloads previously[36]. Calcein was dissolved in PBS at 100 mM. 150 uL of calcein was pipetted gently with 150 uL of pSiNP and 700 uL of 2M calcium chloride under ultrasonication for 15 min. For siRNA loading, we used siIRF5 (IRF5, sense 5'-dTdT-CUG CAG AGA AUA ACC CUG A-dTdT-3' and antisense 5'-dTdT UCA GGG UUA UUC UCU GCA G dTdT-3') and siLuc (luciferase, 5′-CUU ACG CUG AGU ACU UCG A dTdT-3′ and antisense 5′-UCG AAG UAC UCA GCG UAA G dTdT-3′). siRNA was dissolved in RNAse-free water to 150 µM and loaded into pSi at the same volume ratio and process as calcein loading with only RNAse-free water used as solvent.

Liposomal coating. Fusogenic coating (F) and non-fusogenic coating (NF) were prepared from DMPC, DSPE-PEG, and DOTAP at the molar ratio of 76.2:3.8:20 and 96.2:3.8:0, respectively. The lipid films were prepared by evaporating the organic solvent, with 725.5 µg of DMPC, 151.6 µg of DSPE-PEG (methoxy or maleimide terminated), and 196.3 µg of DOTAP (F) or 916.0 µg of DMPC and 151.6 µg of DSPE-PEG (methoxy or maleimide terminated) (NF). The DiI-incorporated films were added with 26.3 µg of DiI (1.25 mg/ml in 100% ethanol). The films were then hydrated with payload-pSi solution and prepared by film hydration/extrusion; the pSi-hydrated lipid was heated to 40ºC with constant magnetic stirring for 10 min. Then the mixture was extruded through 200 nm polycarbonate membrane 20 times. CRV was conjugated to maleimide-terminated PEG by mixing 100 uL of 1 mg/mL CRV (in deionized water) in 1 mg/ml of the liposomal pSi (by lipid mass) overnight at 4ºC. Particles were washed three times at each step by centrifugation in Microcon-30kDa Centrifugal Filter Unit (EMD Millipore) by spinning at 5000g at 25ºC. The loaded siRNA concentration was quantified by NanoDrop 2000 spectrophotometer (Thermo Fisher Scientific, ND-2000) after each step of particle formation by checking the ultraviolet absorption of the supernatant and pellet of each wash. Nanoparticle size and zeta-potential were measured by dynamic light scattering (DLS, Zetasizer ZS90, Malvern Instruments), and structural morphology were visualized by JEOL 1200 EX II TEM. Samples were prepared by dropping 5 uL of the sample on the TEM grid, drying off excess solvent after 1 min, and dropping 5 uL of uranyl acetate for negative staining.

Bacterial culture. All bacterial work was performed in an approved BSL-2 facility with a clean hood. MRSA was cultured by incubating 50 µL of the bacteria in 10 mL of the cation adjusted Mueller Hinton Broth (CAMHB), and PA01 was cultured by incubating 50 uL of bacteria in 10 mL of the brain heart (BH) infusion broth (Fisher Scientific) for 16h in a shaking incubator at 37ºC and shaking at 200 RPM with the cap loose. The culture was re-introduced to the lag phase from the stationary phase by sub-culturing at 1:100, 1:250, and 1:400 dilutions in fresh 5

mL of the broth for 2h in a shaking incubator at 37ºC and shaking at 200 RPM with the cap loose.

Cell culture and confocal microscopy. J774a.1 macrophage cells were cultured in DMEM supplemented with 10% FBS and 1% penicillin/streptomycin. All cells were incubated at 37ºC in 5% CO_2.

All confocal microscopy images are representative of at least three independent trials and of at least 1 x 10^6 cells per slide. Lysosomal co-localization with DiI-loaded or siRNA-loaded particles was observed by seeding 0.3 x 10^6 cells on top of 22 mm round coverslips (BD Biocoat Collagen Coverslip, 22 mm) in a 6-well plate, growing to 80% confluence. The cells were pre-stained with LysoTracker Green (Thermo Fisher Scientific) for 1h at 37ºC in 5% CO_2 according to manufacturer's instructions. The cells were then washed with PBS three times, and then treated with 10 µL of DiI-loaded nanoparticles for 10 min incubation at 37℃ in 5% CO_2. The cells were washed with PBS three times to remove any particles that were not taken up, and the wells were filled with 1 mL of PBS and immediately subjected to live-cell imaging by confocal microscopy (Zeiss LSM 710 NLO).

For imaging Cy3-tagged siIRF5 as a model siRNA, 0.3 x 10^6 cells were seeded on 35 mm petri dishes, and grown to 80% confluence. The cells were treated with 10 µL of DiO-loaded fusogenic or non-fusogenic particles loaded with Cy3-tagged siIRF5 for 10 min at 37℃ in 5% CO_2. The cells were washed with PBS three times to remove any particles that were not taken up, then fixed in 1% paraformaldehyde (PFA, Santa Cruz Biotechnology) for 10 min at 4˚C, then washed with PBS three times. The coverslips were mounted on glass slides with ProLong® Diamond Antifade Mountant with DAPI (Life Technologies), dried and kept in the dark until examined by confocal microscopy (Zeiss LSM 710 NLO). For Cy3 imaging, λ_{ex} = 550 nm and λ_{em} = 580-630 nm band-pass was used.

***In vitro* knockdown quantification.** *In vitro* knockdown efficiencies of the nanoformulations were quantified using two-step quantitative real-time reverse transcription polymerase chain reaction (qRT-PCR, Roche LightCycler 96). J774a.1 cells were seeded on a 24-well plate at 2×10^4 cells per well and grown to 50% confluency overnight. The cells were incubated with the desired nanoformulations or Lipofectamine 2000 at 20 pmol siRNA dose per well. 24h or 7 days post-incubation, the cell media was removed, and RNA was purified using the QIAshredder and RNeasy Mini Kit (Qiagen, Valencia, Ca). cDNA was transcribed from the purified RNA using the BIORAD iScript cDNA Synthesis Kit and heat-treated in the Eppendorf Vapo.protect Mastercycler thermal cycler. cDNA was mixed with IRF5 primers, or the control HPRT primers (IRF5 forward: AATACCCCACCACCTTTTGA; IRF5 reverse: TTGAGATCCGGGTTTGAGAT; HPRT forward: GTCAACGGGGGACATAAAAG; HPRT reverse: CAACAATCAAGACATT-CTTTCCA) and iQ SYBR Green Supermix according to the manufacturer's instructions. qRT-PCR analysis was performed in the BIORAD 96-well white Multiplate PCR Plates using the Roche LightCycler 96. The quantification was performed at n=6 and in RNAse- and DNAse-free laminar flow hood dedicated to RNA work. Quantified knockdown was statistically evaluated using One-way ANOVA with Tukey's HSD post-hoc analysis.

***In vivo* infection model.** All animal work was conducted using 6-8 week old male Balb/C mice. For MRSA muscle infection model, the bacteria underwent a 16h incubation in CAMHB. Then, MRSA was sub-cultured at 1:100, 1:250, and 1:400 dilutions in 5 mL of fresh broth for 2h to reach growth phase. The optical density at 600 nm was measured using a cuvette spectrometer with the broth set as the blank. Five mL of bacterial culture at $OD_{600} \approx 0.5$ was centrifuged, the bacteria were washed by centrifugation in PBS three times, and re-suspended in 500 μL of PBS for inoculation, resulting in $OD_{600} \approx 2.25$. Each mouse was intramuscularly injected in the right hind thigh with 50 μL of the MRSA stock (equating to

approximately 1.25 x 10^8 CFU/mouse). For the PA01 pneumonia model, the bacteria underwent a 16h incubation in brain heart infusion broth. Then, PA01 was sub-cultured at 1:100, 1:250, and 1:400 dilutions in 5 mL of fresh BH broth for 2.5h to reach growth phase. The optical density at 600 nm was measured using a cuvette spectrometer with the broth set as the blank. 5 mL of bacterial culture at $OD_{600} \approx 0.7$ was centrifuged, the bacteria were washed by centrifugation in PBS three times, and re-suspended in 1 mL of PBS for inoculation. Each mouse was infected by intratracheal catheter injection of approximately 1 x 10^9 CFU of bacteria in 50 μL of PBS. All treatment-injections were performed 3d (MRSA) or 24h (PA01) after inoculation of the bacteria.

In vivo **IRF5 knockdown efficiency.** 8 week-old male Balb/C mice were infected as described above. Infected mice were intravenously injected with 100 μL of PBS or siLuc- or siIRF5-loaded fusogenic and non-fusogenic pSiNPs with or without CRV at 23.2 µmol/kg lipid, corresponding to 69 µg/kg siRNA, and 0.3 mg/kg pSi in 100 μL PBS. Twenty-four hours post-injection and circulation, MRSA infected mice were sacrificed for popliteal lymph node and muscle harvest, and PA01 infected mice were sacrificed for brochoalveolar lavage (BAL) and lung harvest. BAL was performed by intratracheal instillation of a mouse catheter, with a suture tied around the trachea to prevent leakage. 1 mL of PBS was injected into the lungs through the catheter, and aspirated back out. The process was repeated three times to collect up to 2.5 mL of the BAL fluid. Harvested lymph nodes, muscles and lungs were homogenized, and along with BAL fluid, the homogenates were separately treated with Dead Cell Removal MicroBeads (Miltenyi Biotec) for magnetic separation on an LS column according to the manufacturer's instructions. The collected cells were then treated with Anti-F4/80 microbeads (Miltenyi Biotec) for magnetic separation on an LS column according to the manufacturer's instructions for macrophage purification.

The *in vivo* knockdown of IRF5 was quantified using two-step quantitative real-time reverse transcription polymerase chain reaction (qRT-PCR, Roche LightCycler 96). The cell

pellets or the lung homogenates were lysed and RNA was purified using the QIAshredder and RNeasy Mini Kit (Qiagen, Valencia, Ca). cDNA was transcribed from the purified RNA using the BIORAD iScript cDNA Synthesis Kit and heat-treated in the Eppendorf Vapo.protect Mastercycler thermal cycler. cDNA was mixed with IRF5 primers, or the control HPRT primers (IRF5 forward: AATACCCCACCACCTTTTGA; IRF5 reverse: TTGAGATCCGGGTTTGAGAT; HPRT forward: GTCAACGGGGGACATAAAAG; HPRT reverse: CAACAATCAAGACATT-CTTTCCA) and iQ SYBR Green Supermix according to the manufacturer's instructions. qRT-PCR analysis was performed in the BIORAD 96-well white Multiplate PCR Plates using the Roche LightCycler 96. The quantification was performed at n=6 and in RNAse- and DNAse-free laminar flow hood dedicated to RNA work. Relative knockdown was statistically evaluated using One-way ANOVA with Tukey's HSD post-hoc analysis.

Nanoparticle targeting and biodistribution. 6-8 week old male Balb/C mice were infected as described above. 3 days (MRSA) or 24h (PA01) post-infection, infected and healthy mice were intravenously injected with DiI- and siIRF5-loaded fusogenic pSiNPs with or without FAM-CRV conjugation, at 23.2 µmol/kg lipid, corresponding to 24 µg/kg siRNA, and 0.5 mg/kg pSi 100 µL in PBS. For MRSA infection models, the DiI-loaded particle localization in the ipsilateral (right) and contralateral (left) muscles was visualized using the IVIS 200 (Perkin Elmer) with 4 s exposure time on the DsRed excitation and emission filters. Both healthy and infected animals were sacrificed and harvested for organs 1h and 24h post-injection. ImageJ was used to quantify the fluorescence of each muscle, and averaged over the three mice per group.

For the PA10 infection model, homing to infected lungs was validated using flow cytometry. 24h post-infection, mice were intravenously injected with DiI- and siIRF5-loaded fusogenic pSiNPs with or without FAM-CRV conjugation, at 23.2 µmol/kg lipid, corresponding to 24 µg/kg siRNA, and 0.5 mg/kg pSi 100 µL in PBS. 1h and 24h post-injection, the mice were

sacrificed and BAL fluid and lungs were harvested. The BAL fluid and the lung homogenates were treated with Dead Cell Removal MicroBeads (Miltenyi Biotec) for magnetic separation on an LS column according to the manufacturer's instructions. The collected cells were then treated with Anti-F4/80 microbeads (Miltenyi Biotec) for magnetic separation on an LS column according to the manufacturer's instructions to collect only the macrophages. The macrophages were then processed with the LSRFortessa flow cytometer (BD Biosciences) to analyze the number of cells containing the particles' DiI signals (ex: 561 nm/50 mW; em: 582/15 nm), and analyzed using the Flowing Software.

In vivo **therapeutic efficacy in MRSA muscle infection.** 8 week-old male Balb/C mice were infected as described. 3 days post-infection, infected mice were intravenously injected with 200 μL of PBS, 145 mg/kg of vancomycin, non-fusogenic particles with siIRF5 and CRV conjugation, fusogenic particles with sham siRNA (siLuc, luciferase encoding siRNA) conjugated with CRV, or fusogenic particles with siIRF5 and CRV conjugation at 23.2 µmol/kg lipid, corresponding to 24 µg/kg siRNA, and 0.5 mg/kg pSi in 100 μL PBS. To confirm clearance of bacteria from the muscles, the number of colony-forming units (CFU) of MRSA was determined from titering of muscle homogenates. At days 3, 7, and 14 post-IV injection, mice were sacrificed for photographic record of muscle abscess and muscle harvest. The muscles were weighed, gently washed in PBS, and then homogenized. The homogenates were serially diluted to a dilution factors of 10^2, 10^8, 10^{12}, and 10^{16}, and plated on agar-coated petri dishes and incubated at 37°C overnight at n=2 per dilution factor. The colonies were counted n=4 for each dilution factor, and divided by the muscle mass. The average CFU/g was quantified using counts from 2 plates at equivalent dilution factors from 3 mice (n = 2 plates x 3 mice = 6).

In vivo **therapeutic efficacy in PA01 lung infection.** 8 week-old male Balb/C mice were infected as described. 24h post-infection, infected mice were intravenously injected with 200 μL of PBS, 100 mg/kg of tobramycin, non-fusogenic particles with siIRF5 and CRV

conjugation, fusogenic particles with sham siRNA (siLuc, luciferase encoding siRNA) conjugated with CRV, or fusogenic particles with siIRF5 and CRV conjugation at 23.2 µmol/kg lipid, corresponding to 24 µg/kg siRNA, and 0.5 mg/kg pSi in 100 µL PBS. At 7 days post-injection (healthy and F-siIRF5-CRV) or at *ad mortem* (infected and NF-siIRF5-CRV), the lungs were inflated and harvested for fixation in 4% paraformaldehyde (PFA). The fixed lungs were paraffinized and sectioned for hematoxylin and eosin (H&E) and Gram staining. The stained slides were histopathologically evaluated by Dr. Kent Osborn (Associate Director, Animal Care Program, UCSD).

To confirm clearance of bacteria from the muscles, the number of colony-forming units (CFU) of PA01 was determined from titering of lung homogenates. At 7 days post-IV injection, mice were sacrificed for lung harvest. The lungs were weighed, gently washed in PBS, and then homogenized. The homogenates were serially diluted to a dilution factors of 10^2 and 10^{12}, and plated on agar-coated petri dishes and incubated at 37°C overnight at n=3 per dilution factor. The colonies were counted for each dilution factor, and divided by the muscle mass. The average CFU/g was quantified using counts from 2 plates at equivalent dilution factors from 2 mice (n = 3 plates x 2 mice = 6).

Finally, a survival challenge was performed with infected mice, who were intravenously injected 24h post-infection with the treatment compounds. Each group had 7 mice, which were tallied daily for survival. Moribund mice that showed signs of expiring within 5h were sacrificed according to the IACUC guidelines. The resulting data were statistically evaluated using One-way ANOVA and post hoc comparisons using Tukey's HSD test at $p < 0.05$.

6.4   Fusogenic nanoparticle characterization

Lipid-coated porous silicon nanoparticles (pSiNPs) is a core-shell structure, with a dense siRNA-loaded porous silicon cluster as the core, and a targeting peptide-conjugated lipid coating as the shell (**Fig 6.1a**).[10,13] The core pSiNPs were prepared by electrochemical etch of silicon wafers followed by sonication. The siRNA loading and pSiNP cluster formation was induced by calcium chloride to form a calcium silicate.[14,15] The core particle mixture is then used to hydrate the lipid film, and the particles are mechanically extruded through 200 nm polycarbonate membrane to form the stable core-shell structure.

In order to observe for fusogenic uptake and cytosolic delivery of siRNA, we conducted confocal microscopy to visualize the intracellular localization of the particle in J774a.1 macrophage cell line. The left panel on **Figure 6.1b** shows a lysosome (green)-stained cell treated with lipophilic DiI (red)-loaded fusogenic nanoparticles. The red DiI signal stained the cell's plasma membrane, indicating successful fusion of the particles that allowed the transfer of DiI from the particle's lipid bilayer to the cell's plasma membrane. This mechanism is further supported by the fact that the DiI-labelled particle did not co-localize with the lysosomes, indicating a non-endocytic uptake. The right panel on **Figure 6.1b** shows a cell treated with Cy3 (red)-labelled siRNA- and lipophilic DiO (green)-loaded fusogenic nanoparticles. The green DiO signal stained the plasma membrane as before, and the Cy3-labelled siRNA were found dispersed in the cytoplasm, particularly in the perinuclear region.

Next, the same experiment was performed using non-fusogenic particles, which maintain an identical structure to the fusogenic particles, and differ only in the composition of the lipid shell. The non-fusogenic lipid coating is that of a more conventional liposome that typically is endocytosed by cells.[10,13,16,17] The left panel on **Figure 6.1c** shows a lysosome (green)-stained cell treated with lipophilic DiI (red)-loaded non-fusogenic nanoparticles. The red DiI and green lysosome signals co-localized, and there was no visible staining of the plasma membrane, which indicates an endocytic uptake. The right panel on **Figure 6.1c** shows a cell treated with

Cy3 (red)-labelled siRNA- and lipophilic DiO (green)-loaded non-fusogenic nanoparticles. Again, the green DiO and red Cy3-labelled siRNA signals co-localized with no visible plasma membrane staining, which indicates an endocytic uptake, and entrapment of the siRNA payload within the lysosomes. As literature shows that 70% of the endocytosed siRNA is excreted out of the cell with the majority of the remaining 30% degrading within the acidic lysosomal compartments[18-20], the fusogenic delivery of siRNA is expected to obtain much higher gene silencing effect.

6.5   *In vitro* and *in vivo* gene silencing efficiency

With distinct uptake pathways between fusogenic and non-fusogenic particles, we conducted *in vitro* quantifications of gene silencing effect using quantitative real time-polymerase chain reaction (qRT-PCR). **Figure 6.2a** shows that fusogenic nanoparticles that were loaded with siRNA against the *Irf5* gene (siIRF5) and conjugated with the activated macrophage-targeting peptide, CRV (F-siIRF5-CRV) attained approximately 86% silencing effect, comparable to the 80% obtained by the commercially available Lipofectamine 2000 loaded with siIRF5 (LF-siIRF5). On the other hand, the non-fusogenic particles with the same siIRF5 payload and the CRV homing peptide was only able to obtain approximately 45% gene silencing efficiency, which was statistically significantly less effective than its fusogenic counterpart (p=0.001).

To determine how long the silencing effect lasted, we further incubated the transfected J774a.1 macrophages for a week, and conducted another qRT-PCR analysis of the *Irf5* gene expression (**Fig 6.2b**). While the NF-siIRF5-CRV particle-treated cells recovered the gene expression from 55% to approximately 90%, the F-siIRF5-CRV particle-treated cells were able to maintain the expression below 50%, with the level increasing from 14% to approximately only

37%. The result was comparable to, yet better than, that of LF-siIRF5, which also recovered the gene expression from 20% to 45%. This result indicates that F-siIRF5-CRV formulation as a therapeutic may require less frequent dosing than the conventional endocytic formulations.

Additionally, we determined the cytotoxicity of the nanoformulations compared to the commercial standard, Lipofectamine 2000, which is known to become increasingly cytotoxic with incubation time. **Figure 6.3** shows that at equivalent doses of siRNA treatment in J774a.1 macrophages, Lipofectamine 2000 (LF-siIRF5) decreases the cell viability beginning from 4h of incubation to a significant 22% viability at 24h of incubation ($p < 0.03$). In contrast, the particle formulations maintain >80% cell viability up to 6h of incubation, and retain approximately 60% viability even at 24h of incubation ($p_{F\text{-}siIRF5\text{-}CRV} < 0.035$; $p_{NF\text{-}siIRF5\text{-}CRV} < 0.048$; $p_{F\text{-}siIRF5\text{-}mPEG} < 0.039$). Thus, the nanoformulations present a more biosafe transfection method compared to the benchmark Lipofectamine 2000.

Next, we determined the *in vivo* gene silencing efficiency of the fusogenic nanoparticles in mouse models of infection. To establish the MRSA muscle infection as an antibiotic-resistant infection model, we intramuscularly injected MRSA colonies in the right hind thigh, and allowed the abscess to form over 3 days before intravenously injecting the treatment formulations. After 24h, we harvested the right popliteal lymph node and the right hind thigh muscles for homogenization and macrophage purification. The *Irf5* gene expression was quantified in the purified macrophages using qRT-PCR. **Figure 6.2c** shows that while PBS, fusogenic formulation with the CRV homing peptide and siRNA against luciferase (siLuc) as negative control (F-siLuc-CRV), and the fusogenic formulation with siIRF5 but no homing peptide (F-siIRF5-mPEG) obtained negligible gene silencing effect, the NF-siIRF5-CRV treatment obtained approximately 40% knockdown (p=0.023), while the F-siIRF5-CRV treatment obtained a dramatic 89% knockdown (p=0.001) in macrophages of the infection site.

We also established the a *P. aeruginosa* pneumonia in mice as a Gram negative infection model by inserting a catheter in the mouse trachea and allowing the mouse to inhale PA01 strain of *P. aeruginosa* for lung infection. After 24h, we intravenously injected the treatment formulations for another 24h circulation. Then we performed bronchoalveolar lavage (BAL) to collect the fluid, and harvested the lungs post-BAL for homogenization and macrophage purification. Again, the *Irf5* gene expression was quantified in the purified macrophages using qRT-PCR. **Figure 6.2d** shows that only the F-siIRF5-CRV formulation induced a significant knockdown of approximately 83% (p=0.001) in the macrophages of the pneumonia. Thus, we have validated that the fusogenic nanoparticles are able to induce a stronger RNAi effect than non-fusogenic particles, as well as non-targeted particles *in vivo*.

6.6   *In vivo* infection homing to MRSA and PA01 infection

While fusogenic particles excelled in inducing strong gene silencing effect, they must also home to specific cell types to minimize off-target effects. Thus, we evaluated the targeting efficiency of CRV-conjugated particles to infected tissues. The CRV peptide targets the retinoid X receptor beta (RXRB), which transports from cytosolic to transmembrane region upon macrophage activation[21], thus we expect CRV-conjugated particles to be present in not only the infected tissue, but also in local lymph nodes.

Figure 6.4a shows DiI-loaded particle localization in the MRSA muscular infection model. Infected mice were intravenously injected with PBS, fusogenic formulation with siIRF5 but no homing peptide (F-mPEG), non-fusogenic fusogenic formulation with siIRF5 and the CRV peptide (NF-CRV), or the fusogenic fusogenic formulation with siIRF5 and the CRV peptide (F-CRV). At 1h and 24h point post-injection, the mice were sacrificed along with a healthy control, and the hind thigh muscles (both the contralateral (C) muscle on the opposing

222

side of the infection, and the ipsilateral (I) infected muscle) were harvested for *ex vivo* imaging using the IVIS 200 system. The imaging showed strong accumulation with the F-CRV formulation, whereas the NF-CRV and F-mPEG formulations showed moderately low accumulation. The ImageJ quantification of the signal (**Fig 6.4b**) showed the same trend, where the F-CRV formulation showed significantly higher accumulation (p=0.001) at both 1h and 24h points compared to the other formulations. Additionally, the F-mPEG (p_{1h}= 0.038; p_{24h}=0.032), NF-CRV (p_{1h}= 0.046; p_{24h}=0.001), and F-CRV (p_{1h}= 0.001; p_{24h}=0.001) groups showed significantly discrete accumulation to the ipsilateral muscle compared to the contralateral muscle.

For CRV-mediated particle accumulation to PA01 pneumonia, we utilized flow cytometry to quantify DiI signal in purified macrophages from the BAL fluid and lung homogenates of PA01-infected mice (**Fig 6.4c**). At 1h post-intravenous injection of PBS, DiI-loaded F-mPEG, NF-CRV, and F-CRV formulations, there was no visible difference in DiI signal accumulation in macrophages. However, 24h post-injection, F-CRV formulation showed great increase in accumulation to 22.55% of macrophages showing positive DiI signals. Meanwhile, the F-mPEG and NF-CRV formulations did not show great changes in accumulation.

We showed similar findings in the previous report regarding Staphylococcus aureus pneumonia models, where both the CRV peptide and fusogenic coating were required to obtain macrophage targeting and uptake into the cells.[10] The lack of notable accumulation in both MRSA muscular infection and PA01 pneumonia models using non-fusogenic particles despite the CRV-conjugation may be due similar reasons. Both models confirm that CRV-conjugated fusogenic nanoparticles are superior in macrophage targeting in infected tissues.

6.7 *In vivo* **therapeutic efficacy in MRSA muscle infection**

As the fusogenic particle's ability to selectively home to target macrophages and silence the *Irf5* gene have been validated, we next investigated the therapeutic efficacy of its treatment. **Figure 6.5a** shows photographic tracking of MRSA-induced abscess in the hind thigh. Mice were intravenously injected with PBS, 145 mg/kg vancomycin, fusogenic formulation with the CRV homing peptide and siRNA against luciferase (siLuc) as negative control (F-siLuc-CRV), and the non-fusogenic formulation with siIRF5 with the CRV peptide (NF-siIRF5-CRV), or fusogenic formulation with siIRF5 with the CRV peptide (F-siIRF5-CRV). At 3, 7, and 14 days after the injection, mice were sacrificed for abscess observation. While PBS- and F-siLuc-CRV injected mice showed large abscess formation over time, the vancomycin- and NF-siIRF5-CRV injected mice showed a marked reduction in the abscess size, although the infection visibly persisted for over the 14 days. On the other hand, the F-siIRF5-CRV treatment group showed great reduction in the abscess size within 3 days of treatment, and by 7 days, the abscess was completely unidentifiable by eye, and showed no visible difference from the healthy control.

In order to quantifiably determine the therapeutic effect, we homogenized the thighs at each time point and conducted a serial dilution for agar plating. The number of colony forming units (CFUs) grown on the agar plate from the homogenate dilutions were counted and the thighs were weighed and are reported in **Figure 6.5b** CFUs per mass. Similar to the photographic findings, the PBS and F-siLuc-CRV treatments resulted in over 1×10^{15} CFU/g in the thigh throughout the 14 days, while the vancomycin and NF-siIRF5-CRV treatments resulted in a moderate decrease in the bacteria titer to over 1×10^9 CFU/g by day 14. In contrast, the F-siIRF5-CRV treatment resulted in less than 6×10^2 CFU/g by day 14, and was not statistically different from the healthy control counts (p>0.9). Thus, the F-siIRF5-CRV therapeutic is able to recover the MRSA-infected thigh to a healthy state within one week of injection.

6.8   *In vivo* therapeutic efficacy in PA01 lung infection

Finally, we tested for similar therapeutic effects of the fusogenic particles in the PA01 pneumonia model. First, we intravenously injected non-fusogenic formulation with siIRF5 with the CRV peptide (NF-siIRF5-CRV), or fusogenic formulation with siIRF5 with the CRV peptide (F-siIRF5-CRV) in mice with PA01 pneumonia, with additional healthy and infected mouse groups with no injections as positive and negative controls, respectively. At the end-point (7 days post-injection for healthy and F-siIRF5-CRV groups, and *ad mortem* (under 7 days) for infected and NF-siIRF5-CRV groups), mouse lungs were inflated and harvested for histopathological analyses (**Fig 6.6a**). While the NF-siIRF5-CRV lung showed a similar trend of excessive inflammation with neutrophil infiltration, with presence of Gram negative rods in the Grams stain (**Fig 6.6a NF-siIRF5-CRV inset**). On the other hand, the F-siIRF5-CRV treatment group showed a normal morphology with expanded alveoli and no presence of Gram negative bacteria.

Similar trend was found when we quantified for bacteria titer in the lung homogenates at the same end-points (*ad mortem* for mice that were moribund under 7 days post-injection, and the 7-day point for surviving mice). While PBS, 100 mg/kg Tobramycin, fusogenic formulation with the CRV homing peptide and siRNA against luciferase (siLuc) as negative control (F-siLuc-CRV), and the non-fusogenic formulation with siIRF5 with the CRV peptide (NF-siIRF5-CRV) showed over 1×10^{12} CFU/g, the F-siIRF5-CRV formulation significantly decreased the titer to approximately 1×10^2 CFU/g in 7 days (p<0.005), which was not significantly different from the healthy control (p=0.9).

Lastly, we tallied the survival of PA01 pneumonia-carrying mice that were treated with PBS, 100 mg/kg tobramycin, NF-siIRF5-CRV, F-siLuc-CRV, or F-siIRF5-CRV. Mice were infected on day 0, and the therapeutics were intravenously injected on day 1, and mice were observed for the following 7 days. **Figure 6.6c** shows that while the PBS, NF-siIRF5-CRV, and

F-siLuc-CRV groups yielded less than 20% survival rate, the tobramycin treatment group yielded a moderate 30% survival. The mediocre result attained by the standard antibiotic benchmark may be due to the fact that tobramycin is clinically administered at 1 mg/kg three times daily in humans[22], while the literature's intravenous dosing range of tobramycin in mouse models ranges from 10-400 mg/kg/day.[23-26] The treatment regimen used in the present study used a single administration of 100 mg/kg at 24h post-infection to match the single-dose regiment followed by the nanoformulations. In fact, a single administration of the F-siIRF5-CRV formulation rescued 6 out of 7 mice in its cohort to complete recovery within 7 days of treatment, which was significantly more effective than all other treatment groups (p<0.024). Thus, the F-siRF5-CRV treatment in mice was found to be an effective immunotherapy against MRSA muscular and PA01 lung infection models.

6.9   Discussion and Conclusions

Bacterial infection has returned as an increasing threat in the era of antibiotic-resistance, and solutions to reduce its threat have become a high priority globally. While there have been increasing research into antibiotics development and FDA clearance of novel classes of antibiotics to combat against the prevailing "superbugs", it is inevitable that further mutations that lead to resistance development will occur.[1,2,4,5,27-31] Moreover, Gram negative bacteria have remained a challenging target to treat due to their secondary cell wall. Thus, the present study aimed to develop a solution that is independent of small molecule antibiotics, by utilizing our body's own immune system.

The fusogenic porous silicon nanoparticles were first introduced as a potential immunotherapy platform when it demonstrated outstanding *in vivo* homing to activated macrophages, significant gene silencing effect that led to an *Irf5*-depleted anti-inflammatory

immune response. This effect helped focus the immune system in clearing out the bacteria and minimizing auto-immune damage caused by fibrosis and excessive inflammation.[10] As immunotherapy offers a solution that should operate regardless of the pathogen type, we explored its effect in antibiotic-resistant (MRSA) and Gram negative (*P. aeruginosa*) bacterial infections in deep tissues (muscle and lungs) that are difficult-to-reach by standard oral or dermal administrations.

The fusogenic nanoparticles carrying siIRF5 and the CRV homing peptide demonstrated potent therapeutic potential in both MRSA muscular and PA01 lung infections, which indicates its wide-spectrum coverage of most bacterial infection types (Gram positive, Gram negative, and antibiotic-resistant). This outcome also leads us to investigate diseases beyond the most obvious source of pathogenesis; infections may not require solutions to simply eradicate the pathogens, and pathogens themselves may not be the primary contributors to patient mortality.

The fusogenic formulation presented in this study serves as a generalizable anti-inflammatory therapeutic, which may have potential in other diseases characterized by excessive immune response (e.g. autoimmune disorders, inflammatory bowel disease, atherosclerosis, etc.). Moreover, simple exchange of the targeting peptide and the siRNA payload will form an entirely different therapeutic that may be used in other diseases that require gene modulations. As siRNA and RNAi-mediated gene silencing induces a transient yet relatively lasting (>7 days) effect, the fusogenic particles present an excellent platform technology for gene therapy.

6.10   References

1   Davies, J. & Davies, D. Origins and Evolution of Antibiotic Resistance. *Microbiology and Molecular Biology Reviews : MMBR* **74**, 417-433, doi:10.1128/MMBR.00016-10 (2010).

2   Ventola, C. L. The antibiotic resistance crisis: part 1: causes and threats. *P T* **40**, 277-283 (2015).

3   Lewis, K. Platforms for antibiotic discovery. *Nat Rev Drug Discov* **12**, 371-387, doi:10.1038/nrd3975 (2013).

4   Nikolaidis, I., Favini-Stabile, S. & Dessen, A. Resistance to antibiotics targeted to the bacterial cell wall. *Protein Science : A Publication of the Protein Society* **23**, 243-259, doi:10.1002/pro.2414 (2014).

5   Manohar, A., Ahuja, J. & Crane, J. K. Immunotherapy for Infectious Diseases: Past, Present, and Future. *Immunol Invest* **44**, 731-737, doi:10.3109/08820139.2015.1093914 (2015).

6   Roux, D., Pier, G. B. & Skurnik, D. Magic bullets for the 21st century: the reemergence of immunotherapy for multi- and pan-resistant microbes. *J Antimicrob Chemother* **67**, 2785-2787, doi:10.1093/jac/dks335 (2012).

7   Babb, R. & Pirofski, L. A. Help is on the way: Monoclonal antibody therapy for multi-drug resistant bacteria. *Virulence* **8**, 1055-1058, doi:10.1080/21505594.2017.1306620 (2017).

8   Navalkele, B. D. & Chopra, T. Bezlotoxumab: an emerging monoclonal antibody therapy for prevention of recurrent Clostridium difficile infection. *Biologics* **12**, 11-21, doi:10.2147/BTT.S127099 (2018).

9   Saylor, C., Dadachova, E. & Casadevall, A. Monoclonal antibody-based therapies for microbial diseases. *Vaccine* **27 Suppl 6**, G38-46, doi:10.1016/j.vaccine.2009.09.105 (2009).

10   Kim, B., Pang, H. B., Kang, J., Park, J. H., Ruoslahti, E. & Sailor, M. J. Immunogene therapy with fusogenic nanoparticles modulates macrophage response to Staphylococcus aureus. *Nat Commun* **9**, 1969, doi:10.1038/s41467-018-04390-7 (2018).

11   DeLeon, S., Clinton, A., Fowler, H., Everett, J., Horswill, A. R. & Rumbaugh, K. P. Synergistic Interactions of Pseudomonas aeruginosa and Staphylococcus aureus in an In Vitro Wound Model. *Infection and Immunity* **82**, 4718-4728, doi:10.1128/IAI.02198-14 (2014).

12   Sydnor, E. R. & Perl, T. M. Hospital epidemiology and infection control in acute-care settings. *Clin Microbiol Rev* **24**, 141-173, doi:10.1128/CMR.00027-10 (2011).

13   Kim, B. & Sailor, M. J. Synthesis, Functionalization, and Characterization of Fusogenic Porous Silicon Nanoparticles for Oligonucleotide Delivery. *JoVE*, e59440, doi:doi:10.3791/59440 (2019).

14   Kang, J., Joo, J., Kwon, E. J., Skalak, M., Hussain, S., She, Z.-G., Ruoslahti, E., Bhatia, S. N. & Sailor, M. J. Self-Sealing Porous Silicon-Calcium Silicate Core–Shell Nanoparticles for Targeted siRNA Delivery to the Injured Brain. *Advanced Materials*, n/a-n/a, doi:10.1002/adma.201600634 (2016).

15   Choi, E., Lee, J., Kwon, I. C. & Kim, S. Cumulative directional calcium gluing between phosphate and silicate: A facile, robust and biocompatible strategy for siRNA delivery by amine-free non-positive vector. *Biomaterials*, doi:/10.1016/j.biomaterials.2019.04.006 (2019).

16   Kim, J., Santos, O. A. & Park, J.-H. Selective photosensitizer delivery into plasma membrane for effective photodynamic therapy. *Journal of Controlled Release* **191**, 98-104, doi:http://dx.doi.org/10.1016/j.jconrel.2014.05.049 (2014).

17   Lee, J., Kim, J., Jeong, M., Lee, H., Goh, U., Kim, H., Kim, B. & Park, J.-H. Liposome-Based Engineering of Cells To Package Hydrophobic Compounds in Membrane Vesicles for Tumor Penetration. *Nano Letters* **15**, 2938-2944, doi:10.1021/nl5047494 (2015).

18   Gilleron, J., Querbes, W., Zeigerer, A., Borodovsky, A., Marsico, G., Schubert, U., Manygoats, K., Seifert, S., Andree, C., Stoter, M., Epstein-Barash, H., Zhang, L., Koteliansky, V., Fitzgerald, K., Fava, E., Bickle, M., Kalaidzidis, Y., Akinc, A., Maier, M. & Zerial, M. Image-based analysis of lipid nanoparticle-mediated siRNA delivery, intracellular trafficking and endosomal escape. *Nature biotechnology* **31**, 638-646, doi:10.1038/nbt.2612 (2013).

19   Sahay, G., Querbes, W., Alabi, C., Eltoukhy, A., Sarkar, S., Zurenko, C., Karagiannis, E., Love, K., Chen, D., Zoncu, R., Buganim, Y., Schroeder, A., Langer, R. & Anderson, D. G. Efficiency of siRNA delivery by lipid nanoparticles is limited by endocytic recycling. *Nature biotechnology* **31**, 653-658, doi:10.1038/nbt.2614 (2013).

20   Wang, Y. & Huang, L. A window onto siRNA delivery. *Nature biotechnology* **31**, 611-612, doi:10.1038/nbt.2634 (2013).

21   Tang, T., Wei, Y., Kang, J., She, Z. G., Kim, D., Sailor, M. J., Ruoslahti, E. & Pang, H. B. Tumor-specific macrophage targeting through recognition of retinoid X receptor beta. *J Control Release* **301**, 42-53, doi:10.1016/j.jconrel.2019.03.009 (2019).

22   Rybak, M. J., Boike, S. C., Levine, D. P. & Erickson, S. R. Clinical use and toxicity of high-dose tobramycin in patients with pseudomonal endocarditis. *J Antimicrob Chemother* **17**, 115-120 (1986).

23   De Leo, L., Di Toro, N., Decorti, G., Malusa, N., Ventura, A. & Not, T. Fasting increases tobramycin oral absorption in mice. *Antimicrob Agents Chemother* **54**, 1644-1646, doi:10.1128/AAC.01172-09 (2010).

24   Louie, A., Liu, W., Fikes, S., Brown, D. & Drusano, G. L. Impact of meropenem in combination with tobramycin in a murine model of Pseudomonas aeruginosa pneumonia. *Antimicrob Agents Chemother* **57**, 2788-2792, doi:10.1128/AAC.02624-12 (2013).

25   Potel, G., Caillon, J., Fantin, B., Raza, J., Le Gallou, F., Lepage, J. Y., Le Conte, P., Bugnon, D., Baron, D. & Drugeon, H. Impact of dosage schedule on the efficacy of gentamicin, tobramycin, or amikacin in an experimental model of Serratia marcescens endocarditis: in vitro-in vivo correlation. *Antimicrob Agents Chemother* **35**, 111-116 (1991).

26   Wold, J. S. & Turnipseed, S. A. Toxicology of vancomycin in laboratory animals. *Rev Infect Dis* **3 suppl**, S224-229 (1981).

27   Conly, J. M. & Johnston, B. L. Where are all the new antibiotics? The new antibiotic paradox. *The Canadian Journal of Infectious Diseases & Medical Microbiology* **16**, 159-160 (2005).

28   Fair, R. J. & Tor, Y. Antibiotics and Bacterial Resistance in the 21st Century. *Perspectives in Medicinal Chemistry* **6**, 25-64, doi:10.4137/PMC.S14459 (2014).

29   Garzoni, C. & Kelley, W. L. Staphylococcus aureus: new evidence for intracellular persistence. *Trends Microbiol* **17**, 59-65, doi:10.1016/j.tim.2008.11.005 (2009).

30   Rai, J., Randhawa, G. K. & Kaur, M. Recent advances in antibacterial drugs. *International Journal of Applied and Basic Medical Research* **3**, 3-10, doi:10.4103/2229-516X.112229 (2013).

31   Shlaes, D. M., Sahm, D., Opiela, C. & Spellberg, B. The FDA Reboot of Antibiotic Development. *Antimicrobial Agents and Chemotherapy* **57**, 4605-4607, doi:10.1128/AAC.01277-13 (2013).

6.10   Figures and Tables
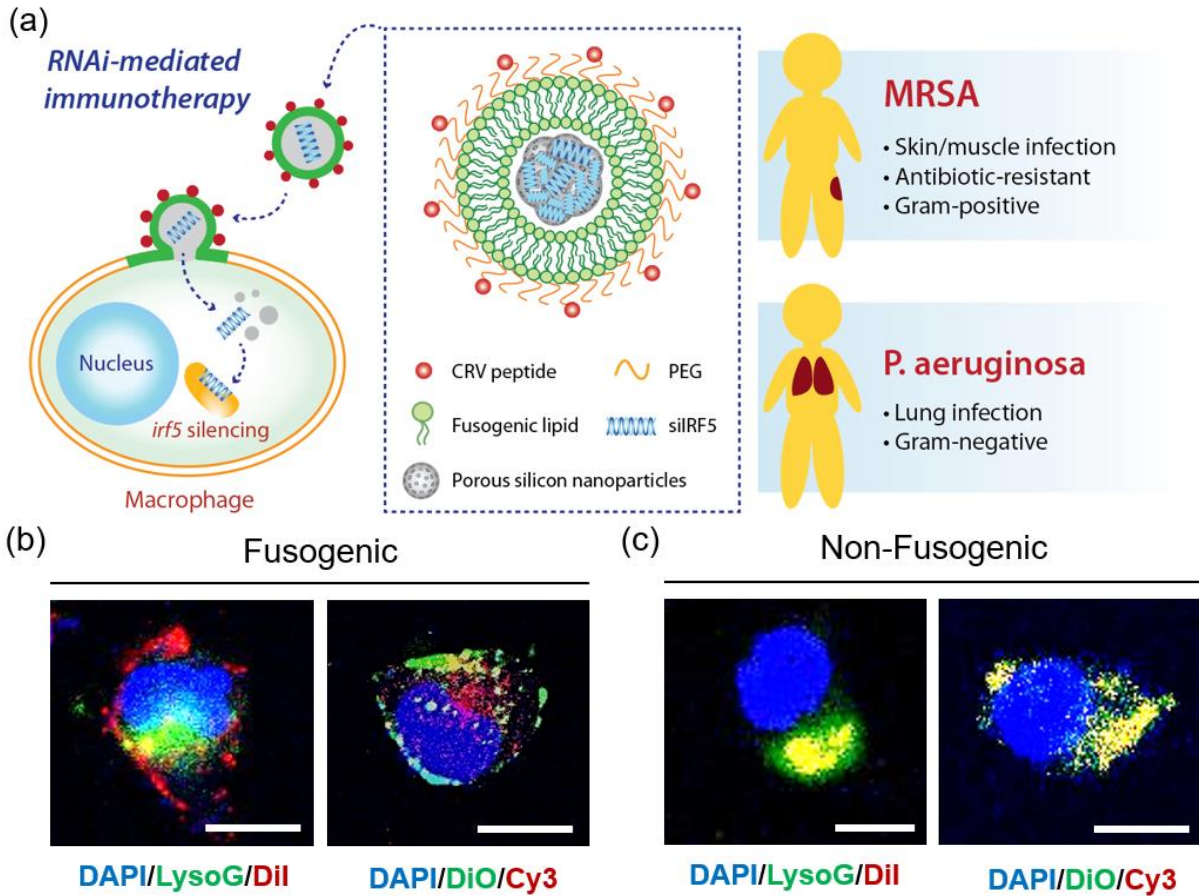
Figure 6.1. Fusogenic porous silicon nanoparticles directly delivers siIRF5 into the cell cytoplasm.
(a) Schematic of fusogenic porous silicon nanoparticles (F-pSiNPs) mode of action in delivering and silencing the irf5 gene in macrophages, as a therapeutic strategy against Methicilin-resistant *Staphylococcus aureus* (MRSA) and *Pseudomonas aeruginosa*; **(b)** confocal microscope image of J774a.1 macrophages cells treated with lipophilic DiI-loaded F-pSiNPs with lysosome (LysoG; LysoTracker Green) and nuclei (DAPI) staining (left), and lipophilic DiO- and Cy3-siRNA loaded F-pSiNPs (right); **(c)** confocal microscope image of J774a.1 macrophages cells treated with DiI-loaded non-fusogenic porous silicon nanoparticles (NF-pSiNPs) with lysosome (LysoG; LysoTracker Green) and nuclei (DAPI) staining (left), and DiO- and Cy3-siRNA loaded F-pSiNPs (right).
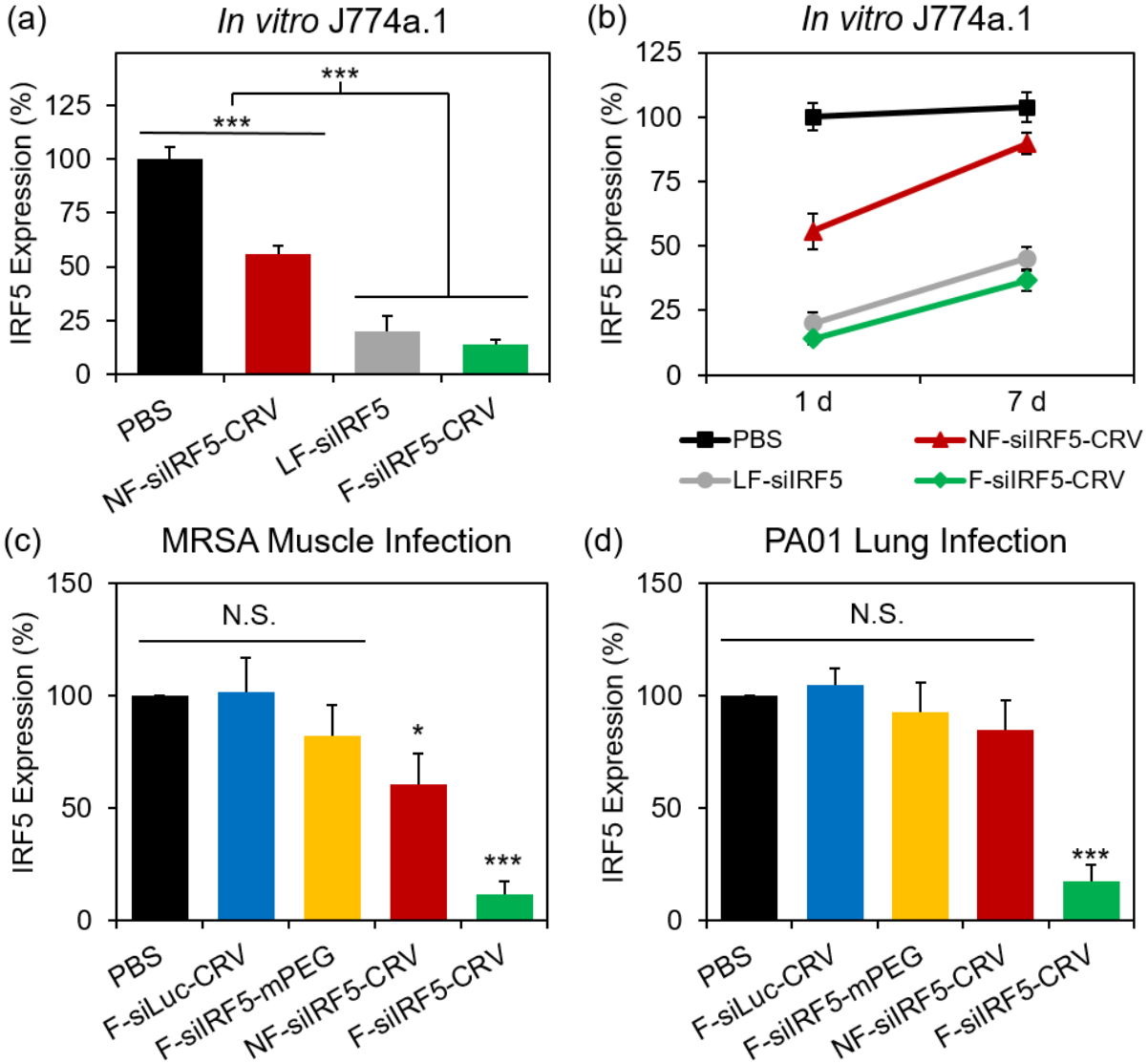
Figure 6.2. *In vitro* and *in vivo* gene silencing efficiency of fusogenic nanoparticles.
(a) *in vitro* knockdown of *irf5* gene expression in J774a.1 macrophages treated with PBS, non-fusogenic pSiNPs loaded with siIRF5 and conjugated with CRV peptide (NF-siIRF5-CRV), Lipofectamine 2000 with siIRF5 (LF-siIRF5), or fusogenic pSiNPs loaded with siIRF5 and conjugated with CRV peptide (F-siIRF5-CRV). Bars represent standard deviation with n=6; *** represent p<0.01 from One-way ANOVA with Tukey's post hoc analyses; **(b)** *irf5* gene expression change from 1 day to 7 days post-transfection of J774a.1 macrophages with PBS, NF-siIRF5-CRV, LF-siIRF5, or F-siIRF5-CRV. Bars represent standard deviation with n=6; **(c)** *irf5* gene expression in purified macrophages from the MRSA muscle infection site of mice that were intravenously injected with PBS, fusogenic pSiNPs loaded with siLuc and conjugated with CRV peptide (F-siLuc-CRV), fusogenic pSiNPs loaded with siIRF5 without peptide conjugation (F-siIRF5-mPEG), NF-siIRF5-CRV, or F-siIRF5-CRV. Bars represent standard deviation with n=6; *** represent p<0.01 from One-way ANOVA with Tukey's post hoc analyses; **(d)** *irf5* gene expression in purified macrophages from the PA01 lung infection of mice that were intravenously injected with PBS, F-siLuc-CRV, F-siIRF5-mPEG, NF-siIRF5-CRV, or F-siIRF5-CRV. Bars represent standard deviation with n=6; *** represent p<0.01 from One-way ANOVA with Tukey's post hoc analyses.
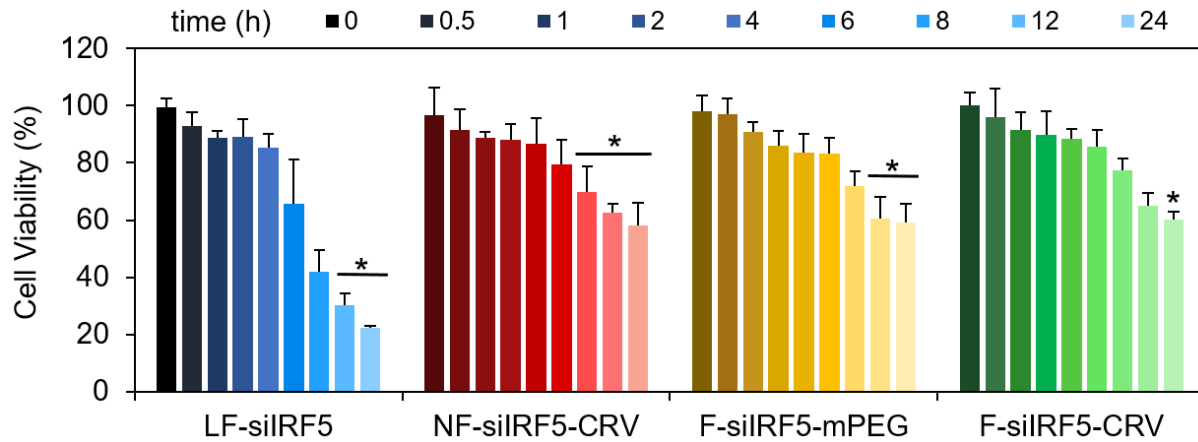
Figure 6.3. *In vitro* **cytotoxicity of transfectant agents in relation to incubation time.**
J774a.1 macrophages were incubated with equimolar doses of siRNA against *Irf5* (siIRF5) with
Lipofectamine 2000 (LF-siIRF5), non-fusogenic pSiNPs loaded with siIRF5 and conjugated with CRV
peptide (NF-siIRF5-CRV), fusogenic pSiNPs loaded with siIRF5 without homing peptide (F-siIRF5-
mPEG), or fusogenic pSiNPs loaded with siIRF5 and conjugated with CRV peptide (F-siIRF5-CRV).
Cells were incubated with the formulations for 0.5-24h, and the cytotoxicity was quantified using the
CCK assay. Bars represent standard deviation with n=3; * represent $p < 0.05$ from One-way ANOVA
with Tukey's HSD post hoc analyses.
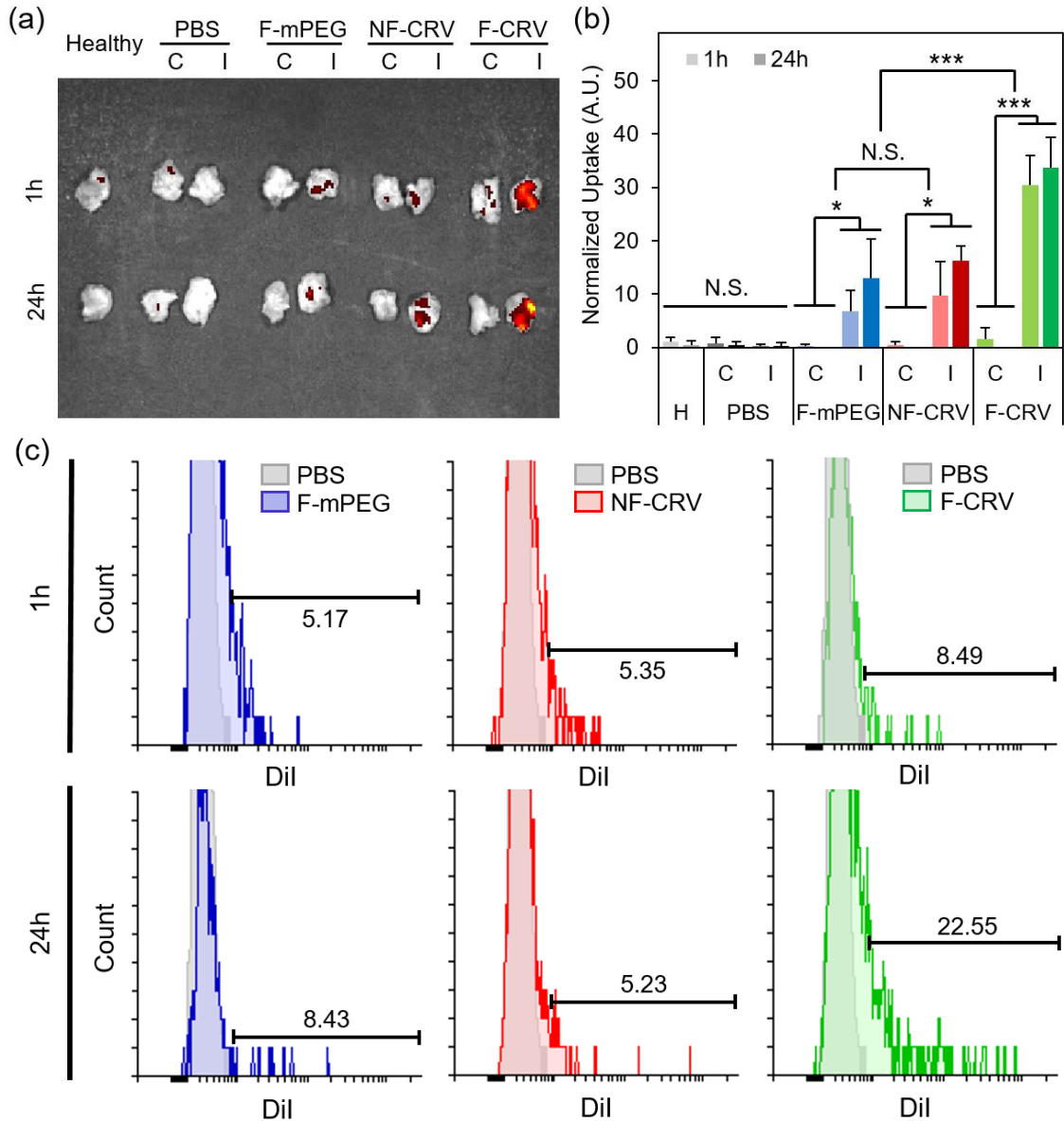
**Figure 6.4. *In vivo* infection homing to MRSA and PA01 infection.**
(a,b) DiI signal accumulation in hind leg muscles ('C' represents the contralateral muscle to the infected side, and 'I' represents ipsilateral muscles with the infection) of healthy (H) mice, and MRSA-infected mice. Mice were intravenously injected with PBS, DiI-loaded fusogenic pSiNPs loaded with siIRF5 without peptide conjugation (F-mPEG), DiI-loaded non-fusogenic pSiNPs loaded with siIRF5 and conjugated with CRV peptide (NF-CRV), or DiI-loaded fusogenic pSiNPs loaded with siIRF5 and conjugated with CRV peptide (F-CRV); **(a)** representative image obtained by IVIS 200; **(b)** ImageJ quantification of the DiI accumulation signal. Bars represent standard deviation with n=3; N.S. represents no significance, * represent p<0.05 and *** represent p<0.01 from One-way ANOVA with Tukey's HSD post hoc analyses; **(c)** DiI signal quantification using flow cytometry of macrophages purified from the bronchoalveolar lavage (BAL) fluid and the infected lung homogenates. Samples were harvested from mice intravenously injected with DiI loaded F-mPEG, NF-CRV, or F-CRV. Data is representative of n=3.
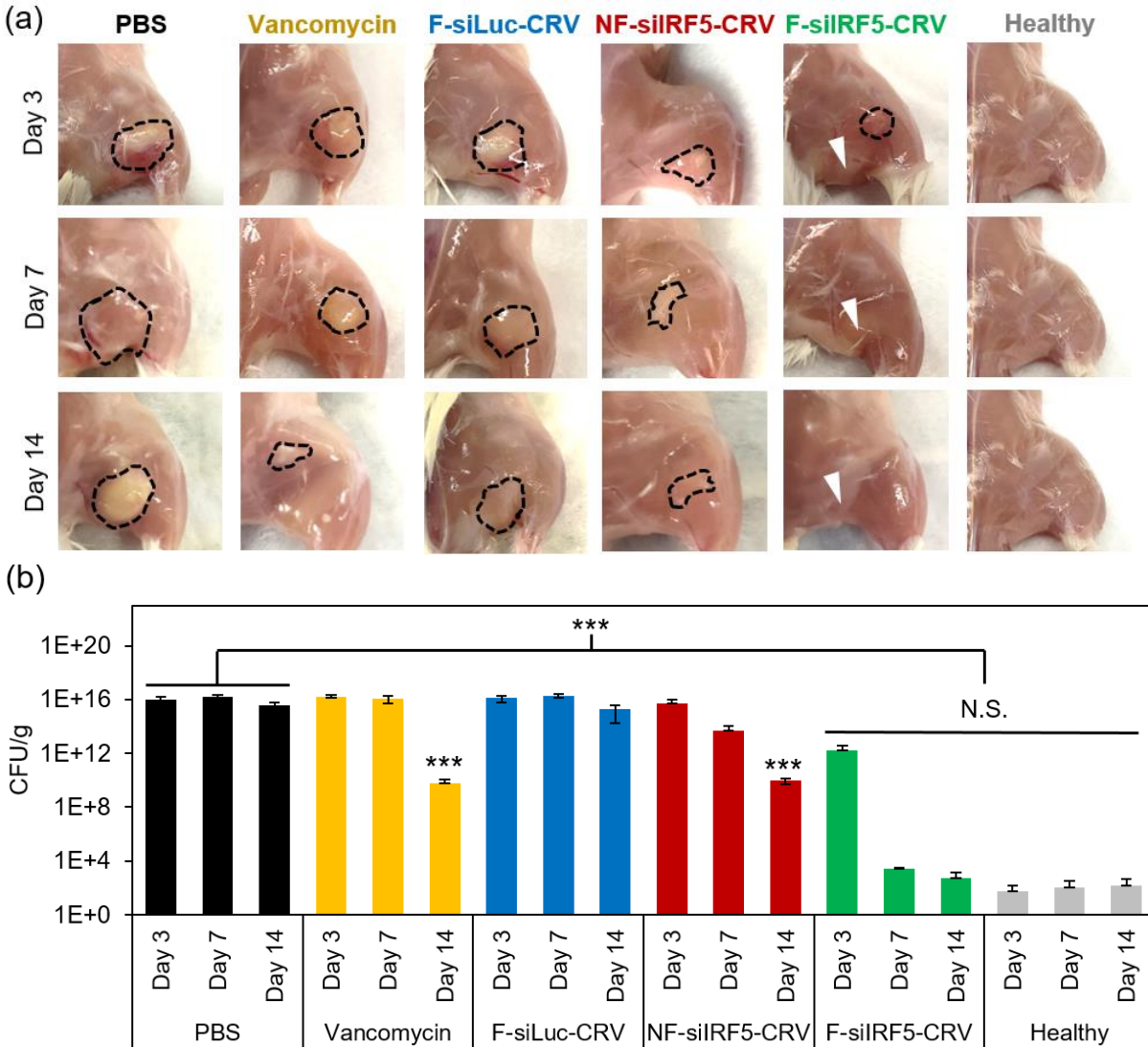
Figure 6.5. *In vivo* **therapeutic efficacy in MRSA muscle infection.**
(a) Photographs of healthy hind leg muscles and MRSA-infected hind leg muscles of mice that were intravenously injected with PBS, 145 mg/kg vancomycin, fusogenic pSiNPs loaded with siLuc and conjugated with CRV peptide (F-siLuc-CRV), non-fusogenic pSiNPs loaded with siIRF5 and conjugated with CRV peptide (NF-siIRF5-CRV), or fusogenic pSiNPs loaded with siIRF5 and conjugated with CRV peptide (F-siIRF5-CRV). Mice were sacrificed and imaged at days 3, 7, and 14 post-injection. Dotted lines outline abscess, and white arrowheads indicate popliteal lymph nodes; **(b)** Bacterial titer from muscles of healthy and MRSA-infected mice intravenously injected with PBS, 145 mg/kg vancomycin, non-fusogenic, targeted nanoparticle containing siIRF5 (NF-siIRF5-CRV), fusogenic, targeted nanoparticle containing siRNA against luciferase, as a negative control for siIRF5 (F-siLuc-CRV), and fusogenic, targeted nanoparticle containing siIRF5 (F-siIRF5-CRV). Animals were infected on day 0 and therapeutic or control injections were given on day 1. Bars indicate standard deviation with n=6. *** represent $p < 0.01$ from One-way ANOVA with Tukey's HSD post hoc analyses.
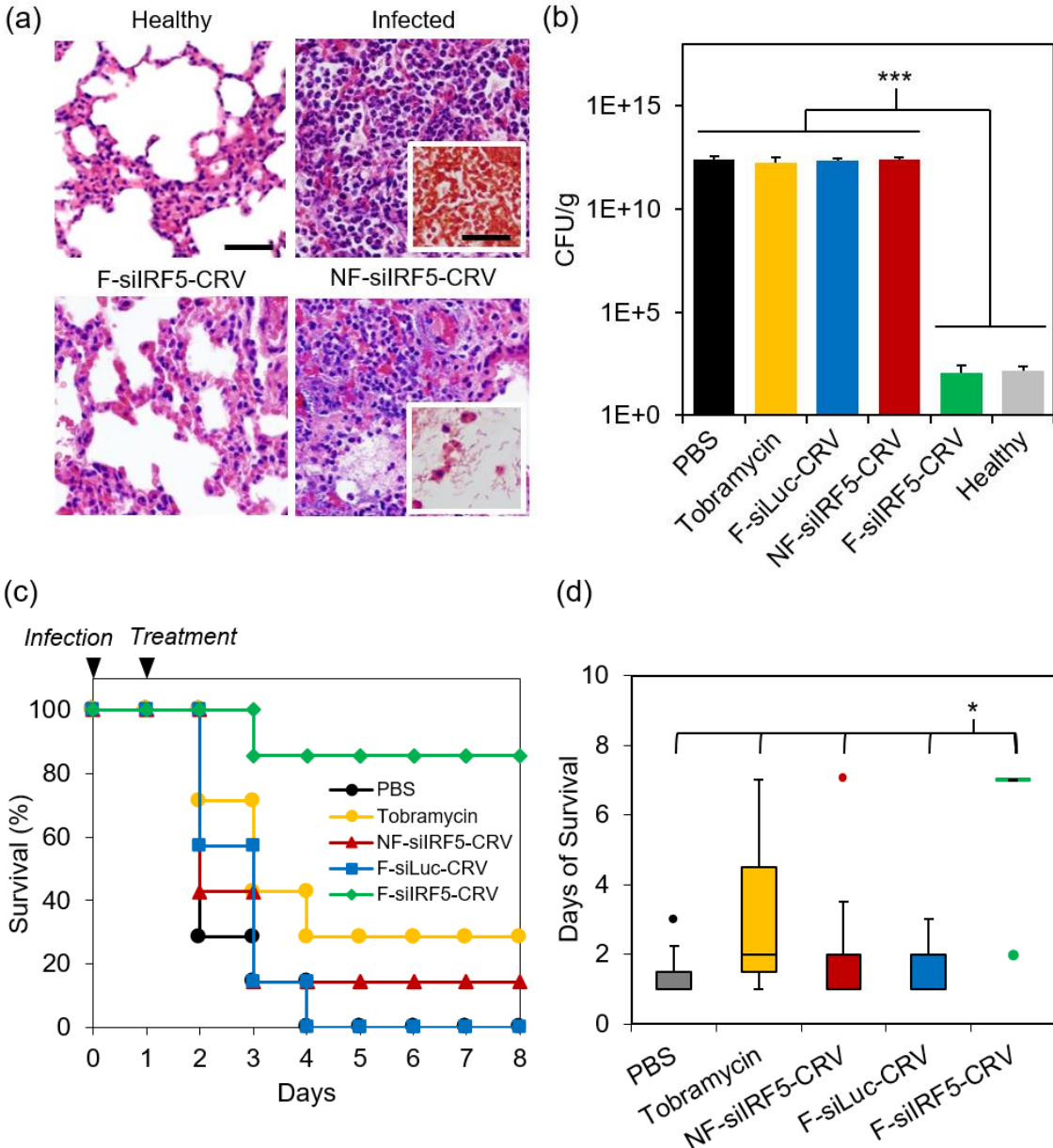
Figure 6.6. *In vivo* **therapeutic efficacy in PA01 lung infection.**
(**a**) H&E stained sections of mouse lungs subjected to histopathological analyses. Top left panel shows healthy mouse with no treatment, top right panel shows lung of infected mouse with no treatment (inset shows Gram stain), bottom left panel shows lung of infected mouse treated with F-siIRF5-CRV, and bottom right panel shows lung of infected mouse treated with NF-siIRF5-CRV (inset shows Gram stain of PA01 populations in the lung); (**b**) Bacterial titer from lungs of healthy and PA01-infected mice intravenously injected with PBS, tobramycin, fusogenic, targeted nanoparticle containing siRNA against luciferase, as a negative control for siIRF5 (F-siLuc-CRV), non-fusogenic, targeted nanoparticle containing siIRF5 (NF-siIRF5-CRV), and fusogenic, targeted nanoparticle containing siIRF5 (F-siIRF5-CRV). Titers were analyzed at either *ad mortem* (PBS, Tobramycin, F-siLuc-CRV, NF-siIRF5-CRV) or at 7 days post-injection (F-siIRF5-CRV). Bars indicate standard deviation with n=4; (**c**) Mouse survival post-infection (at day 0) and post-therapeutic injection (at day 1) of PBS, Tobramycin, NF-siIRF5-CRV, F-siLuc-CRV, or F-siIRF5-CRV, as indicated. Each group has n=8 mice. (**d**) Average days of survival of mice from (**c**) post-infection (at day 0) and post-therapeutic injection (at day 1). *** represent $p<0.01$ and * represent $p<0.05$ from One-way ANOVA with Tukey's HSD post hoc analyses.

Chapter six, in full, is currently being prepared for submission for publication. **Kim, B.**, Yang, Q., Bhatia, S., Ruoslahti, E., Sailor, M.J. Wide-spectrum immunotherapy against bacterial infection using fusogenic nanoparticles. Manuscript in Preparation. The author of this dissertation was the primary author of the material.

Chapter 7:

Conclusions and Perspectives

7.1   Summary Remarks

This thesis presents the design, synthesis, and application of a novel and effective nanoplatform for the delivery of oligonucleotides. Fusogenic porous silicon nanoparticles are able to diversely target different cell types (e.g. macrophages, tumor cells) by altering the homing peptide decorated on the surface, and consistently attain potent gene silencing effect (>90% *in vitro*, >75% *in vivo*) regardless of the sequence to be knocked down (e.g. *Pi3kγ, Rev3l, Irf5*). The overall therapeutic efficacy of the fusogenic formulations achieved highly positive outcome of disease eradication in cancer, as well as bacterial infections (Gram positive, Gram negative, and antibiotic-resistant types).

7.2   Future Directions

The findings reported in the thesis are exciting, and motivate further explorations to answer more downstream questions that have arisen. The following questions are suggested continuation routes for future studies:

- How can the synthesis of fusogenic nanoparticles be translated into a high-throughput system that meets cGMP requirements?

- How long does the effect of FNP-mediated gene silencing last in relation to transfection duration, siRNA dose, and particle dose?

- What effect does plasma membrane localization (e.g. lipid raft) have on the fusion efficiency?

- Can FNP-mediated immunogene therapy alone attain complete anti-tumor effect if multiple gene expressions were terminated?

- Would mice retain immunity against bacterial infection post-successful FNP therapy if they were re-challenged with the same bacteria?

7.3 Wider Implications

With increasing interest and highlight on novel gene modulating molecules, the fusogenic nanoplatform offers a simple delivery vehicle for not only oligonucleotides, but also other payloads, such as ZFNs, TALENS, or CRISPR/Cas9 complexes. With flexible and facile porous silicon modification to alter pore size, particle size, and loading chemistry, simple optimization are expected to yield stable fusogenic particles for the delivery of a wide range of payloads. Thus, the work presented in the thesis has strongly demonstrated the generalizability of the fusogenic porous silicon nanoplatform as a potential research aid, as well as a clinical formulation for gene therapy.